Multiphysics Modeling and Validation of Material Removal in Conventional and Vibration-Assisted Micro-EDM

Doctoral Thesis

by

Mohd Sohaib Raza

(2017MEZ0020)

DEPARTMENT OF MECHANICAL ENGINEERING

INDIAN INSTITUTE OF TECHNOLOGY ROPAR

June 2023

Multiphysics Modeling and Validation of Material Removal in Conventional and Vibration-Assisted Micro-EDM

A Thesis Submitted

In Partial Fulfillment of the Requirements

for the Degree of

DOCTOR OF PHILOSOPHY

by

Mohd Sohaib Raza

(2017MEZ0020)

DEPARTMENT OF MECHANICAL ENGINEERING

INDIAN INSTITUTE OF TECHNOLOGY ROPAR

June 2023

Mohd Sohaib Raza: *Multiphysics Modeling and Validation of Material Removal in Conventional and Vibration-Assisted Micro-EDM*

This Thesis

is

Dedicated

To

"My loving parents"

Rafath Sultana and ***Mohammed Abdul Jaleel***

Who have always filled my heart with love, encouraged my studies,

and showed me that investing in education is the true wealth of life

Declaration of Originality

I hereby declare that the work which is being presented in the thesis entitled **Multiphysics Modeling and Validation of Material Removal in Conventional and Vibration-Assisted Micro-EDM** has been solely authored by me. It presents the result of my own independent investigation/research conducted during the time period from **January 2018** to **June 2023** under the supervision of **Dr. Chandrakant K. Nirala**, Assistant Professor, Mechanical Department, Indian Institute of Technology Ropar. To the best of my knowledge, it is an original work, both in terms of research content and narrative, and has not been submitted or accepted elsewhere, in part or in full, for the award of any degree, diploma, fellowship, associateship, or similar title of any university or institution. Further, due credit has been attributed to the relevant state-of-the-art and collaborations with appropriate citations and acknowledgments, in line with established ethical norms and practices. I also declare that any idea/data/fact/source stated in my thesis has not been fabricated/ falsified/ misrepresented. All the principles of academic honesty and integrity have been followed. I fully understand that if the thesis is found to be unoriginal, fabricated, or plagiarized, the Institute reserves the right to withdraw the thesis from its archive and revoke the associated Degree conferred. Additionally, the Institute also reserves the right to appraise all concerned sections of society of the matter for their information and necessary action. If accepted, I hereby consent for my thesis to be available online in the Institute's Open Access repository, inter-library loan, and the title & abstract to be made available to outside organizations.

Signature

Name: Mohd Sohaib Raza
Entry Number: 2017mez0020
Program: Ph.D.
Department: Mechanical
Indian Institute of Technology Ropar
Rupnagar, Punjab 140001

Date:

Acknowledgments

First and above all, I praise ***Allah, the almighty*** for providing me this opportunity and granting me the capability to proceed successfully by the *sadaqah* of his beloved ***prophet Muhammad (pbuh)***. The main source of motivation behind pursuing this *PhD* at first is the order of my beloved ***Shaikh Syed Kazim Pasha Qadri Al Moosavi Al Jeelani (Rehmathullahi alaihi).*** This piece of work would not have been accomplished without the blessings of my ***parents*** and support of my brothers ***(Sohail Akram, Musaib Shuja, Abdul quader shurjeel*** and sisters ***(Afshan Tabassum, Bushra Fatima, Ayesha siddiqua)***. A special mention to my wife (***Sana)*** who has been extremely supportive of me throughout this entire process. She has raised our first baby (***Haider Hasan)*** in my absence with utmost care and love and has made countless sacrifices to help me get to this point. This thesis appears in its current form due to the assistance and guidance of several people. I would therefore like to offer my sincere thanks to all of them.

I wish to thank my supervisor **Dr. Chandrakant K. Nirala**, Assistant Professor, Department of Mechanical Engineering, IIT Ropar, for introducing me to this exciting field of research. Dr. Nirala is not only a scholarly instructor but also a portrait of inspiration and encouragement, without whom it would have not been possible for me to complete my work. I appreciate all his contributions of time, ideas, and funding to make my Ph.D. experience productive and stimulating.

I would further like to express my appreciation to the members of my Doctoral Committee: **Prof. Navin Kumar** (Chairperson, Professor, Mechanical Department, IIT Ropar), **Dr. Anupam Agrawal** (Associate professor, Mechanical Department, IIT Ropar,), **Dr. Ravi Kant** (Assistant professor, Mechanical Department, IIT Ropar), **Dr. Suman Kumar** (Assistant professor, Electrical Department, IIT Ropar), for reviewing my research work and providing me the technical guidance from time to time to improve the quality of my work. I also thanks **Prof. Sounak Kumar Choudhury** from IIT Kanpur, **Prof. I.A.Palani** from IIT Indore, and **Prof. Grzegorz Krolczyk** from Opole University of Technology, Poland for providing important insights in my synopsis seminar and evaluating my thesis.

Special regards to my lab mates, colleagues and friends, for always standing by my side in every difficulty and sharing a great relationship as compassionate friends.

Mohammed Sohaib Raza

Certificate

This is to certify that the thesis entitled **Multiphysics Modeling and Validation of Material Removal in Conventional and Vibration-Assisted Micro-EDM**, submitted by **Mohd Sohaib Raza (2017mez0020)** for the award of the degree of **Doctor of Philosophy** of Indian Institute of Technology Ropar, is a record of bonafide research work carried out under my guidance and supervision. To the best of my knowledge and belief, the work presented in this thesis is original and has not been submitted, either in part or full, for the award of any other degree, diploma, fellowship, associateship or similar title of any university or institution.

In my opinion, the thesis has reached the standard fulfilling the requirements of the regulations relating to the Degree.

Signature of the Supervisor
Dr. Chandrakant K. Nirala
Department of Mechanical Engineering
Indian Institute of Technology Ropar
Rupnagar, Punjab 140001, India
Date:

Lay Summary

In today's world, there is a growing demand for small and precise products in various industries. To meet this demand, micromanufacturing processes need to continually improve in terms of accuracy and surface quality. One machining method that stands out is electrical discharge machining (EDM), which can work with hard materials. However, when downscaled to micro-EDM, it faces challenges like low material removal rate, surface roughness, and tool wear. Understanding the interactions between the plasma and electrodes in micro-EDM is still limited, highlighting the need for process modeling. To address this, a numerical model using the finite element method is developed to estimate plasma parameters and understand heat transfer mechanisms in micro-EDM. The model predicts plasma channel diameter, temperature distribution, and heat flux. Experimental observations are compared with simulation results, showing good agreement. Additionally, a pulse monitoring system (PMS) is introduced to monitor discharge pulses in real-time. The PMS provides information on discharge energy, material removal, and tool wear, enabling better control of the micro-EDM process. The thesis also explores the use of ultrasonic vibration assistance in micro-EDM to improve machining performance. A comparative study between unassisted and vibration-assisted micro-EDM is conducted, showing that vibrations increase the stability of the process and enhance the material removal rate by up to 35%. The output of the plasma model is utilized to predict crater formation with and without vibration assistance, and the model is validated through single discharge experiments.

Abstract

With the ever-increasing demand for small and precise products across various industries, micromanufacturing has become more critical than ever. Micromanufacturing processes must continuously improve to produce components with tighter tolerances, higher accuracy, and superior surface integrity to meet the growing demand for such products. Non-conventional machining methods have gained immense importance in the manufacturing industry due to the high demand for precise and micro components of hard-to-cut materials. Electrical discharge machining (EDM) comes with the advantage of machining materials irrespective of their hardness. Still, it has inherent disadvantages, such as low material removal rate (MRR), debris adhesion, high surface roughness, tool wear, etc. Most of these issues are magnified when the process of EDM is downscaled to micro-EDM. Despite numerous experimental attempts, there is still less understanding of all the interactions between the plasma and electrodes in the micro-EDM process, emphasizing the necessity for process modeling. A numerical model using the multiphysics finite element method is developed to estimate the plasma parameters, such as the plasma channel diameter and temperature distribution in the radial and axial directions. The numerical model also predicts the heat flux distribution and explains the plasma-electrode interactions via different heat transfer mechanisms such as conduction, convection, radiation, and thermionic effect. Experimental plasma diameters obtained from high-speed imaging of the discharge process were compared with the simulation results to discuss the validity of the proposed model. Percentage errors varying from 5.06 % to 14.5 % are observed. A pulse monitoring system (PMS) is then presented to monitor the discharge pulses for a controlled RC-based micro-EDM in real-time. The acquired information from the developed PMS explains the variations in discharge energy, material removal, and tool wear with increasing machining depth. After exploring the fundamentals of the process, the Hybridization of the micro-EDM process is analyzed to improve the machining performance by conducting a comparative study between the unassisted and ultrasonic vibration-assisted micro-EDM. Vibrations assistance enhanced the machining stability by increasing the percentage of contributing discharges by 19%. The ultrasonic vibrations proved beneficial in addressing the primary issue associated with the micro-EDM process, i.e., low MRR with a maximum of 35% increment. Finally, the output of the plasma model is utilized to predict the crater formation with and without vibration assistance. The crater model is validated using single discharge experiments to discuss the material removal mechanism with vibration assistance.

List of Publications from Thesis

Journals

1. **Sohaib Raza**, Hreetabh Kishore, Chandrakant Kumar Nirala, K.P. Rajurkar, Multiphysics modeling and high-speed imaging-based validation of discharge plasma in micro-EDM, CIRP Journal of Manufacturing Science and Technology, Volume 43, 2023, Pages 15-29, https://doi.org/10.1016/j.cirpj.2023.02.006.
2. **Raza, S.,** Nadda, R. & Nirala, C.K. Real-time data acquisition and discharge pulse analysis in controlled RC circuit based Micro-EDM. Microsystem Technologies (2023). https://doi.org/10.1007/s00542-023-05432-x.
3. **Sohaib Raza** and Chandrakant Kumar Nirala, "Multiphysics simulation of plasma channel formation during micro-electrical discharge machining", AIP Advances 11, 025138 (2021) https://doi.org/10.1063/5.0028665.
4. **Raza, S**., Nadda, R. & Nirala, C.K. Discharge Pulse Analysis Based Machining Responses in Vibration-assisted µEDM Processes. *MAPAN* **37**, 777–792 (2022). https://doi.org/10.1007/s12647-022-00591-0.
5. **Raza, S**., Nadda, R. & Nirala, C.K. Analysis of Discharge Gap using Controlled RC based Circuit in µEDM Process. *J. Inst. Eng. India Ser. C* **103**, 21–27 (2022). https://doi.org/10.1007/s40032-021-00711-w.
6. **S. Raza,** R. Nadda, and C.K. Nirala, "Sensors-based discharge data acquisition and response measurement in ultrasonic assisted micro-EDM drilling," Measurement: Sensors 29, 100858 (2023). https://doi.org/10.1016/j.measen.2023.100858
7. **Raza, S.,** Airao, J., and Nirala, C. K. (July 26, 2023). "Performance Measurement and Discharge Data Based Analysis of Ultrasonic Assisted µEDM for Ti6Al4V." ASME. J. Micro Nano-Manuf. September 2023; 10(3): 031004. https://doi.org/10.1115/1.4062819.
8. **Sohaib Raza**, Chandrakant Kumar Nirala. "Comparative Analysis of Single Crater Parameters in Ultrasonic Assisted and Unassisted Micro-EDM of Ti6Al4V using Discharge Plasma Imaging". *Nanotechnology and Precision Engineering (Under Review).*

Conferences

1. **Sohaib Raza**, Sujit Kadam, Hreetabh Kishore and Chandrakant Kumar Nirala, "Simulation of Crater Formation During the Micro EDM Process using the ALE Method", *World Congress on Micro and Nano Manufacturing* (WCMNM-22), *KU Leuven, Mechanical Engineering Department, September 19-22, 2022, Belgium.*
2. **Sohaib Raza**, Chandrakant Kumar Nirala, "Sensors based real-time pulse categorization in controlled RC-circuit Micro-electrical discharge machining", *Measurement, Sensor Systems and Applications Conference, Qilu University of Technology and the Shangdong Academy of Science Laser Institute, 24-26 August 2022.*
3. **Sohaib Raza**., Nadda, R. & Nirala, C.K. *"*Discharge Gap Analysis of Controlled RC based µEDM Process*". In 11th international conference on precision, Meso, micro and Nano Engineering (COPEN 11). Indian Institue of Technology Indore, India. December 12-14, 2019.*

Table of Contents

List of Figures

List of Tables

Notations and Abbreviations

F_a	Fraction of energy to anode	$P_{in,e}$	input power to the electrons
F_c	Fraction of energy to cathode	p_w	work done by the species for plasma expansion
F_d	Fraction of energy to dielectric	P_{rad}	power loss from plasma due to radiation
V_{in}	Open circuit voltage	I	discharge current
T_b	Boiling point (K)	C_{peff}	Effective specific heat
R	Heat source radius (m)	Q_{inele}	power loss due to inelastic collisions
k	Thermal conductivity (W/mK)	Q_{el}	power loss due to elastic collisions
h	Convective heat transfer coefficient (W/m^2K)	P_{wall}	power lost by the species at the electrode wall
T_s	Solidus temperature (K)	P	discharge power
T_l	Liquidus temperature (K)	$\dot{q}$	internal energy generation per unit volume
T_m	Melting temperature (K)	H	specific enthalpy
T_e	Evaporation temperature (K)	V	total velocity vector of the flow
ρ_s	Solid density (kg/m^3)	S_h	factor that includes latent heat
ρ_l	Liquid density (kg/m^3)	$q(t)$	Time varying heat flux
L_m	Latent heat of melting (J/kg)	Erfc	error function
β	Thermal expansion coefficient (K^{-1})	J_0	Bessel function
C_p	Specific heat (J/(kg K)	J_1	Bessel function
K	Thermal conductivity (W/m K)	$U(t)$	tool tip displacement
ε	Radiation emissivity	A	vibration amplitude
Q_p	Plasma heat flux (W/m^2)	F	Vibration frequency
$\frac{\partial \gamma}{\partial T}$	Temperature derivative of the surface tension (N/mK)	J	Current density (A/m^2)
μ	Dynamic viscosity (Pa. s)	$Q_{j,v}$	current source (A/m^2)
α	Thermal diffusivity (m^2/s)	E	Electric field strength
n_e	Electron density	Q_{rad}	net volumetric emission coefficient (W/m^3)
T_e	Electron temperature	Q_p	Plasma heat source
K	Boltzmann constant	P	dielectric density
e	Electron charge	U	velocity vector
φ	potential difference	P	fluid pressure

n_o	initial electron density	F	volume force vector
φ_w	cathode potential	Q_b	cumulative heat flux at the electrode boundary
n_{se}	common ion/electron density	N	the unit normal vector perpendicular to the electrode surface
N_e	numbers of electrons	V_{ion}	plasma ionization potential
N_i	numbers of ions	φ_s	work function of the cathode electrode surface
A_s	Richardson's constant in (A/m^2K)	T_{off}	Transistor off time
C	Capacitance	t_d	Ignition delay time
D_f	Discharge frequency	R_a	Average roughness
E_{tp}	Actual supplied energy of pulse	Δt	time duration between the two consecutive data points
E_{max}	Maximum discharge energy	F	centrifugal force
T_{on}	Transistor on time	ω	angular velocity of the rotor
H_f	Latent heat of fusion	q_{lv}	Latent heat of vaporization
P_{atm}	Atmospheric pressure	P_{atm}	Recoil pressure
P_{atm}	Acoustic pressure	F_{us}	Ultrasonic frequency
γ	Surface tension	V_{mesh}	Mesh velocity
F_{ev}	Metal vapor flux	Cs	Velocity of sound in m/s
V_{max}	Open circuit voltage	CNC	Computer numerical control
V_{RT}	Real-time volume	FEM	Finite element modeling
m	mass of the eccentric rotor	MHD	Magneto hydrodynamics
ALE	Arbitrary Lagrangian-Eulerian	BC's	Boundary conditions
MRR	Material removal rate	PMS	Pulse monitoring system
TWR	Tool wear rate	DAQ	Data acquisition system
EDM	Electrical discharge machining	CAD	Computer aided design
IEG	Interelectrode gap	RC	Resistance capacitance
SEM	Scanning electron microscope	RPM	Rotations per minute
VRD	Volume removed per discharge	SR	Surface roughness
EPF	energy partition factor	ERM	Eccentric rotating mass
LTE	Local thermal equilibrium	MEMS	Micro electro mechanical systems

Chapter 1

Introduction

1.1 Background

1.1.1 Importance of micro-EDM in micromanufacturing

Micromanufacturing refers to the fabrication of miniature components and structures with dimensions ranging from a few micro meters to a few hundred micro meters [1]. The origins of micromanufacturing can be traced back to the 1950s when the semiconductor industry started using photolithography to create intricate patterns on silicon wafers. Micromanufacturing techniques allow for the fabrication of devices with micro-features essential in biomedical devices, aerospace, automobiles, energy, semiconductors, biotechnology, electronics, and communication. Microsystems-based products, such as medical implants, drug delivery systems, diagnostic devices, connectors, switches, micro-reactors, micro-engines, micro-pumps, and printing heads, add significant value to many companies and contribute to a sustainable economy. Micromanufacturing processes must continuously improve to produce components with tighter tolerances, higher accuracy, and repeatability to meet the growing demand for such products [2]. The continuous research and development of micromanufacturing techniques are thus vital to meet the future needs of micromanufacturing. The challenges in the micromanufacturing techniques differ, although most technologies are derived from the existing macro-scale manufacturing methods.

Conventional manufacturing processes such as turning, drilling, milling, and grinding have been used for years to produce various components and products. However, these processes have certain limitations, particularly when machining materials that are difficult to machine or require very high precision. Conventional machining methods are unsuitable for micromanufacturing because they generate excessive heat and vibration, damaging small and delicate structures. There are well-developed techniques based on Micro Electro Mechanical Systems (MEMS) among the various micromanufacturing processes [3]. These MEMS-based processes include photolithography, chemical-etching, plating, and LIGA. However, there are certain limitations to MEMS techniques. They are primarily restricted to working with silicon or silicon-like materials and can only fabricate features in 2D or 2.5D. Additionally, the significant capital investments and the need for cleanroom environments hinder their ability to meet the growing demands of micromanufacturing, which require diverse materials, complex 3D geometries, and high levels of accuracy.

As the demand for smaller and more precise components increased, traditional

machining methods became less effective. This has led to the development of non-conventional manufacturing processes, which offer new and innovative ways to machine materials. Unconventional manufacturing processes, such as EDM, laser cutting, and ultrasonic machining, offer several advantages over conventional techniques. For example, these processes can be used to machine materials that are difficult or impossible to machine using conventional methods. They also offer higher precision and accuracy and the ability to produce complex and intricate shapes. One of the most important unconventional manufacturing processes is EDM, which uses a series of electrical discharges to remove material from a workpiece. Micro-EDM is essentially the same but a downscale version of EDM, allows for the precise and intricate shaping of complex geometries with high accuracy. It offers numerous advantages in the context of micromanufacturing. Its ability to operate at a microscopic level makes it ideal for producing intricate features, microstructures, and microcomponents with extremely fine detail. The process is capable of working with a wide range of electrically conductive materials, including metals, alloys, and even advanced ceramics, expanding its applicability across various industries. Additionally, it enables the production of micro-sized parts with high aspect ratios, such as deep micro-holes and small cavities, which are difficult to achieve using other techniques.

1.1.2 Historical background of EDM and features of micro-EDM

EDM was discovered in the late 1940s by two Russian scientists, B.R. Lazarenko and N.I. Lazarenko, who were attempting to develop a process to machine tough metals. However, the process was not fully developed until the 1960s, when it was commercialized by the Swiss company Agie. The early versions of EDM used a process known as "spark erosion," where a high-frequency electrical discharge erodes metal from a workpiece. This process was slow and limited to machining conductive materials only. In the 1960s, a new technique known as "die sinking" EDM was developed, which allowed for faster and more precise machining of complex shapes. Die-sinking EDM involves using a specially shaped electrode to erode a workpiece submerged in a dielectric fluid to prevent arcing. A computer-controlled the process, allowing for greater precision and accuracy. In the 1980s, wire EDM was developed, allowing for machining very fine and intricate shapes. Wire EDM involved using a thin wire as the electrode, which was fed through the workpiece in a controlled manner. This allowed for exact cuts and intricate shapes to be created. The development of micro-EDM was a natural extension of these earlier processes. Micro-EDM involves using a small electrode, typically less than 500

microns in diameter, to machine miniature components and structures. The process is generally performed in a dielectric fluid, which helps to cool the workpiece and prevent arcing.

Some advantages and superiority of micro-EDM over other nonconventional manufacturing methods like laser cutting:

- *Capability to machine difficult-to-cut materials*: Beneficial for machining materials that are difficult to cut using other non-conventional methods, such as ceramics, composites, and hardened steels. This is because micro-EDM relies on thermal energy generated by a series of electrical discharges to erode the material rather than relying on cutting or ablation, like in laser cutting.
- *High accuracy and precision*: Known for its ability to achieve very high levels of accuracy and precision, which makes it a popular choice for manufacturing miniature components such as microelectromechanical systems (MEMS) and precision molds. This is because micro-EDM does not introduce significant heat-affected zones that can cause distortion, and the process allows for precise control over the depth and shape of the machined features.
- *Ability to machine complex shapes*: Capable of machining intricate and complex shapes with ease, making it an ideal choice for producing molds, dies, and other components with complicated geometries. The process allows for fabricating sharp corners and narrow slots, which are difficult to machine using other nonconventional methods.
- *High surface finish quality*: Can produce excellent surface finishes with roughness values as low as a few micrometers. This is because the process removes material through spark erosion, which does not create burrs or other surface defects like mechanical machining processes do.
- *Minimal thermal damage*: A non-contact machining process, meaning there is no direct contact between the tool and the workpiece. This results in minimal thermal damage to the workpiece, which is particularly important for materials prone to distortion or cracking when exposed to high temperatures, such as ceramics.

While laser cutting has some advantages over micro-EDM, such as faster cutting speeds and the ability to cut through thicker materials, it is less accurate and less precise. Laser cutting can also introduce thermal distortions and cause heat damage to the machined material, which can be a limitation in specific applications. Overall, micro-EDM remains a highly competitive option for machining intricate and complex shapes, and it is the preferred method for many applications that require high precision, accuracy, and surface quality.

1.2 Basic principle, Challenges, and Possible Solutions

EDM consists of a pair of conductive electrodes called a tool and workpiece submerged in a dielectric fluid. When sufficient interelectrode gap (IEG) is maintained between the tool and the workpiece, high-frequency electrical discharges are created, causing the material to be removed from both electrodes. The process can be controlled to produce extremely fine features with sub-micron accuracy. A plasma column is formed between the tool and the workpiece during a single discharge, as shown in Figure 1.1. The plasma-electrode interactions result in crater formation and material removal. Different stages of the process are identified as gap ionization, plasma column formation, plasma implosion at the end of pulse-on time, and eventually, ejection of molten material from the tool and work electrodes [4]. Despite the advantages stated in the previous section, it has inherent disadvantages, such as low material removal rate (MRR), debris adhesion, high surface roughness, etc. [5,6]. The extent of these shortcomings of the EDM process magnifies when the process is performed at a micro-scale due to a very narrow IEG of about 1-10 microns. Hybridization of the EDM process with ultrasonic vibrations has been identified as a feasible technique to overcome the inherent disadvantage of poor flushing of the debris and the frequent short-circuiting phenomenon [7,8]. Various modes of ultrasonic vibrations during the EDM process were studied, such as the vibrations applied to the workpiece electrode, tool electrode, and dielectric medium. Applying vibration to the workpiece offers several advantages. Firstly, it increases the MRR, allowing for faster machining. During the vibration of the workpiece, its forward and backward movement causes pressure variations in the IEG at high frequencies. This contributes to the expulsion of debris from the IEG and enhances the efficiency of the flushing process. Continuous supply of recovered insulating medium into the machining zone improves stability and significantly increases the MRR. Applying ultrasonic vibrations to the tool electrode during the micro-EDM is identified as a challenging task as the direction of the tool feed becomes parallel to the direction of the ultrasonic vibration and increases the probability of tool deflection. Such an approach in the micro-EDM has enhanced machining performance and increased the potential of fabricating precise and intricate geometries with high aspect ratios.

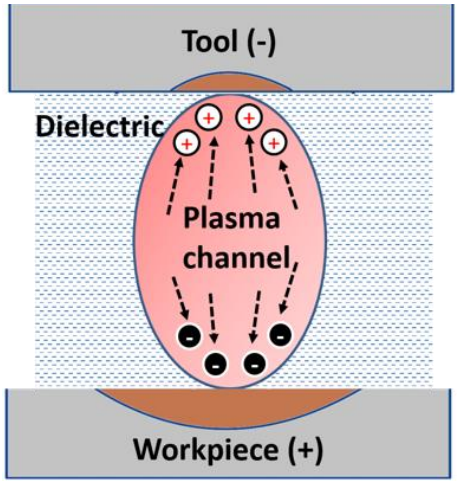

Figure 1.1 Plasma-electrode interactions in the IEG

Although EDM has been studied extensively in the literature from the modeling of crater formation and the experimental perspective, there is a clear gap in the modeling and simulation of plasma channel formation. The commonly used assumption of the plasma channel as a heat source in most literature gives a reasonably good approximation when the EDM is performed at a macro scale. However, in micro-EDM, the size effect significantly influences some critical aspects of the process physics, such as the highly concentrated current density due to a very small IEG and the hydrodynamics of the dielectric fluid in the narrow opening. The fraction of energy entering the electrodes is substantially different for macro and micro-EDM due to very short pulse duration, low voltage/current, etc. The numerical study of the plasma formation can help gain insights into the multiphysics processes and would be vital for tackling the difficulties in experimental research [9,10]. Plasma modeling can help understand the physical mechanisms at the plasma-electrode interface controlling material removal. Additionally, plasma modeling can aid in designing new micro-EDM systems and optimizing process parameters such as pulse duration, pulse frequency, and voltage. As the EDM process depends upon the input electrical energy supplied by the circuit, monitoring the real-time current and voltage signals is essential to evaluate the stability of the process.

1.3 Motivation, Objectives, and Scope

1.3.1 Motivation

The demand for micro-EDM has been growing quickly, primarily driven by the increasing demand for micro and nanoscale components in various industries, including aerospace, medical devices, and microelectronics. The global market for EDM is expected to grow significantly in the coming years, with industries and research organizations' increasing

adoption of EDM technology. The overall market value of the EDM is expected to account for USD 4450 million by 2028, with a large percentage of the share contributed by the automotive and aerospace industry, as shown in Figure 1.2. The increasing demand for electric and light vehicles requires precise and intricate automotive parts with a high strength-to-weight ratio, further strengthening EDM's and micro-EDM's market value. The evolution of Industry 4.0 and automation are also expected to drive the global market of EDM.

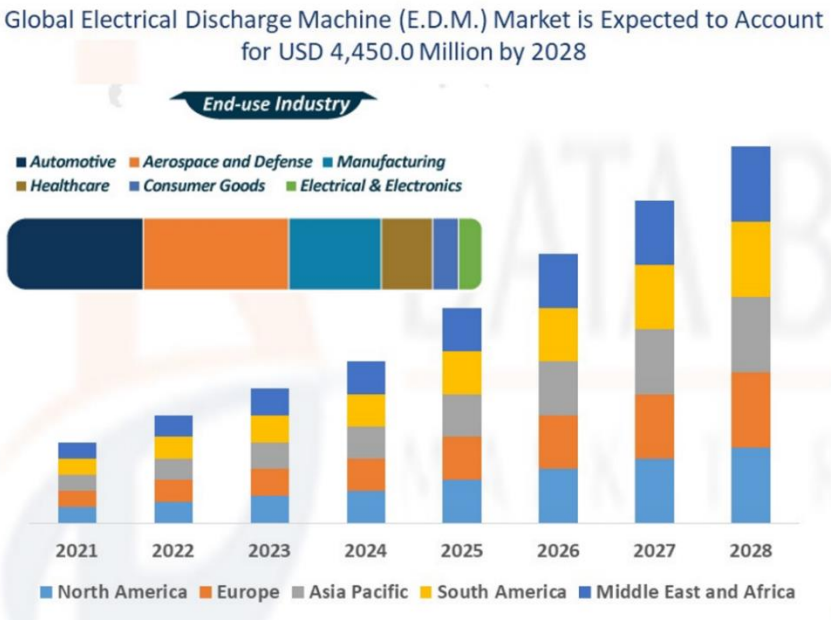

Figure 1. 2 Forecast of the global EDM market [11]

Despite numerous experimental attempts, there is still no comprehensive understanding of all the interactions among the process parameters and the machining characteristics in the micro-EDM process. This emphasizes the necessity for process modeling. Several researchers have attempted to develop finite element models for plasma channel formation to address this challenge. For instance, Katz and Tibbles proposed a dimensionless model to simulate plasma channel formation [11]. The model lacks an explanation of the spatial expansion of plasma, the temperature and heat flux distribution, and its interaction with the workpiece material. Dhanik and Joshi proposed a variable mass-expanding plasma model that considers plasma a time-variable energy source to the cathode and anode [12]. Despite these efforts, the existing models still have limitations regarding accuracy and computational efficiency, which hinders their practical applications. Most of the earlier models are primarily based on macro-EDM, which may not fully capture the physics of micro-EDM. In addition, the previous attempts to model the micro-EDM relied heavily on the empirical models of the plasma channel radius. The available experimental data may limit the accuracy of earlier models, particularly for high-

speed imaging of plasma behavior. Some models may not accurately capture the transient behavior of the plasma channel, particularly during the initial stage of channel formation. Therefore, there is a need for the development of a more robust and accurate finite element model for the plasma channel formation during the micro-EDM process. Such a model can enable better understanding and control of the machining behavior, leading to improved process efficiency and product quality. Additionally, the proposed model can be validated using high-speed imaging of plasma which can further enhance the reliability and accuracy of the model. Following points could be highlighted as motivation towards the proposed work.

- Most EDM and micro-EDM models assume the plasma channel as a heat source to predict crater formation. However, the stochastic process and involvement of multiphysics phenomena such as electrodynamics, thermodynamics, and hydrodynamics demand the modeling of plasma formation.
- The stochastic nature of the micro-EDM process results in the non-isoenergetic nature of the discharge pulses for an RC-based micro-EDM, and hence challenging to create predictive models and integrate the process with automation and Industry 4.0. Therefore, a pulse monitoring system (PMS) appropriate to the type of micro-EDM power supply is essential to categorize the discharge pulses based on their electrical characteristics and their effect on the process stability and efficiency.
- The ultimate aim of modeling the plasma and crater formation along with developing the PMS is to increase the performance of the micro-EDM process. Efforts have been made to hybridize the micro-EDM with vibrations, with most of the literature focusing on the workpiece vibration. However, there are studies related to tool electrode vibration. Still, they are less inclined towards micro-EDM, and a detailed analysis of the machining performance concerning the electrical behavior of the discharge pulses is needed.

1.3.2 Objectives

With the primary goal of Multiphysics modeling and validation of material removal in conventional and vibration-assisted micro-EDM, the following objectives are set to achieve:

1. To develop a finite element model for the plasma channel formation during the micro-EDM process and validation using high-speed imaging.
2. To develop a pulse monitoring system for a controlled RC-based micro-EDM circuit and analyze the nature of discharge pulses obtained during the machining.

3. To implement an ultrasonic vibration-assisted micro-EDM tool holder and perform the experimental analysis on the effect of ultrasonic vibrations on machining outcomes.

1.3.3 Scope of the Work

This research aims to enhance the effectiveness of micro-EDM by gaining a fundamental understanding of the physics underlying the process. A numerical model using the multiphysics finite element method is developed to estimate the plasma parameters, such as the plasma channel diameter and temperature distribution in the radial and axial directions. The numerical model also predicts the heat flux distribution responsible for material melting and subsequent removal. The coupled numerical model also explains the plasma-electrode interactions via different heat transfer mechanisms such as conduction, convection, radiation, and thermionic effect. Experimental plasma diameters obtained from high-speed imaging of the discharge process were compared with the simulation results to discuss the validity of the proposed model. The output of the plasma model is utilized to predict the crater formation. The crater model was validated using single discharge experiments. The modeling work is focused solely on a single discharge operation of micro-EDM, and its scope will be limited to that specific operation.

A pulse categorization strategy is proposed next to monitor the discharge pulses of a controlled RC-based micro-EDM circuit in real time. While being acquired through various sensors, signals are processed in NI LABVIEW-based data acquisition (DAQ) system. Extensive virtual instrumentation categorizes the discharge pulses as contributing, semi-contributing, and non-contributing towards material removal. The developed PMS is simultaneously used to estimate the real-time discharge energies of individual pulses and their histograms with the machining progress. The acquired information from the developed PMS explains the variations in discharge energy, material removal, and tool wear with increasing machining depth. The modeling of the plasma and crater formation and a comprehensive understanding of pulse monitoring helps explore the micro-EDM process's hybridization. It is achieved by conducting comparative studies between the unassisted and ultrasonic vibration-assisted micro-EDM at low frequency and then at an ultrasonic frequency. The characteristics of the discharge waveforms were captured using a data acquisition system, and various machining outcomes were measured, such as recast layer, MRR, TWR, and surface roughness.

1.4 Summary of the Research Work

1.4.1 Methodology

The methodology includes the finite element modeling of the plasma channel formation and expansion with high-speed imaging used for experimental validation, as shown in Figure 1.3. The output from the plasma model is used as input to model the crater formed during the micro-EDM. The crater model is validated by conducting single discharge experiments and the 3D profilometry for the depth and diameter of the crater formation. A pulse monitoring system is developed for the controlled RC-based circuit to study the stability of the process at different machining parameters and depths of machining by conducting micro-EDM drilling experiments. An in-depth study of the discharge pulse behavior helps determine the scope of improvement in the process. A low-frequency vibration setup is developed first as preliminary work to assess the effect of vibrations on the MRR and surface roughness by comparing the machining outcomes of the unassisted and vibration-assisted experiments. An ultrasonic vibration-assisted tool holder is then developed for thorough experimentation and to reduce the limitations of the low-frequency tool holder. Critical machining outcomes such as the discharge pulse nature, MRR, TWR, recast layer, and surface roughness are compared between the normal micro-EDM and the vibration-assisted micro-EDM.

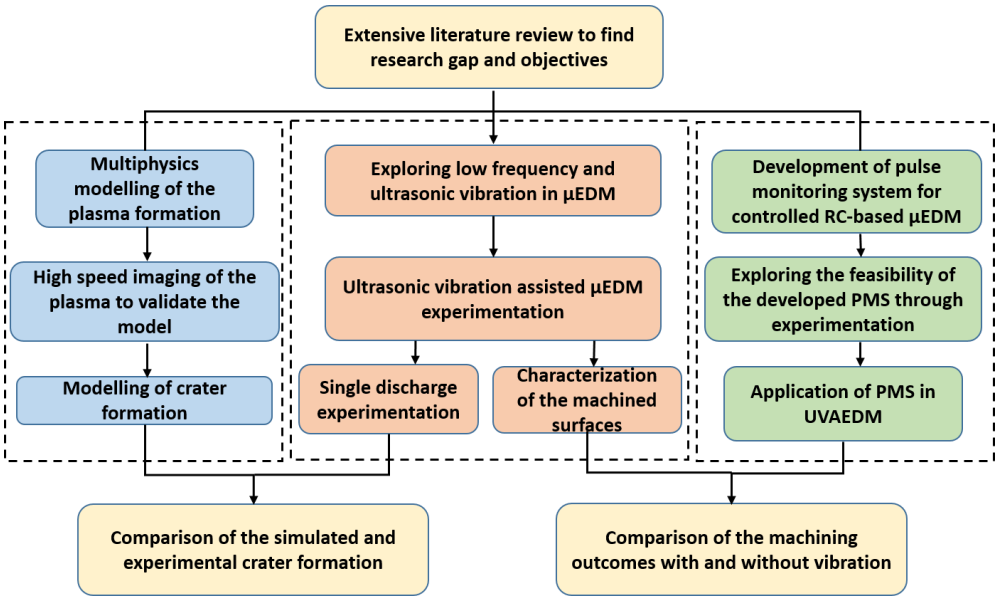

Figure 1.3 Flowchart of the methodology followed in the study

1.4.2 Thesis outline

The outline of the thesis is as follows:

Chapter 1 Introduces the micro electrical discharge machining process with a detailed

discussion of its applications and limitations. It also includes an introduction to the ultrasonic-assisted micro-EDM process as a solution to poor material removal rate and surface integrity in micro-EDM. Moreover, motivation towards the proposed research is presented by exploring the need and benefits of modeling, monitoring, and hybridizing the micro-EDM.

Chapter 2 Presents a detailed review of recent research on plasma modeling techniques for simulating the micro-EDM plasma and crater formation. Moreover, it also includes a review of the vibration-assisted micro-EDM process considering experimental and modeling studies. From the literature review, research gaps are identified to set the objectives.

Chapter 3 Involves the finite element modeling of the plasma channel formation using COMSOL multiphysics during the micro-EDM process. It also includes validating the proposed model with the high-speed imaging of the plasma channel with a detailed discussion on temperature and heat flux distributions.

Chapter 4 Discusses developing a pulse monitoring system for a controlled RC-based micro-EDM power supply using NILABVIEW. Experiments were performed to calculate the discharge energy of the individual pulses and classify the pulses into different categories. The results also compare the MRR and surface quality concerning the nature of discharge pulses obtained during the machining.

Chapter 5 A low-frequency vibration setup is utilized first as preliminary work to determine the effect of vibrations on the MRR and surface roughness by comparing the machining outcomes of the unassisted and vibration-assisted experiments. Given the high frequency of the discharge pulses in micro-EDM, an ultrasonic vibration-assisted tool holder is used for thorough experimentation. A thorough investigation is performed to analyze the effect of ultrasonic vibrations on the nature of discharge pulses, MRR, tool wear rate, recast layer formation, and surface roughness.

Chapter 6 Modeling and simulation of the crater formed during the vibration assistance micro-EDM is performed with the help of the plasma modeling results obtained from Chapter 3. The results of the model are validated using the single discharge experiments.

Chapter 7 Concludes with the results obtained from the vibration-assisted micro-EDM experiments and FEM modeling of plasma and crater formation. It also covers the limitation and future scope concerning the developed experimental setup and finite element model.

Chapter 2

Literature Review

2.1 Introduction

The chapter presents a comprehensive review of research and development in understanding the fundamental principles of the EDM process, focusing mainly on the micro-EDM. It aims to cover various aspects, including recent technological advancements, identified issues, and potential strategies for improvement based on existing research. The literature review is carried out with a focus on modeling and hybridization of the micro-EDM. The literature review is organized into several sections, beginning with an overview of micro-EDM and the theoretical framework for plasma channel formation. Subsequent sections are dedicated to relevant literature on modeling the EDM process, followed by the hybridization of the micro-EDM. The final section summarizes the literature review's main findings and discusses gaps in the literature.

2.2 Overview of the EDM Process

Unconventional machining of difficult-to-cut conductive materials with high accuracy, low heat-affected zone formation, and the ability to cut intricate geometries entitles EDM as the most versatile technology in micromachining. It utilizes controlled electrical discharges to remove material from a workpiece, typically made of conductive materials such as metals or alloys. EDM is particularly well-suited for machining hard and brittle materials that are challenging to process otherwise using conventional methods [13]. The EDM process uses a power supply that generates high-frequency electrical pulses between a tool and the workpiece shown in Figure 2.1. These electrical pulses create rapid and continuous sparks in a localized region called the interelectrode gap (IEG). The IEG contains dielectric fluid, acting as a medium for electric discharge. During the EDM process, intense heat is generated at the spark gap as the electrical discharge occurs. This heat causes the localized melting and vaporization of the workpiece material, resulting in the removal of small particles through a process known as spark erosion. The dielectric fluid flushes away the debris and helps maintain a stable insulating environment for the following discharge.

The tool electrode used in EDM is typically made of a conductive material, such as copper alloys, tungsten, or graphite. It is carefully fabricated to achieve the intended shape of the machined feature. The tool and workpiece are positioned nearby but do not make physical contact. Instead, the electrical discharges between them erode the workpiece material,

gradually shaping it according to the electrode's geometry. EDM offers several advantages, including creating complex and intricate shapes and fabricating MEMS, regardless of the material's hardness [14]. Additionally, the non-contact nature of the process allows for machining delicate and fragile components without causing damage [3]. Despite its advantages, it is also essential to acknowledge the limitations of EDM. One limitation is the relatively slower MRR than other machining processes. Additionally, EDM often faces challenges in effectively flushing the debris from the IEG. This inadequate flushing can contribute to forming a recast layer on the machined surfaces, which may affect the surface integrity and quality of the final product [15,16]. Inadequate flushing also promotes arcing, which harms the process stability and induces dimensional inaccuracies in the fabricated parts [17,18]. Recognizing and addressing these limitations is crucial for further advancements and improvements in the EDM process.

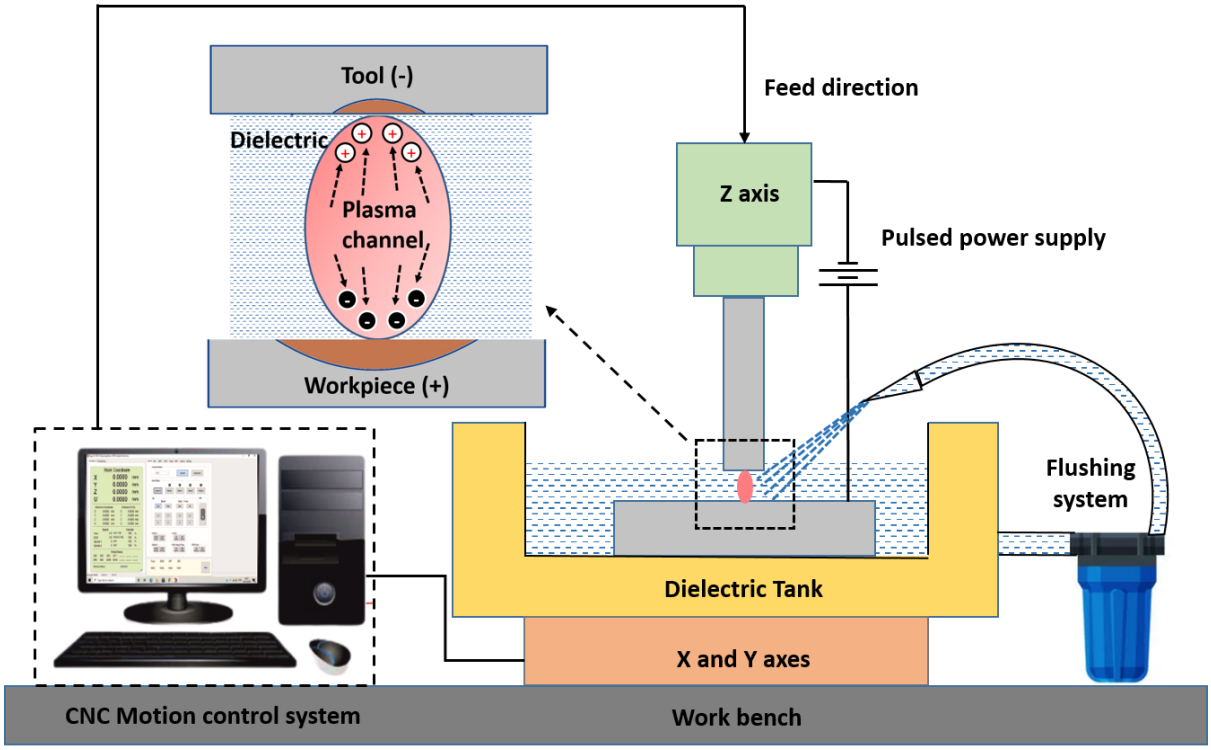

Figure 2.1 EDM configuration with different components

2.2.1 Principle of Electrical Discharge Machining

The involvement of multi-physical phenomena with inherently stochastic nature poses challenges to fully understanding the EDM process. [2,19]. The primary mechanism behind a single discharge responsible for crater formation can be understood through Figure 2.2 and the following steps in detail.

- *Tool-workpiece configuration*: The tool and workpiece are positioned in close proximity, with a small gap containing dielectric fluid. The process begins when the tool electrode is fed constantly toward the workpiece and the EDM power supply is switched on. A potential difference exists between the tool and workpiece acting as cathode and anode for die-sinking EDM. The voltage level is typically in the range of tens to hundreds of volts. This voltage creates a high electric field in the IEG consisting of the dielectric as the tool approaches the workpiece [20,21].
- *Cold emission and dielectric breakdown*: The electric field causes a breakdown of the dielectric fluid in the spark gap, leading to the ionization of the IEG. The breakdown starts with the cold emission of the electrons from the cathode, as the electric field strength exceeds the dielectric strength of the fluid [22]. This leads to the ionization of the IEG involving the collision of electrons with fluid molecules, resulting in the separation of charges and the creation of free electrons and positively charged ions.
- *Plasma Formation*: The dielectric fluid breakdown with a high degree of ionization results in a conductive plasma channel. This plasma channel allows the electric current to flow between the tool and the workpiece. The plasma comprises highly energized and ionized gas particles, including electrons, ions, and neutral atoms. The electrons being lighter particles with high density moves with higher velocities and impact the workpiece (anode) to generate high-density collisions in the vicinity.
- *Plasma expansion and spark Generation*: The established plasma channel creates the path for the electrons to accelerate from the cathode toward the anode while ionizing the IEG. This cyclic process results in a barrage of electrons accelerating towards the workpiece, called the avalanche motion of electrons. The plasma formation and expansion result in current flowing through the plasma channel, causing a localized discharge known as a spark. The spark is characterized by a rapid and intense release of energy in the form of heat and light with a simultaneous fall in voltage and current rise. Free electrons facilitate the discharge in the plasma that carries the electric current.
- *Melting and evaporation*: The spark generates exceptionally high temperatures in the IEG, reaching several thousand degrees Celsius. This intense heat causes the localized melting and vaporization of the electrode material near the spark root [23]. The combination of two phenomena primarily generates heat. First is the collisions between the charged particles with the dielectric molecules and the bombardment of the charged

particles on the respective electrodes. Second is the joule heating or the ohmic heating resulting from the high-density current flow and the resistance of the plasma channel.

- *Plasma Collapse*: Once the discharge is complete, the pulse-off time starts to withdraw the voltage applied at the electrode boundaries. As a result, the plasma channel collapses or deionizes to allow the surrounding high-pressure dielectric fluid to re-establishes its insulating properties in the IEG, preparing for the subsequent discharge. The collapse of the plasma channel occurs due to the sudden switching off the applied voltage, leading to the recombination of ions and electrons and the neutralization of charged species.
- *Material Removal*: The high-pressure dielectric flowing into the plasma channel due to its collapse cools and quenches the molten metal. This results in the form of spherical debris that gets flushed out of the IEG due to high pressure. The dielectric fluid flowing through the spark gap flushes away the debris particles, preventing re-deposition and helping to maintain a stable discharge [24]. The crater forms due to the combination of thermal effects, vaporization, and the force exerted by the plasma pressure on the molten material.
- *Repeated Discharges*: The process of voltage application, breakdown, spark generation, material removal, and plasma collapse is repeated multiple times per second at the next nearest gap, depending on the specific EDM parameters, such as pulse duration and frequency [25]. The repetition of discharges allows for continuous material removal and shaping of the workpiece. Through the cumulative effect of numerous repeated discharges, the workpiece material undergoes incremental material removal, gradually shaping it according to the geometry of the tool electrode. The repetition and controlled removal of material result in the desired shape and features on the workpiece.

These technical details highlight the phenomena of ionization, plasma formation, spark generation, thermal effects, material removal, and plasma collapse that occur during a single discharge in the EDM process.

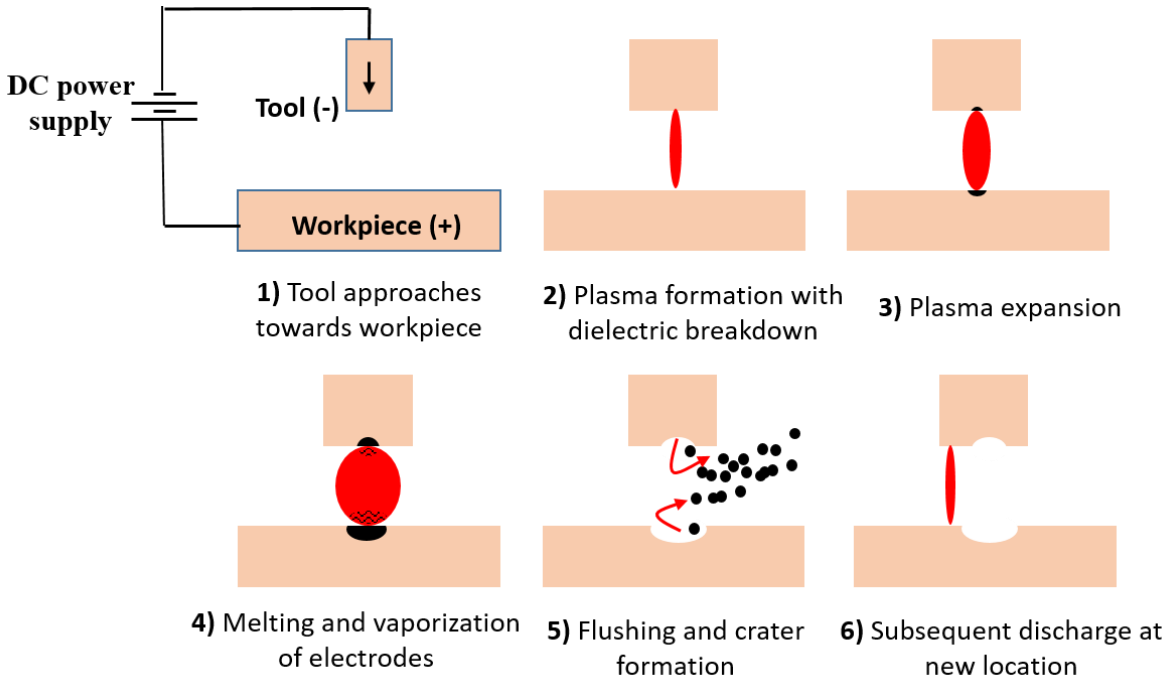

Figure 2.2 Step-by-step mechanism of a single discharge

2.2.2 Macro vs. Micro EDM

Fundamentally, micro-EDM follows the exact physical mechanism of macro-EDM explained in the previous section [26]. However, the following distinctive features of the micro-EDM separate the two concerning the scale, process capabilities, and scope of application.

Electrode Size and Discharge Phenomena:

The electrode size used in the macro-EDM is large and in the range of conventional milling and drilling tools. Hence the macro-EDM electrodes can be fabricated easily with traditional electrode manufacturing techniques and provide reasonable material removal rates for larger-scale components. In contrast, micro-EDM utilizes considerably smaller electrodes due to the reduced dimensions of the machined features [23]. Fabricating microelectrodes involves advanced techniques such as micro-WEDM grinding, electroforming, etc. The design complexity increases as micro-scale electrodes often require intricate features to achieve the desired precision. The size of the plasma channel formed during the macro-EDM is much lesser than the tool diameter, whereas they are comparable during the micro-EDM process [27]. Macro-EDM operates at higher energy levels, resulting in larger craters and more significant debris removal. The discharge energy in macro-EDM is typically several tens to hundreds of micro joules. In micro-EDM, the discharge energy is significantly lower, typically in the range of a few micro joules or even below a micro joule [28,29]. This lower discharge energy leads

to smaller craters and finer debris particles, facilitating higher precision and surface quality in micro-scale machining. The reduced discharge energy in micro-EDM allows for better control and minimizes the risk of thermal damage to the workpiece. The melting and flushing are regarded as the dominant material removal mechanism during the macro-EDM contrast to melting and vaporization during the micro-EDM [30].

Material Removal Rate, Surface Finish, and Accuracy:

Macro-EDM typically achieves higher material removal rates compared to micro-EDM. The larger spark gaps and higher discharge energies in macro-EDM enable faster material removal, making it more suitable for machining larger components. On the other hand, micro-EDM operates at lower energy levels, resulting in slower material removal rates. However, micro-EDM focuses on achieving intricate geometries and high precision rather than rapid material removal [31,32]. For example, Zahiruddin et al. have reported the material removal per pulse as 1.90 μm^3 for micro and 972.5 μm^3 for macro-EDM [33]. Micro-EDM offers superior surface finishes and higher dimensional accuracy compared to macro-EDM. The reduced spark gap and lower discharge energy in micro-EDM result in finer surface textures and improved dimensional precision. The smaller spark gap allows for higher resolution and finer control over the material removal process, contributing to enhanced surface quality and accuracy in micro-scale machining. Additionally, the reduced discharge energy minimizes the possibility of thermal distortion and improves the overall accuracy of micro-scale features [34].

Application Scope:

Macro-EDM is commonly employed in mold-making, aerospace, and automotive industries, where larger-scale components are manufactured [35]. It is suitable for machining components with dimensions ranging from millimeters to meters. Micro-EDM finds its application in electronics, medical devices, microfluidics, and MEMS, where miniaturization and high precision are crucial [36,37]. Micro-EDM is designed to handle features with dimensions typically ranging from micrometers to a few millimeters. A comparison of the various aspects of macro and micro-EDM is presented in Table 2.1 [38].

Table 2.1 Comparison of macro and micro-EDM

Scale	Type	Voltage(V)	Current (A)	MRR (mm^3/s)	Surface roughness (µm)	IEG (µm)	Discharge energy (µJ)

EDM	Milling	20-200	>3	0.002-0.5	3-25	10-500	100-1000
	Die-Sinking	30-300		0.002-0.8	2.5-30		
	Wire EDM	30-120		5-15	0.127-0.254		
Micro-EDM		10-120	< 3	0.2e-6-1e-6	0.05	<10	<30

2.2.3 Micro EDM power supply

Two types of EDM power supplies, RC-based and transistor-based, have been found consistently in the literature depending on the application [39]. Below is a brief discussion on their distinctive features, advantages, and applications.

RC Power Supply

The capacitive discharge power supply is widely used in micro-EDM due to its ability to generate short, high-energy pulses [40]. It consists of a capacitor that stores electrical energy before discharging it through the spark gap between the tool and the workpiece. The energy stored in the capacitor is directly proportional to the capacitance and the square of the charging voltage. The pulse duration is determined by the discharge time of the capacitor [38]. It can be adjusted by controlling the capacitance, charging voltage, and spark gap characteristics. The capacitance and the voltage influence the energy delivered during a single discharge. Higher capacitance and voltage result in more energy delivered to the spark gap.

Usage and Advantages: Micro-EDM applications benefit from the capacitive discharge power supply's ability to generate high-energy pulses in a short duration. It is suitable for precise material removal and finishing of micro-scale features [41]. This power supply is often used for micro-hole drilling, micro-milling, micro-cutting, and other applications requiring controlled material removal. The short pulse duration allows for minimal heat generation and reduced thermal effects, making it advantageous for machining delicate or heat-sensitive materials. The energy-controlling capability enables fine-tuning of material removal rates and accuracy.

Transistor-based Power Supply

The pulse generator power supply is generally employed in macro-EDM to produce controlled electrical pulses with specific characteristics. It provides precise control over the energy input during the discharge process, allowing for accurate machining of micro-scale features [42]. The pulse generator power supply enables the adjustment of various pulse parameters,

including pulse duration, frequency, and amplitude [2]. The pulse duration refers to the time the electrical pulse is applied. It can be adjusted to control the material removal rate and accuracy. Shorter pulses are typically used for fine machining, while longer pulses are employed for higher material removal rates. The duty cycle represents the ratio of the pulse duration to the total period of the pulse. It determines the percentage of time the power supply is actively delivering energy.

Usage and Advantages: The transistor-based power supply offers precise control over the electrical pulses, allowing for accurate and controlled material removal [43]. It is commonly used for EDM applications that require high material removal rates and controlled delivery of the discharge energy [44]. By adjusting the pulse parameters, the power supply enables customization of the machining process to suit different materials, geometries, and accuracy requirements. The ability to control pulse duration, frequency, and amplitude allows for optimizing material removal rates, surface quality, and electrode wear.

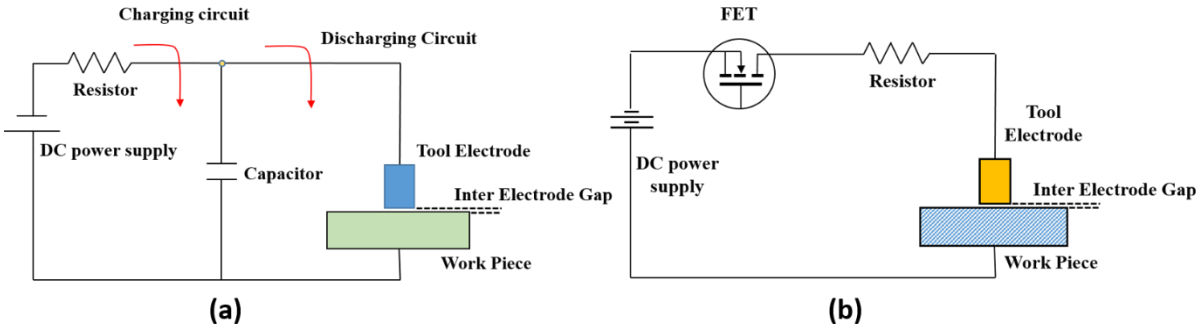

Figure 2.3 (a) RC- based power supply (b) Transistor-based power supply

Controlled RC-based power supply

A controlled RC-based power supply is a modified version of the conventional RC-based power supply [45], as shown in Figure 2.4 (a). It is advantageous over the traditional RC-based power supply because it controls the discharge timing. The discharge current can flow through the discharging circuit only during the transistor on time, which the Mosfet controls. As a result, a pulse counting and monitoring system would become more realistic and dependable for monitoring continuous machining.

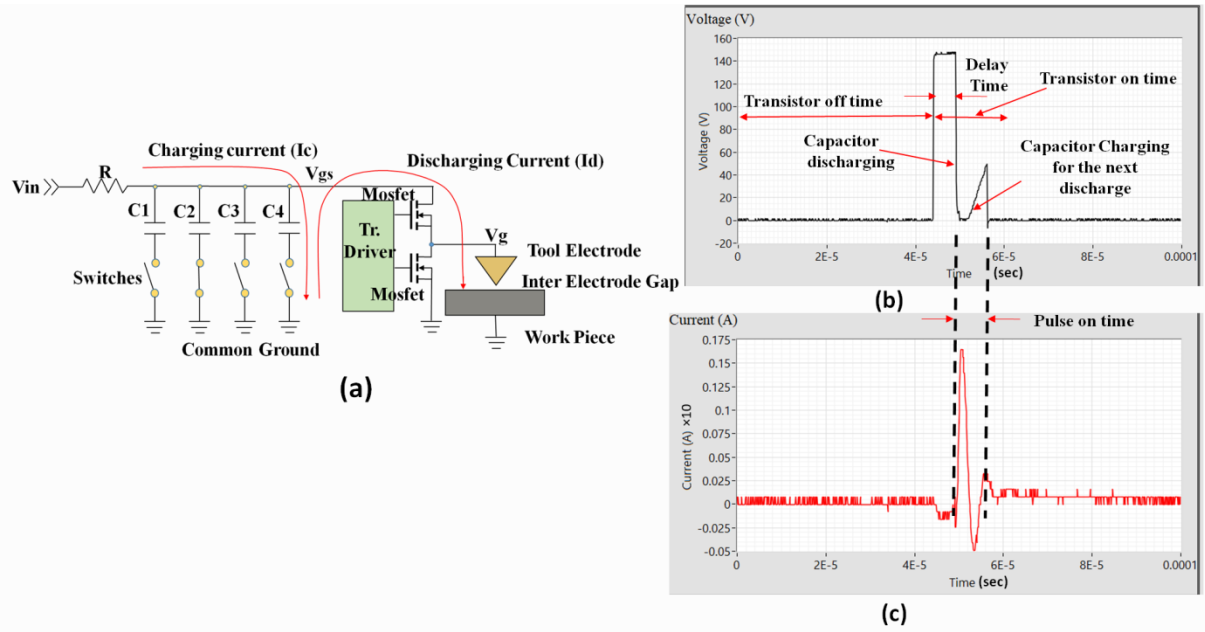

Figure 2.4 (a) Schematic of a controlled RC circuit in µEDM, (b) a typical voltage pulse, and (c) a current pulse

2.3 Modeling of micro-EDM process

Understanding and predicting their behavior is crucial to ensure effective control and performance of machining processes. One approach to achieve this is modeling the underlying complex physical phenomenon leading to the material removal, which was otherwise challenging to understand through experiments [46,47]. However, EDM poses unique challenges compared to conventional machining methods due to its stochastic nature involving multiple physical phenomena and shorter timescales [48]. In EDM, the machining region at the micrometer scale consisting solid, liquid, gas, and plasma states, all coexisting within a brief period ranging from nano to microseconds [49]. Explaining the fundamental material removal mechanism in EDM requires incorporating principles from thermodynamics, plasma physics, magnetohydrodynamics, and fluid dynamics. Various assumptions and simplifications must be made to develop models that capture these principles.

2.3.1 Size effect in modeling of EDM

Micro-EDM exhibits significantly shorter pulse durations, typically in the order of nano to microseconds, as opposed to macro-EDM. Furthermore, the energy density of the discharge in micro-EDM stays considerably more significant than its macro-scale version [33]. Several factors often disregarded in macro-scale modelings, such as the viscosity of the dielectric and magnetohydrodynamics, have a more significant impact on determining the plasma parameters in micro-EDM. Unlike the macro scale variant, the current and voltage in micro-EDM cannot

be averaged over time to calculate the pulse power since they vary as a function of time in an RC-pulse generator, commonly used in micro-EDM. The existing theories that explain breakdown phenomena and plasma expansion in EDM are less effective when applied to micro-EDM. For instance, the bubble mechanism theory employed to elucidate dielectric breakdown in EDM cannot be directly extrapolated to micro-EDM. The rapid breakdown phenomena observed in micro-EDM defy the slow bubble expansion characteristic of a longer pulse [50]. Also, the study of the discharge phenomenon in narrow gaps is limited because of its experimental difficulties [51].

Most of the available models for conventional EDM primarily focus on cathode erosion. According to DiBitonto et al., while the machining process initially leads to the rapid erosion of the anode surface due to electron bombardment, material removal subsequently slows down due to the expansion of the plasma channel [52]. The time-dependent expanding radius reduces the local heat flux near the anode surface. Additionally, since the plasma radius is small near the cathode surface in macro-EDM, the power density is higher, resulting in deeper craters. Consequently, the workpiece is most often connected to the cathode in macro-EDM. However, in micro-EDM, the expansion of the plasma radius at the anode is comparatively less significant because of concise pulse duration. Under these conditions, rapid material removal caused by the impact of high-velocity electrons becomes more prominent. As a result, the workpiece in micro-EDM is connected to the anode instead of the cathode. Yeo et al. have proved that applying Dibitonto's model to micro-EDM resulted in serious prediction errors due to the short pulse duration [53]. Zahiruddin and Kunieda observed that the micro-EDM process's energy density was much higher than the conventional variant [54]. This higher power density increases material removal and plasma flushing efficiency (PFE) and reduces heat loss to the surrounding fluid medium. Moreover, the heat lost to the dielectric medium during the discharge period cannot be disregarded in micro-EDM.

2.3.2 Modeling approaches

Although various approaches are present in the literature for modeling the micro-EDM process, a few of the most prominent are as follows.

Analytical or mathematical models: These models utilize the theoretical understanding of the involved physical phenomenon and solve the related mathematical equations to study the material removal mechanism. The goal is to simplify the process into a mathematically interpretable form by making appropriate assumptions. The accuracy of an analytical model relies on the chosen assumptions. If the process is oversimplified, the model may be less

accurate, while omitting assumptions can lead to increased complexity and longer solving time. Developing analytical models requires a deep understanding of the process. For example, a thermo-mathematical model was proposed to optimize the input energy pulse by Erden et al. [55]. It was concluded that finding the analytical solution to the complex energy interactions during the EDM process is challenging. Salonitis et al. and Kashif et al. proposed a simplified theoretical model for material removal and surface roughness [56,57]. They considered the shape of the crater as circular paraboloid and ellipsoid, which is a critical and not feasible assumption under all machining conditions

Empirical models: In this approach, extensive experimentation is conducted to establish correlations between controllable parameters and machining performance characteristics. Various machining variables are altered during the experiments to observe their effects on machining outcomes, such as MRR and surface roughness. The obtained data is then used to fit the input variables into empirical equations capable of predicting output parameter variations [58]. However, the universality of empirical models is debatable, as their effectiveness largely depends on specific machining conditions and the characteristics of the machine tool being used [59].

Numerical models: Numerical methods are employed to solve the governing equations of the process with efficient computational time and sufficient accuracy. In this approach, the analytical and empirical equations can be utilized to establish the boundary conditions (BCs). One commonly used method is the Finite Element Method (FEM), which involves analyzing the interactions between plasma and electrode material by solving the heat conduction equation to generate a thermal distribution profile. This technique is widely applied in micro-EDM. An overview of plasma modeling for developing temperature distribution and crater geometry is presented in the following sections.

2.3.3 Plasma channel modeling

Background of Spark/arc models

An electrical discharge generally follows the breakdown of a dielectric medium under the influence of an applied electrical potential between two electrodes. A simultaneous rise in the discharge current occurs in a few microseconds or even less time, depending upon the input voltage and capacitance setting. The spark channel between the two electrodes is a mixture of highly ionized gases called plasma. Among the various breakdown mechanism, the streamer breakdown is assumed to be the most prominent mechanism behind the formation of the plasma

channel in the micro gaps filled with dielectric fluids [60,61]. An essential characteristic of the electrical discharge is the volt-ampere characteristic (VAC) which defines the discharge power obtained through a single discharge where the discharge voltage decreases with an increase in the current [62,63]. One of the earliest theoretical approaches to modeling arc discharges is the block model of electric arc [64–66]. These models are based on the mathematical equations of the arc conductance and are purely theoretical, lacking multiphysics connectivity while modeling a process such as micro-EDM. The above theoretical models could not describe every detail of the processes inside the plasma channel and give way to more numerical studies regarding the dynamics of spark discharges. The numerical models that incorporate electromagnetics, heat transfer, and conservation of mass and energy are called magnetohydrodynamic models (MHD) [67–69]. Free-burning argon arc was studied in these models, and the temperature profile of the arc region was modeled using the MHD equations. A mathematical model of the electrical discharge in the presence of metal vapors in argon at an atmospheric temperature is reported in [70]. It was concluded that the presence of metal vapors in the arc region changes the conductivity of the plasma channel, which affects the temperature distribution in the electrodes. Thermodynamic properties of the thermal plasma formed by inert gases at varying pressures between 0.1 and 10 MPa while assuming local thermal equilibrium (LTE) conditions inside the plasma channel are reported in [71]. Thermal plasma properties of different gas-metal vapor mixtures were studied in welding plasma processes. The dependencies of plasma properties on the different types of metal vapors and their concentrations are explained by Cressault et al. [72]. The modeling approach and the relevant literature specific to plasma modeling concerning EDM are discussed in the following section.

Modeling of EDM plasma

For a highly stochastic process like EDM involving multi-physical phenomena, the cumulative material removal can be estimated by analyzing and combining the individual contribution of the single discharges. Figure 2.5 illustrates the machining zone during a single discharge, where the heat from the plasma is dissipated into the tool, workpiece, and dielectric medium in different proportions. The fractions of discharge energy transferred to the tool, workpiece, and dielectric medium are denoted by Fa, Fc, and Fd, respectively.

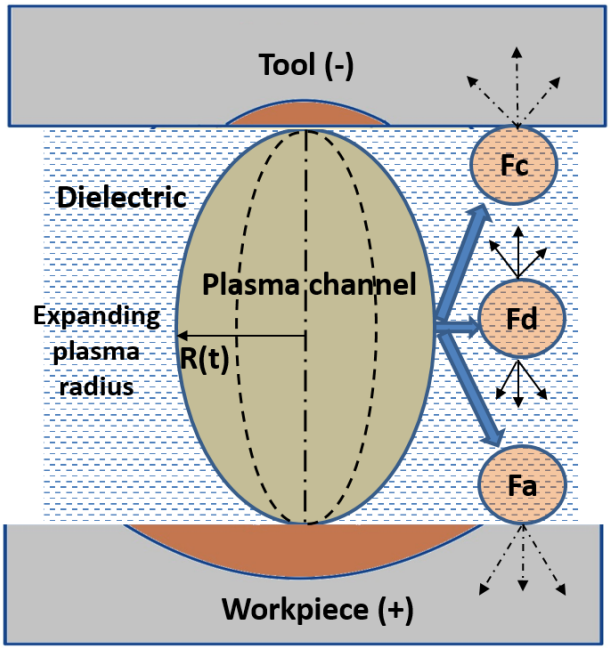

Figure 2.5 Plasma channel interactions during a single discharge [41]

The formation of a plasma channel in EDM is primarily explained by two theories in the literature: the bubble mechanism [73–75] and the electron impact ionization mechanism [76,77]. Wiessner et al. experimented with the electric discharge in liquid and gaseous media and concluded that discharge occurs inside a gas bubble even in a liquid medium [78]. According to the bubble mechanism, plasma formation is divided into three stages for better comprehension: the breakdown phase, the heating phase, and the material removal phase [79]. Zhang et al. and Maradia et al. have investigated the role of bubble dynamics on the discharge phenomenon and concluded that it affects the material eroded from the workpiece [80,81]. In the initial stage, the potential difference between the tool and workpiece is reduced due to charged particles in the IEG approaching the micro peaks at the electrode surfaces. As the potential barrier weakens, the local electron density increases. The bombardment of electrons with dielectric fluid particles leads to the heating of the liquid and the formation of vapor bubbles on the electrode's micro peaks. The bubbles expand further, and a discharge occurs once the bubble pressure surpasses a threshold value with the abrupt stoppage of the input power supply stops [82]. According to the bubble expansion model, the dielectric breakdown occurs due to the local instability caused by inhomogeneity in the dielectric and irregularities on the electrode surface. In contrast, the electron impact ionization model advocates that the ionization of the dielectric molecules due to their collision with the accelerated electrons results in dielectric breakdown.

The bubble expansion model for EDM effectively explains the plasma channel formation and subsequent discharge phenomena with longer pulse durations. Hence, it can be applied for modeling the macro-EDM where the discharge phenomenon occurs at a sufficiently large scale from hundreds of microseconds to a few milliseconds. However, for short pulses in the microsecond or sub-microsecond range, the bubble mechanism is insufficient to explain the rapid discharge physics. In such cases, the electron impact ionization theory, also called the streamer model, can be used effectively [83]. According to the impact ionization theory, breakdown occurs when the developing electron avalanche becomes a streamer. Schoenbach et al. (2008) have studied the breakdown phenomenon in minimal spark gaps consisting of water as a dielectric between pin and plane electrodes [84]. They have concluded that the discharge initiated at the interface of the already existing bubbles inside the dielectric by the impact ionization within those bubbles. To apply the impact ionization theory to the dielectric environment of the micro-EDM, Dhanik and Joshi proposed a modified breakdown model consisting of both the bubble and streamer mechanisms [79]. According to this model, the breakdown process begins with bubble nucleation at the cathode and eventually expands due to the increased density of charged particles. When the bubble characteristics meet the criteria for electron impact, instantaneous ionization of the dielectric fluid column occurs, resulting in a breakdown. The modified model combines the bubble mechanism and streamer model to explain micro-EDM plasma [85]. Characterizing the plasma channel in micro-EDM involves computing the plasma column's electron density and temperature distribution. These plasma parameters can be calculated using analytical models by Mujumdar et al. [85], optical spectroscopy by Nagahanumaiah et al. [86], photomultipliers Albinski et al. [87], and other methods. Furthermore, understanding the plasma formation mechanism helps explain distinctive phenomena associated with micro-EDM, such as the cooling effect produced by the high iron content in the plasma, as explained by Adineh et al. [88].

Two approaches are commonly used in modeling plasma channels for EDM: the fluid dynamics approach and the kinetics approach.

Fluid dynamics approach: In the fluid dynamics approach, certain simplifying assumptions are made. These include

- Uniform temperature, pressure, and density throughout the plasma channel.
- Time-independent properties of the dielectric fluid.
- Considering a cylindrical or spherical shape for the plasma.
- Neglecting the role of particle bombardment in heat transfer.

- Uniform expansion with a constant energy fraction to the plasma.

Early models for plasma channels in conventional EDM include the cylindrical plasma model proposed by Van Dijk and Snoeys [89]. This model approximates the discharge process using a constant mass cylindrical plasma. The power distribution during plasma generation is calculated using electron emission theory, and continuity and momentum equations are employed to determine the plasma parameters. However, this model does not account for radiative heat transfer and heat loss during dielectric fluid vaporization and ionization and tends to underestimate plasma pressure. Lhiaubet and Meyer introduced a new model that uses an expanding spherical plasma [90]. In this model, the properties of the diatomic plasma are assumed to be temperature-independent. However, this cathode erosion model does not consider the pressure variation parameter in the energy balance equations and tends to overestimate the temperature and pressure of the plasma. Pandey and Jilani assumed that the cathode spot temperature is equal to the boiling point temperature of the material (T_b) and derived Equation (2.1) that relates the spot temperature to the plasma radius (R) [91]. The equation is as follows:

$$T_b = \frac{E \times F_c \times 10^6}{k \times R \times \pi^{3/2}} \tan^{-1}\left[\frac{4 \times \alpha \times t_{on} \times 10^6}{R^2}\right]^{1/2} \quad (2.1)$$

Where:

T_b is the boiling point temperature in K. R is the heat source radius in m. k is the thermal conductivity in W/mK. α is the thermal diffusivity in m^2/s. t_{on} is the pulse duration in µs. E is the total discharge power in W, and F_c is the cathode energy fraction.

Eubank et al. developed a model with a variable mass cylindrical plasma [92]. This model incorporates the unsteady behavior of plasma expansion by using an unsteady energy balance equation with varying mass. The continuity and momentum equations were solved to establish a relationship between plasma radius and time. Heat transfer from the plasma was the sole reason for material removal in the fluid dynamics method. In EDM models, high-voltage, high-current discharges with long discharge times are often used to estimate the plasma radius, which can lead to overestimation. The authors have proposed a relationship between the radius of the cylindrical plasma and discharge duration from their plasma model for low-current, low-voltage discharges in small spark gaps. Equation (2.2) represents the suggested plasma radius, which may be specific to their model.

$$R = 0.059 t_{on}^{0.79} \quad (2.2)$$

One early approach to the micro-EDM plasma channel and its interaction with the electrode material was conducted by Katz and Tibbles [11]. The input variables were considered dimensionless, including discharge current, discharge voltage, spark duration, dielectric permittivity, and electrode diameter. Using the least-square regression method, they calculated the electrode current density, micro crater area, channel power dissipation, and plasma channel expansion rate. Dhanik and Joshi made significant contributions to the micro-EDM plasma by considering different stages of discharge formation [79]. They combined the bubble mechanism (for bubble initiation) and electron impact ionization mechanism (for bubble expansion and dielectric breakdown) to explain the rapid breakdown phenomena in micro-EDM. The plasma model developed by Dhanik and Joshi utilized a cylindrical plasma in water as the dielectric medium, similar to the model by Eubank et al. [92]. However, Mujumdar et al. criticized the model for its limited understanding of plasma chemistry and for using cylindrical plasma instead of spherical plasma [93]. Chu et al. identified limitations in previous models that failed to consider certain important aspects of the micro-EDM process [94]. These aspects included the role of magnetic pinch force, viscous force, and fluid surface tension. The authors proposed a comprehensive model incorporating these factors to address these limitations to predict the plasma radius, pressure, and temperature. This modified model was also utilized to determine the heat source and provide boundary conditions for the crater surface.

Fluid kinetics approach: The kinetics model focuses on analyzing the density and distribution of different particles in the plasma. Assuming that ions and electrons follow Boltzmann's distribution, analyzing electron generation using Poisson's equation and solving the mass and momentum equations allow for predicting material removal volume due to electro-mechanical erosion. Unlike other approaches focusing on fluid flow and heat transfer, the fluid kinetics approach emphasizes the movement and interactions of plasma species, such as electrons and ions.

Researchers have combined theoretical analysis, numerical simulations, and experimental validation to develop and refine plasma models based on the fluid kinetics approach to predict key plasma parameters. The most prominent among them is the thermo-electric model proposed by Singh and Ghosh [95]. The common assumptions made during the kinetic modeling of the EDM plasm are as follows.

- Workpiece is considered a semi-infinite region, extending indefinitely in one direction.

- The spark is treated as a uniform and circular heat source with a constant diameter located on the surface of the electrode.
- Material properties, except yield strength, are assumed to be independent of temperature.
- The heat input rate to the system remains constant throughout the discharge time.
- The potential drop occurs primarily in the sheath near the cathode and the plasma region near the sheath [96].
- The Spark ending is followed by material yielding, indicating a change in its mechanical properties.
- Within the spark channel, there are no variations in potential, ion, electron densities, or ion velocity in the radial direction. These properties remain constant throughout the spark channel.

Singh and Ghosh proposed a model comprising two stages: plasma analysis and sheath analysis. Due to the inability of the plasma region to accommodate the potential drop between the electrodes, a thin layer of charge called the "plasma sheath" is formed between the cathode and the plasma. This sheath region sustains the voltage drop and interacts with the electrode surface, removing material. The plasma analysis establishes the necessary boundary conditions for the subsequent sheath analysis. In their plasma analysis, Singh and Ghosh assumed quasi-neutrality, with electrons and ions following a Boltzmann distribution according to equation 2.3.

$$n_e(x') = n_o \exp(e\phi(x') / kT_e) \tag{2.3}$$

Where the electron density (*ne*) varies along *x'* in the direction of the dropping voltage, n_o is the initial electron density, *e*, and φ are the electron charge and potential difference, *Te* is the electron temperature, and *k* is the Boltzmann constant. The authors employed one-dimensional mass and momentum conservation equations for ions and electrons to analyze the plasma region, similar to the Navier-Stokes equations. These equations allowed them to determine the voltage (φo) and the common ion/electron density (n) at the interface between the sheath and plasma.

$$\phi_o(x') = -(kT_e / e)\ln 2 \tag{2.4}$$

$$n = 1/2(n_o) \tag{2.5}$$

The sheath region was analyzed utilizing momentum equations for individual particles, Poisson's equation for the electric field within the sheath region, and the potential boundary condition derived from the plasma region analysis. They expressed the electric field (E) in the

sheath region as a function of distance, represented by the equation provided by Singh and Ghosh.

$$E^2(x) = \frac{4}{\varepsilon_o} e n_{se} (\phi_o \phi_w)^{1/2} \tag{2.6}$$

In this equation, φ_w represents the cathode potential, and n_{se} denotes the common ion/electron density at the sheath/plasma interface. Using the calculated electric field, the potential difference at the sheath, and the density of the electrons, the authors further proposed an electro-mechanical model for material removal.

Mujumdar et al. proposed a plasma model for micro-EDM that focused on a single-pulse discharge between parallel plates [85]. They used a global approach in their model, averaging the densities of plasma species and applying the Maxwellian energy distribution. By combining the particle balance equation, plasma dynamics, and energy balance, they calculated the temperature and pressure of the plasma. The researchers used Power balance equations to estimate the temperature of the different plasma components. Due to the comparable mass of the heavy species, i.e., positive ions and the neutral molecules, they have assigned a common temperature of T_g while the electrons were assigned a separate temperature of T_e calculated using the following equations.

$$\frac{d}{dt}\left(\frac{3}{2} N_e k T_e\right) = P_{in,e} - P_{w,e} - P_{rad,e} - Q_{el,e} - Q_{inel,e} - Q_{c,e} - P_{wall,e} \tag{2.7}$$

$$\frac{d}{dt}\left(\sum_{i}^{ions,neutrals} C_{vi} N_i k T_g\right) = Q_{el,g} + Q_{c,g} - P_{w,g} - P_{wall,i} \tag{2.8}$$

Where N_e and N_i are the numbers of electrons and ions, T_g and T_e are the temperature of heavy particles and the electrons. K is the Boltzmann constant, $P_{in,e}$ is the input power to the electrons, p_w is the work done by the species for plasma expansion, and P_{rad} is power loss from plasma due to radiation. Q_{el} and Q_{inele} are the power loss due to elastic and inelastic collisions of the species, Q_{ce} is the power loss due to columb interactions, and P_{wall} is the power lost by the species at the electrode wall. According to their model, the average electron temperature was estimated to be around 6,817 K, with an electron density of 8.9×10^{23} m^{-3}. According to Mujumdar et al., the conductivity of the dielectric fluid was directly related to the material removal by increasing the electron density in the plasma channel [97].

Subbu et al. have conducted experimental investigations using optical emission spectroscopy to examine plasma temperature and electron density, which has provided valuable insights into the characteristics of the plasma [98]. The temperature and density of the plasma

were analytically calculated using the line pair method and the Saha equation. The plasma temperature was 5000-8000 K with four order increment in electron density with increasing energy. To simulate the crater profile on the workpiece and tool, well-defined plasma boundary conditions (BCs) are necessary. These include plasma radius, heat source shape, heat intensity distribution profile, plasma temperature distribution, plasma pressure, and electron density. These BCs can be determined through modeling the plasma channel or experimental methods such as optical spectroscopy. The following section presents a detailed discussion of the plasma parameters used in the literature to model material removal in the EDM process.

2.3.4 Plasma Parameters (Energy Fraction, Heat Flux, Spark Radius)

To accurately simulate material erosion caused by plasma interaction, precisely defining the boundary conditions (BCs) is vital. These BCs encompass various parameters that play a role in the model's governing equations. These parameters include the plasma radius, heat flux distribution, energy partition factor, discharge intensity, electron density, plasma pressure, and temperature. The energy partition factor (EPF) specifically represents how the discharge energy is distributed among the electrodes and the surrounding dielectric fluid. It characterizes the proportion of energy distribution to each component during the plasma interaction process.

Energy partition factor: In macro-EDM, the heat dissipation in the electrodes is significant, while various researchers often neglect the energy loss to the dielectric medium. However, similar EPF's can not be used in micro-EDM with short-pulse durations and high power densities. Further, the experimental determination of EPF is difficult due to the size effect during the micro-EDM. Studies have been conducted to indirectly calculate the energy distribution ratio in micro-EDM using the obtained crater geometries. For example, Zahiruddin and Kunieda found that the energy distribution to the anode ranges from 6.6% to 10.8%, while the cathode receives 3.3% to 3.7% of the energy. Through inverse analysis, Shao and Rajurkar estimated the energy partition to the anode as 9.4% and to the cathode as 3.6% [99]. The energy partition factor during the micro-hole drilling of Inconel 718 was studied by comparing the FE and statistical analysis [49]. The anode fraction of energy was proportional to the discharge current. Shabgard et al. concluded that the EPF varies with EDM's parametric settings, and the plasma flushing efficiency depends on the fraction of energy absorbed by the respective electrodes [100]. The regression analysis has also been used to develop relationships between energy fraction and discharge parameters by Hoang et al. [101]. The following table presents

the energy partition factor used by different researchers for arriving at the material erosion during the macro and micro-EDM.

Table 2.2 Energy partition factors used by different researchers

Literature	Process	Anode (%)	Cathode (%)
Bigot et al. (2016)	μ-EDM	11.09	1.19
Maradia et al. (2015)	EDM	28-36	15-45
Shao and Rajurkar (2013) [99]	μ-EDM	9.4	3.6
Shabgard et al. (2013) [100]	EDM	4-36	4-9
Zahiruddin and Kunieda (2010)	μ-EDM	6.6 - 10	3.3 - 3.7
Xia et al. (1996) [102]	EDM	40-48	25-34
DiBitonto et al. (1989)	EDM	8	18.3
Pandey and Jilani (1986)	EDM	50	50
Van Dijck (1973)	EDM	50	50

Heat Flux: Heat flux represents the spatial distribution of heat intensity in the plasma channel and significantly affects the simulation results. Different types of heat flux have been used for the heat source in plasma. Some common heat flux types include:

1. *Point heat source*: The heat load is assumed to be applied at a single point [52].
2. *Uniformly distributed heat source with constant magnitude*: Heat flux density is assumed to be the same over the entire area, and the energy intensity is considered independent of time [103,104].
3. *Uniformly distributed heat flux with time-dependent magnitude*: The heat flux is distributed evenly along the plasma column, but the intensity varies with time [105,106].
4. *Gaussian heat flux with constant magnitude*: In this approach, the heat flux density is assumed to be maximum at the center of the plasma channel and decreases gradually towards the periphery. The heat flux distribution follows a Gaussian function, and the magnitude of energy density is considered constant throughout the discharge process.

This approach, as proposed by Das et al., provides a simplified representation of the heat transfer mechanism in the plasma [107].

5. *Gaussian heat flux with time-varying magnitude*: In this approach, the magnitude of energy density at a specific point varies over time [108]. It takes into account the expansion of the plasma during the discharge period. Mujumdar et al. introduced this model, where the heat flux follows a Gaussian distribution, varying in magnitude with time.

These different heat flux distributions offer advantages and are suitable for different scenarios. The choice of heat flux model depends on the specific characteristics of the plasma discharge being studied and the accuracy required for the simulation. An optimal Gaussian distribution was proposed by Zhang et al. to develop a parametrized model in which the depth and diameter of the crater were predicted based on the melting temperature isotherms [109]. In experimental investigations of discharge plasma using high-speed imaging and light emission spectroscopy, it has been observed that light intensity and electron density are maximum at the center of the plasma channel. Therefore, using a Gaussian heat flux assumption is the most realistic approach. The selection of the heat flux approximation depends on the specific requirements and available computational resources.

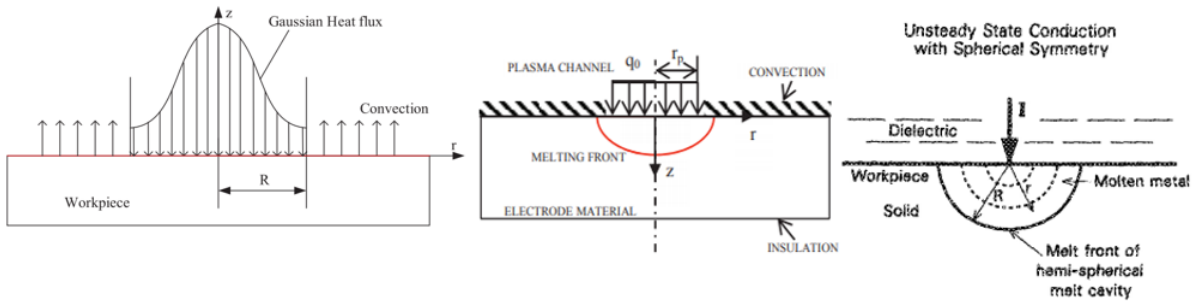

Figure 2.6 Types of heat fluxes used in the literature [46,52,110]

Plasma radius:

Once the heat flux is chosen, the spark radius must be estimated. The spark radius can be determined from plasma models or empirical relationships from extensive experimentation. However, selecting an appropriate empirical formula for spark radius estimation is challenging, as it can be influenced by factors such as electrode types, dielectric medium, and flow pressure. The accuracy of the predicted crater dimensions depends on the accuracy of the spark radius estimation. Various spark radius equations used by different researchers are consolidated in Table 2.3 for reference. In addition to heat flux and spark radius, plasma flushing efficiency

(PFE) is an essential factor to consider [111]. PFE is defined as the ratio of the actual volume removed from the crater to the volume of the molten pool. When determining the boundary of the crater at the isothermal line above the melting temperature, not all of the melted material may be effectively flushed out from the machining zone. This can introduce significant errors in the calculation of crater dimensions. To achieve an accurate model, the PFE can be incorporated into the model to account for the incomplete flushing of molten material. Tan and Yeo model the overlapping craters with time-varying uniformly distributed heat flux [110]. Melting isotherms were used to calculate the plasma flushing efficiency between 19-34%, depending on the input energy.

Table 2.3 Plasma radius equations used in the literature

Reference	Plasma radius equation	Remarks
Dilip et al. (2019)	Constant spark radius (20% of the tool)	R_0, a, b, and c can be found out empirically by analysis of machined craters [112]
Yeo et al. (2007) and Zhang et al. (2015)	$R_{anode} = 0.0284(t_{on}^{0.9115})$ $R_{cathode} = 0.0425 t_{on}^{0.0895}$	Empirical equation [53,109]
Hoang et al. (2015)	$R_0 \rho^a I^b t_{on}^c$	Empirical equation [101]
Shao and Rajurkar (2013)	$0.788 t_{on}^{0.75}$	Empirical equation [99]
Shabgard et al. (2013)	$2.04e^{-3}(I^{0.43} t_{on}^{0.44})$	The empirical equation is derived by Ikai and Hashigushi [113]
Kansal et al. (2008)	$Z p^m t_{on}^n$	Developed by solving the mathematical model of DiBitonto et al. (1989) by integration (Erden, 1983)
Tan and Yeo (2008)	$0.059 t_{on}^{0.79}$	An empirical model developed from single-spark experiments [110]
Allen and Chen(2007)	Constant spark radius (5μm)	The plasma channel by Dhanik and Joshi is used to calculate the plasma radius [114]

In the above table, I is the discharge current, P is the discharge power, t_{on} is the discharge period, and ρ is the dielectric material density. The empirical constants *are z, m, n, R0, a, b,* and *c*.

2.3.5 Simulation of Crater Formation

In the electro-thermal modeling of EDM and micro-EDM, the material removal process can be explained by considering the melting and superheating of the electrode material. To simulate it, partial differential equations related to heat transfer must be solved to obtain the

temperature distribution on the surface. Electro-thermal models are commonly used to model micro-EDM temperature distribution and craters formation. Following are some significant assumptions made in the electro-thermal models of EDM. Figure 2.7 shows an electrothermal model with various BCs applied to the workpiece [41].

1. Homogeneity of the tool and workpiece material: The tool and workpiece materials are assumed to have uniform properties throughout.
2. Material properties: The material properties of the tool and workpiece can be either temperature-dependent or independent, depending on the specific approach.
3. Single plasma channel formation: For simplification, most researchers assume the formation of a single plasma channel per pulse.
4. Neglecting radiation losses: In many models, energy loss due to radiation is neglected for simplicity.
5. Assumptions related to heat flux: Assumptions regarding the shape (circular/pointed), type (uniform/Gaussian), and time dependence (constant/time-dependent) of the heat flux are made in the models.
6. Assumptions related to heat transfer modes: The models consider heat transfer modes such as convection and radiation to the dielectric medium and conduction to the electrodes.
7. Axis-symmetrical assumption: A two-dimensional analysis of the plasma-electrode interaction is typically performed on half of the interaction zone, assuming axis symmetry.

These assumptions help simplify the process and provide a reasonable representation of the electro-thermal phenomena occurring during micro-EDM.

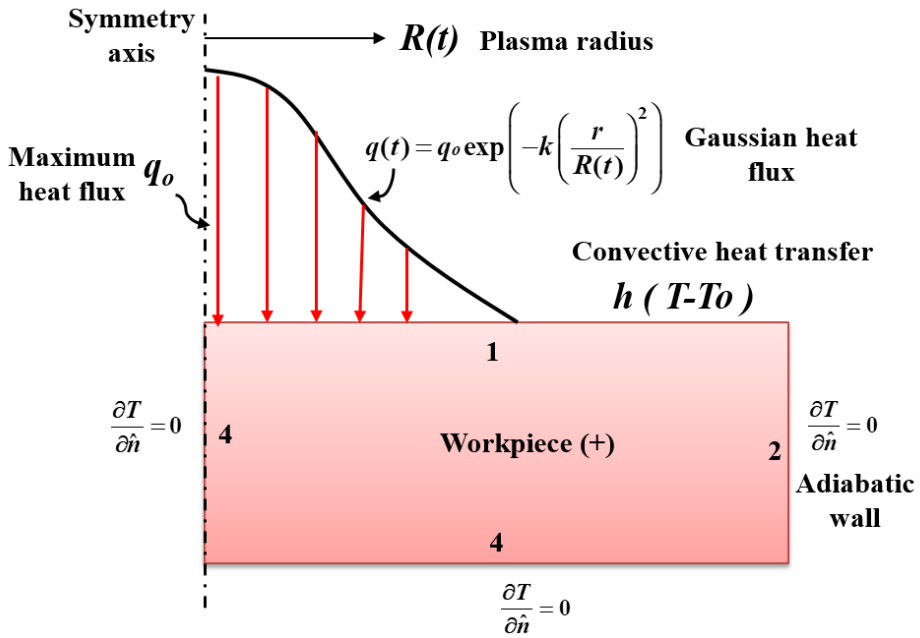

Figure 2.7 Electro-thermal model with boundary conditions [41]

In the heat transfer analysis of micro-EDM, Fourier's law of conductive heat transfer equation is used to determine the temperature distribution in the discharge zone. The equation, denoted as Eq. (2.9), is as follows:

$$\frac{\partial^2 T}{\partial x^2} + \frac{\partial^2 T}{\partial y^2} + \frac{\partial^2 T}{\partial z^2} + \frac{\dot{q}}{k} = \frac{1}{\alpha}\frac{dT}{dt} \tag{2.9}$$

Where T is the temperature, (x, y, z) are the Cartesian coordinates, $\dot{q}$ represents the internal energy generation per unit volume (Joule effect), k is the coefficient of thermal conductivity, α is the thermal diffusivity, and t represents time. The thermal diffusivity α is calculated using Eq. (2.10)

$$\alpha = \frac{k}{\rho C_p} \tag{2.10}$$

The heat equation is written as shown in Eq. (2.11) to solve the heat transfer model numerically

$$\rho C_p \frac{\partial T}{\partial t} + \rho C_p \bar{u} \cdot \nabla T = \nabla \cdot \left(k \nabla T\right) + Q \tag{2.11}$$

The boundary conditions (BCs) for the heat transfer model include the inward heat flow condition, expressed by Eq. (2.12):

$$n \cdot (-k \nabla T) = q \tag{2.12}$$

All other boundaries are considered as adiabatic walls, defined by Eq. (2.13):

$$n \cdot (-k \nabla T) = 0 \tag{2.13}$$

In energy transfer and fluid motion cases, Navier-Stokes equations based on the conservation of mass, momentum, and energy are used to describe the physics of material removal, given by the equation Eq. (2.14)

$$\frac{d}{dt}(\rho h) + \nabla \cdot (\rho V h) = \nabla \cdot (k \nabla h) + S_h \tag{2.14}$$

Where h is the specific enthalpy, V is the total velocity vector of the flow, and S_h is the factor that includes latent heat during melting and vaporization. Considering these equations, the heat transfer and fluid flow aspects of material removal in micro-EDM can be analyzed and simulated. The boundary conditions (BCs) vary depending on the applied heat flux in the electro-thermal model with Gaussian heat flux. For this specific case, the BCs for the electro-thermal model with Gaussian heat flux are described as follows:

Boundary 1: At boundary 1, Gaussian heat flux is applied for a length equal to the plasma radius (R). Beyond this point, convective heat transfer occurs from the electrode surface to the dielectric liquid. Mathematically, the BCs at boundary 1 can be summarized as shown in Eq. (2.15):

$$k \frac{\partial T}{\partial y} = \begin{cases} q(t), r \leq R \\ h(T - T_o), r > R \end{cases} \tag{2.15}$$

Where k is the thermal conductivity, $q(t)$ represents the varying heat flux, h is the convective heat transfer coefficient, and T_0 is the ambient temperature.

Boundaries 2, 3, and 4: At boundaries 2, 3, and 4, the heat transfer is assumed to be zero as the walls are simplified as insulated surfaces.

$$k \frac{\partial T}{\partial \hat{n}} = 0 \tag{2.16}$$

Where n̂ is the normal unit vector. It should be noted that when the heat source disappears after the discharge period, boundary 1 is wholly subjected to convective heat transfer.

Researchers have proposed and tested various approaches to solving the heat transfer and fluid flow governing equations of micro-EDM. Some of the important studies and models developed by different researchers regarding the modeling of crater formation are as follows. Yeo et al. [53] used the integral transform method to solve the heat transfer equations. The temperature distribution was calculated by solving the integral Eq. (2.17), and the measured crater edge temperature was correlated with the temperature profile to approximate the crater dimensions. The volume, depth, and diameter were predicted using the temperature distribution with an error of 6.6%, 0.4%, and 3.6%, respectively.

$$T(r,z,t)=\frac{qR}{2K_t}\int_0^{\infty} J_o(\lambda r)J_1(\lambda r)\times\begin{bmatrix} e^{-(\lambda z)}erfc\left(\frac{z}{2\sqrt{\alpha t_{on}}}-\lambda\sqrt{\alpha t_{on}}\right)- \\ e^{-(\lambda z)}erfc\left(\frac{z}{2\sqrt{\alpha t_{on}}}+\lambda\sqrt{\alpha t_{on}}\right)\end{bmatrix}\frac{d\lambda}{\lambda} \quad (2.17)$$

R is the heat source radius, erfc is the error function, and J_1 and Jo are Bessel functions. Allen and Chen [114] used the ANSYS platform to simulate the temperature profile during a single spark. Constant heat flux and non-expanding plasma were assumed for material ablation. The temperature-dependent material properties were considered, and the elements with temperatures above the melting points were "killed" to create the crater geometry. Murali and Yeo used the ANSYS platform to predict titanium alloys' temperature profile and residual stress [115]. Temperature-dependent material properties were incorporated, and a Gaussian distribution was used for the heat flux by taking the spark radius from Patel et al. A fraction of the discharge energy of the capacitor is taken as input energy to the heat source model. The heat transfer equations were solved to determine the diameter-to-depth ratio of the micro craters. A good agreement was obtained between the simulation and experimental results, with a diameter-to-depth ratio of 3.45 to 3.99. Tao et al. used the finite volume method to compare the near-dry and wet EDM processes [29]. Near dry EDM was found to have craters with larger diameters with lower depths in both simulation and experiments. Jithin et al. considered gaussian heat distribution with empirical plasma radius as a heat source for SS 304 [111]. The authors observed that lower discharge energies produced a high aspect ratio crater as the high energy settings resulted in larger radial heat distribution.

Kumar and Yadava suggested finite element approximation equations to solve the heat transfer model for micro-EDM [116]. They studied the effect of spark radius on crater dimensions and material removal rate (MRR) by adopting the spark radius modeled by Dhanik and Joshi. Galerkin FE formulation was adopted for calculating the temperature distribution inside the workpiece. The authors have calculated the energy and heat flux going into the electrode and concluded that applied energy was inversely proportional to the energy going into the electrodes. Further, the increasing spark radius also affects the crater depth by reducing it due to a decrease in peak heat flux near the center. Weingaertner et al. concluded that incorporating the latent heat of vaporization and fusion showed a better prediction of the crater dimensions [117]. Mujumdar et al. developed a modified melt pool model for micro-EDM using a level set method to distinguish the solid and liquid fractions in the workpiece [118]. The heat transfer model was solved using COMSOL Multiphysics software, and the role of

surface tension gradient (Marangoni stress) in defining fluid motion in the melt pool was included. The model was simulated by inputting the plasma properties using the level set method. The predicted crater depths were shallower compared to the experiments. Shao and Rajurkar combined heat transfer and fluid flow equations to simulate the crater geometry [119]. The role of surface tension gradient in determining the crater shape was emphasized in their model. The simulation predicts an 11% smaller crater diameter and overestimates the crater depth and volume. The authors point out the plasma flushing efficiency for the over-estimation. Kuriachen et al. solved a three-dimensional electro-thermal model using a finite volume method [120]. A transient thermos-physical model with a fully charged capacitor and 100% plasma flushing efficiency was considered to plot 3D temperature distribution profiles. The fluid motion in the mushy zone (where the solid and liquid states coexist) in the discharge crater was incorporated to predict the crater geometry accurately. The authors have discretized the Fourier equation into the flux form for solving the temperature distribution following the method initially suggested by Somashekhar et al.[121].

Dilip et al. has incorporated fluid motion in the molten pool to accurately predict the crater geometry [112]. The authors have considered the separate temperature-dependent material properties in solid, liquid, and mushy zones to predict the crater profiles accurately. Their model showed that the irregular shape of the crater is due to the motion of the top and subsequent layers of the molten pool. The error in predicting crater diameter ranged from 5.19% to 5.64%, and the error in crater depth ranged from 10.58% to 17.47%. Yang et al. [4] analyzed the material removal process of micro-EDM using a molecular dynamics model. The plasma flushing efficiency (PFE) was identified as 2% to 5%, indicating that a significant amount of the molten pool is resolidified during crater formation. They explained the bulge formation during machining as the ejection of molten material from the crater center due to high-pressure plasma. The authors have concluded that part of the ejected material transforms into debris, and the remaining material is deposited on the surfaces of the electrodes. The crater geometry depends upon the density of the powder, with denser powders creating larger craters. Somashekhar et al. developed a multi-spark FE model with Gaussian heat distribution to estimate the temperature distribution in the radial and axial direction, which can be used to model the crater geometries [121]. Guo et al. [122] established an atomic continuum model by combining molecular dynamics and temperature models. They thoroughly analyzed the material removal phenomena in micro-EDM by studying temperature, stress, and material microstructure evolution under thermal load and particle bombardment. Material removal occurs in clusters at the start of the discharge and gradually settles down to single atoms. The

authors argued thermal shock responsible for such behavior during the material removal. Joshi and Pandey combined the FEM with ANN (artificial neural networks) to model the EDM with gaussian distributed heat source [46]. MRR, surface roughness, and crater diameter were predicted accurately, while tool wear was overestimated. A summary of the critical findings in the literature regarding the modeling of the plasma and crater formation is provided in the table.

Table 2.4 Highlights of the literature on EDM modeling

Literature	Observations
Dilip et al. (2019)	The mushy zone was modeled with the help of the naiver-stokes equation considering temperature-dependent physical properties with an error of 14%.
Kliuev et al. (2019)	During the EPF study of micro-hole drilling of Inconel 718, the anode fraction of energy was proportional to the discharge current.
Weingaertner et al. (2012)	Incorporation of the latent heat of vaporization and fusion showed a better prediction of the crater dimensions.
Tao et al. (2012)	FEM was used to compare near-dry and wet EDM processes. Dry EDM produced craters with larger diameters and lower depths in simulation and experiments.
Jithin et al. (2018)	Gaussian heat distribution with empirical plasma radius was considered a heat source for SS 304. Lower discharge energies produced a high aspect ratio crater.
Mujumdar et al (2018)	The conductivity of the dielectric fluid was found to have a direct relation to the material removal by increasing the electron density in the plasma channel.
Chu et al. (2016)	The effect of the magnetic pinch force was incorporated into the bubble expansion model. Crater's depth depends on the capacitance settings.
Somashekhar et al. (2015)	A Multispark FE model with Gaussian heat distribution was developed to estimate the temperature distribution in a radial and axial direction.
Shao and Rajurkar (2015)	The role of surface tension gradient in determining the crater shape was emphasized in the model, which showed an error of 11%
Zhang et al. (2015)	An optimal Gaussian distribution was proposed to develop a parametrized model. The depth and dia of the crater were predicted based on the melting temperature isotherms.
Hoang et al.(2014)	A regression model was developed for the EPF. The EPF was sensitive to the dielectric density and the conductivity of the workpiece material.
Guo et al. (2014)	The atomistic continuum model compares the combined and individual thermal and electrical actions responsible for the material removal.
Mujumdar et al. (2014)	The plasma model was developed using combined bubble dynamics, plasma chemistry, and particle balance equations.
Mujumdar et al. (2014)	Crater model was simulated by inputting the plasma properties using the level set method. The predicted crater depths were shallower compared to the experiments.

Shao et al. (2013)	An indirect approach was proposed to calculate the energy partition factor using the crater geometry. The estimated percentage of energy to the anode was 9.4%.
Shabgard etal. (2013)	EPF varies with the EDM's parametric settings, and the plasma flushing efficiency depends on the fraction of energy absorbed by the respective electrodes.
Subbo et al. (2012)	The plasma temperature calculated using the line pair method and the Saha equation was 5000-8000 K with 4 order increments in electron density with increasing energy.
Zahiruddin et al. (2012)	High energy density was reported with micro-EDM, and the conduction losses in the workpiece were low compared to the macro-EDM.
Joshi and Pandey (2009)	FEM was combined with ANN to model the EDM. MRR, SR, and crater diameter were predicted accurately, while tool wear was overestimated.
Tan and Yeo (2008)	Melting isotherms were used to calculate the plasma flushing efficiency between 19-34%, depending on the input energy.
Katz and Tibbles (2005)	The input variables are formulated as a dimensionless group. Least-square regression method is used to calculate plasma parameters.
Dhanik and Joshi (2005)	The authors have combined the bubble and electron impact ionization mechanisms to explain the rapid breakdown phenomena during the micro-EDM.
Das et al. (2003).	Gaussian heat flux distribution with a constant magnitude of energy during discharge. High values of residual stresses were observed on the crater surface.
Patel et al. (1989)	Uniformly distributed heat flux with a constant spark radius was used to model the anode erosion.

2.4 Hybridization of the micro-EDM process

Hybrid machining processes have emerged as an effective solution in the micromachining industry for processing difficult-to-cut materials with intricate geometries [123–125]. Although various definitions exist, a hybrid machining process is broadly defined as the simultaneous application of different energies at the same machining area to remove the material [126,127]. The main aim of the hybrid machining processes is to utilize the advantages of involved processes while addressing the shortcomings of the individual processes to generate a "1+1=3" kind of effect, as discussed by Schuh et al. [128]. Electrical discharge machining comes with the advantage of machining the materials irrespective of their hardness. Still, it has inherent disadvantages such as low material removal rate, debris adhesion, high surface roughness, etc. [5,6]. The extent of these shortcomings of the EDM process magnifies when the process is performed at a micro-scale, i.e., micro-EDM, due to a very narrow IEG of about 1-10 microns [129]. Hybridization of the EDM process with ultrasonic vibrations has been identified as a great technique to overcome the inherent disadvantage of poor flushing of

the debris and the frequent short-circuiting phenomenon [7,8]. One of the main challenges in micro-EDM is the adhesion and accumulation of debris in the small spark gap, which can lead to arcing and disrupt the machining process. However, the use of vibration can help address this issue. A definite enhancement in the MRR was observed in the literature by assisting the EDM process with ultrasonic vibrations of any frequency with additional advantages, such as reduction in the TWR and surface roughness [130].

2.4.1 Principle of vibration-assisted EDM

Vibration-assisted EDM (VAEDM) is a hybrid machining process in which a range of vibrations are applied to the tool, workpiece, or dielectric fluid to improve the flushing of debris from the narrow IEG [131–133]. VAEDM combines the principles of traditional EDM with mechanical vibrations to enhance the material removal process. The principle behind VAEDM involves the application of controlled vibrations to assist in removing debris from the IEG. These vibrations are combined with the electrical discharge pulses, improving machining efficiency and enhancing surface finish. One of the fundamental mechanisms behind the improved performance with vibration assistance is cavitation. Ultrasonic vibrations generate high-frequency pressure waves in the dielectric fluid used during EDM. These pressure waves induce the formation and collapse of microscopic bubbles, known as cavitation [134]. These bubbles collapse near the workpiece surface and create localized micro-jets and shock waves, as shown in Figure 2.18. These phenomena contribute to dislodging debris, eroding the workpiece material, and increasing the material removal rate.

In addition to the cavitation, vibration assistance imparts another mechanism in the IEG known as agitation. The ultrasonic vibrations cause the dielectric fluid to agitate vigorously. This agitation enhances the circulation and distribution of the dielectric fluid around the spark gap and electrode-workpiece interface [135]. As a result, the dielectric fluid effectively removes debris and transports it away from the machining zone, preventing the debris's agglomeration. Thus the vibration assistance Improves flushing, reduces the chances of debris re-deposition, maintains stable and consistent spark gaps, and enhances overall machining performance. Furthermore, ultrasonic vibration assistance contributes to lowering the recast layer formation. EDM process often forms the recast layer on the finished workpiece surface, which hampers the effectiveness of the spark discharge, increases the surface roughness, and limits the machining efficiency. Ultrasonic vibrations disrupt and reduce this recast layer's thickness, facilitating a more efficient spark discharge and improving material removal rates [136]. Various modes of ultrasonic vibrations during the EDM process were studied, such as

the vibrations applied to the workpiece electrode, tool electrode, and dielectric medium [137,138]. In micro-EDM, the application of vibration proved beneficial by improving the machining conditions when applied to either of the electrodes or the dielectric.

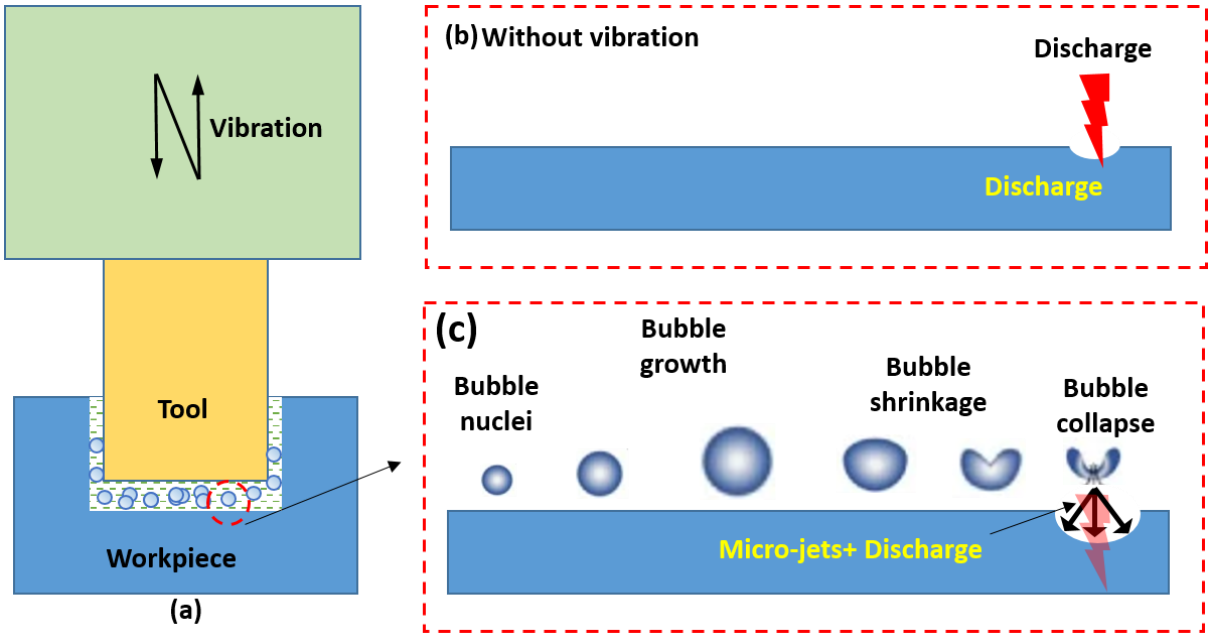

Figure 2.8 (a) Tool-work arrangement in vibration-assisted EDM (b) workpiece surface without vibration (c) workpiece surface with cavitation mechanism during vibration

2.4.2 Ultrasonic vibration assistance to the workpiece

Ultrasonic vibration assistance to the workpiece is relatively simple compared to tool vibrations. The system described in Figure 2.9 utilizes ultrasonic vibration to enhance machining. An ultrasonic pulse generator generates a sinusoidal wave with the desired frequency, which is applied to a piezoelectric transducer (PZT). The PZT is attached at the bottom of the dielectric tank through the ultrasonic horn, designed to facilitate the transfer of ultrasonic vibration to the workpiece with the desired amplitude, as depicted in Figure 2.9. The system enhances machining performance and productivity by utilizing ultrasonic vibration and maintaining a proper spark gap and dielectric pressure. Additionally, it enables the machining of high aspect ratio features [31]. Vibration can also improve the stability of the micro-EDM, reducing instances of abnormal discharges.

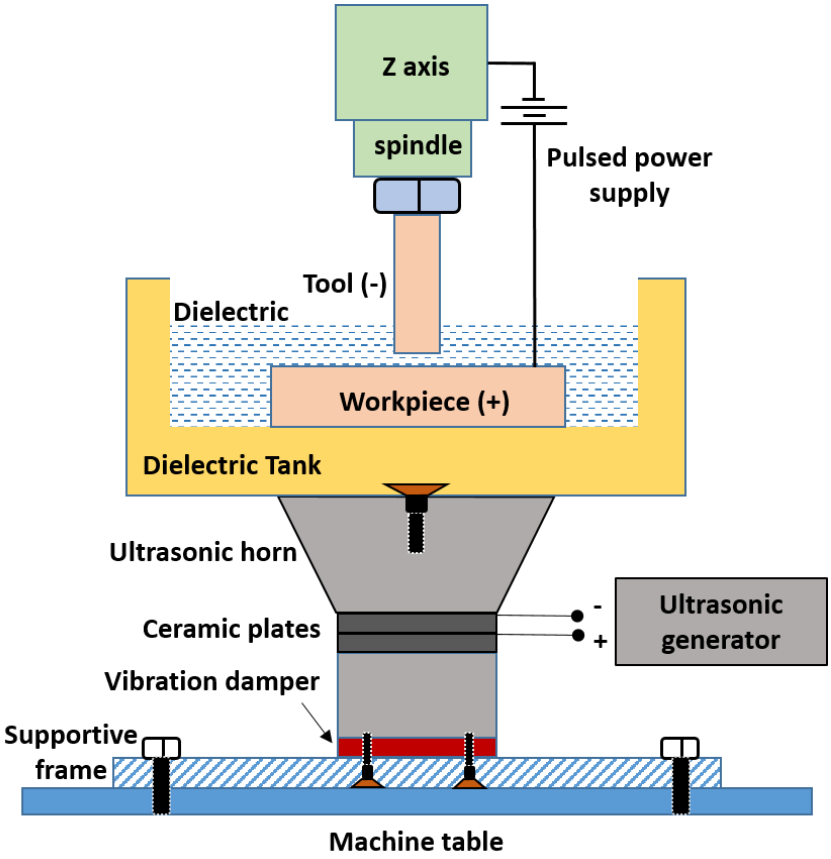

Figure 2.9 Ultrasonic vibration-assisted to the workpiece using piezo transducers

Research conducted on ultrasonic vibration on the workpiece demonstrated that stable machining and reduced machining time are achieved with a combination of high-frequency and low-amplitude vibrations [139]. Garn et al. studied the micro-EDM boring process, specifically examining vibrations' effects on the workpiece [140]. Their findings indicated that the machining time decreased as the vibration frequency increased due to reduced arcing duration. Lin et al. proposed a hybrid approach to improve the EDM process by combining ultrasonic vibration-assisted EDM with a magnetic field [141]. The researchers observed a 34% increase in the MRR attributed to the ultrasonic vibration-assisted magnetic force, which resulted in the debris explosion. Likewise, Mastud et al. investigated the vibration-assisted micro-EDM process under simulated conditions [142]. They discovered that during the upward and downward motion of the workpiece, a flow reversal occurred, imparting oscillatory motion to the dielectric and debris particles.

Furthermore, the researchers concluded that applying vibrations to the workpiece caused compression and expansion of the dielectric fluid at the discharge gap [143]. The applied vibration increased debris velocities, improving flushing and enhancing dielectric flow behavior. In deep hole drilling of titanium alloy with an aspect ratio of more than 15, ultrasonic

vibrations increased the effective pulse discharge ratio [144]. This increase was due to the reduced sedimentation of the eroded debris on the machined surface, improving the EDM process efficiency [145]. Chang et al. also found that ultrasonic vibrations facilitated the flow of working fluid and improved discharge efficiency during EDM milling experiments [146]. In separate studies, Schubert et al. and Molik et al. provided evidence that the superposition of ultrasonic vibrations positively impacted dielectric cleaning and homogenization. This effect improved the EDM process's accuracy and performance [147,148]. Jujhar et al. assisted a high-carbon, high-chromium workpiece with ultrasonic vibration at 25 KHz with an amplitude range of 1-10 microns to investigate the machined surface's hardness and surface damage [149]. The authors have concluded that ultrasonic vibration assistance has increased the microhardness of the machined surface while at the same time decreasing the white layer formation. Jafferson et al. performed micro-EDM milling on AISI 304 stainless steel with a combined and separate assistance of ultrasonic vibrations and magnetic field [150]. The authors reported an enormous improvement in machining performance when both approaches were adopted separately instead of combined. Tong et al. investigated the machining performance of the non-circular profiles with vibration assistance and concluded that high-frequency vibrations combined with low amplitude produced better machining performance [139]. The authors have also concluded that the vibration amplitude set according to a favorable discharge gap increased the machining performance by imparting better dielectric fluidity and gap evacuation.

2.4.3 Ultrasonic Vibration assistance to the tool electrode

Applying vibration to the tool electrode during the micro-EDM is identified as a challenging task as the direction of the tool feed becomes parallel to the direction of the ultrasonic vibration. This increases the probability of tool wear, breakage, and deflections as the tool electrode is in the micron range [151]. The setup depicting ultrasonic vibration assistance to the tool electrode is shown in Figure 2.10. Piezo stack actuators are generally used between the spindle head and the collect to provide ultrasonic vibration to the tool electrode. Zhang et al. have explored the ultrasonic vibrations of 21 KHz frequency with a range of amplitudes from 5-15 microns on a ceramic workpiece with a steel electrode [152]. The authors have expressed the vibration using the following equation.

$$U(t) = A\sin(2\pi ft + \phi) \tag{2.18}$$

U(t) is the tool tip displacement, *A* is the vibration amplitude, and *f* is the frequency. The velocity of the vibrating tool tip can be given as

$$V(t) = \frac{dU(t)}{dt} = 2\pi f A \cos(2\pi ft + \phi) \tag{2.19}$$

The authors have observed an increase in MRR with increasing amplitudes, and the surface roughness varied from 3 to 6 µm at an amplitude of 5 µm. Uhlmann and Domingos have machined seal slots in high-temperature resistant materials for turbine components by assisting the conventional EDM process using a piezo actuator [153]. The authors have varied the amplitude from 2-16 µm and frequency from 100-1000 Hz to conclude that high vibration frequency and low amplitudes had increased the MRR. They concluded that the MRR was increased by 11%, and the tool wear was reduced by 21% while machining the slots with an aspect ratio of 12. Several researchers have argued that the increase in MRR was due to the rise in the gap between the electrodes during the pulse off time, which assists easy removal of debris and exposes fresh work surface during the subsequent pulse on time [154,155]. Qixuan et al. have applied ultrasonic vibrations to the micro-EDM on Ti-6Al-4V material and studied the optimization of the processing parameters [156]. The authors observed a 2.4 times increment in the MRR, and the tool wear ratio decreased by 65 % when the vibrations were applied at 6 µm amplitude. Hirao et al. observed a seven-time increase in MRR with surface finish (SF) deterioration when ultrasonic vibrations were applied to the tool electrode at a conventional scale [157].

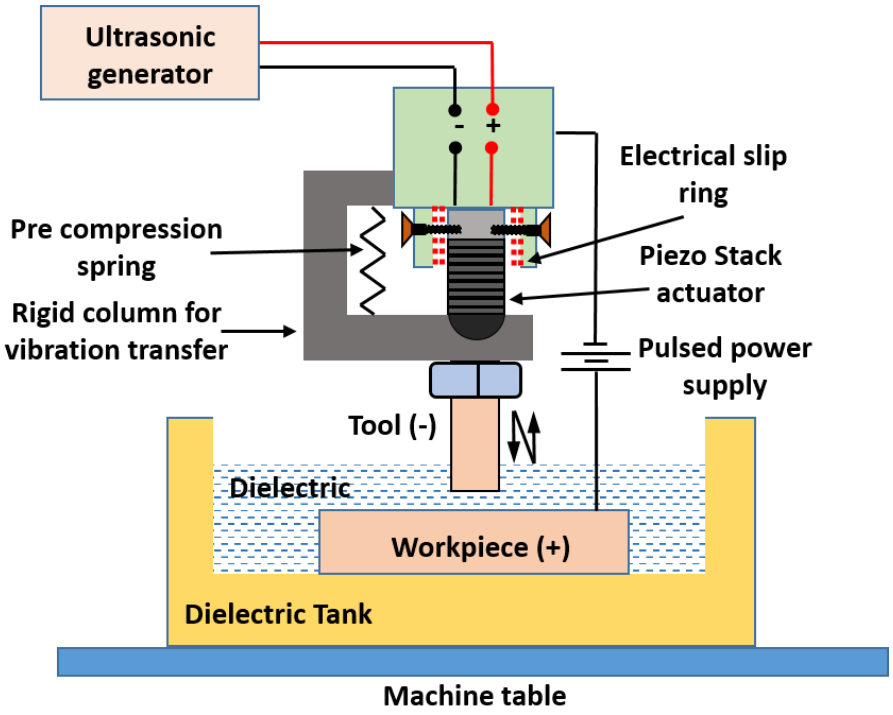

Figure 2.10 Ultrasonic vibration-assisted to the tool using piezo stack actuator

Vibration assistance to the tool electrode is anticipated to be more beneficial, especially in reverse-μEDM, a variant of μEDM. Reverse-micro-EDM is an emerging variant of micro-EDM generally used to fabricate arrayed microstructures with high aspect ratios [158]. In contrast to conventional micro-EDM, a reversed polarity is used in which the electrode attached to the spindle is treated as a workpiece with positive polarity to ensure high material removal. Further, an auxiliary device has been developed to assist the tool electrode with vibration in the conventional EDM process [131]. They used a voice coil motor in their setup as a vibration source. The authors have found that MRR was better with vibration assistance than the conventional unassisted EDM. A very high increase in MRR was observed when ultrasonic vibrations were applied to the tool electrode for machining ceramic-coated Nickel alloy at a conventional scale using a piezoelectric actuator [154]. Introducing vibrations helps increase the IEG during the pulse-off period, causing effective debris removal, which increases the MRR and stability of the discharges and reduces the arcing. Effective debris removal as a cause of vibrations exposes the fresher work surface to the tool rather than debris to decrease the tool wear [155].

2.4.4 Ultrasonic vibration assistance to the dielectric

In micro-EDM processes, vibration is often applied to the dielectric fluid, particularly when a powder-mixed electrolyte is used. This vibration can be achieved using ultrasonic vibrations instead of a stirrer [137]. While a stirrer effectively spreads the powder throughout the dielectric fluid and prevents powder deposition at the bottom of the tank, it has limitations in avoiding powder agglomeration. In micro-EDM, it is not advisable to use straight or indirect flushing methods due to the delicate nature of the micro-tool and the flushing flow. Therefore, vibration is preferred as it helps maintain the stability of the process. The purpose of introducing high-frequency vibration to the dielectric fluid is to enhance the kinetic energy of tiny debris particles. This effectively removes debris from the narrow spark gap, minimizing the occurrence of short circuits during the spark discharge. Another advantage of vibrating the dielectric fluid is its cost-effectiveness compared to vibrating the tool or workpiece electrodes. An ultrasonic bath is a common approach to applying vibrations to the dielectric. However, commercially available high-frequency baths can also be used to achieve the desired vibration of the dielectric fluid. Typically, the vibration frequency range in an ultrasonic bath is maintained between 40 and 45 kHz to increase the kinetic energy of debris particles.

In recent studies, researchers have explored the application of ultrasonic vibration to the dielectric fluid in micro-EDM processes, aiming to improve machining efficiency and

surface quality. Prihandana et al. conducted experiments where ultrasonic vibration with a frequency of 43 kHz was applied to an ultrasonically activated bath, resulting in increased kinetic energy of discharge debris [137]. This led to a significant improvement in MRR and surface quality. Schubert et al. investigated the immersion of a vibrating sonotrode in the dielectric fluid [159]. They could effectively increase the processing speed by aligning the high-intensity region near the machining zone. Ghiculescu et al. developed WEDM equipment that utilized cavitation effects produced through longitudinal oscillations of an acoustic chain immersed in dielectric liquid [160]. The dielectric fluid in a hopper maintained the relative position between the workpiece and the electrode, ensuring precision in machining while achieving an increased machining rate. Ichikawa and Natsu conducted experiments to investigate the effects of applying ultrasonic vibrations to the machining fluid in micro-EDM with a 40 µm tungsten rod as a tool and SUS 304 as a workpiece [161]. Their findings revealed a significant increase in machining speed with a decrease in lateral gap and tool wear ratio by introducing ultrasonic vibration. In addition, the vibration assistance enabled the process to be carried out at higher feed rates, increasing productivity.

2.4.5 Low-frequency vibration-assisted EDM

Low-frequency vibrations can be combined easily at a low cost with the micro-EDM process compared to high-frequency ultrasonic vibrations, as the latter imposes the need for the resonant system [162]. During the micro-EDM drilling of deep holes, as high as 60% reduction in machining time was observed with low-frequency vibrations at an amplitude of 4 µm [163]. However, increasing the amplitude at the same frequency did not show further improvement in MRR. During the low-frequency vibration assistance, the increase in MRR and enhancement of overall machining performance was more pronounced at low input energy settings of the micro-EDM power supply [164,165]. Jahan et al. fabricated micro holes with aspect ratios as high as 16.7 during low-frequency vibration assistance with increased MRR due to improved flushing and reduced short circuits [166]. Recently, attempts have been made by Singh et al. to assist the workpiece with low-frequency vibrations in the micro-EDM drilling process with different materials to explore the workpiece dependency and material-independent effect, respectively [167,168]. They have concluded that vibration assistance was more effective at low energy settings and for materials with higher thermal and electrical conductivities, like copper alloys. The surface finish was also material dependent and superior for materials with low thermal conductivity. Mollik et al. concluded that vibration assistance

to the workpiece was more effective by homogenizing and cleaning of dielectric when low energy settings were applied in the micro-EDM drilling process [148].

Ununе et al. have used workpiece vibration in the micro-EDM milling process for difficult-to-cut Inconel 718 material [169]. The authors observed an increased MRR and decreased TWR due to enhanced dielectric action in the IEG. In a recent study, Ununе and Mali studied the effect of low-frequency vibrations in micro-EDM drilling on the Inconel 718 workpiece with varying capacitances, voltage, rotational speed, and frequencies. They have concluded that increasing the vibration frequency enhances the accuracy and surface finish and decreases the tool wear ratio [170]. The micro-EDM milling tool was assisted with low-frequency vibrations by Raza et al. to examine the machining performance and observed a 48% drop in the machining time with increased surface finish [171]. The authors have also explored the reverse micro-EDM process and found that it was more beneficial by a 57 % increase in machining efficiency.

Table 2.5 Highlights of the literature on vibration-assisted EDM

Literature	Findings
Molik et.al(2022)	vibration assistance to the workpiece was more effective by homogenizing and cleaning of dielectric when low energy settings were applied in the µEDM drilling process
Raza et al. (2022)	48% reduction of machining time with increased dimensional accuracy, but the surface finish deteriorated.
Singh et al.(2021)	vibration assistance was more effective at low energy settings and for materials with higher thermal and electrical conductivities, like copper alloys.
Qixuan et al.(2021)	The authors observed a 2.4 times increment in the MRR, and the tool wear ratio decreased by 65 % when the vibrations were applied at 6 µm amplitude.
Ununе et al.(2020)	Inconel 718 showed increased MRR and decreased TWR due to enhanced dielectric action in the IEG.
Kishore et.al(2019)	Applying vibration on the tool electrode is anticipated to be more beneficial, especially in the case of Reverse-µEDM.
Hirao et al.(2018)	A seven-time increase in MRR with deterioration in the surface finish (SF) was observed when ultrasonic vibrations were applied to the tool electrode at a conventional scale.
Uhlmann and Domingos(2016)	The MRR was increased by 11%, and the tool wear was reduced by 21% with vibration-assisted EDM setup using a piezoelectric actuator.
Mastud et.al(2015)	Compression and expansion of the dielectric fluid increase the velocities of debris, which contributes to effective flushing.

Y. C. Lin et al. (2014)	34% increase in the MRR due to the explosion of debris by the ultrasonic vibration-assisted magnetic force.
Schubert et al.(2013)	Dielectric vibrations effectively increase the processing speed by aligning the high-intensity region near the machining zone.
Garn et al(2011)	The machining time reduces as the frequency of vibration increases because of the reduction in the arcing duration.
Jahan et al.(2009)	A decrease in stability and accuracy of machining with an increase in amplitude and frequency of vibration has been observed.
M. M. Sundaram et.al(2009)	Effective debris removal as a cause of vibrations exposes a fresher work surface to the tool rather than debris to decrease the tool wear.

2.5 Summary of the literature survey and research gap

In summary, hybridizing the micro-EDM with vibration assistance has proven advantages in all aspects of machining, such as MRR, TWR, accuracy, and surface quality. However, less attention has been given to modeling the actual plasma channel, especially in micro-EDM, considering the plasma channel as a heat source. Although experimental results back up the assumption of plasma as a heat source, the existing heat source models are primarily inclined toward macro-EDM. The applicability of such models to micro-scale EDM is debatable and proven inappropriate by several researchers particularly due to the high energy density and low conduction losses in the workpiece reported with micro-EDM. The following research gaps can be identified based on the extensive literature review in the above sections.

- *Limited insights into plasma column formation:* Although the formation and expansion of plasma columns have been extensively studied in arc physics and macro-EDM literature, there is a lack of in-depth understanding and insights into the process of plasma column formation, specifically in the context of micro-EDM models. Also, more experimental studies need to characterize plasma formation and expansion. Addressing this research gap would contribute to a better understanding of the role of plasma columns in both macro and micro-EDM processes.
- *Lack of integration of plasma characteristics in EDM models:* Many existing EDM models do not incorporate comprehensive insights into plasma column formation and its associated factors. Consequently, there is a need to bridge this research gap by developing EDM models that consider the properties of thermal plasmas, arc physics, and their behavior under different conditions, tailored explicitly for electrical discharge machining processes.

- *Insufficient analysis of tool electrode vibration in micro-EDM:* While studies have focused on assisting the workpiece with vibrations in micro-EDM, there is a lack of detailed analysis specifically related to the tool electrode vibration. The existing literature is less inclined towards micro-EDM, and there is a need for a comprehensive examination of the machining performance concerning the electrical behavior of the discharge pulses when the tool electrode is subjected to vibrations.
- *Limited understanding of the mechanism and effects of vibrations on micro-EDM:* The primary mechanism behind the material removal in vibration assistance has not been understood through modeling and experimental perspective. Also, there is a lack of detailed analysis on the nature of discharge pulses, MRR, TWR, recast layer thickness, and surface topography when ultrasonic vibrations are applied. Therefore, investigating the effects of ultrasonic vibrations on these parameters would contribute to a better understanding of the stability and performance of the machining process.
- Need for a pulse monitoring system for ultrasonic vibrations: There is a need for pulse monitoring studies that can effectively monitor the impact of ultrasonic vibrations on the continuous micro-EDM process. Such a system would help in correlating the stability of the machining process with different input energy parameters, providing valuable insights into the relationship between vibration-assisted μEDM and machining performance.

Chapter 3

Multiphysics Modeling and High-Speed Imaging of Micro-EDM Plasma

3.1 Introduction

Finite element modeling (FEM) is one of the most commonly used techniques for simulating plasma channel formation during arc/spark generation. The purpose of this chapter is to present a comprehensive study of the plasma channel formation during the micro-EDM process using finite element modeling. The numerical model of the plasma channel formation is developed using well-established current conservation, heat transfer, and fluid equations in the literature. In addition to the plasma formation, the numerical model also predicts the heat flux distribution responsible for material melting and subsequent removal. The coupled numerical model explains the plasma-electrode interactions via different heat transfer mechanisms such as conduction, convection, radiation, and thermionic effect. The chapter will also describe the validation of the developed model using high-speed imaging of the plasma channel formation to ensure the accuracy and reliability of the model. The study aims to investigate the effects of voltage and capacitance on the plasma channel formation during the micro-EDM process. The results will be presented regarding the plasma channel characteristics, such as diameter, temperature, heat flux distributions, and their dependence on the input parameters.

3.2 Numerical model for the plasma channel formation

3.2.1 Assumptions

A 2D axis-symmetric model for the plasma channel formation during the micro-EDM process is shown in Figure 3.1. Some of the main assumptions made during the simulation are:

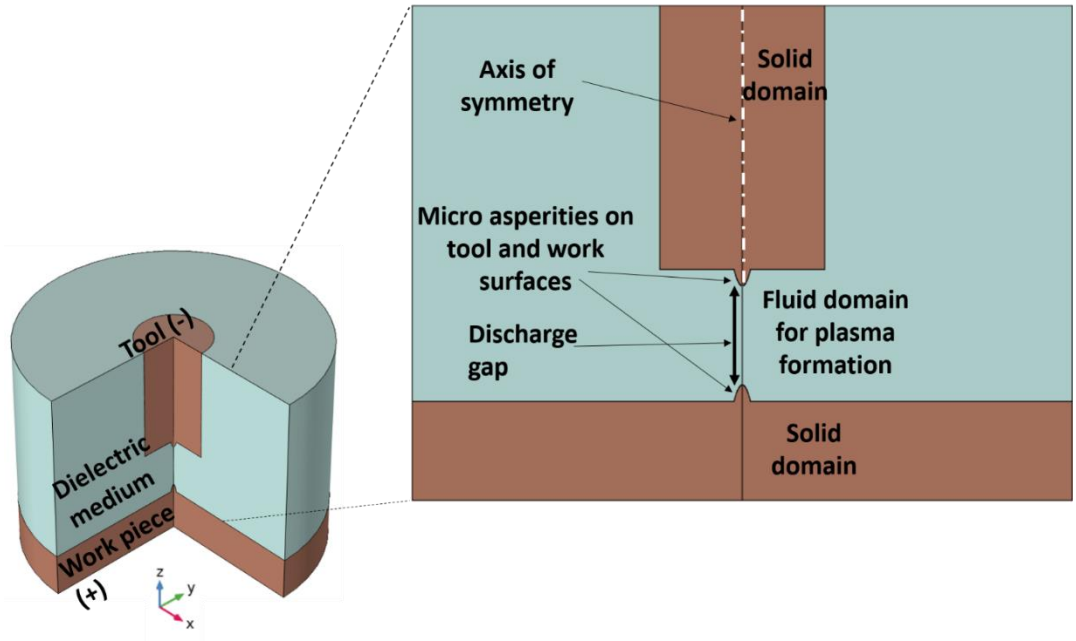

Figure 3.1 2D axisymmetric model of micro-EDM

1) Local thermal equilibrium (LTE) condition is assumed for the plasma channel formations as the EDM plasmas fall under thermal plasmas. This implies that the temperatures of the heavy particles and the electrons are equal inside the plasma channel.

2) Discharge is assumed to have occurred at the shortest distance between the micro asperities emerging from the tool and work surfaces.

3) A single discharge is assumed to occur in the gap during the applied pulse duration.

4) Dielectric fluid is considered inviscid and incompressible.

5) The plasma is considered fully ionized, i.e., a mixture of two components, electrons and ions.

3.2.2 Electric field and current-related equations

The formation of the plasma channel in micro-EDM occurs due to the transformation of the input electric energy into heat energy. The electric current module determines the parameters for computing the plasma heat source. Three fundamental quantities must be considered to calculate the plasma heat source: current density, electric field strength, and the electric potential across the IEG. The equations of current conservation and Ohm's law, given by Eq. (3.1) and Eq. (3.2), respectively, govern the current flow within the fluid domain, which is the dielectric [172,173].

$$\nabla \cdot J = Q_{j,v} \tag{3.1}$$

$$J = \sigma E + \frac{\partial D}{\partial t} + J_c \tag{3.2}$$

Where $E = -\nabla V$, J is a vector representing current density, $Q_{j,v}$ is the current source in A/m^2, E is the vector of electric field strength, and V is a scalar quantity representing the electric potential. The electric current interface solves the above three equations, and the obtained values of the density and strength of the electric field are used as input to compute the properties of the plasma channel formed using Eq. (3.3).

$$Q_p = \frac{\partial}{\partial t}\left(\frac{5k_bT}{2q}\right)\left(\nabla T \cdot J\right) + E \cdot J + Q_{rad} \tag{3.3}$$

Here Q_{rad} is the net volumetric emission coefficient in W/m^3 k_b the Boltzmann constant and Q_p the plasma heat source responsible for forming the plasma channel in the dielectric medium. The plasma source here consists of three different components. First is the electron enthalpy transport term, which is nothing but the effect of the electronic fluxes inside the plasma channel and depends on the temperature of the plasma and the current density. The second is the Joule heating effect, and the last is the effect of radiation emissions.

3.2.3 Heat transfer and fluid flow

After obtaining the plasma heat source from the current conservation equations is applied to the dielectric using Eq. (3.4).

$$\rho C_p \frac{\partial T}{\partial t} + \rho C_p u \cdot \nabla T = \nabla \cdot \left(k \nabla T\right) + Q \tag{3.4}$$

Cp is the dielectric's specific heat, ρ is the dielectric density, and u is the unit vector. Here, the last term on the right side of the equation represents the plasma source term. This thermal energy source was obtained from the electrical module and contributes heat transfer in the dielectric area surrounding the tool and workpiece to form the plasma channel. Using the LTE approximation, the plasma in the IEG can be considered an electromagnetic viscous fluid. The corresponding mass and momentum conservation equation is defined by the Navier-Stokes equations as given in Eq. (3.5) and Eq. (3.6) [174].

$$\rho(\nabla \cdot u) = 0 \tag{3.5}$$

$$\rho\left(\frac{\partial u}{\partial t}+u\cdot\nabla u\right)=\nabla\cdot\left[-pI+K-\frac{2}{3}\mu(\nabla\cdot u)\right]+F \tag{3.6}$$

Where u is the velocity vector, p is the fluid pressure, F is the volume force vector, μ is the dynamic viscosity, and K is the viscous stress tensor in Pa given as $K=\mu\left(\nabla u+(\nabla u)^{T}\right)$.

3.2.4 Plasma-electrode interaction

The plasma channel that forms in the IEG propagates radially and impacts the cathode and anode boundaries, which are the surfaces of the tool and work electrodes. The boundary heat source is coupled between the electric and heat transfer modules and accounts for the electromagnetic surface losses. The heat transfer equation at the electrode boundaries can be expressed as follows.

$$Q_b=-n\cdot(-k\nabla T) \tag{3.7}$$

Where Q_b is the cumulative heat flux at the electrode boundary, k is the thermal conductivity of the electrode material, and n is the unit normal vector perpendicular to the electrode surface and in the direction of the plasma channel.

The energy balance at the cathode and the anode interfaces is explained in the following Eq. (3.8).

$$Q_{cathode,\,input}=Q_{plasma,\,output}+Q_{ions}-Q_{thermionic}-Q_{radiation} \tag{3.8}$$

Equation 7 shows that, along with the heat flux from the plasma channel and the radiation loss from the cathode surface, two additional components contribute to the heat flux at the electrode boundary. The first component results from positive ion bombardment at the cathode surface. The second is the cooling effect produced by the thermionic emission from the cathode surface due to its heating up. Therefore, the heat flux equation at the cathode boundary can be expressed as shown in Eq. (3.9).

$$Q_{cathode}=Q_{plasma}\cdot(n)+\left|J_{ion}\right|V_{ion}-\left|J_{elec}\right|\phi_s-\varepsilon\sigma_b T_s^{4} \tag{3.9}$$

Where $Q_{cathode}=-k_c\nabla T_c$, $Q_{plasma}=-k_{pl}\nabla T_{pl}$. k_c is the thermal conductivity of the cathode, k_{pl} is the thermal conductivity of plasma, T_c and T_{pl} represents the temperature fields in the cathode and the plasma, respectively. T_s, is the surface temperature of the cathode and signifies the dependency of the net heat flux into the cathode on the local surface temperature [175]. V_{ion} is the plasma ionization potential depends upon the dielectric medium, φ_s is the work function

of the cathode electrode surface, J_{elec} and J_{ion} are the normal current densities of the electrons and the ions, respectively, as given in Eq. (3.10).

$$\left|J_{ion}\right| = \left|J \cdot n\right| - \left|J_{elec}\right| \tag{3.10}$$

Here $J \cdot n$ is the total normal current density, the summation of ion and electron densities, respectively. The current density of the electrons can be computed as

$$\left|J_{elec}\right| = \begin{cases} J_R(T), if \left|J \cdot n\right| > J_R(T) \\ \left|J \cdot n\right|, if \left|J \cdot n\right| \le J_R(T) \end{cases} \tag{3.11}$$

The normal current density of the electrons is taken as equal to the term $J_R(T)$ called the Richardson-Dushman current density; if the total normal current density becomes greater than $J_R(T)$ otherwise, it becomes equivalent to the total current density. The Richardson-Dushman current density is defined as given in Eq. (3.12).

$$J_R(T) = A_R T^2 \exp\left(-\frac{q\phi_{eff}}{k_B T}\right) \tag{3.12}$$

Where A_R is the Richardson's constant in A/m^2K^2, q is the electron charge, ϕ_{eff} is the effective work function. The energy balance at the anode interface is given as

$$Q_{anode,\,input} = Q_{plasma,\,output} + Q_{electrons,\,condensation} - Q_{radiation} \tag{3.13}$$

The electrons bombarding the anode surface generate heat, and there is no ion current present in the vicinity of the anode. Considering the heat flux from the plasma channel and the radiation loss, the resistive heating at the anode is given in Eq. (3.14).

$$Q_{anode} = q_{plasma} \cdot (n) + \left|J \cdot n\right| \phi_s - \varepsilon\sigma_b T^4 \tag{3.14}$$

Where $Q_{anode} = -k_a \nabla T_a$ and $Q_{plasma} = -k_{pl} \nabla T_{pl}$, k_a is the thermal conductivity of the anode, k_{pl} is the thermal conductivity of plasma, T_a and T_{pl} represent the temperature fields in the anode and the plasma, respectively. A schematic diagram depicting the plasma-electrode interactions in the IEG is shown in Figure 3.2.

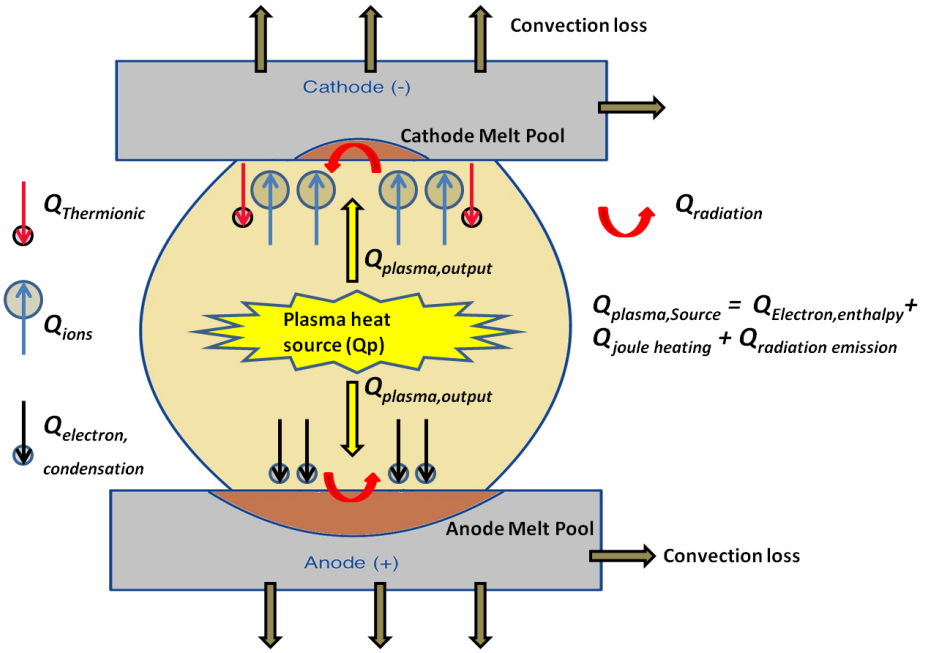

Figure 3.2 Plasma-electrode interactions in the IEG

3.2.5 Computational domain and boundary conditions

Figure 3.3 depicts the computational domain for the 2D axisymmetric model. Air is considered the dielectric fluid in the IEG because the narrow IEG was mainly filled with air bubbles due to the successive discharges occurring at very high frequencies [176]. The air bubbles in the IEG effectively eliminate the inertial effects of the dielectric liquid around the discharge gap, which was expected to hinder the expansion of the plasma channel. When the micro-EDM was performed in liquid and air, no difference was observed in the volume and size of the generated debris when the IEG was filled with liquid dielectric [177]. The area for expanding plasma channels in the simulation was determined by the rapid increase in the degree of ionization at temperatures above 5000 K [178]. ABLKJ represents the tool electrode (cathode) made of tungsten in Figure 3.3, while EFGHI represents the workpiece (anode) made of SS304 steel. The axis of symmetry is denoted by AF, about which all the reference diameters, widths of electrodes, and the dielectric domain are measured.

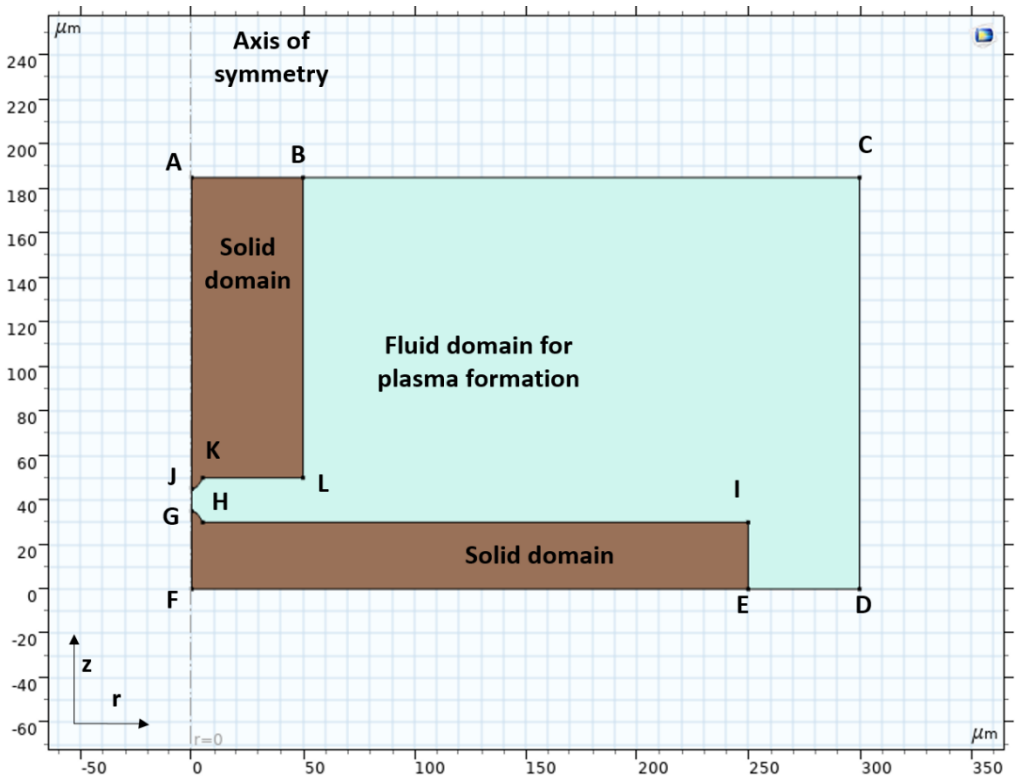

Figure 3.3 Computational domain for the simulation of micro-EDM (indicative)

Figure 3.4 illustrates the flow of the numerical simulation model and the physics involved. The thermophysical properties of the dielectric medium vary with temperature, are shown in Figure 3.5 [179]. An electric current module is active in all the dielectric areas, and the boundary conditions of the electric domain are applied to the surfaces of the tool and workpiece electrodes. At the start of the simulation, a fully charged capacitor is considered to mimic the instantaneous onset of the discharge typically observed during the micro-EDM process [121]. Circuit connections are applied at the two nearest peaks of the cathode and anode electrodes to simulate a single plasma channel. The proposed multiphysics model considers a coupling between the electric currents and heat transfer in fluid equations to determine the plasma heat source responsible for plasma channel formation. Thus, electromagnetics, heat transfer in fluids, and laminar flow are used to calculate the heat flux generated and temperature distribution in the plasma channel. As a result, during the simulation, the heat transfers in fluids, electric current, and laminar flow modules are active in the fluid domain.

In the computational domain illustrated in Figure 3.3, the cathode is denoted by JL, and GI represents the circuit's anode. Furthermore, the boundaries BC, CD, and DE are considered to be open boundaries to the atmosphere, which define the heat flux based on the fluid's inflow or outflow, as expressed by the following equations:

$$-n \cdot q = \begin{cases} 0, if n \cdot u \geq 0 \\ \rho \Delta H (u \cdot n), if n \cdot u < 0 \end{cases}.$$

No conductive heat flux occurs when the fluid flow exits the simulation domain through a boundary. On the other hand, if the fluid flow enters the domain, the conductive heat flux is proportional to the flow rate and the sensible enthalpy at the boundary. The heat flux at the electrode surfaces facing the plasma is determined by equations 3.8 and 3.13, which account for conductive, convective, and radiative heat fluxes from the plasma, as well as thermionic emission and electron condensation for the cathode and anode. The outer surfaces of the tool and workpiece are set to an ambient temperature of 293 K, and a convective heat flux condition is applied to their exterior surfaces (FEI and ABL) to dissipate heat.

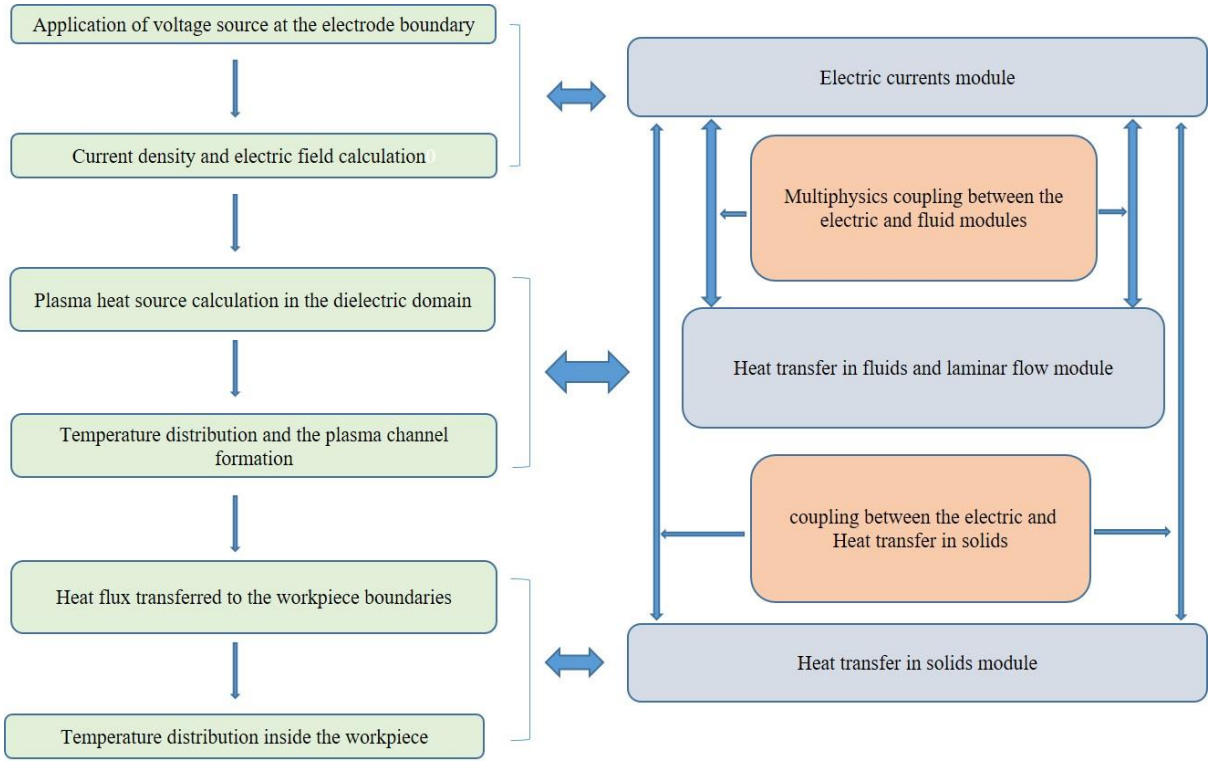

Figure 3.4 Flow of the numerical simulation model and the physics involved

3.2.6 Thermo-physical properties of the dielectric

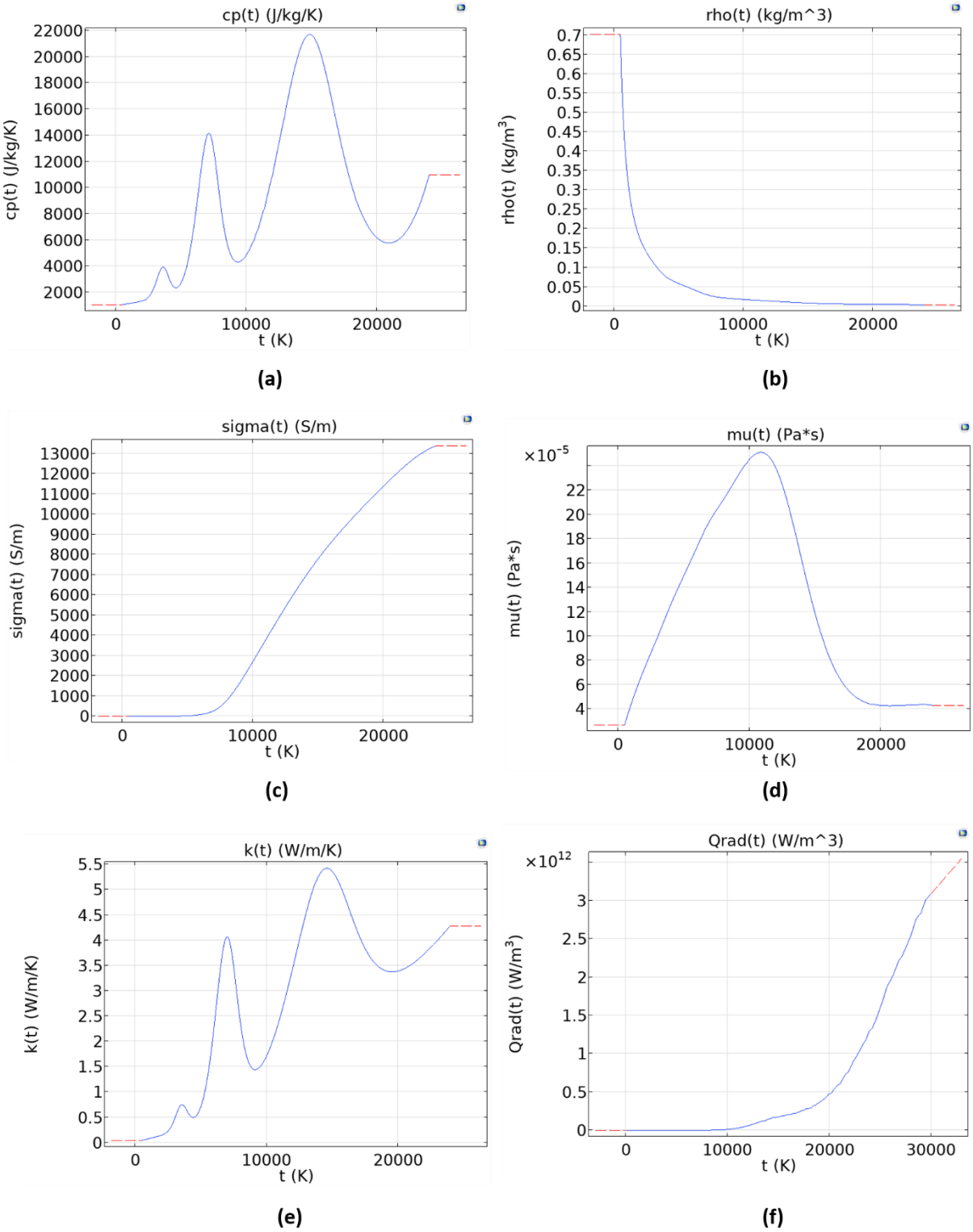

Figure 3.5 Temperature-dependent thermophysical properties of air (a) specific heat (b) Density (c) surface tension (d) viscosity (e) thermal conductivity, and (f) Total emission coefficient

3.3 Experimental validation of micro EDM plasma

Experimental verification was conducted to validate the numerical results obtained. Figure 3.6 shows the essential work-tool arrangement for micro-EDM, and Table 1 provides the specifications of the tool-work used in the experiments. The experiments were conducted using a high-precision multi-purpose CNC machine tool (Model: DT 110i, Make: MIKROTOOLS Pvt Ltd.) with a resolution of 0.1 μm in the three axes. Combinations of five voltage and three capacitance levels were considered to analyze the variation in plasma channel formation. These parameter levels were chosen at equal intervals in the available range with the machine tool. During the machining process, voltage and current signals were acquired using a data acquisition system (model: PXIe-5114; make: National Instruments) with a sampling rate of 250 MS/s, bandwidth of 125 MHz, 2 GHz processor, 4 GB RAM, and at a resolution of 8 bit. The plasma channel formed during the IEG was recorded using a high-speed video camera (Make: FastCam Mini ux100, 3600 fps at full resolution) that could capture up to 3600 fps at full resolution.

Figure 3.7 shows the plasma channel captured by the high-speed video camera. However, it was later discovered that the duration of the spark was much shorter than the camera's capturing speed, as shown in the current and voltage pulses captured in Figure 3.8. The plasma was re-recorded at 200000 fps with a reduced resolution to address this issue, meaning each frame represented about 5 μs. Although the actual spark length was still much shorter (0.3 μs) than the camera's maximum capacity, the authors conducted numerous experiments to verify the plasma's fully grown diameter. The maximum diameter of the plasma was then chosen from the available large set of data, which increases the probability of picking the fully-grown plasma diameter. An error bar showing the variation in the maximum diameter for different trials was provided in Figure 3.10 based on the revised imaging. The experiments were repeated three times for a single parametric combination to obtain an accurate measurement of the plasma channel diameter. Table 3.1 lists the different parametric combinations along with their corresponding machining parameters.

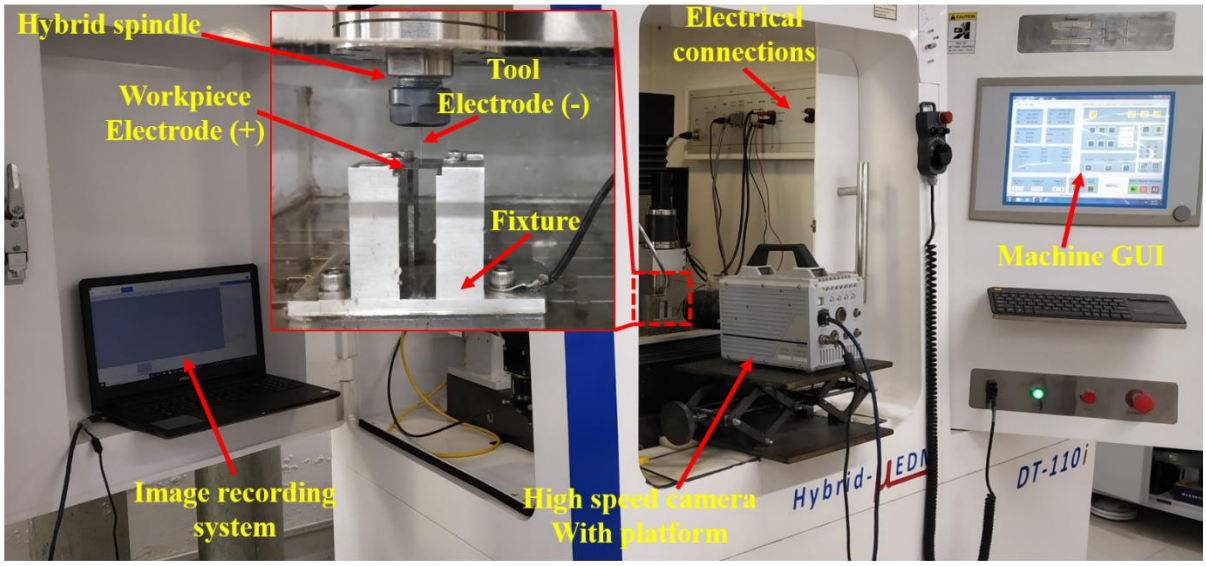

Figure 3.6 Experimental setup during the micro-EDM

Table 3.1 Essential machining parameters for plasma channel formation

Operating Parameters	Values
Workpiece electrode (Anode)	SS304 plate (0.3 mm thick)
Tool electrode diameter (Cathode)	0.5 mm (Tungsten)
Spindle speed	1000 RPM
Feed rate	1 μm/s
Open circuit Voltage	90 V, 95 V, 100 V, 110 V & 120 V
Capacitance	1 nF, 10 nF, and 100 nF

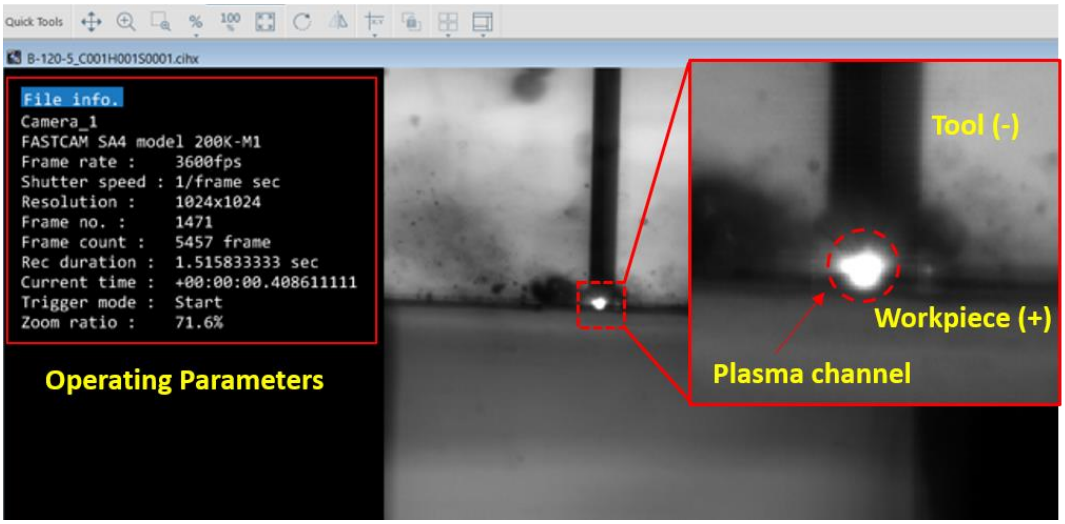

Figure 3.7 High-speed camera interface for plasma diameter measurement

The images of the plasma formation captured during the experiments are examined using ImageJ software to measure the diameter of the plasma channel precisely. After machining, the sample is collected and cleaned in an ultrasonic bath before being examined under a scanning electron microscope (SEM). Micro-craters created on the workpiece surface by a single discharge were photographed for each parametric combination.

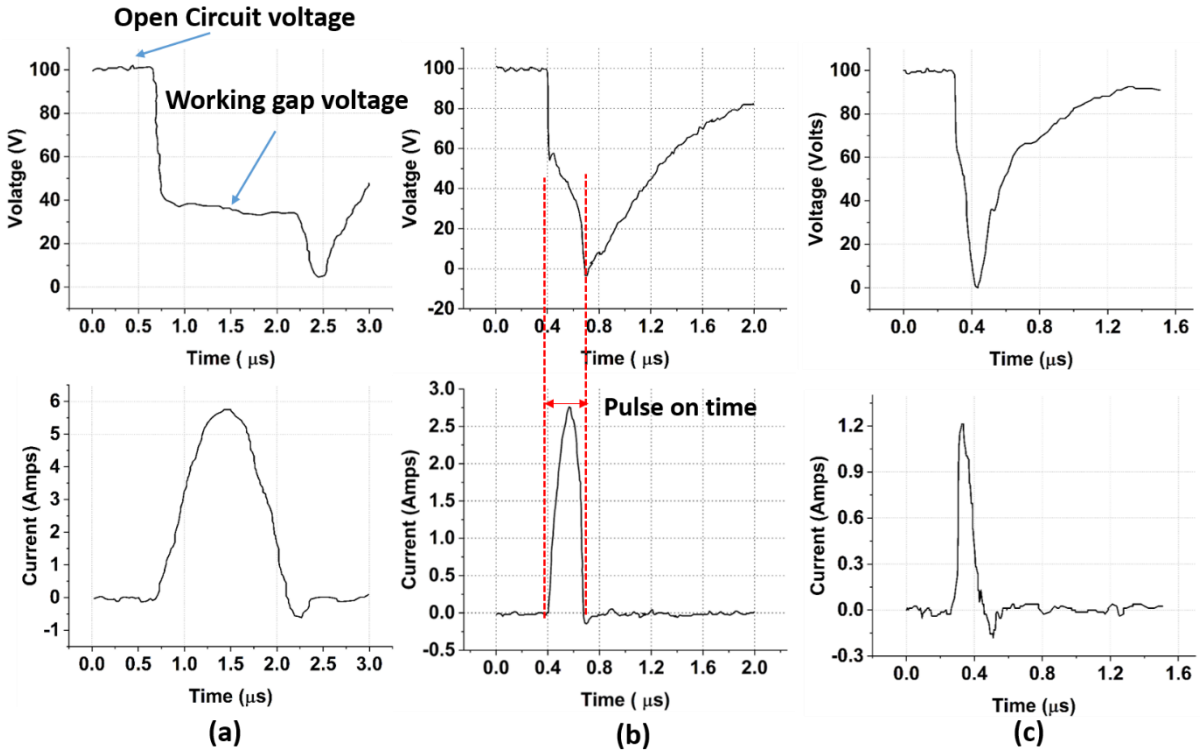

Figure 3.8 Discharge pulse data (a) 100 nF (b) 10 nF (c) 1 nF

3.3.1. Effect of machining parameters on the plasma channel diameter

Figure 3.9 shows the high-speed experimental images of the plasma channel diameters created in the IEG during micro-EDM. Figure 3.10 displays graphs that compare the simulated and experimental plasma diameters at different parametric settings of voltage and capacitances.

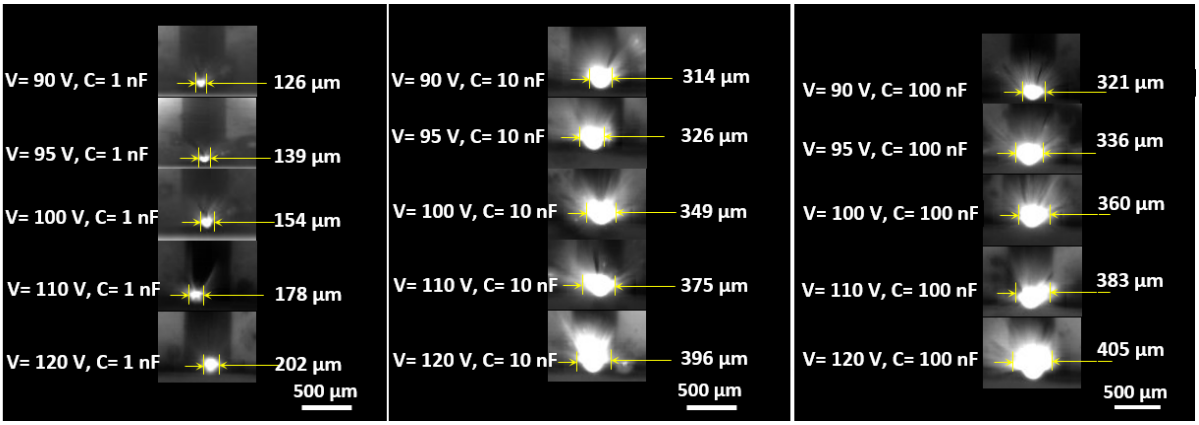

Figure 3.9 Experimental imaging of the plasma channel in micro-EDM with diameter values

The experimental results showed that the diameter of the plasma channel increased as the voltage and capacitance settings were increased. At the lowest energy setting of 90 V and 1 nF, the measured plasma diameter was approximately 126.4 µm, consistent with the simulated values. As the voltage was increased while keeping the capacitance constant, an increasing trend in the plasma diameter was observed. However, the values deviated slightly from those in the low-energy settings. The plasma channel's diameter was approximately doubled with increased intensity when machining was performed at 10 nF and 100 nF compared to 1 nF. This implies that as the capacitance value increased from 1 to 10 nF, the plasma channel diameter increased rapidly, but the increase was gradual when the capacitance was changed from 10 to 100 nF. Even though the energy input was increased ten times in both cases, the plasma channel diameter did not increase proportionally. This highlights the importance of using ideal parametric settings for optimized performance in micro-EDM machining and the limitations in selecting these settings. The height of the plasma channel in micro-EDM is also affected by the voltage between the electrodes. It was observed that increasing the voltage tends to increase the height of the plasma channel along with the diameter. When the capacitance was increased to 10nF, the plasma diameter increased by more than double. This is expected because the energy dissipated in the IEG strongly depends on capacitance, resulting in a tenfold increase in energy input. When the capacitance was increased further to 100 nF, the diameter of the plasma channel increased, but not as much as the increase observed when the capacitance was increased from 1 to 10 nF. The comparison between the

simulated and experimental plasma diameters in Figure 3.10(d) revealed that the percentage error ranged from 5.06% to 14.5%.

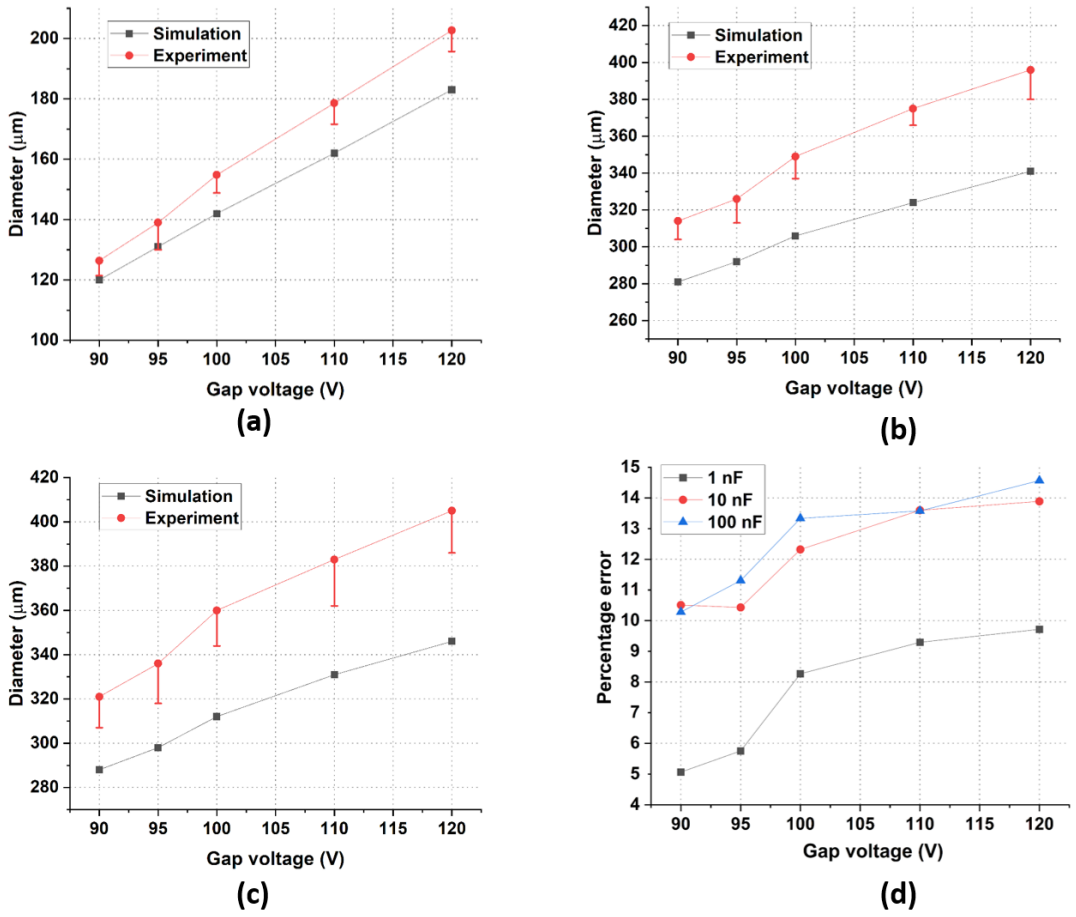

Figure 3.10 Comparison of the experimental and simulated plasma channel diameters at (a) 1 nF, (b) 10 nF, (c) 100 nF, and (d) percentage error

The simulated growth of the plasma channel for the parametric settings of 100 V and 10 nF is shown in Figure 3.11. Figure 3.11(a) and (b) represent a zoom-in view of the initiation of plasma channel formation along with the temperature rise of the IEG, the cathode, and the anode electrodes. Figure 3.11(c) shows the rapid expansion of the plasma channel during the discharge or pulse on time at about 0.096 μs. Figure 3.11(a) shows that the temperature near the cathode increases at the start of the discharge because of the cold emission. Once a sufficient degree of ionization was reached, electrons broke the dielectric barrier, and a plasma channel was established between the two electrodes. The plasma channel formation results in electron avalanche motion, and rapid expansion of the plasma channel starts, as shown in Figure 3.11(c).

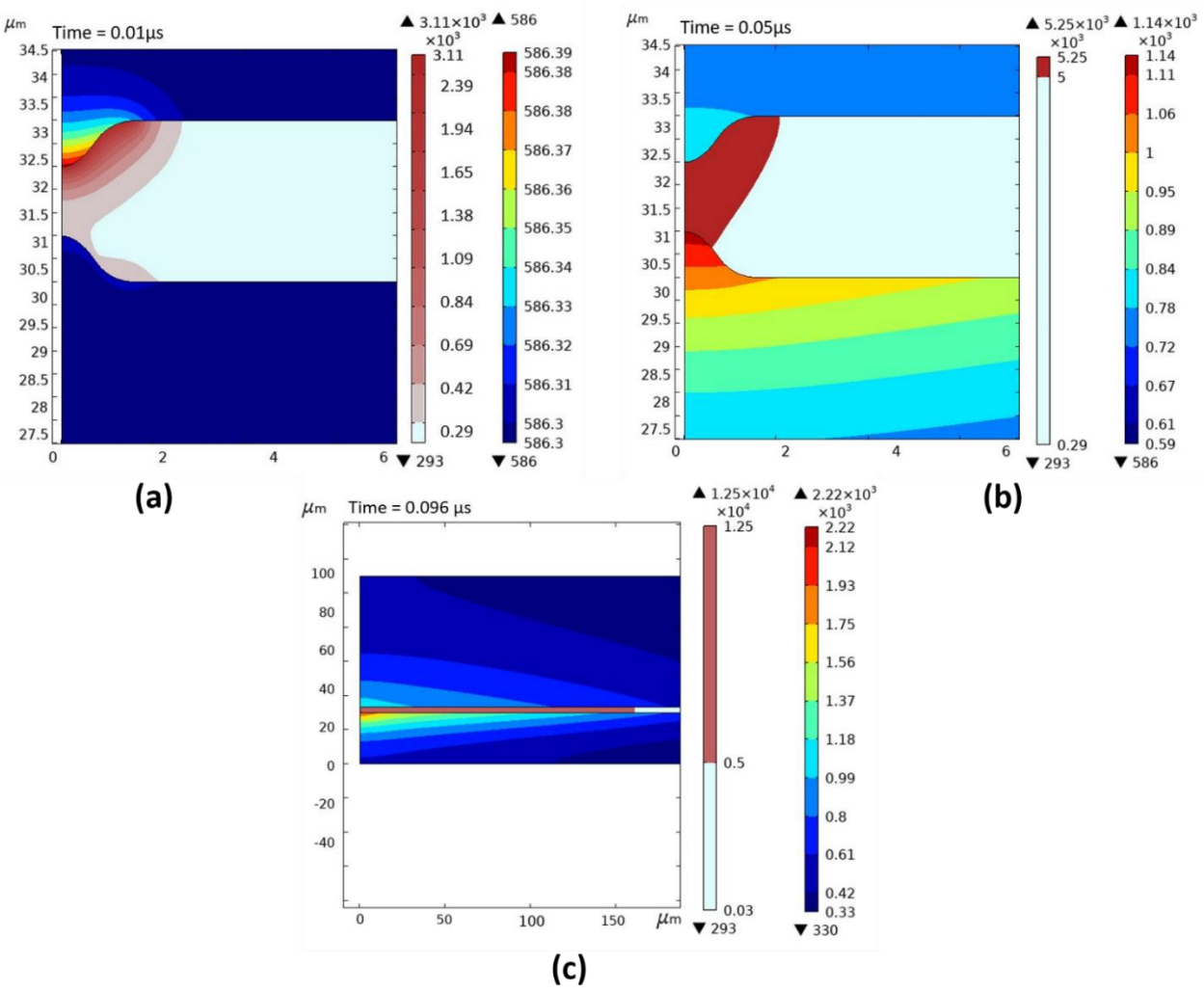

Figure 3.11 Plasma channel and temperature distribution at (a) 0.01 µs (b) 0.05 µs (c) 0.096 µs

3.3.2 Effect of machining parameters on temperature and heat flux distribution

The temperature distribution of the plasma channel along the workpiece surface at a capacitance of 10 nF with varying voltages is shown in Figure 3.12. The temperature at seven different instances was selected to depict the time-varying behavior of the plasma temperature along the surface of the workpiece. It can be seen that the maximum temperature of the plasma channel increases from 9800 K to 15200 K when the voltage is increased from 90 to 120 volts, keeping the capacitance constant. Another important observation from the temperature distribution is the slope of the curve at different instances of the pulse on time, i.e., the time duration during which current flows in the IEG. At the start of the discharge, i.e., at 0.04 µs and 0.09 µs, the temperature curve was steeper, suggesting a sudden increase in the temperature, which was more concentrated towards the center of the plasma channel. As time progresses, the peak temperature value of the curve decreases with a more spread along the

workpiece surface, suggesting the plasma channel's extinguishing phase. The increase in the peak temperature with increasing open circuit voltage at constant capacitance contributes to higher heat flux at the workpiece surface and leads to a broader crater formation.

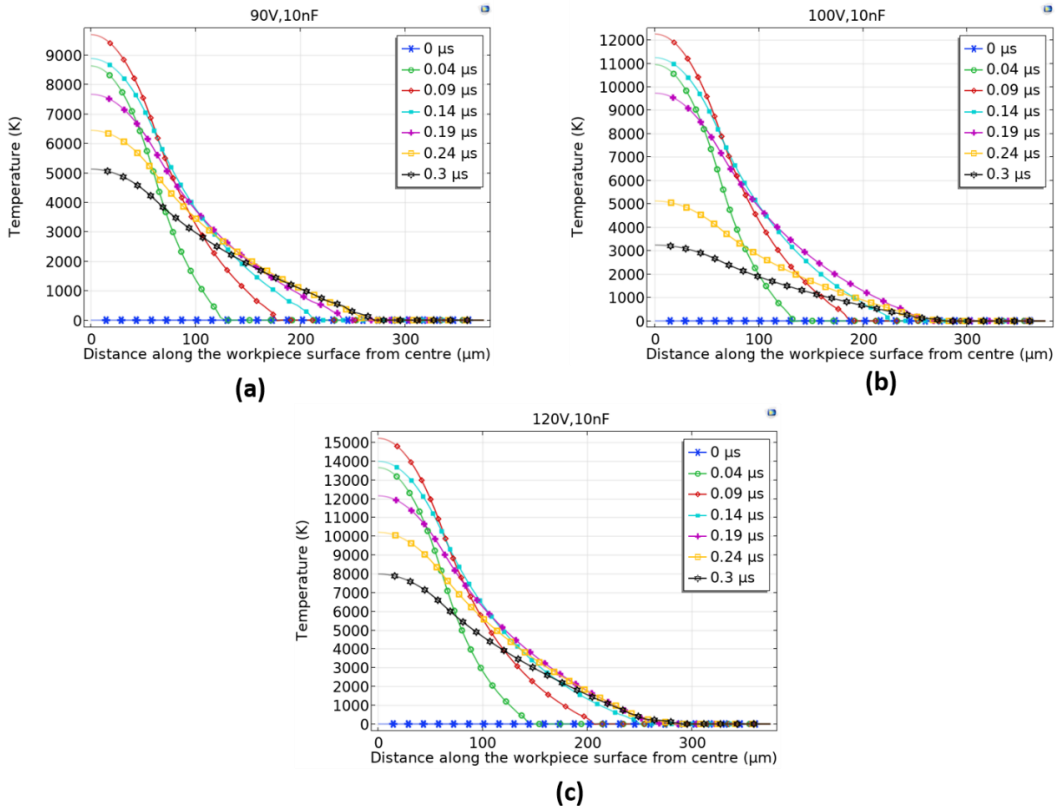

Figure 3.12 Temperature distribution along the workpiece surface at (a) 90 V, 10 nF (b) 100 V, 10 nF(c) 120 V, 10 nF

Another convenient way of understanding the temperature distribution inside the plasma channel is to understand the radial and axial variation of temperature with a pulse on time, as shown in Figure 3.13. It shows the geometry of the simulation domain, consisting of the tool electrode, workpiece, and dielectric medium where the plasma formation takes place. Points A-G are taken equidistantly from the center of the plasma channel to understand the radial distribution of the temperature. In contrast, the points H, A, and I show the axial distribution of the temperature inside the plasma channel. It can be seen that the temperature increased more rapidly with time near the center of the plasma channel than at the points far away from the center. It indicates that very high temperatures prevailed for longer durations at the center of the plasma channel than in the radial vicinity. Hence, the heat flux will be much more in magnitude and concentrated at the center than at the radial positions inside the plasma channel. It only leads to crater formation below the arc root, and the crater's depth will be much deeper at the center than the radial surroundings, as reported in the literature [180].

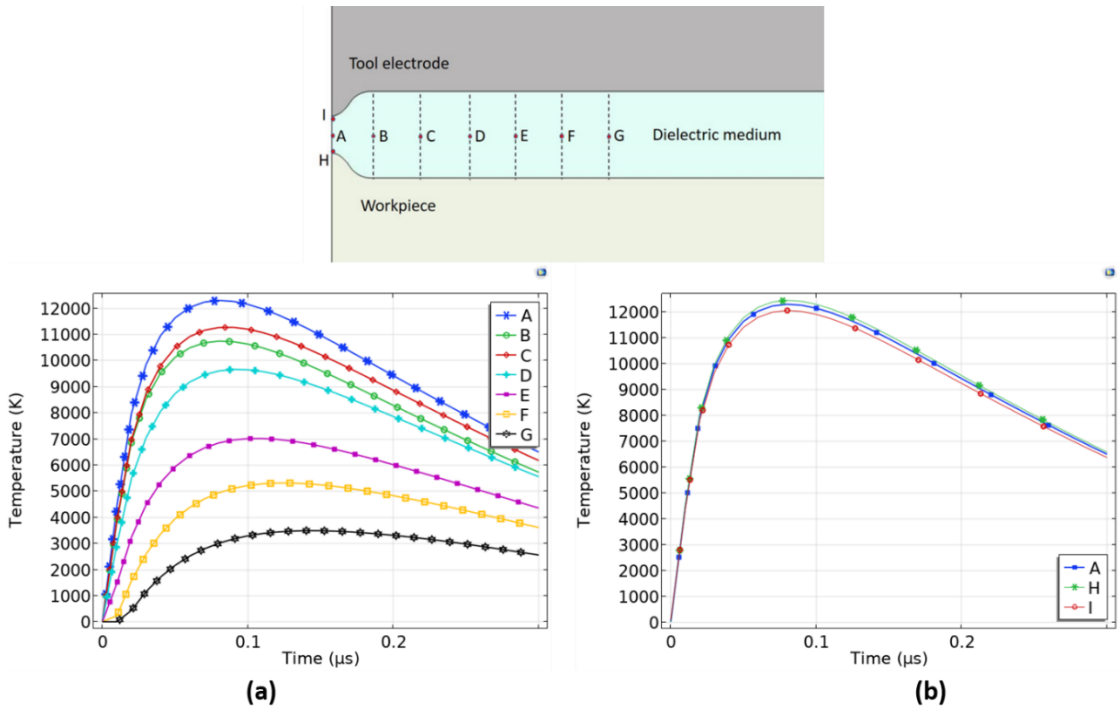

Figure 3.13 Temporal distribution of temperature along (a) Radial (b) axial directions in the plasma channel

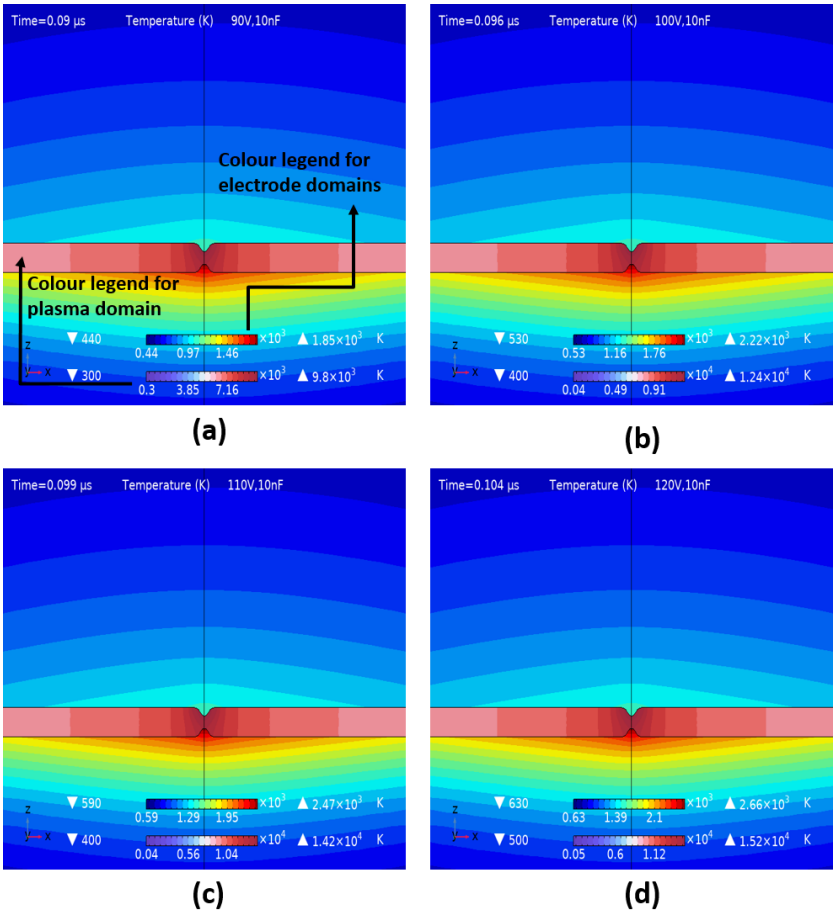

Figure 3.14 Temperature distribution in all domains at (a) 90 V,10 nF (b) 100 V,10 nF (c) 110 V,10 nF (d) 120 V,10 nF

Figure 3.14 shows the temperature distribution in the IEG, tool, and workpiece domains at 10 nF and varying voltage settings. It can be observed that the peak temperature of the plasma and the electrodes increase with an increase in the open circuit voltage. In addition, the temperature increase of the workpiece was more significant in magnitude and spread on a broader area than the tool electrode, indicative of more material removal from the workpiece. The main reason for this is the micro-EDM's polarity and the difference between the thermal conductivity of the tool and workpiece electrodes. The tool is of tungsten with relatively higher conductivity and dissipates heat faster than the stainless steel workpiece.

The variation of total heat flux at the workpiece surface for parametric settings of 100 V and 10nF is shown in Figure 3.15(a). Figure 3.15(b) confirms the observation made during the study of the temperature distribution inside the plasma channel. A sudden increase in the heat flux near the center of the workpiece becomes flattened at the radial distance from the center of the plasma channel towards the outer side. The time-dependent variation of the heat flux inside the plasma channel along the workpiece surface at different radial points is shown

in Figure 3.15(a). Another important observation that can be made from this graph is that the rate of increase in the heat flux at the center of the plasma was significantly higher compared to that at the other radial positions. This indicates the very high density of the charge carriers at the center of the IEG. The collisions between the charge carriers and the dielectric molecules resulted in an intense and rapid ionization at the center of the IEG, giving rise to higher heat fluxes towards the center. High heat fluxes prevail at the center for longer durations compared to its radial vicinity promoting the formation of hemispherical craters during the micro-EDM process. The temporal and radial heat flux distributions are not constant but time-dependent, as shown in Figure 3.15. Hence considering constant heat fluxes during the craters simulation would result in severely wrong approximations during the micro-EDM process.

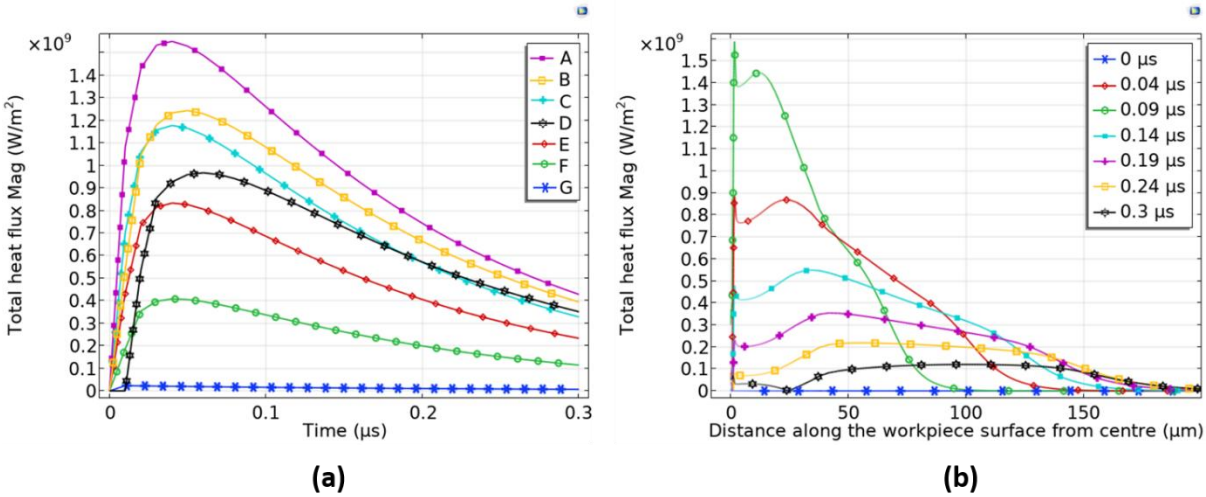

Figure 3.15 (a) Variation of heat flux magnitude with pulse on time at different radial positions (b) Heat flux distribution along the workpiece surface at 100 V,10 nF

3.3.3 Effect of machining parameters on the crater diameter

SEM images of the diameter of the craters formed during the micro-EDM at different discharge conditions are shown in Figure 3.16. Row 1, 2, and 3 refer to the diameters of the discharge craters formed at varying gap voltages and constant capacitances of 1nF, 10 nF, and 100 nF, respectively. It can be observed that the crater diameter increased with an increase in the voltage and capacitance, which was also the case with the plasma channel diameter, as described earlier. Similar observations were made by Singh et al. when the micro-EDM was performed at constant capacitance with varying voltage settings with copper as the workpiece electrode [181]. The percentage increase in crater diameter was more significant when capacitance was increased from 1 to 10 nF compared to when the capacitance increased from 10 to 100 nF. The discharge energy rose with the same proportions in both cases, i.e., from 1

to 10 nF and 10 to 100 nF, while the corresponding crater diameter didn't increase in the same ratio. This indicates the losses in the micro-EDM process when performed at high energy settings compared to lower energy settings. A comparison between the simulated molten diameter of the discharge crater and the experimental crater diameters is shown in Figure 3.17. The difference between the simulated molten diameter and the observed crater diameter can be attributed to the resolidification of molten material. An increase in the difference between the simulation and the experimentation at higher energy settings may be due to more material being resolidified than at lower energy. Although more material is melted at higher voltage, a large percentage of it does not get ejected and resolidified. For example, the percentage error found varied from 8.8 % to 19.5 % when the simulated molten dimeters were compared with the experimental crater diameters, as shown in Figure 3.17(d). The simulated molten diameter to observed crater diameter ratio can be defined as a thermal efficiency ratio and is a function of the applied energy [100]. This ratio can predict the crater diameters for other machining parameters and materials.

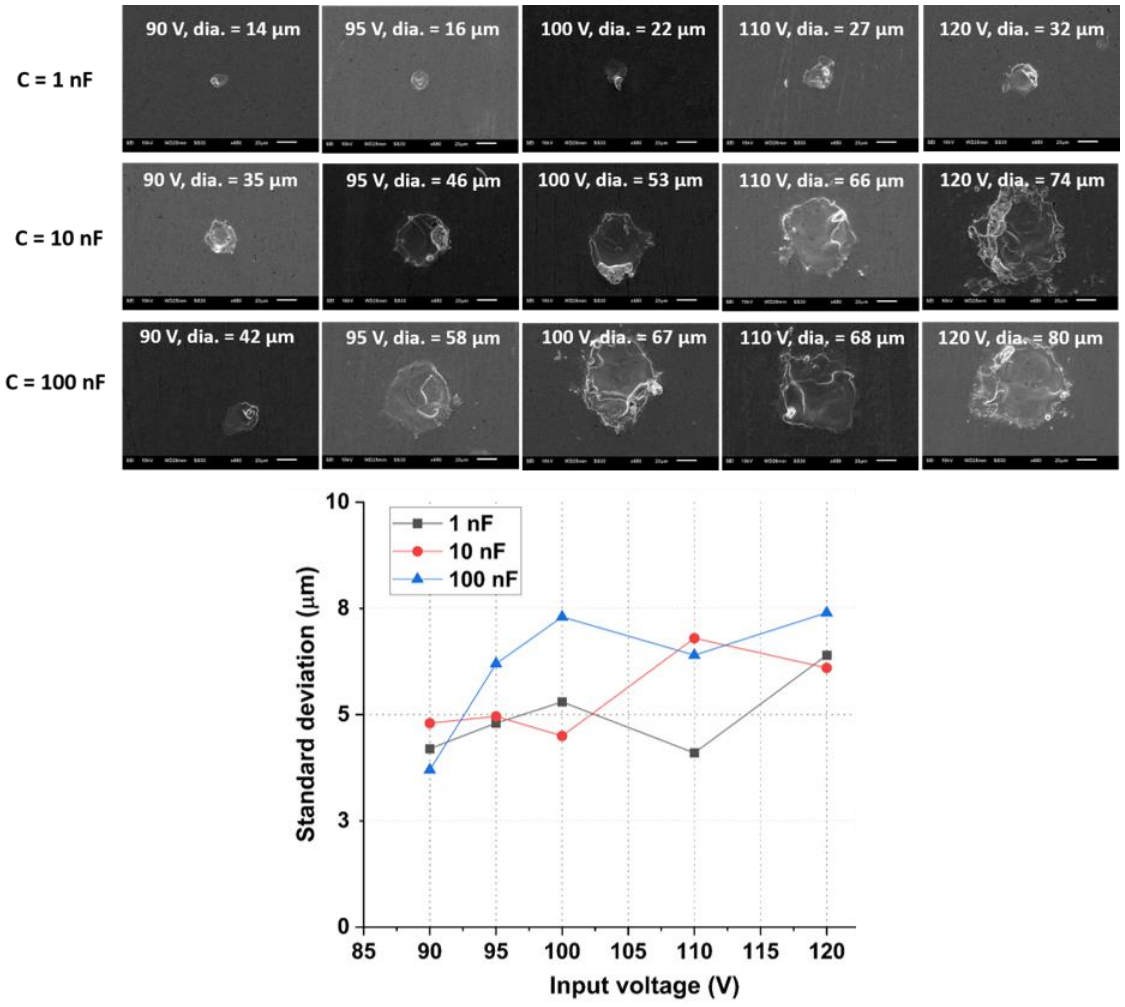

Figure 3.16 SEM images of the crater formed during micro-EDM with standard deviation

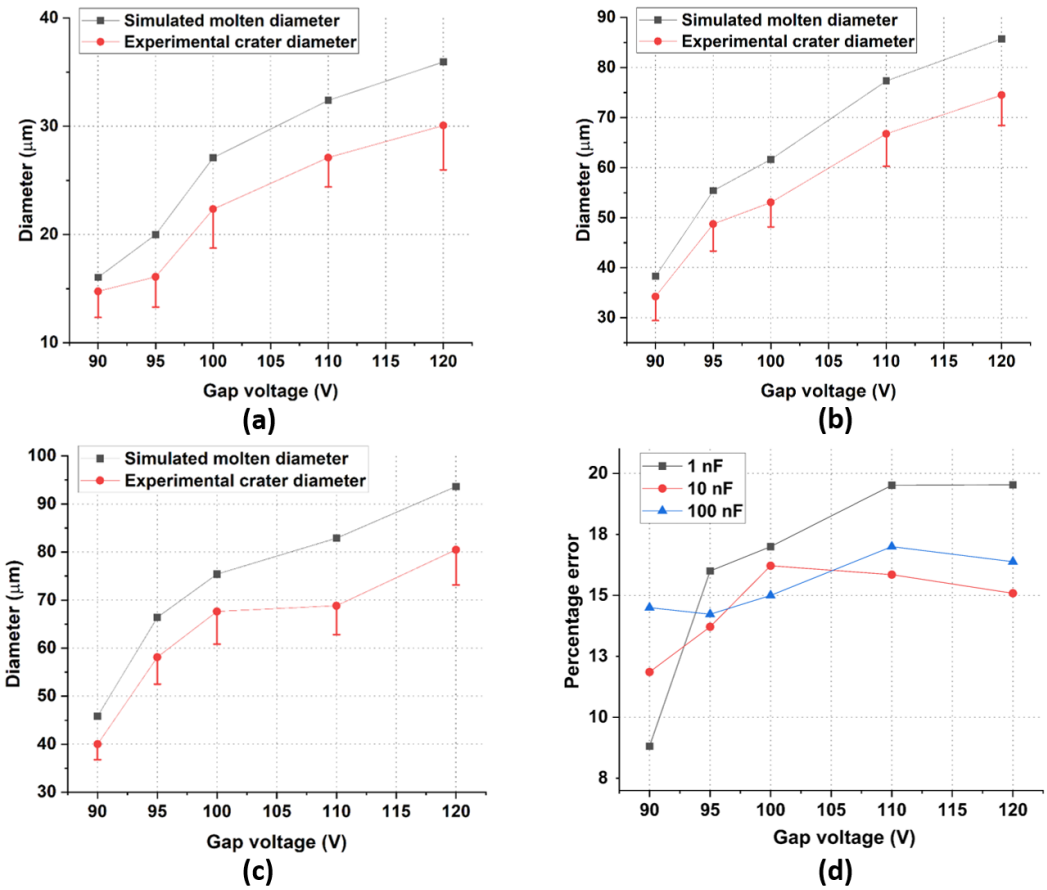

Figure 3.17 Comparison of the experimental and simulated molten diameters at (a) 1 nF (b) 10 nF (c) 100 nF (d) percentage error

3.4 Summary

A numerical model for plasma formation and expansion during the micro-EDM was developed in this chapter using the COMSOL Multiphysics finite element software. The plasma heat source, responsible for the plasma formation, was calculated using the coupling between the electric current and heat transfer in the fluids module. The coupled numerical model considers the enthalpy transport, resistive heating, and radiation emissions as the heat sources for plasma channel formation. The plasma-electrode interactions were computed using the electron and ion current densities and various losses occurring at the respective electrodes. A good understanding of temperature distribution in micro-EDM was obtained by considering the electronic and ionic heat fluxes, the conduction, convection, and radiation at the electrode boundaries. Experimental investigations were performed at various voltage and capacitance settings to capture the diameter of the plasma channel using high-speed imaging. The following conclusion can be made from various outcomes of the plasma model and by comparing the simulated and experimental plasma diameters.

- At the start of the discharge, the temperature near the cathode was greater, imitating the cold emission from the cathode. Once the plasma channel was established, the anode's temperature increased rapidly due to the avalanche motion of electrons toward the anode.
- The proposed numerical model predicts the diameter of the plasma channel and the discharge crater formed during the micro-EDM operation. The simulation and experimentation results were close to each other at low energy settings compared to high-energy settings.
- The diameter of the plasma channel was proportional to the applied energy during the micro-EDM process. The diameter increment was more when the capacitance varied from 1 nF to 10 nF than when the capacitance was increased from 10 nF to 100 nF.
- The expansion of the plasma channel was rapid at the start of the discharge. It gradually stabilized later, confirming the similar behavior of the temperature and heat flux distributions.
- The temperature and heat flux distributions were time-dependent, with more intensive at the center during the start of the discharge due to the prevalence of high temperatures for a longer duration at the center.

Chapter 4

Development of Pulse Monitoring System and Discharge Pulse Analysis in Controlled RC-based Micro-EDM

4.1 Introduction

Monitoring the discharge pulses becomes crucial during the electrical discharge machining as the voltage difference and current are the main driving force for removing the material. In micro-EDM, pulse monitoring is even more critical due to the small scale of the machining and the utilization of an RC-based power supply. Although the RC-based power supply produces low energy discharges suitable for micro-EDM, the timing of the discharge in is not pre-determined and depends upon the state of the IEG. The stochastic nature of the micro-EDM process thus necessitates the need of pulse monitoring. Discharge duration was found to be different for the identical input parameters, leading to the randomness of the pulse characteristics during the μEDM, as described by Liu et al. [182]. According to Sisodiya et al. [183], short circuits during EDM are the primary and most significant factor for the degradation of the finished surface and increase in tool wear. The pulse duration, pulse frequency, and current density must be precisely controlled to ensure the accuracy of the machining process, as studied in the early studies of pulse monitoring in conventional scale EDM [184–186]. This chapter proposes a pulse monitoring system (PMS) to categorize the discharge pulses and monitor the micro-EDM process during continuous machining. While being acquired through various sensors, signals are processed in NI LABVIEW software. Extensive virtual instrumentation categorizes the discharge pulses as contributing, semi-contributing, and non-contributing towards material removal through the developed pulse monitoring system (PMS). The acquired information from the developed PMS explains the variations in discharge energy, material removal, and nature of discharges with increasing machining depth.

4.2 Development of pulse monitoring system for a controlled RC circuit

During the micro-EDM process, the discharge pulses are recognized by various signals recorded using current and voltage probes. The discharge current and voltage data were acquired at a sampling rate of 10MS/s. At such high sampling rates, the data population was sufficiently large for analyzing micro-EDM pulses occurring even with a minimum discharge duration. With the help of the discharge data, different types of discharge pulses were identified, and the PMS was developed, which can be employed during continuous machining. As mentioned earlier, the nature of discharge pulses during micro-EDM is non-iso-energetic,

due to which the tendency of these pulses to remove the material fluctuates from zero to maximum. Nirala et al. developed a PMS for the RC circuit-based micro-EDM process to understand the nature of various discharge pulses and categorize them according to the discharge voltage level [187]. The discharge pulses were classified into different categories based on voltage thresholds, such as contributing (Normal), semi-contributing (Effective), and non-contributing (arcing) pulses. The discharge pulses with higher discharge voltage were considered to contribute more to material removal and are called contributing and semi-contributing pulses [5]. Hence, an effort has been made here to quantitatively estimate the contribution of different discharge pulses and classify them based on their material removal capabilities. A developed PMS based on the LABVIEW is then implemented in the micro-EDM drilling experiment to study the process stability at increasing machining depths while using controlled RC-based micro-EDM.

4.2.1 Methodology for PMS Development

In this section, a detailed strategy is discussed for the development of PMS. The nature of discharge pulses with the controlled RC-based micro-EDM circuit is presented first, followed by the strategy to classify them according to the quantitative energy content. The nature of different voltage pulses captured during the real-time micro-EDM drilling experiment with the controlled RC-based micro-EDM circuit is shown in Figure 4.1. The figure depicts the voltage pulses with a suitable T_{on}, T_{off}, delay time, and the open circuit voltage (V_{max}). It has been observed that due to the extensive delay time, the discharge does not take place during most of the on-time cycles. The delay time is an essential factor affecting the machining efficiency as it is the time consumed for ionizing the IEG, after which the discharge can occur. The delay time is a dynamic parameter with a maximum value equal to the T_{on} only if no discharge occurs during a particular T_{on}. It can also be said that the summation of Δt, the discharge time, and the delay time will equal T_{on}. Figure 4.1(b) depicts the pulse on time as a period during which spark occurrence between the tool and workpiece is possible, depending upon the applied voltage and the IEG. If the discharge does not happen till the end of T_{on}, it is regarded as an open circuit pulse with no discharge. T_{off} is the duration during which the discharge circuit is cut off from the charging circuit. As a result, discharge can never occur during T_{off}. In the captured signals (refer to Figure 4.1), the discharge starting immediately after the delay time at point D is represented as capacitor discharging. After the capacitor's complete discharge, the circuit is switched to the charging position, and point C where the capacitor begins to charge, is represented as a capacitor charging.

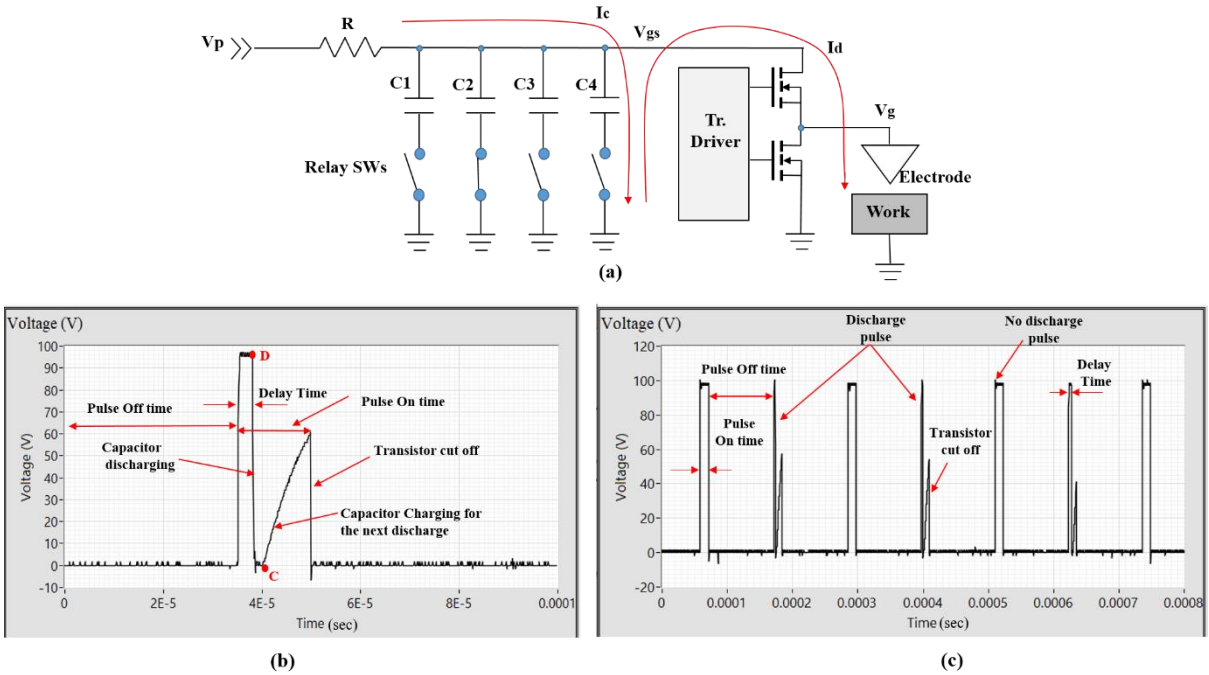

Figure 4.1 (a) Controlled-RC circuit with, (b) nature of single discharge voltage pulse, and (c) voltage pulses

A discharge pulse with a delay time that is equal to T_{on} will be counted as no discharge pulse and appear in the no discharge section. These pulses are not responsible for the removal of material. The pulses whose width is less than the T_{on} will be counted as a discharge pulse and appear in the discharge section, as shown in the front panel of the PMS in Figure 4.2 and the flow chart of Figure 4.4. Once a pulse is categorized as a discharge, it is further classified as contributing, semi-contributing, and non-contributing pulse. The voltage level to which the capacitor can be charged before actual discharge can occur is called the open-circuit voltage (V_{max}). When a fully charged capacitor discharges from V_{max} , it has been observed that the discharge duration Δt of the pulse is more than a pulse that discharges from a lower voltage. In addition, the amplitude of the current pulses decreases with the decreasing V_{max}. Hence, the variable V_{max}, peak current and discharge durations result in non-iso-energetic pulses. Because of these non-iso-energetic pulses, a voltage threshold is essential to monitor and further classify the discharge pulse into various categories. The following section describes the calculation of the voltage thresholds for classifying the discharge pulses into different categories according to their material removal capabilities. By doing so, the developed PMS becomes more dependable and can be utilized to monitor continuous machining.

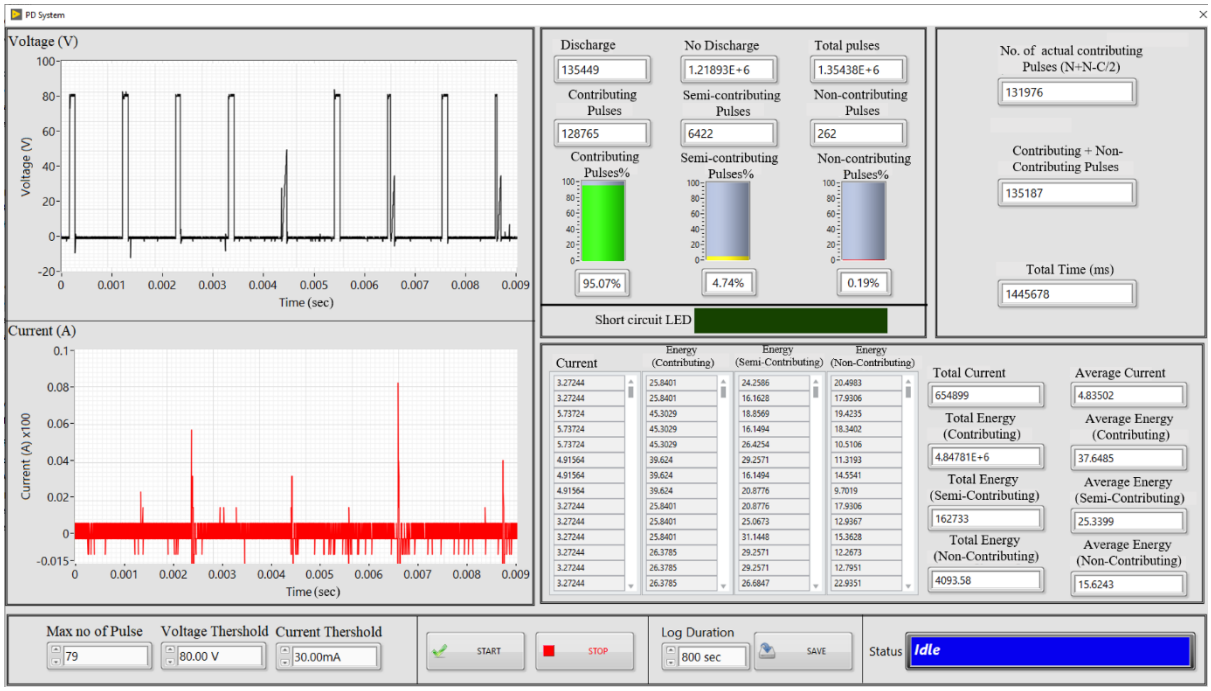

Figure 4.2 The front panel of developed PMS (a screenshot at any moment during the process)

4.2.2 Voltage threshold for the pulse categorization

As discussed earlier, a quantitative method was used in this work to ascertain the contribution of different types of discharge pulses and classify them into various categories. The contribution of different discharge pulses can be quantified by performing several experiments with varying the V_{max} in the range of 100 to 30 volts by gradually decreasing the voltage in the steps of 10 volts. Each experiment was performed for a fixed time, and the workpiece's weight was then measured to quantify the MRR, as shown in Figure 4.3. It can be seen that as the V_{max} decreases from 100 V to 70 V, MRR also starts to drop and becomes approximately less than half compared to that at 100 V. Hence, a threshold of 70% of V_{max} is set for discriminating the contributing discharge from the semi-contributing discharge. When the machining was performed below 70V, MRR further decreased, and below 40 V, it became almost negligible compared to the MRR of the contributing discharges. The decreasing voltage experiments represent the situation when the discharge occurs with a threshold voltage of less than the applied voltage. As the capacitor is not fully charged and discharges with less energy during the machining, the contribution of those discharges would be much lesser towards MRR. These types of pulses are classified as semi-contributing pulses and are distinguished from contributing pulses by defining a threshold range of 40% of V_{max} to 70% of V_{max}. Here semi-contributing discharge corresponds to approximately half of the volume removed per discharge (VRD) compared to the contributing discharges. The contribution of these pulses towards MRR

was less than that of contributing pulses. When the machining was performed below 40 volts, no material was removed as metal-to-metal contact occurred, leading to non-contributing pulses called arcing. These non-contributing pulses hold negligible energy content and do not correspond to any material removal. These unwanted pulses occur when the tool and workpiece are in physical contact. The non-contributing pulses are not considered liable for removing any material from the workpiece during machining. However, the chances of occurring non-contributing pulses in a controlled RC circuit are less compared to the conventional RC circuit due to the capacitor's-controlled charging and discharging.

The decrease in the MRR with the decreasing V_{max} can also be understood with the help of the average discharge current and the discharge energy content, as shown in Figure 4.3(a) and (b). The discharge energy and the discharge current follow the same trend as the MRR, and categorizing the discharge pulses according to the voltage threshold is justified. The flow chart of the pulse strategy using the voltage threshold of the discharge pulses is depicted in Figure 4.4. First, the voltage and current waveforms are acquired using the DAQ system, and the pulse width is compared with the T_{on}. If the pulse width is less than the $T_{on,}$ it is considered for further examination. Otherwise, it is counted as no discharge. Once a pulse is considered further for a discharge, the corresponding amplitude of the current signal is checked for any noise, as the amplitude of current pulses is a more significant parameter [188,189]. If the corresponding discharge current happens to be greater than the noise level, the pulse is confirmed as a discharge. The discharge pulses are then categorized based on voltage thresholds as contributing, semi-contributing, and non-contributing. The final criteria for categorization of the discharge pulses in Figure 4.5 show the current and voltage pulses of the machining process at a V_{max} of 100V and a T_{off} of 100µsec. It can be observed that the amplitude of the current pulses is more significant for the contributing pulses in comparison with the semi and non-contributing pulses, leading to higher MRR for the contributing discharges.

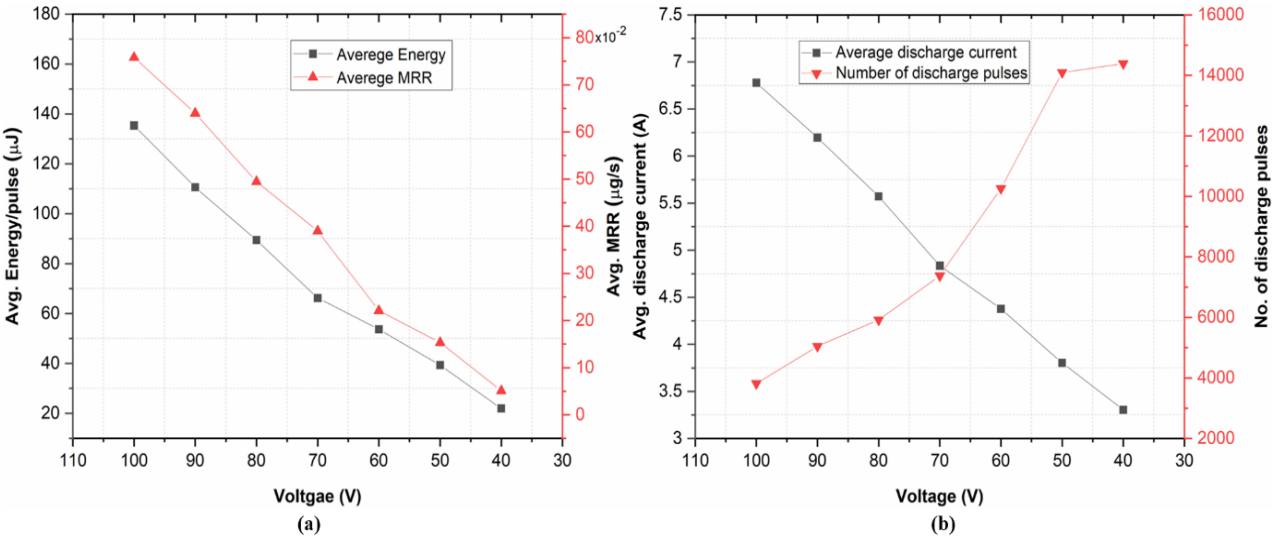

Figure 4.3 (a) Avg. discharge energy per pulse and the Avg. MRR, (b) Variation of Avg. discharge current and the number of discharge pulses with the machining voltage

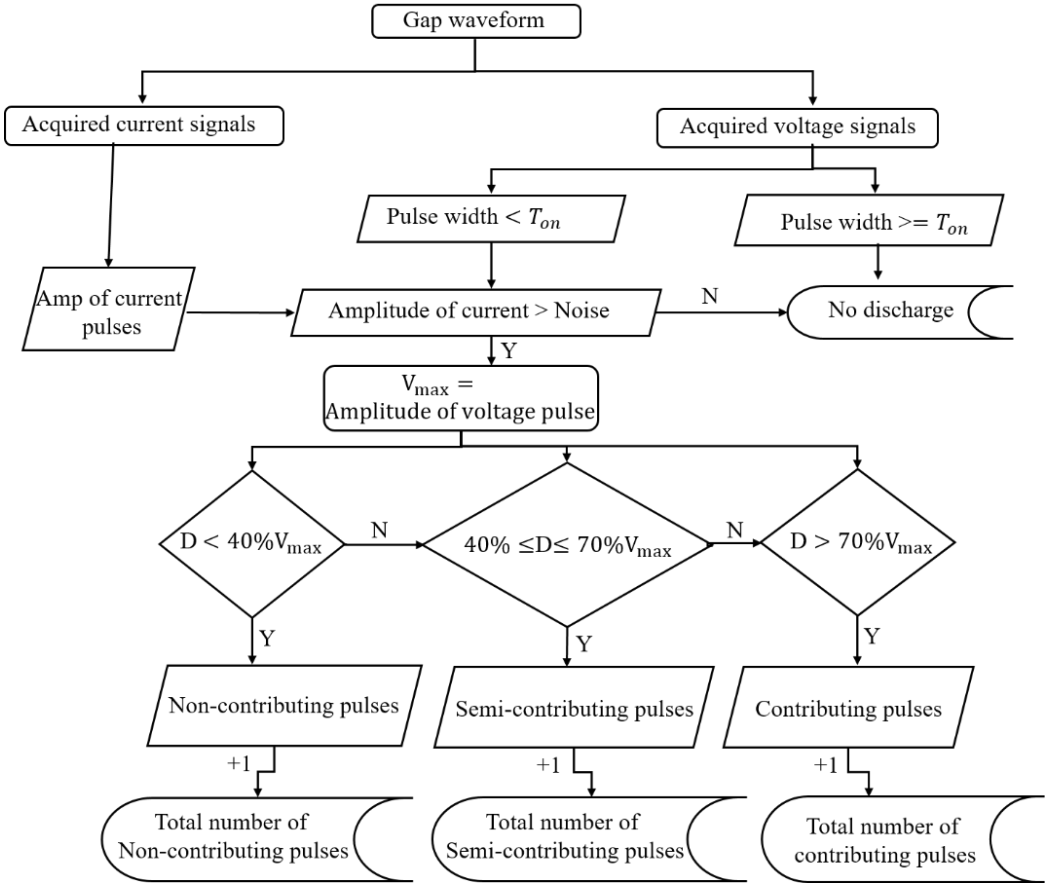

Figure 4.4 Flow chart of the pulse monitoring system

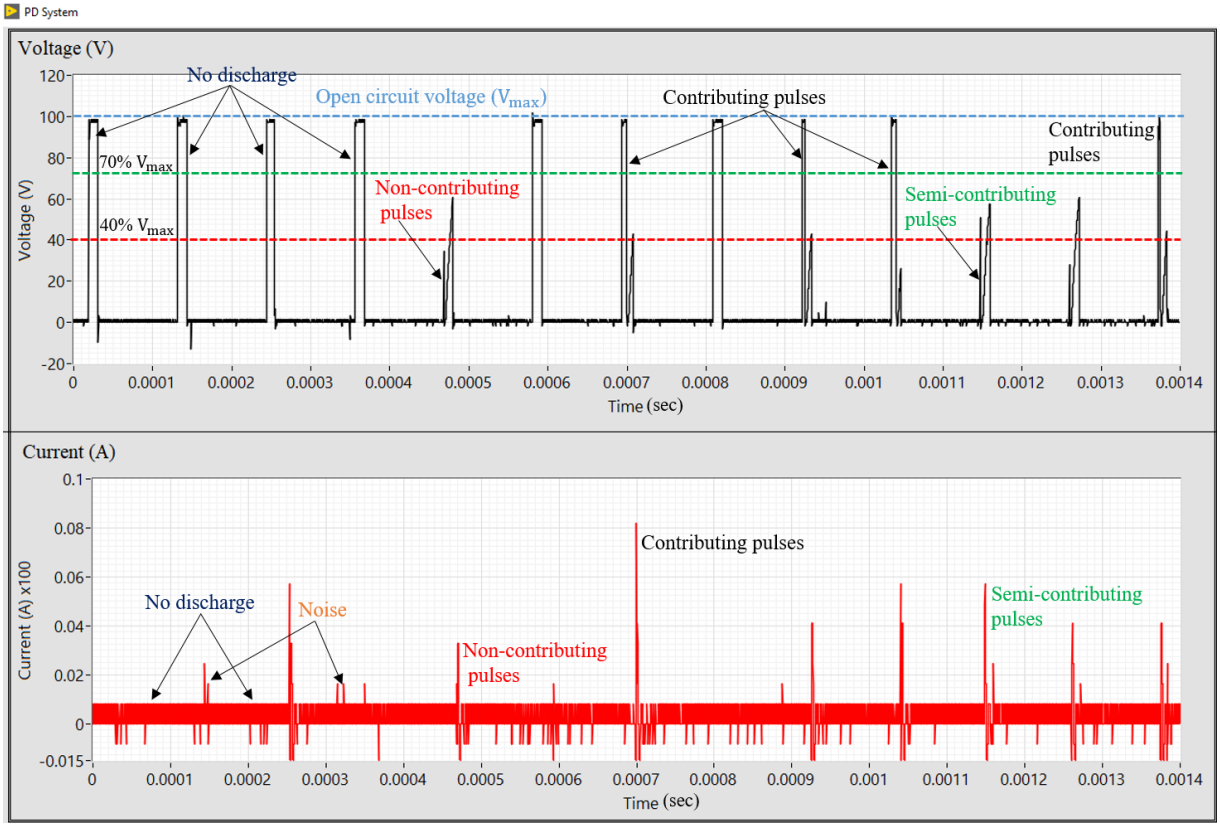

Figure 4.5 Pulse categorization criteria showing different categories of discharge pulses

4.3 Experimental feasibility of the pulse monitoring system

4.3.1 Experimental setup

The present work uses a controlled RC-based micro-EDM machine (model: Hyper 15; make: Sinergy Nanosystems) to conduct the micro-EDM drilling experiments. In this circuit, the charging and discharging of the capacitor are controlled by setting an optimal pulse on time, T_{on}, and pulse off time, T_{off}. The discharge pulses obtained during the T_{on} only make the control RC-based circuit way better regarding organized delivery of discharge energy. The schematic diagram in Figure 4.6 represents the machining setup used for the micro-EDM drilling experiments with all the necessary arrangements for acquiring the machining data. The experimental setup's pictorial view is shown in Figures 4.7(a) and (b), where the workpiece is mounted on the fixture for micro-EDM drilling, and the tool is connected to the spindle. A passive voltage probe (model: 701938; make: YOKOGAWA) with a voltage capturing the range of 600V, an accuracy of ±2%, and a bandwidth of 200MHz was used to record the voltage waveform around the discharge gap. A Hall Effect current clamp (model: CC-650; make: Hantek) with a current capturing range of 20mA to 650A DC, a bandwidth of 400Hz, and a sensitivity of 1mV/A was used to record the current waveform around the discharge gap. The

nature of current and voltage pulses was captured and processed by using a DAQ system. A NI makes DAQ (model: PXIe-5114; make: National Instruments) with a sampling rate of 250MS/s, a bandwidth of 125MHz, a 2GHz processor, 4GB RAM, and a resolution of 8bit was used to acquire and categorize the pulses. The acquired current and voltage signals were imported to the LABVIEW (2018; make: National Instruments) using DAQ for monitoring and classifying the discharge pulses, as shown in Figure 4.7(a).

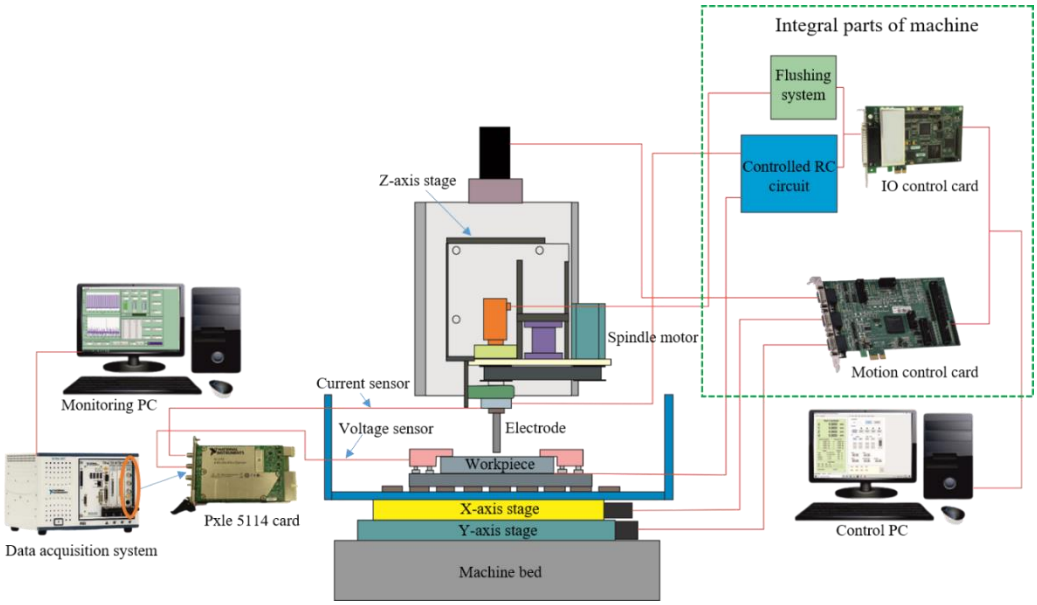

Figure 4.6 Schematic diagram of the micro-EDM drilling setup

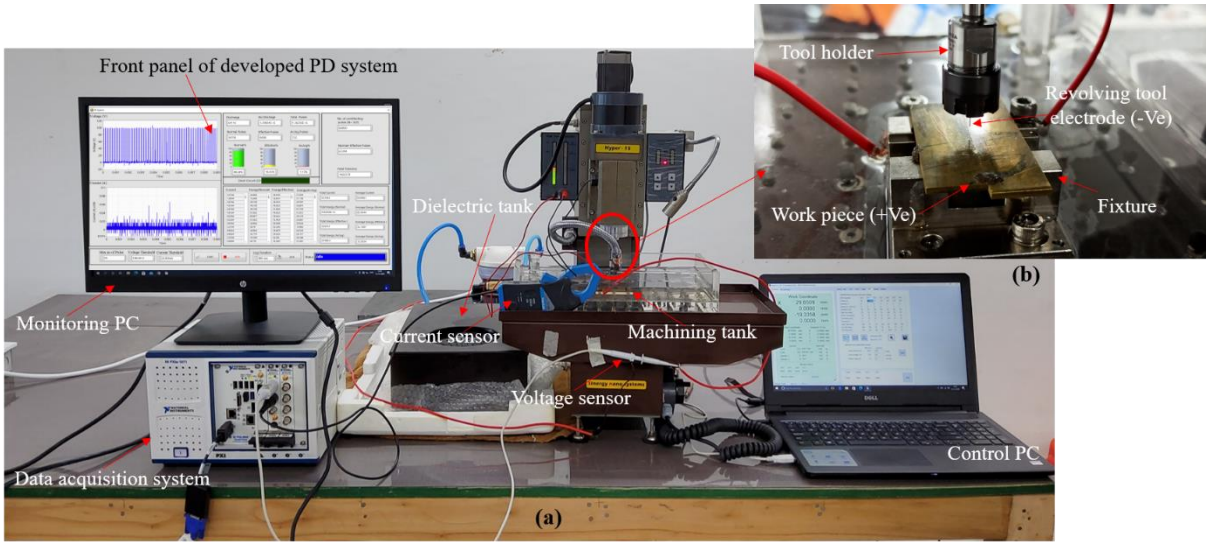

Figure 4.7 (a) Pictorial view of the experimental setup, (b) close view of the machining section

4.3.2 Experimental parameters & machining conditions

A brass plate of 1.5 mm thickness is split from the center with dimensions of 60mm × 15mm and 50mm × 15mm used as a workpiece in the experimentation. The splits were

prepared using wire electrical discharge machining (WEDM) to ensure a smooth and uninterrupted interface. The plates were temporarily joined together, and micro-EDM drilling experiments were performed precisely at the center of their interfaces. The plates were parted after the machining to inspect the longitudinal cross-section of the micro-EDM drilled holes. The CAD model of the workpiece is shown in Figure 4.8. A tungsten electrode with a diameter of 300µm and higher wear resistance and melting point was used as a tool. The fastened brass plates were adjusted on the fixture using a powerful magnet to ensure the workpiece's uniformity with the electrode. A straight polarity (tool connected to the –ve terminal and the workpiece connected to the machine's +ve terminal) is used during the experiments. The experimental conditions and machining parameters adopted during the experimentation are provided in Table 4.1.

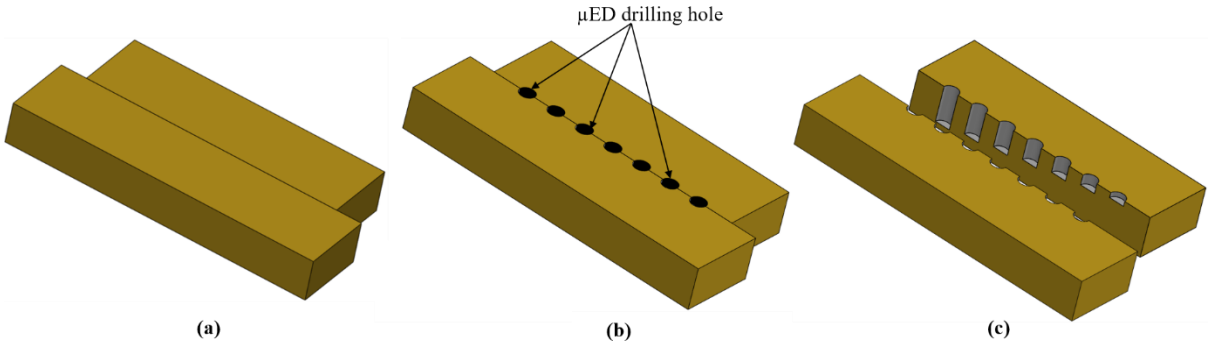

Figure 4.8 Schematic representation of workpiece (a) before machining, (b) after machining, and (c) after splitting the workpiece

Table 4.1 Experimental parameters and machining conditions of micro-EDM drilling

Experimental conditions	
Parameters	micro-EDM drilling
Workpiece material (Anode)	Two brass plates of 1.5mm thickness
Tool material (Cathode)	Tungsten electrode of Ø300µm
Number of experiments	28 experiments at four settings Setting 1: capacitance1nF and voltage 80V Setting 2: capacitance10nF and voltage 80V Setting 3: capacitance1nF and voltage 100V Setting 4: capacitance 10nF and voltage 100V
Process conditions	
Tool rotation speed	1000 Rpm
Pulse on time	10 µs

Pulse off time	100 µs
Capacitance	1 nF and 10 nF
Open circuit voltage	80 V and 100 V
Measured responses	
Offline responses	Overcut, MRR, SR
Online responses	Contributing, semi-contributing, and non-contributing pulses Frequency of pulses The energy of each pulse, Total energy, and Average energy of pulses

4.3.3 Effect of machining parameters on the dimensional accuracy

Micro-EDM drilling experiments were performed with seven different targeted depths starting from 200µm to 1400µm with an increment of 200µm each time. Four different combinations of voltage and capacitances with two voltage levels (100V and 80V) and two capacitance levels (1 nF and 10 nF) were used for machining holes with a diameter of 300 µm. Figures 4.9 and 4.10 show the scanning electron microscopy (SEM) images of the drilled holes with actual depth and the percentage error in the depth. It can be observed that the percentage error in the actual machined depth increases with an increase in the depth of machining. The reason behind this is the increase in tool wear due to difficulty in flushing out the debris from the depth of the machining zone. The taperness of the drilled holes increases when machining at 100V compared to that at 80V due to the increased electric field near the sharp corners at high discharge potentials. Figure 4.11 shows the variation in percentage error in depth with respect to machining depth at various parametric settings. The percentage error follows the same increasing trend at all the parametric settings with the machining depth. When the capacitance was increased at a constant voltage, the error in depth increased significantly compared to when the voltage was increased at constant capacitance. This observation confirms that the dimensional error is more sensitive to capacitance than the machining voltage.

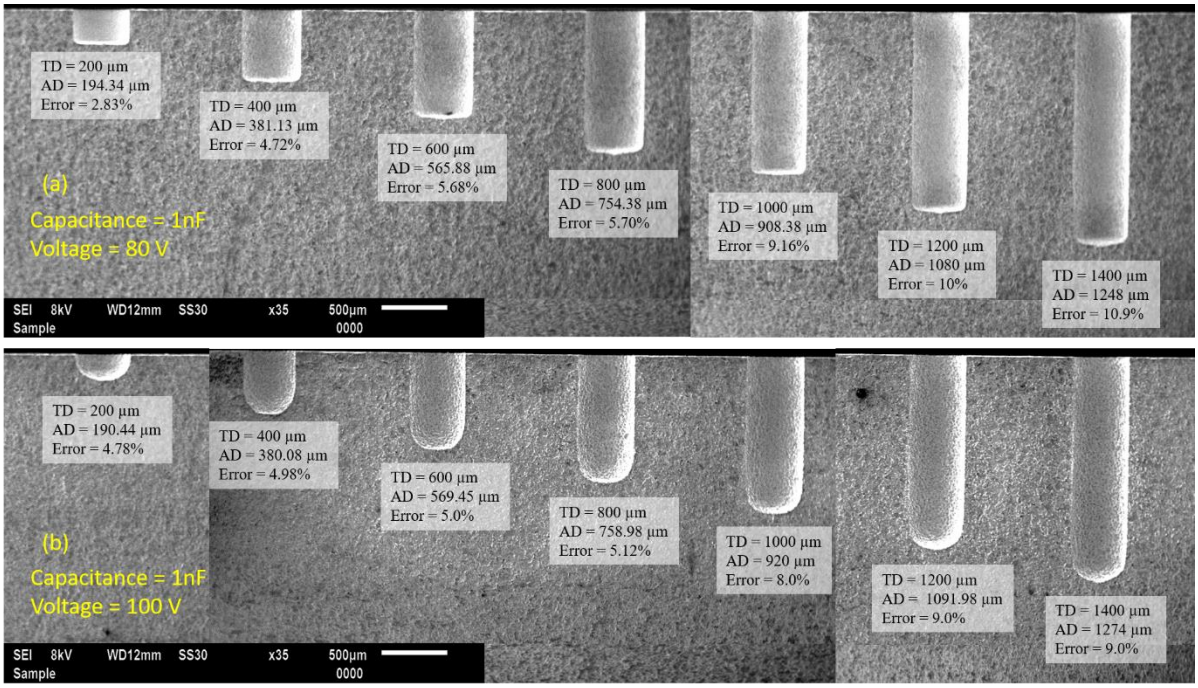

**TD = Target depth, AD = Actual depth

Figure 4.9 SEM images of the machined holes at (a) 80 V, 1 nF (b) 100 V, 1 nF

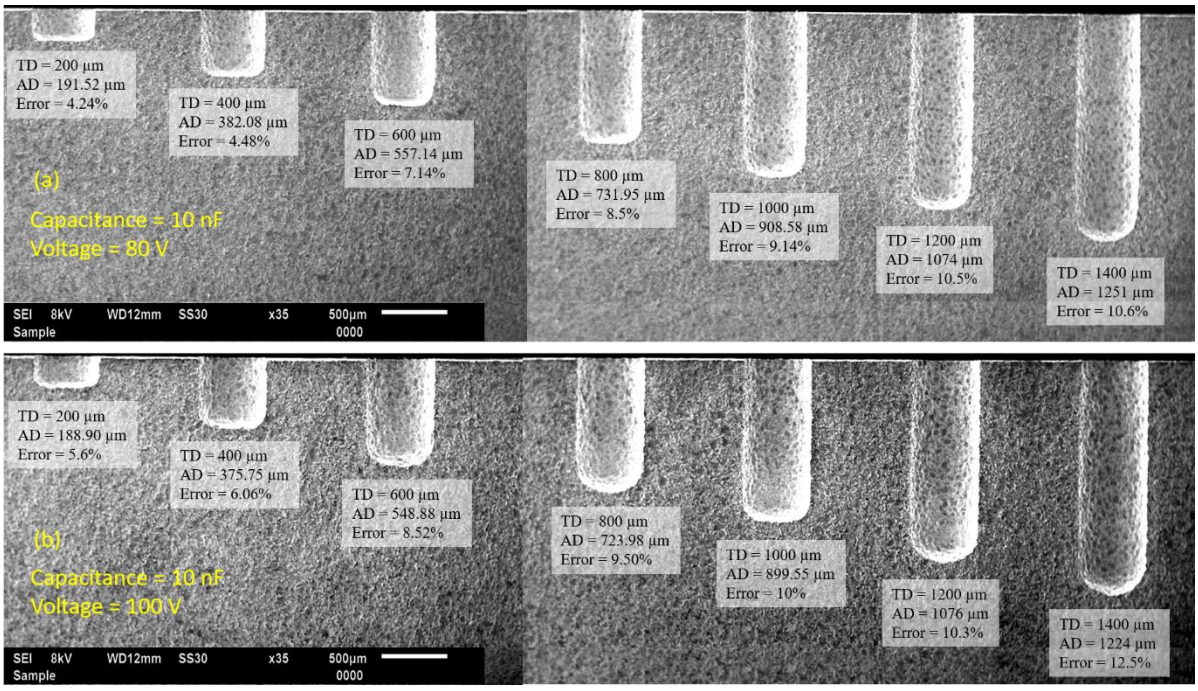

**TD = Target depth, AD = Actual depth

Figure 4.10 SEM images of the machined holes at (a) 80 V, 10 nF, (b) 100 V, 10 nF

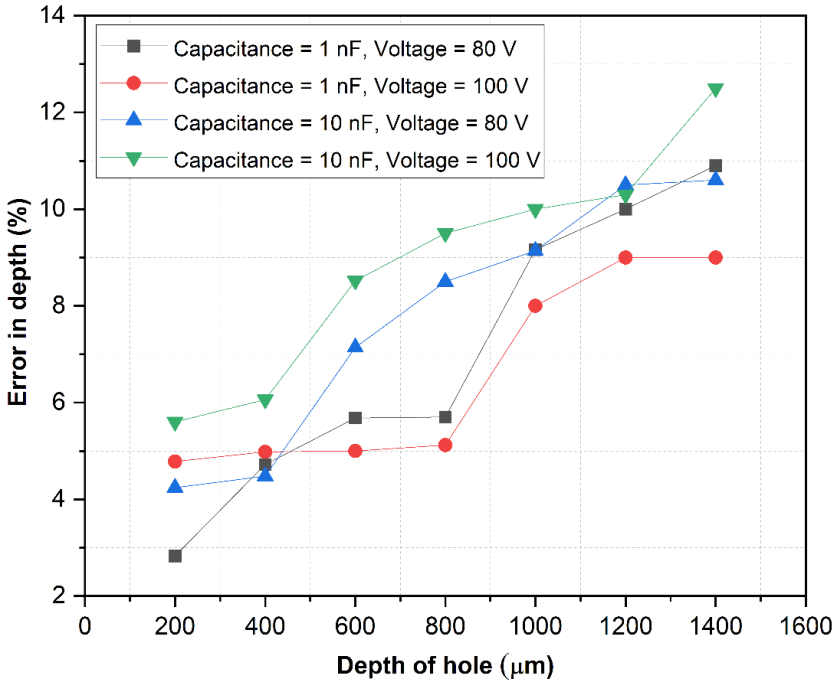

Figure 4.11 Variation of error in depth with the machining depth

Figures 4.12 (a) and (b) show the top view of the SEM images of the drilled micro holes and the overcut in diameter graph at various depths of the holes. It can be observed that the overcut in diameter is proportional to the energy content of the discharges. The machined holes were observed to be more accurate at lower voltage and capacitance, such as 80V and 1nF. The overcut in diameter increases twice with increasing capacitance compared to an increase in the voltage. This observation shows the diametric accuracy's sensitivity to the capacitance settings, which was also the case for the holes' height, as discussed earlier.

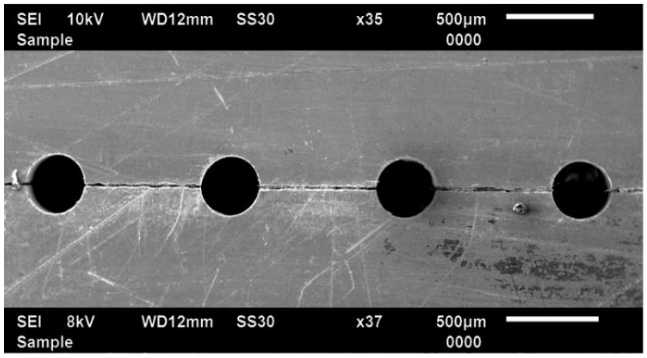

(a)

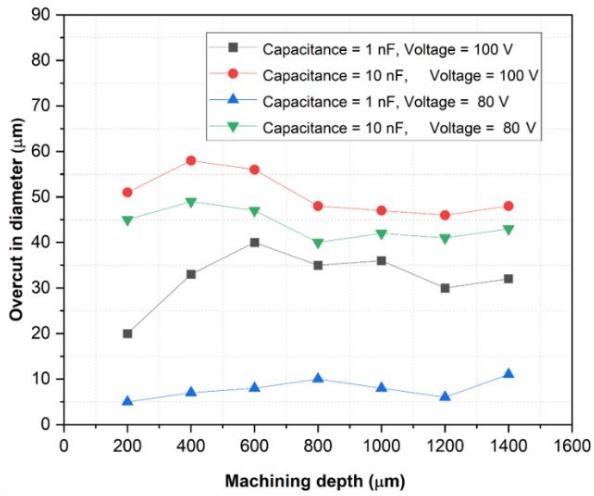

(b)

Figure 4.12 (a) Top view of the machined holes, (b) variation of the overcut in diameter with the machining depth

Figure 4.12 (**a)** Top view of the machined holes, (**b)** variation of the overcut in diameter with the machining depth

4.3.4 Discharge frequency and energy variation with the machining depth

Real-time voltage and current data were captured, and the proposed PMS was used to calculate the frequency and the average discharge energy per pulse. Discharge frequency is the most crucial factor and is directly related to the stability of the micro-EDM process. The higher the discharge frequency, the more stable the machining with minimal arcing and good surface characteristics. Figures 4.13(a) and (b) show the variation of the frequency and the average discharge energy per pulse with increasing depth of the machined holes. The discharge frequency increases with the depth of the machined hole mainly due to the increase in the semi-contributing discharges caused by the trapped debris, poor flushing of the IEG, and more sideways discharges. At a constant voltage, the D_f is one order higher for low capacitance because less time is required for the capacitor's charging and the occurrence of the discharge. On the other hand, the D_f decreases with the increasing voltage at constant capacitance. This is because a small gap is sufficient for the discharge to occur at lower voltages than a higher voltage, as the discharge gap is a function of voltage. As the gap between the tool and electrode is smaller at low capacitance and voltage settings, the PMS becomes very important to identify the nature of discharge as contributing or semi-contributing at high discharge frequencies. An opposite trend was observed for the discharge energy variation compared to the above-discussed trend of the discharge frequency with respect to the depth of the machined holes. Due to the poor flushing of the debris and the dielectric medium's contamination in the depth of the holes, lower discharge gaps are sufficient for discharge to occur, decreasing the energy of a discharge pulse. A significant increase in the discharge energy was observed when the machining was performed by increasing capacitance at constant voltage compared to a minute increase with the increasing voltage at constant capacitance. The discharge energy was also more sensitive toward the capacitance than the voltage, as observed in Figure 4.13(b).

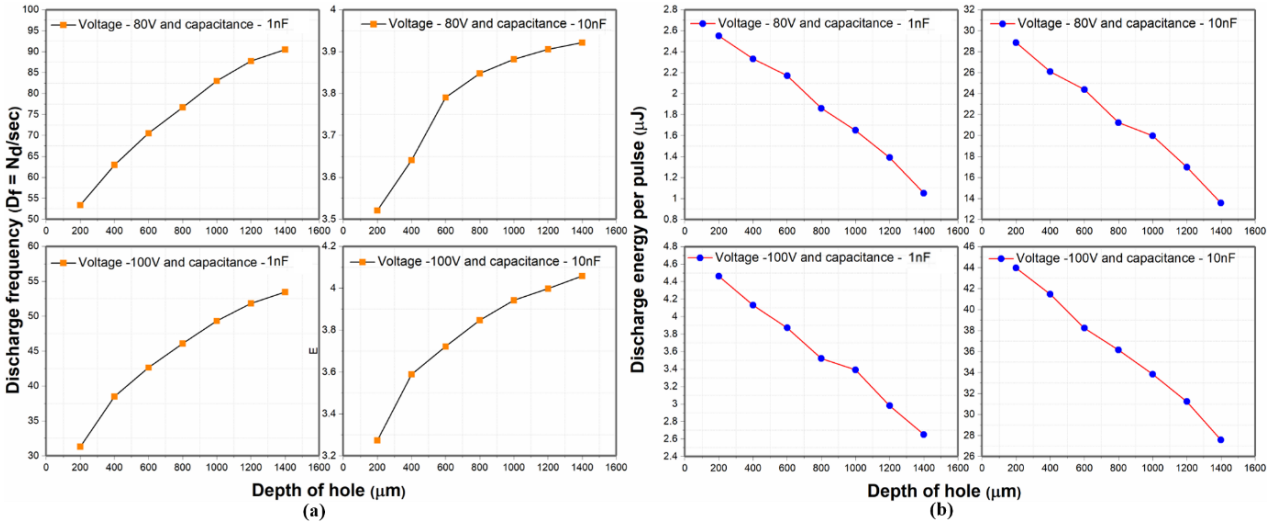

Figure 4.13 (a) Variation of D_f with the depth of the machined hole, (b) Variation of Avg. discharge energy with the depth of the machined hole

4.3.5 Histogram of pulses

The discharge energy of different pulses was computed during the continuous machining with the help of Eq. (1).

$$E_d = \Delta t \times \sum_{i=1}^{N} V_i I_i \tag{1}$$

In the above equation, Δt represents the time duration between the two consecutive data points captured at a predefined sampling rate, measured between point D (the discharging location) and C (the charging location), as shown in Figure 4.1(b). V_i and I_i in the equation are the i^{th} data points in a discharge current and voltage pulse. Arcing or non-contributing discharge pulses deliver an insignificant amount of discharge energy and may cause a negligible or no contribution in removing material. However, as the previous section shows, the contributing and semi-contributing pules cause considerable material removal. Hence, a histogram of the number of discharge pulses was plotted against the discharge energy for both the contributing and semi-contributing discharge pulses to compare the average discharge energies spread at various machining depths. It can be observed from Figures 4.14 and 4.15 that the peak of the average discharge energy curve shifts towards the lower energies for the semi-contributing pulses when compared with the contributing pulses. The peak of the curve shows the average of the discharge energy among all the captured discharge pulses for the same machining duration at different machining depths. The energy histograms also provide a better idea about the frequency of the discharge pulses with respect to the energy content of each discharge. The average discharge energy per pulse for the semi-contributing pulses is

approximately half compared to that of the contributing pulses at all the parametric settings. This observation is the same as discussed in the previous section and validates the developed PMS feasibility for a continuous and longer duration of machining.

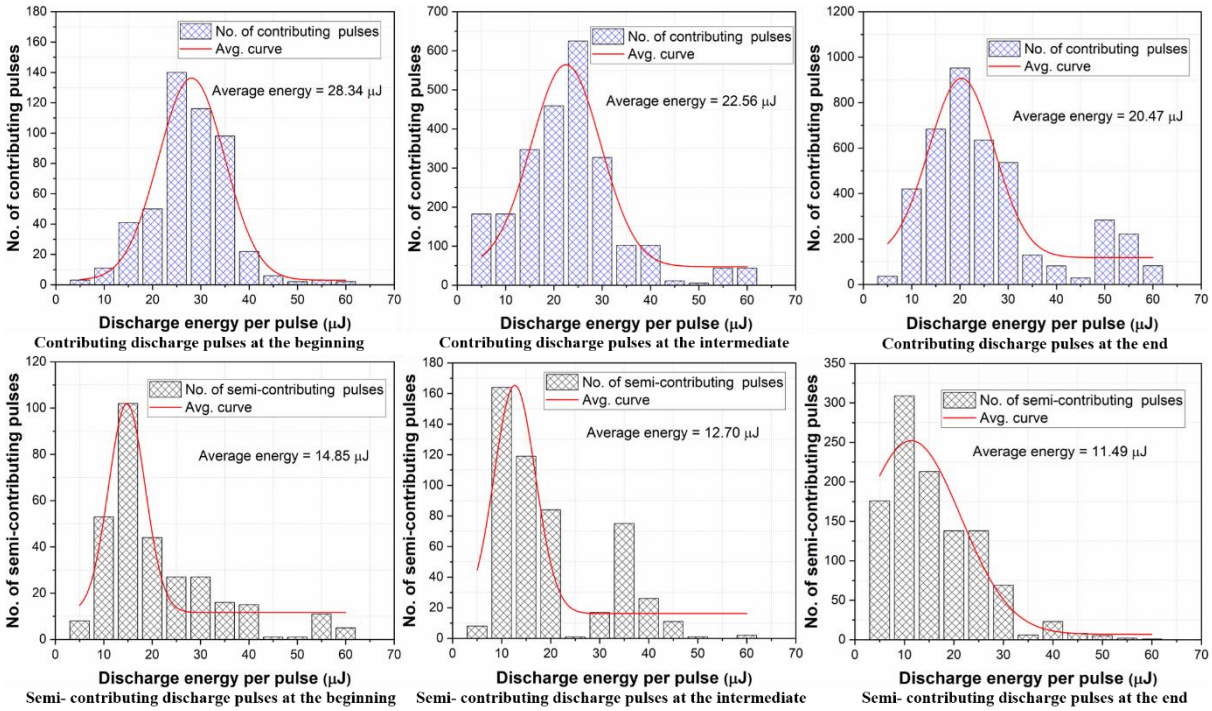

Figure 4.14 Typical variation of the no. of contributing and semi-contributing pulses with the discharge energy at a setting of voltage 80V and capacitance 10nF

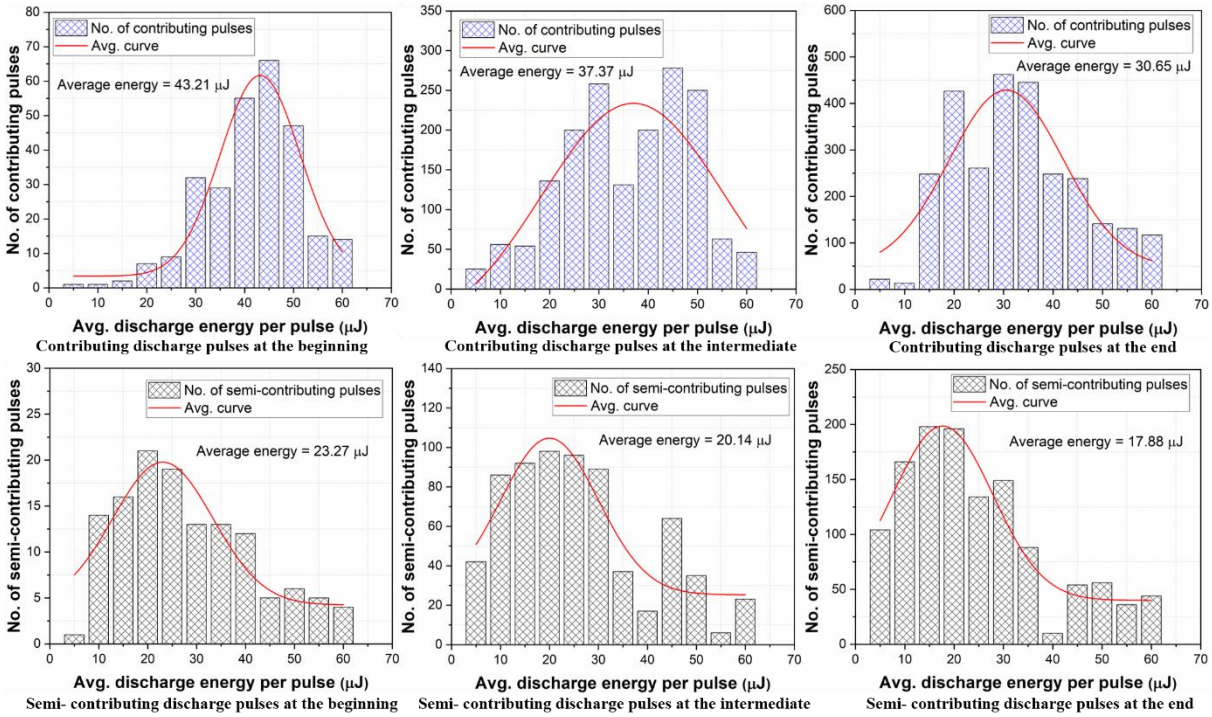

Figure 4.15 Typical variation of the no. of contributing and semi-contributing pulses with the discharge energy at a setting of voltage 100V and capacitance 10nF

Voltage and current signals during three stages, i.e., beginning, intermediate, and end of the micro-EDM drilling process, were captured and depicted in Figure 4.16 to observe the influence of machining depth on the nature of discharges. It can be seen that when the machining was performed at the surface of the workpiece, the number of no-discharge or open-circuit pulses were dominant. The reason is that the discharge can occur only through the tool's tip as the tool has not yet traveled in the depth of the hole. With increasing machining depth, there are chances for discharge to occur not only from the tip but also from the tool's circumferential area due to the debris's contamination. This increases the discharge count in the form of more semi-contributing discharges. When the machining depth was further increased, at the end of the hole, the stability of the process decreased with more arcing or non-contributing discharges. The frequency of abnormal discharges increased due to the difficulty in removing the debris from the depth of the micro holes drilled during the machining. Although the frequency of the discharge increased with the depth of the machining, it couldn't contribute to the material removal as the MRR decreased due to the reduced energy content of the discharges. Hence it can be concluded that the material removal depends mainly on the energy content and not the frequency of discharges. Therefore, a pulse monitoring system is crucial in monitoring the stability and effectiveness of the micro-EDM process during continuous machining.

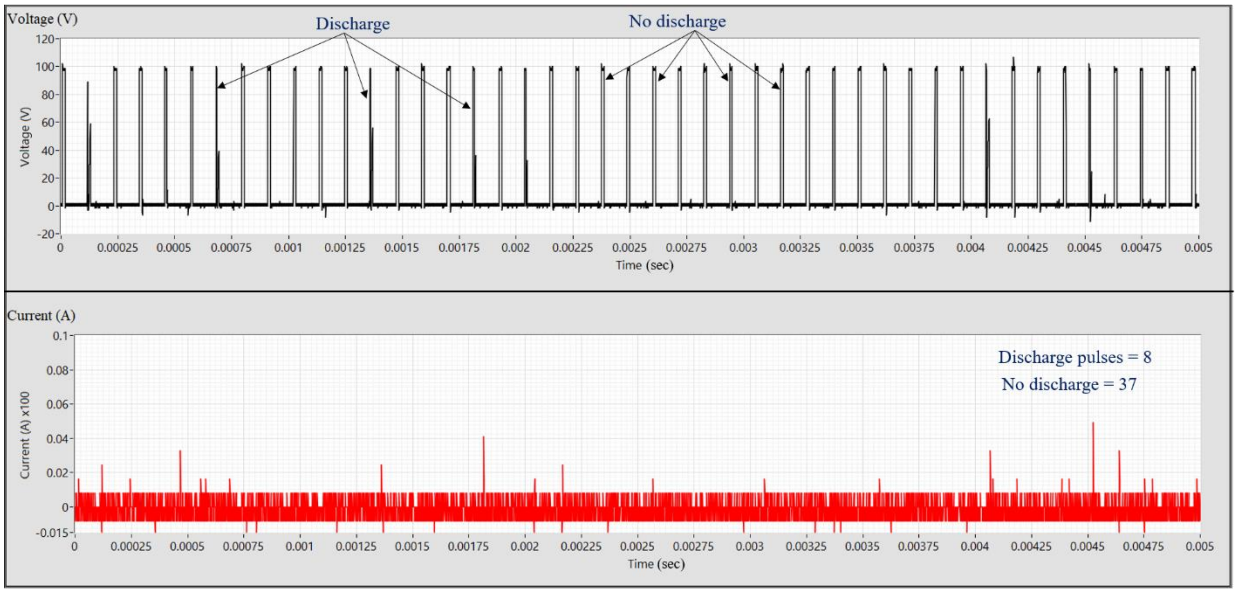

(a)

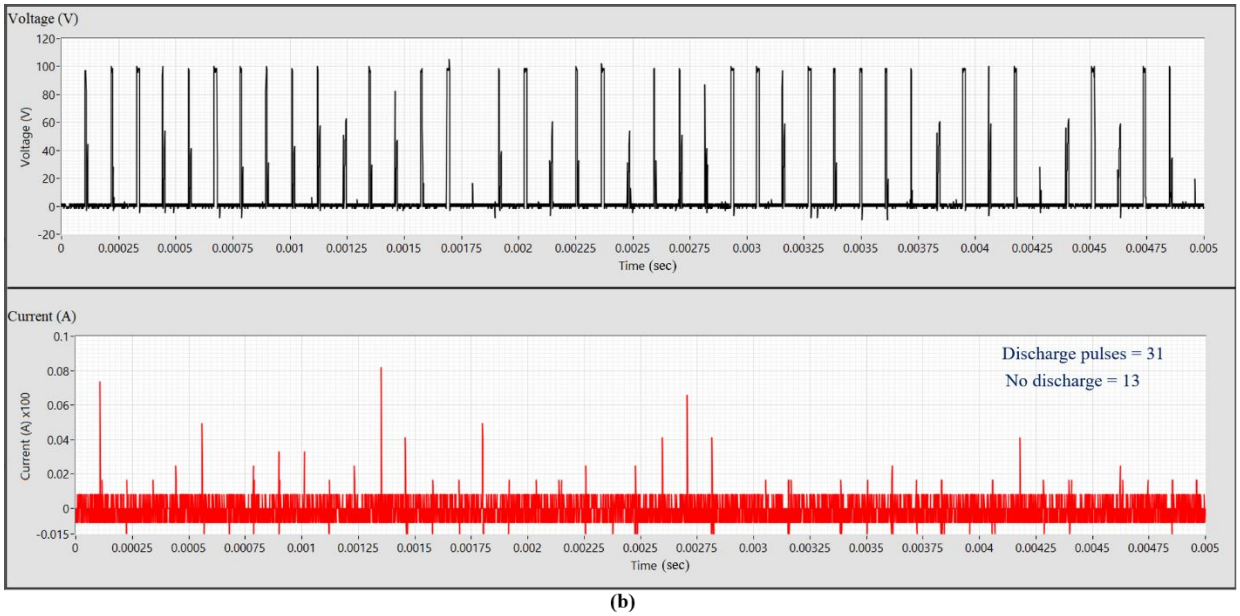

(b)

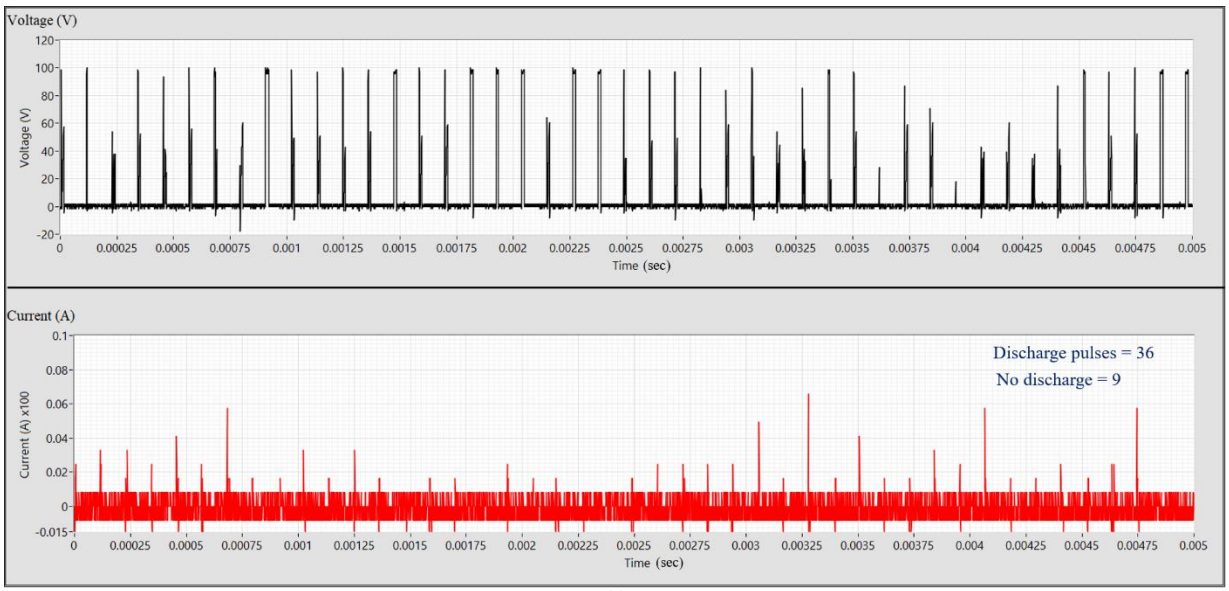

(c)

Figure 4.16 Nature of the discharge pulses with the depth of the machined hole (**a)** at the beginning, (**b)** at the intermediate, and (**c)** at the end

4.3.6 Effect of machining parameters on MRR and surface roughness

MRR is a critical measure in the determination of the potentiality of the micro-EDM process. In the micro-EDM drilling process, MRR is affected by different machining considerations, but the impact of hole depth on MRR is estimated to be significant. The MRR is a function of discharge energy and stability of the process and should decrease with the machining depth as the abnormal pulses have increased in frequency. However, the quantitative assessment of the MRR can further explain the magnitude of the abnormalities in machining with increasing depths, as explained by Nirala and Saha [190]. The variation in MRR and VRD

with the depth of the machined hole is depicted in Figures 4.17(a) and (b). As expected, the MRR and the VRD decrease with increasing machining depth due to the decrease in the efficiency of flushing the debris from the discharge gap and the reduction in the average discharge energy per pulse, as discussed earlier using Figure 4.13. The MRR was observed to be proportional to the voltage and capacitance settings and increases more rapidly with increasing capacitance than the increasing voltage. This may be attributed to the fact that an increase in the capacitance from 1 nF to 10 nF increases the joule energy by ten times. This increment is much higher than the increment in the discharge energy while switching the voltage from 80V to 100V.

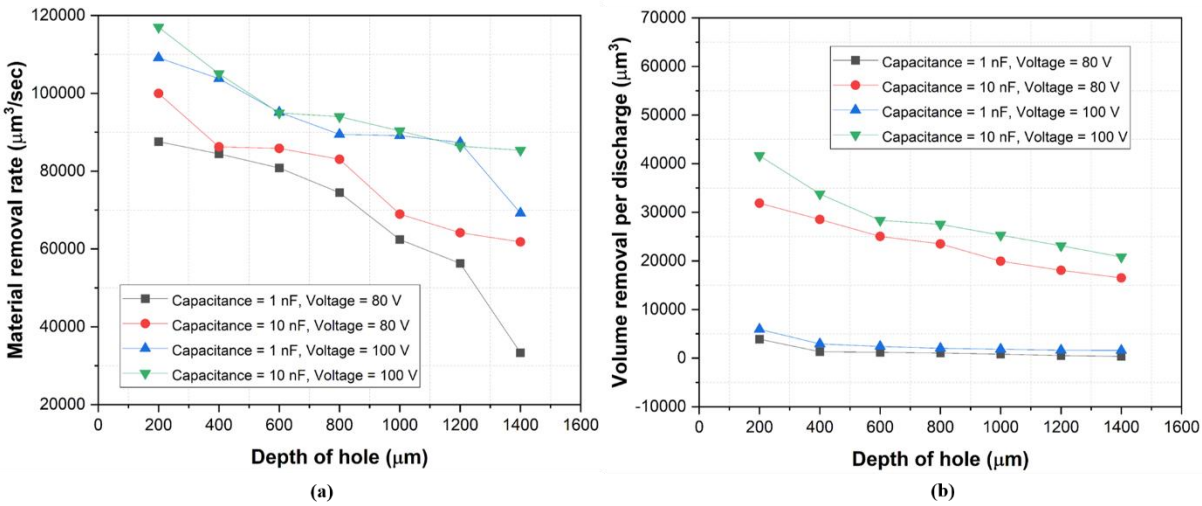

Figure 4.17 (a) Variation of MRR with the depth of the machined hole, (b) Variation of VRD with the depth of the machined hole

Figure 4.18 shows the plots of surface roughness of machined surfaces in terms of R_a at different machining parameters. With increasing discharge energy, the surface roughness of machined holes also increases. The average surface roughness value was more sensitive to capacitance than the voltage. The surface roughness increased from 0.8 μm to 1.4 μm when capacitance increased from 1 nF to 10 nF. The same observation was made at the voltage setting of 100 v. This is because the increase in capacitance increases the discharge energy by ten times, with broader and deeper craters expected to form, and removing large volumes of debris is challenging. It also results in an increased frequency of non-contributing and short-circuit pulses. These non-contributing and short-circuit pulses cause debris deposition on the workpiece, raising the micro craters' peak-to-valley height.

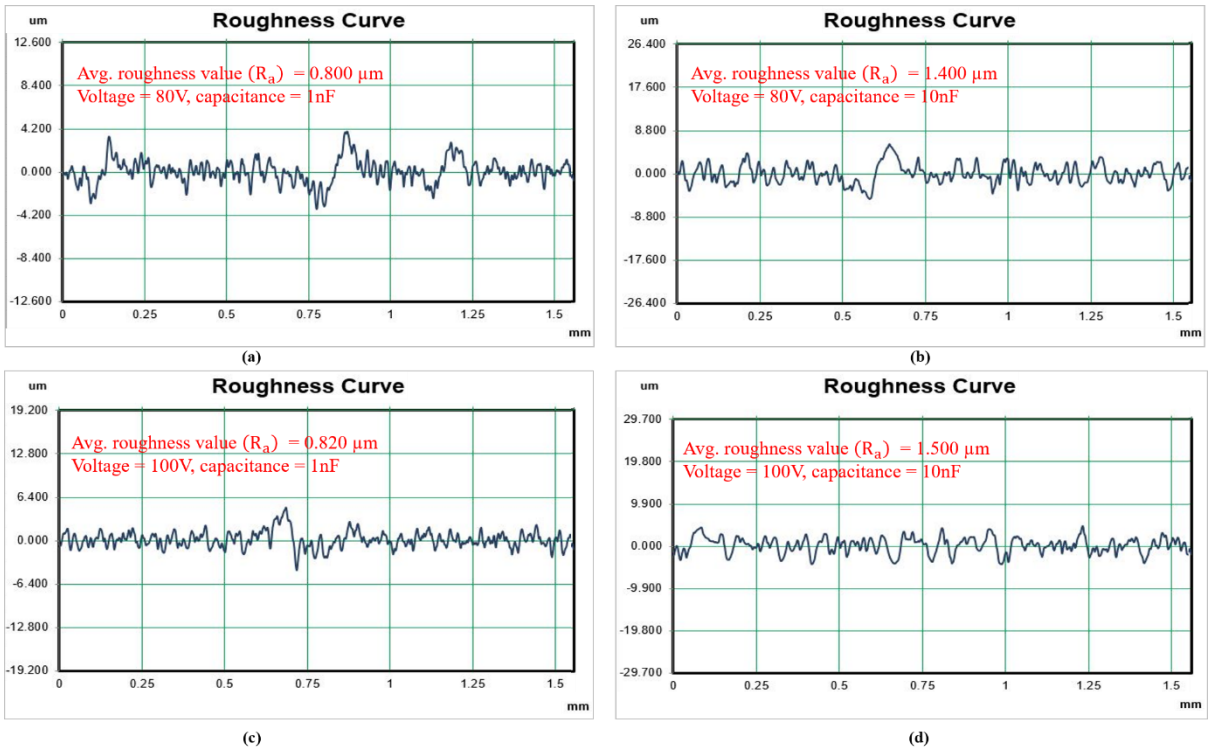

Figure 4.18 Variation of surface roughness with the depth of the machined hole

4.4 Summary

A PMS was developed in this chapter to categorize the discharge pulses as contributing, semi-contributing, and non-contributing during the micro-EDM drilling process. The non-iso-energetic nature of the discharge pulses has been thoroughly discussed based on the voltage and current signals and by quantifying the discharge energy per pulse. Micro-EDM drilling experimentation was performed at the center of a splittable workpiece with varying machining depths to access the drilled holes' crossectional profile. Following conclusions are made after employing the pulse monitoring system in the continuous micro-EDM drilling process at varying machining depths.

- It has been found that the MRR and VRD are the functions of discharge energy and continuously decrease with the depth of the machined hole. It means The stability of the machining and the energy content of the discharges are the primary factors that determine material removal, rather than the frequency of the discharges.
- Discharge frequency and the energy of contributing and semi-contributing discharge pulses showed opposite trends with respect to the depth of machining.
- The average discharge energy was reduced to approximately half for the semi-contributing pulses compared to the contributing discharge pulses.

- The dimensional accuracy of the micro-holes decreased with increasing machining depths. The percentage error rose from 2.83% to 12.5% under the different machining depths and input energy settings.
- The surface roughness was higher at high discharge energies and depended more on the capacitance than the voltage settings.

Chapter 5

Experimental Investigations on Vibration-assisted Micro-EDM

5.1 Introduction

The present chapter covers the experimental investigations to explain the vibration-assisted micro-EDM process's advantages. Initially, a low-frequency vibration setup is employed as a preliminary measure to evaluate the impact of vibrations on the MRR. The machining results of the unassisted and vibration-assisted experiments are compared to ascertain the feasibility of the configuration. Subsequently, an ultrasonic vibration-assisted tool holder is utilized for in-depth experimentation, considering the high frequency of the discharge pulses in micro-EDM. A detailed experimental analysis is performed at different micro-EDM input parameters to examine the impact of ultrasonic vibrations on the micro-EDM milling. A comparative discussion is then carried out regarding the effect of ultrasonic vibration assistance on the machining outcomes, such as the MRR, TWR, Surface finish, and recast layer formation. The discharge pulses with and without vibration from the micro-EDM were monitored using the PMS developed in the previous chapter. The last section compares the machining outcomes during the micro-EDM drilling of blind holes with and without vibrations. The main aim of this study is to explain the machining stability with increasing depth by estimating the discharge energy of pulses in real-time. Furthermore, the offline outcomes, such as overcut in depth and surface roughness, and online data, such as pulse frequency and average pulse energy, were calculated.

5.2 Low-frequency vibration-assisted micro-EDM

5.2.1 Development of low-frequency vibrating tool holder

The low-frequency vibrating tool holder used in the present work operates based on the driven harmonic vibrations generated by an eccentric rotating mass (ERM) motor located within the tool holder's housing. By providing the ERM motor with a direct current (DC) voltage, the eccentric rotor within the motor rotates at an RPM that corresponds to the applied voltage. When the rotor rotates, longitudinal vibrations are transmitted to the collet chuck, causing the tool to vibrate and facilitating debris removal from the IEG. This vibration frequency is directly proportional to the motor's RPM. It helps to increase the likelihood of normal discharges while decreasing the probability of arcing, a significant concern in micro-EDM. The vibrating tool holder consists of several components, including a fixed shaft, housing for the ERM motor, vibrating platform, end cap, collet chuck, ER-11 nut, tool

electrode, and tightening screws, as shown in Figures 5.1(a) and 5.1(b). The motor used in this setup is a 4 mm × 11 mm mini vibration motor with a rated voltage of 3 volts (Make: Precision microdrives; model: 304-103). Detailed sectional views of the vibrating tool holder assembly are presented in Figures 5.2(a) and 5.2(b).

The primary design consideration for the vibrating tool holder was to ensure that its height would be compatible with the Z-axis travel of the spindle, thus enabling easy adjustment. The fixed shaft, which holds the attachment to the machine's spindle and is connected to the housing, was designed and fabricated to accommodate the limited vertical space typically in a micro-EDM setup. The vibration source of the device is provided by an ERM vibration motor placed at the vibrating platform. The primary purpose of the housing is to isolate the ERM motor from the machining environment, preventing its interaction with the dielectric oil.

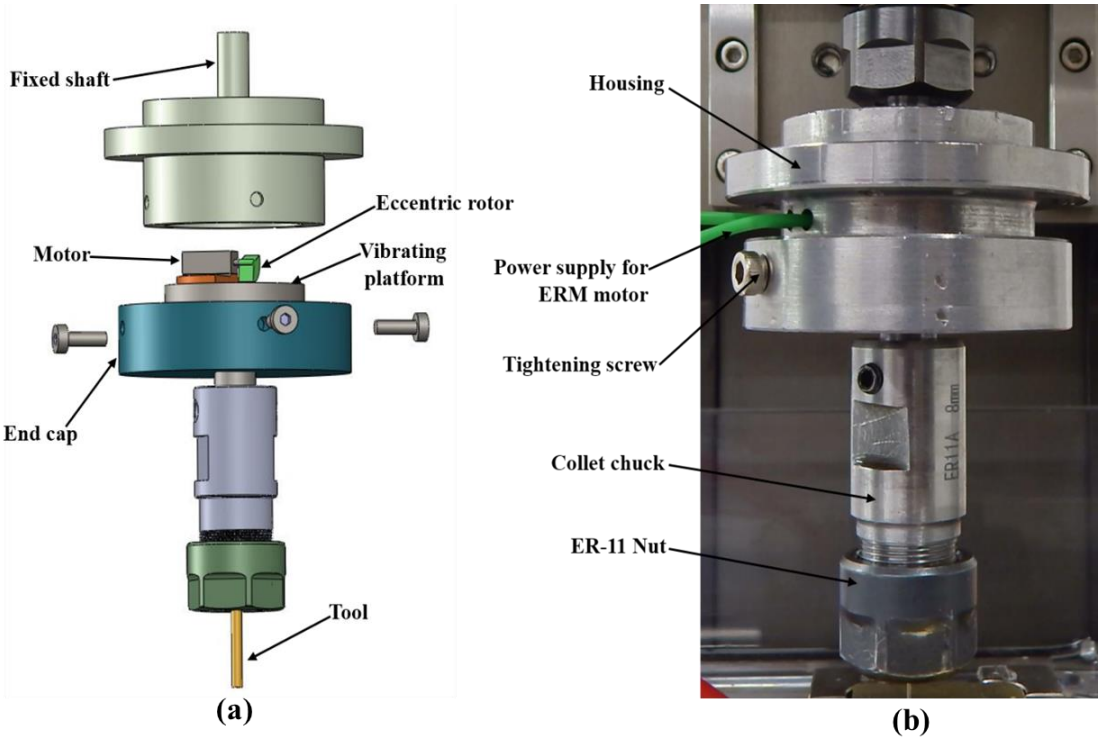

Figure 5.1 (a) CAD model and (b) pictorial view of the vibrating tool holder

An ERM motor contains an asymmetric mass connected to the end of its shaft, as shown in Figure 5.3. As the motor rotates, a centrifugal force is generated due to the non-symmetric geometry of the rotating mass given by Eq. (5.1).

$$F = mr\omega^2 \cos\theta \tag{5.1}$$

Where F is centrifugal force; m is the mass of the eccentric rotor; r is the eccentricity of the rotor; ω is the angular velocity of the rotor.

The ERM motor utilized in the study operates by producing vibrations through centrifugal force, which is driven by inertial force. This type of vibration generation is a cheaper and simpler alternative to piezoelectric or magnetostrictive mechanisms, making it possible to manufacture smaller systems. When mounted on a motion platform, the ERM motor generates the centrifugal force by utilizing the eccentric rotating mass's inertia and can produce vibrations with a pre-defined amplitude. As a result of this centrifugal force, the motor vibrates. When the RPM of the motor rises, the motor continuously moves up and down, generating vibrations at a specific frequency and amplitude. This type of vibration is called driven harmonic vibration, as the vibration is produced by an unbalanced rotating mass's external excitation. The ERM motor systems not only contribute to vibration in the vertical direction but also the horizontal direction. To ensure that these systems vibrate in one direction only, they are usually designed to behave like a system having one degree of freedom. This means that any vibration force generated in the other direction is either dissipated within the construction material of the system or redirected in the longitudinal direction. In the current device, the ERM motor is mounted on the top surface of a circular plate called a vibration platform, as shown in Figure 5.1(a). When the motor shaft rotates, the entire motor and vibration platform vibrate together, with an end cap provided to keep the vibrating platform in place and absorb the lateral vibrations.

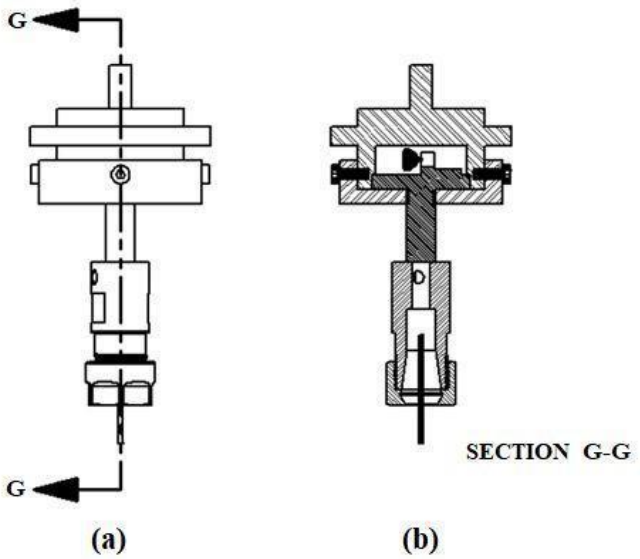

Figure 5.2 (a) Front view and (b) sectional side view of the vibrating tool holder

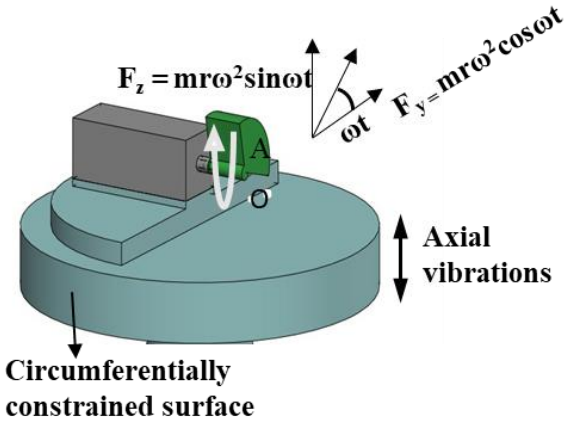

Figure 5.3 Forces acting on the vibrating platform

The following sections deal with the experimental setup and machining conditions under which the experiments were performed to check the feasibility of the vibration assistance to the micro-EDM milling and the reverse-micro-EDM processes.

5.2.2 Experimental setup and machining parameters

An integrated micromachine tool (Make: Sinergy Nanosystems Model: Hyper 15) fabricates microchannels using the micro-EDM milling process. The micro-EDM generator utilized in the machine is a controlled RC-based power supply, unlike a simple RC micro-EDM generator, where the discharge timing is random. The discharge can only occur during the pulse on time of the machine, which can be adjusted through the machining parameters. Figures 5.4(a) and 5.4(b) illustrate the machining setup and the tool-workpiece configuration. The machine used in the experiment has precise linear motor guides and a ball screw-driving mechanism, providing maximum travel of 135 mm×65 mm×65 mm in x, y, and z directions with a work table size of 260 mm ×110 mm ×100 mm. The machine's spindle holds the fixed shaft of the vibrating tool holder, made of mild steel, with the help of an ER-11 collet. An adjustable DC voltage supply provides power to the ERM motor for vibration. Since the fixed shaft of the vibrating tool holder is made of an electrically conductive material, the same voltage difference from the EDM generator is maintained at the IEG. For the micro-EDM milling experiments, a 2 mm thick brass plate measuring 20 mm x 15 mm was chosen as the workpiece, and a 500 µm tungsten electrode was used as the tool electrode. A commercially available EDM oil, ST EDM 250, was used as the dielectric, which has a flashpoint of 117.78 ^{o}C, and a dielectric strength of 47 KV/mm. The experiments were first conducted without attaching the vibration tool holder to the micro-EDM machine, followed by incorporating the vibration attachment into the experimental setup. The vibration frequency was varied using a

function generator that provides the necessary power to the motor. The workpiece was fixed on the fixture using powerful magnets to ensure its flatness with the tool electrode. Straight polarity was used in the experimentation, with the work being positive and the tool negative. The machining parameters and experimental conditions are provided in Table 5.1.

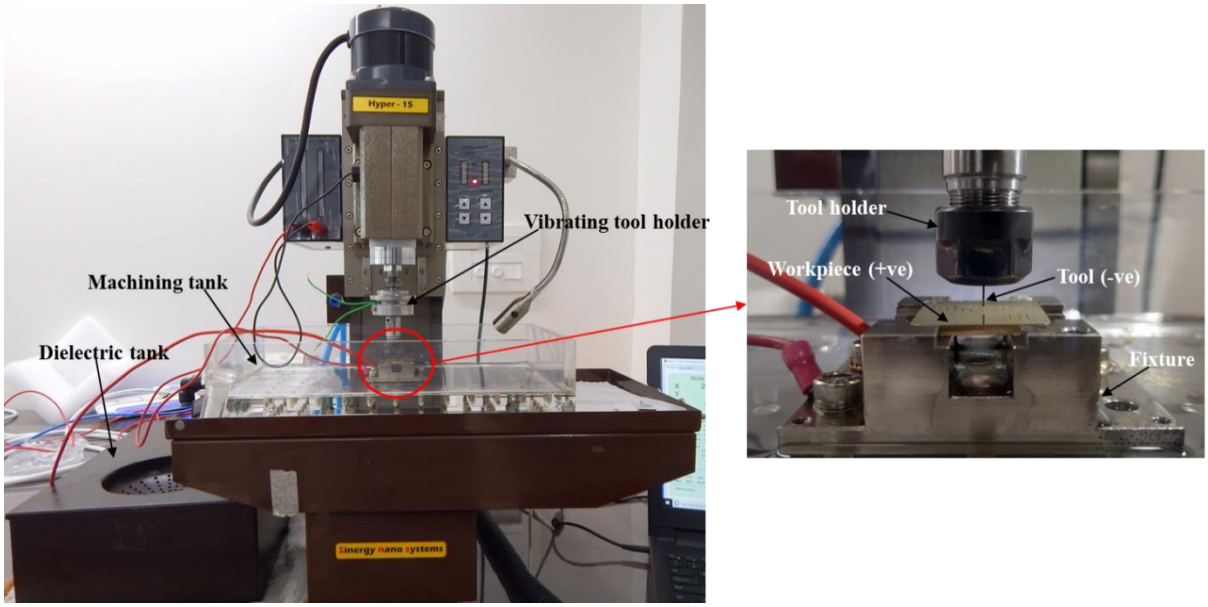

Figure 5.4 Pictorial view of (a) micro-EDM milling setup with retrofittable vibrating tool holder and (b) close view of machining zone

Reverse micro-EDM is a variant of micro-EDM used to fabricate micro-arrayed projections from a surface [191]. Here the tool and workpiece are assumed to be interchanged compared to the typical micro-EDM experiment configuration. Reverse polarity is used in the process as the part held in the spindle is considered the workpiece, and the part in the fixture is assumed to be a tool, as shown in Figure 5.5(a). As the workpiece comes near the fixed tool plate and sufficient voltage is applied between them, sparking occurs resulting in the material removal, as shown in Figure 5.5(b). Sparking occurs at the interface of the solid surfaces of the two electrodes, leading to the replication of the drilled pattern of the fixed tool plate on the moving work electrode. Reverse-micro-EDM is performed on a brass workpiece of 1 mm diameter with a stainless-steel plate as a tool to fabricate micro-arrays with a 100 µm diameter and a height of 2 mm (aspect ratio of 20). The machining parameters and experimental conditions for reverse-micro-EDM are provided in Table 5.1.

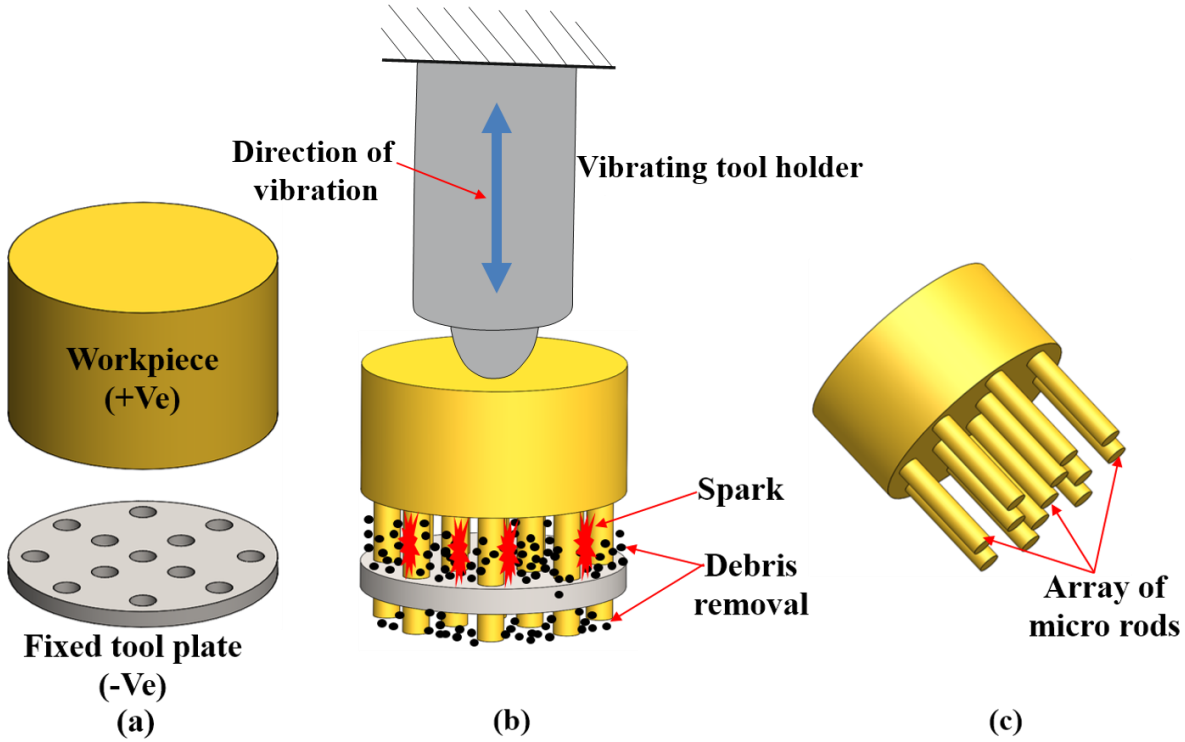

Figure 5.5 Schematic diagram of the reverse-micro-EDM process (a) reverse polarity configuration (b) vibration applied to the tool (c) array of micro rods

Table 5.1 Machining conditions of µED-milling and reverse-micro-EDM

Parameters	**µED-milling**	**Reverse-micro-EDM**
Material	The workpiece (Anode) A brass plate of 2 mm thickness	The workpiece (Anode) Brass rod of 1 mm diameter
	Tool (Cathode) Tungsten rod of 500 μm diameter	Tool (Cathode) SS plate of 100 μm arrayed holes
Tool-electrode in feed rate	60 $\mu m/min$	60 $\mu m/min$
Tool-electrode through feed rate	120 $\mu m/min$	No through feed
Pulse on time	10 μs	10 μs
Pulse off-time	100 μs	100 μs
Capacitance	10 nF	10 nF
Open circuit voltage	100 V	100 V
Vibration frequencies	0 Hz, 100 Hz, 150 Hz	0 Hz, 100 Hz, 150 Hz
Responses		

Online responses	Machining time, Overcut, the height of micro-rods

5.2.3 Effect of low-frequency tool vibrations on micro-EDM Milling

Material Removal Rate (MRR) is a crucial factor in assessing the potential of the micro-EDM process. Microchannels with a width of 500 μm were machined, and the machining time was recorded to evaluate the effect of vibration assistance on the stability of the micro-EDM process. The results showed that using vibration assistance significantly improved the efficiency of the micro-EDM process. Figure 5.6 illustrates the variation of machining time and overcut in width with increased vibration frequency. The machining time for fabricating a 500 μm deep microchannel without vibration assistance was 141 minutes. This time was reduced to 78 minutes at a vibration frequency of 100 Hz, indicating a 44.6% increase in the machining efficiency. Figure 5.7 depicts the variation in machining time with the increasing depth of the micro channels fabricated in the study. The depth of the channel significantly affects the efficiency of the micro-EDM process. When the machining is performed at a greater depth, the removed material fails to find a free path to be flushed away from the machining area. This results in the adhesion and re-solidification of the removed material to the tool and the work surfaces, decreasing the IEG and leading to the arcing phenomenon. A further increase in the microchannel depth severely increases the arcing phenomenon, leading to a steep increase in machining time. Therefore, the micro-EDM parameters should be optimized for the depth of the channel to ensure stable and efficient machining.

The application of vibration at a frequency of 100 Hz resulted in a reduction of machining time by approximately half compared to unassisted micro-EDM during the initial stages, as depicted in Figure 5.7. The improvement in machining efficiency can be attributed to the ease of debris flushing caused by the pressure variation in the machining gap due to the applied vibration. This also reduces the likelihood of the removed material sticking to the electrode and re-solidifying at the work surface. The pressure variation also facilitates the flow of the dielectric oil in the IEG. Increasing the vibration frequency from 100 Hz to 150 Hz led to a further reduction in machining time to 73 minutes, as shown in Figure 5.6.

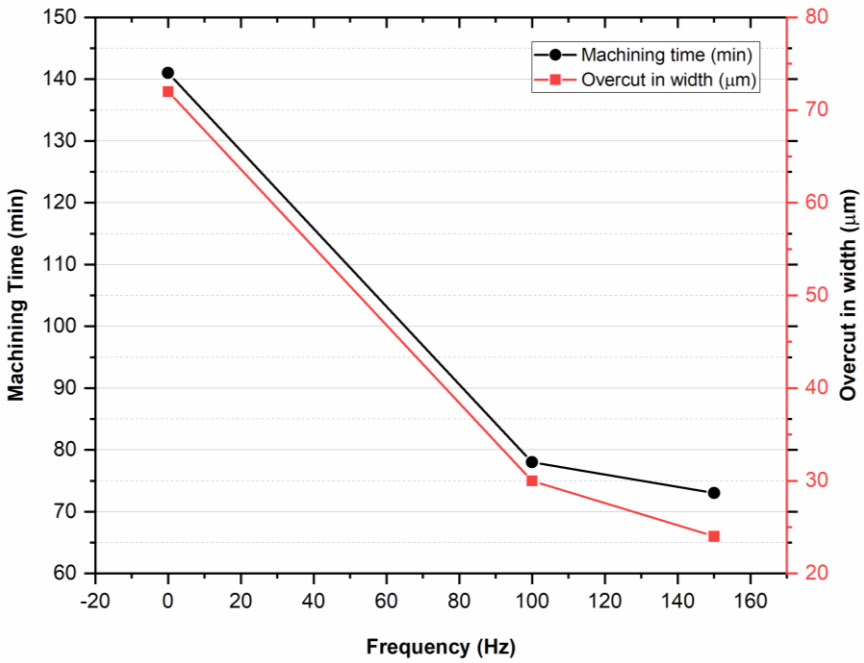

Figure 5.6 Variation of machining time and accuracy of machining with vibration frequency

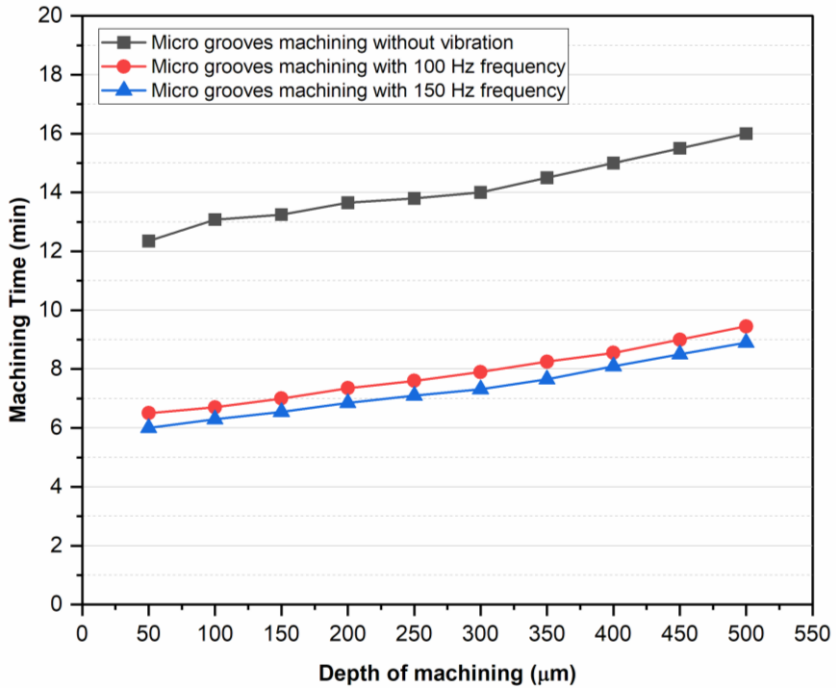

Figure 5.7 Variation of machining time concerning the depth of machining

The machined surface and SEM images of the micro channels for the experimental conditions in Table 1 are depicted in Figure 5.8. The results show that the vibration assistance provided to the micro-EDM process has improved the dimensional accuracy of the machined micro channels, which is consistent with the findings in Figure 5.6. In the absence of vibration assistance, the width of the micro channels was measured at 572 µm, which is 72 µm greater than the targeted width of 500 µm. This overcut can be attributed to the arcing phenomenon,

observed frequently without vibration assistance. However, when vibrations were applied, the width of the micro channels was measured as 530 µm, indicating an increase in dimensional accuracy. Moreover, as the vibration frequency increased, the micro channels' width approached the targeted value, indicating an improvement in accuracy. The increase in dimensional accuracy is due to the reduced frequency of arcing, which prevents debris from adhering to the electrode surface. This finding is consistent with a recent study that applied vibrations to decrease the occurrence of short-circuiting [148].

Furthermore, Unune et al. reported improved machining accuracy and surface quality by introducing low-frequency vibrations [170]. The micro channels' surface topography with and without vibration assistance is presented in Figure 5.9. Upon careful examination of the SEM images, it is evident that there is a noticeable difference between the surfaces machined with and without vibration assistance. The machined surface without vibration shows re-solidified debris in a considerable amount. Compared to that, the vibration-assisted surfaces were cleaner with negligible debris adhesion. This supports the notion that vibration assistance increases machining stability by increasing the flushing action from the IEG.

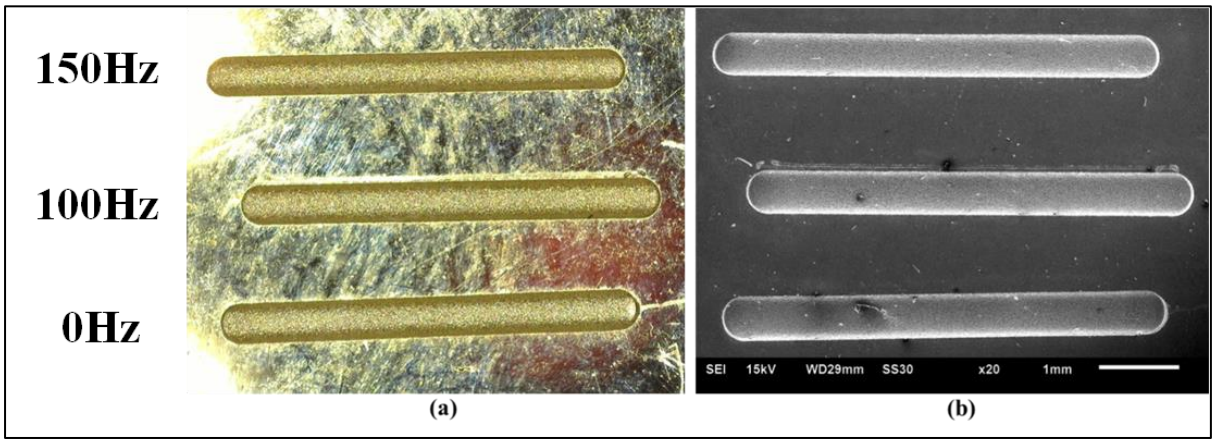

Figure 5.8 (a) Actual machined surface and (b) SEM images of the microchannels

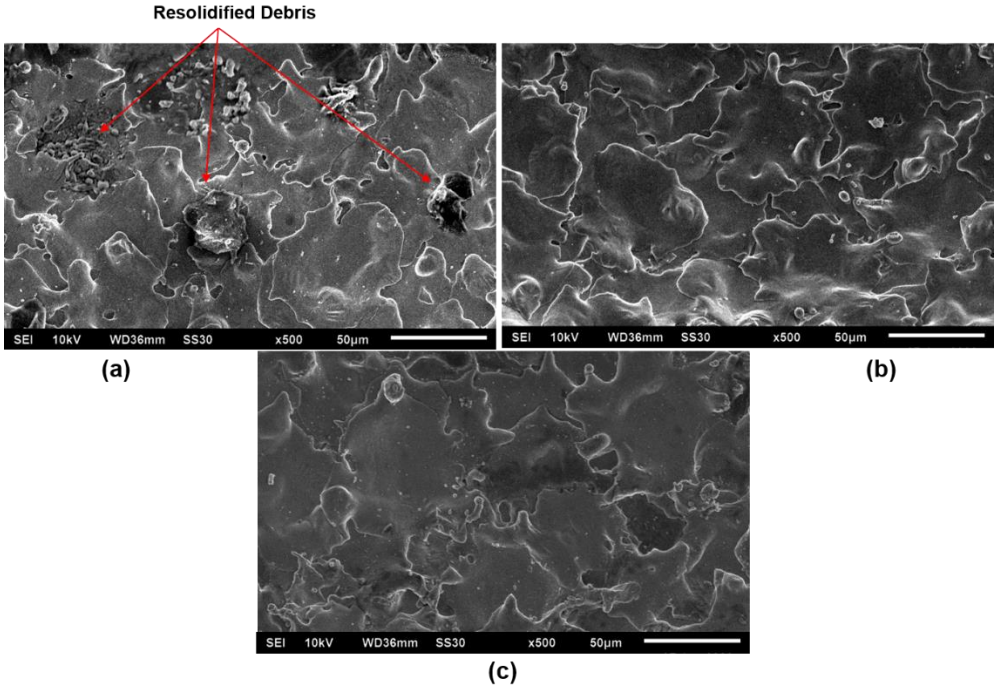

Figure 5.9 SEM images of micro channels (a) without vibration (b) 100Hz (c) 150Hz

5.2.4 Effect of tool vibrations on the reverse-micro-EDM process

Experiments were conducted using reverse-micro-EDM to examine the potential of the vibrating tool holder for producing micro-arrayed structures. Figure 5.10 displays the top view and cross-section of the arrayed microstructures produced with and without vibration assistance. The introduction of 100 and 150 Hz vibration led to a significant decrease in machining time by 48% and 57%, respectively, as illustrated in Figure 11. The reduction in machining time is more significant in reverse-micro-EDM than in normal micro-EDM, which was anticipated as vibrations were applied to the spindle side, and the material was removed from the same side during the reverse-micro-EDM process. Consequently, the likelihood of debris sticking to the work surface and melted material's tendency to re-solidify decreases.

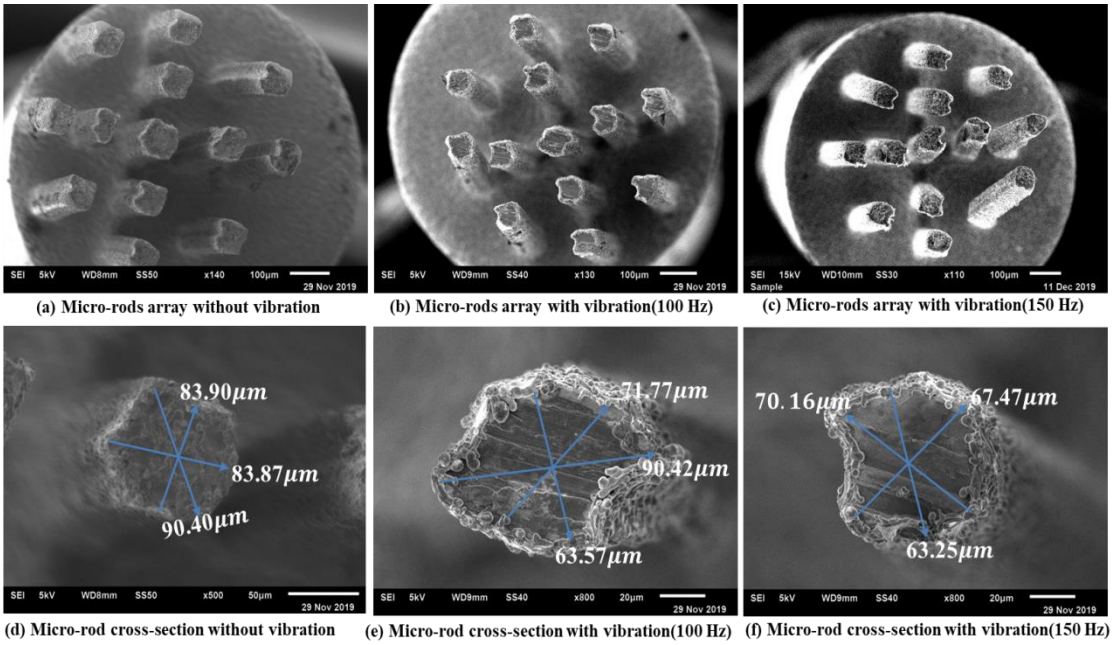

Figure 5.10 SEM images of micro-rod arrays and their cross-section with and without vibration assistance

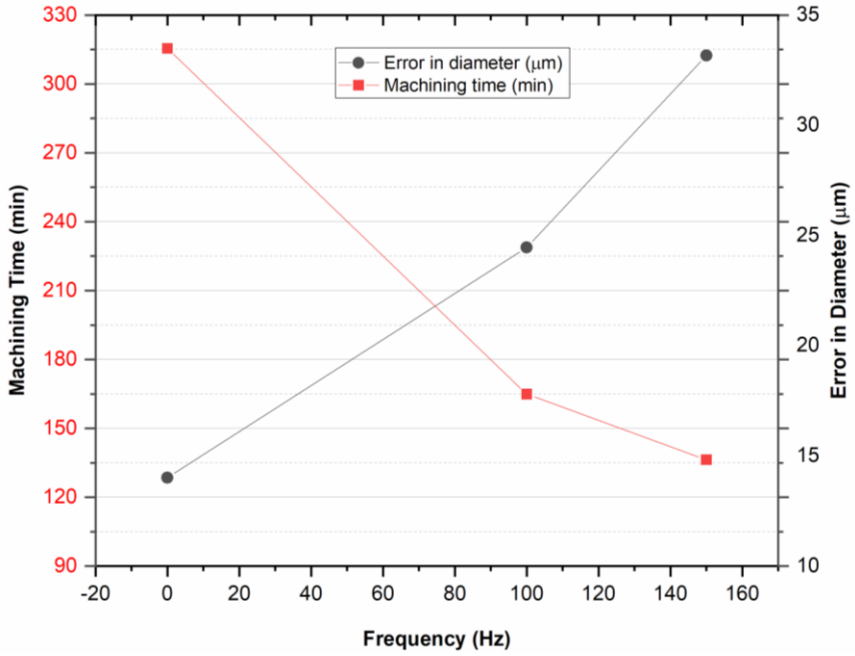

Figure 5.11 Variation of machining time and error in diameter with and without vibration assistance

The enhancement in MRR reflects greater height and smaller diameter of the micro-arrays compared to reverse-micro-EDM without vibration assistance, as shown in the plot and SEM image of Figure 5.11 and Figure 5.12, respectively. While the MRR was indeed increased with vibration assistance, it resulted in poorer straightness of the micro rods at a vibration frequency of 150 Hz. This was attributed to the lateral vibration force that becomes stronger at higher frequencies. Addressing this issue could further improve the accuracy of the micro-

EDM process with vibration assistance. The SEM images of the fabricated micro rods using reverse micro-EDM indicate that the effects of vibration assistance are similar to those observed in the normal micro-EDM process. However, it was observed that the number of discharge craters per unit area increased when the reverse-micro-EDM process was assisted with vibrations. Figure 5.13 shows the machining performance at different depths of the reverse-micro-EDM process. Unlike the normal micro-EDM process, the MRR at the beginning of machining is low but gradually increases and becomes stable towards the end. This is due to the ease of debris removal as the workpiece electrode crosses the thickness of the tool plate.

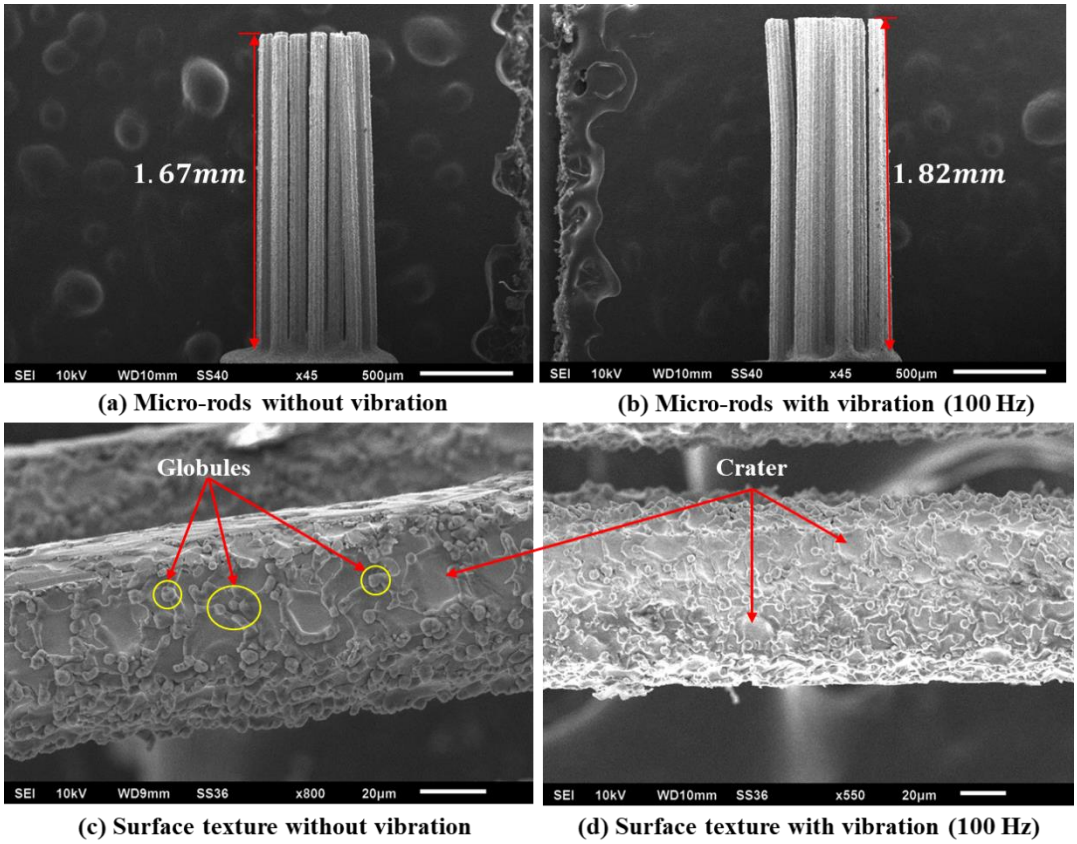

Figure 5.12 SEM images of micro rods height and surface texture with and without vibration assistance

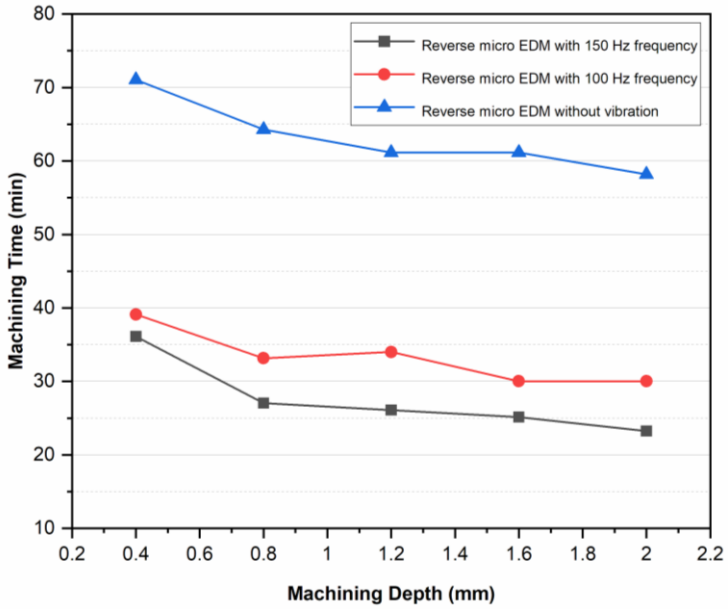

Figure 5.13 Variation of machining time concerning the machining depth

5.3 Ultrasonic vibration-assisted micro-EDM

The preliminary study with the setup developed in the previous section showed increased MRR. However, Considering the high frequency of discharges in the micro-EDM, an ultrasonic vibration-assisted setup is developed to enhance the machining performance with more extensive experimentation. A careful observation of the available literature revealed that most studies related to the vibration-assisted micro-EDM focus on assisting the workpiece with vibrations instead of the tool electrode. However, there are studies related to tool electrode vibration. Still, they are less inclined towards micro-EDM, and a detailed analysis of the machining performance concerning the electrical behavior of the discharge pulses is needed. The present work aims at exploring the feasibility of the ultrasonic vibrations to the tool electrode in the micro-EDM process by studying the outcomes such as the MRR, TWR, nature of discharge pulses, recast layer thickness, surface topography, etc. The pulse monitoring system developed in the previous chapter is used to monitor the effect of ultrasonic vibrations on the nature of discharges to correlate the stability of the machining with different input energy parameters.

5.3.1 Experimental setup and machining parameters

Micro-EDM milling experiments were performed with a 1 mm diameter brass electrode on a Ti6Al4V plate with 20 mm x 5 mm x 2 mm dimensions. The machining was performed only with half of the circular tool electrode with a targeted depth of 500 µm so that semi-cylindrical slots are machined. This orientation of the tool and workpiece is shown in Figure

5.14 and is adapted to examine the recast layer formation, surface topographies of the walls of the machined slots, and the tool wear. The machining parameters with the measured responses are shown in Table 5.3. The experiments were performed on the Hyper-15 micromachining tool (Manufacturer: Synergy Nano Systems), and the machining data was captured using a data acquisition system (Manufacture: National Instruments). PXI-5114 oscilloscope captures the voltage and current signals at 10 MS/s. The current and voltage waveforms during the machining were recorded using a passive voltage probe (model: 701938; make: YOKOGAWA) and a hall effect sensor (model: CC-650; make: Hantek), which can measure a voltage of 600 V. Pulse monitoring system developed in chapter 4 is simultaneously used to analyze the discharge waveforms using the data acquisition system. The complete experimental setup with the DAQ system is shown in Figure 5.15. The optical images of the machined surfaces were acquired using the digital microscope (model:DSX510 make: Olympus) microscope and the SEM images were taken using a scanning electron microscope (model: 6610LV make: JEOL).

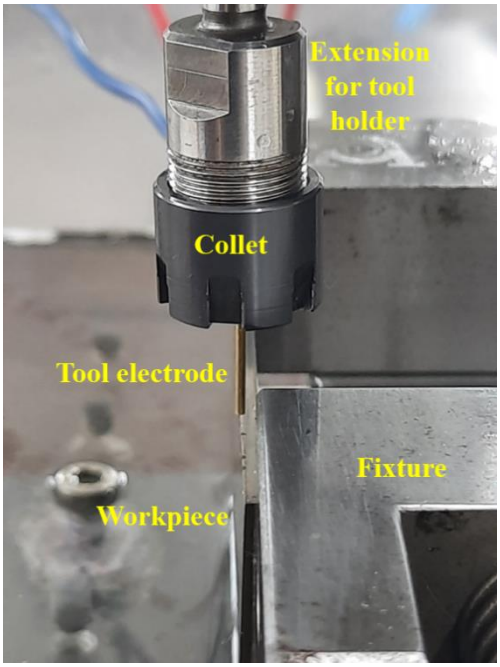

Figure 5.14 Enlarged view of the tool and work electrodes arrangement

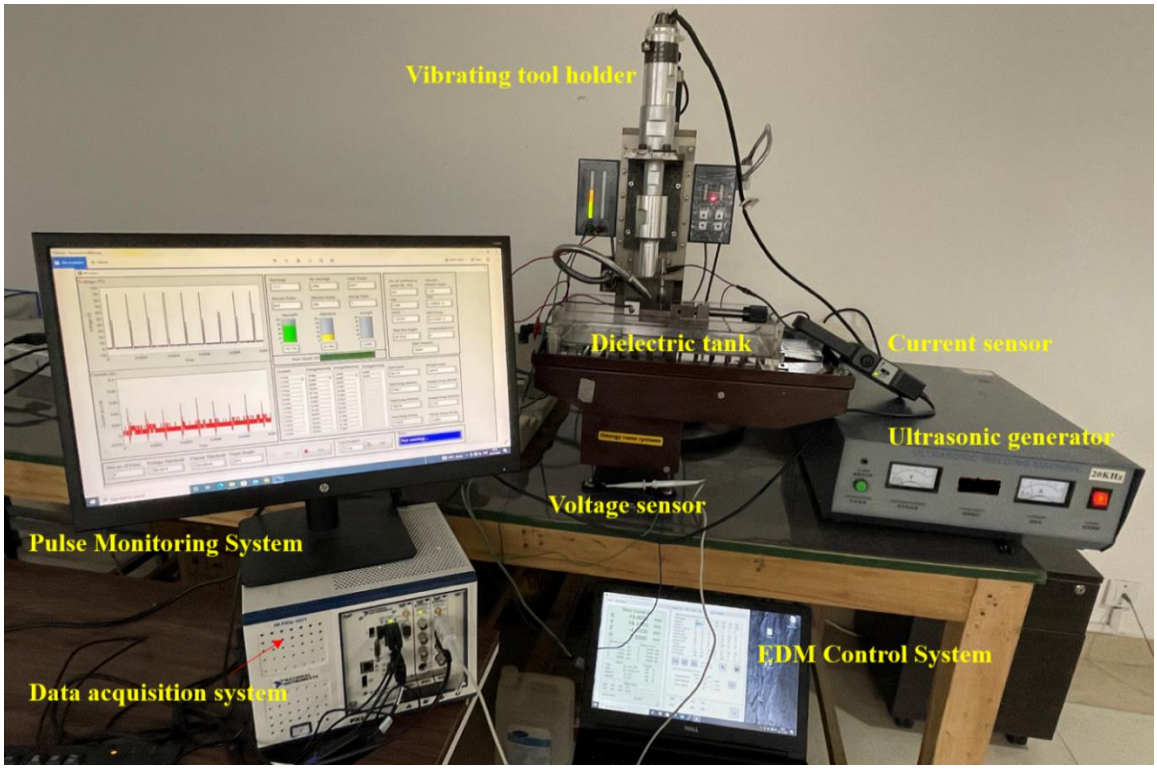

Figure 5.15 Pictorial view of the experimental setup

5.3.2 Measurement of vibration amplitude

The amplitude of the ultrasonic vibration at the tip of the tool electrode is the most critical factor to be controlled while developing the tool holder for the micro-EDM machine. An on-machine non-contact electric touch probe measures the ultrasonic vibration amplitude at different input voltage settings. First, the bottom edge of the tool electrode was brought in contact with the workpiece surface by providing a deficient feed of 0.1 µm/Sec with the G31 skip function code, as shown in Figure 5.15(a). The G31 function in CNC machines feeds the tool in the direction of the workpiece surface and stops the Z-axis motion as soon as the tool enters the workpiece's diminutive vicinity. The z-axis is then zeroed at the stopped position to mark the reference level, as shown in Figure 5.16(b), and the tool is lifted sufficiently above the work surface. Now the tool is assisted with the ultrasonic vibrations, and the z-axis is brought down with the sub-micron feed to ensure greater accuracy. When the vibrating tip of the tool electrode moves towards the workpiece with the G31 command in effect, the z-axis stops at a distance from the reference zero line. That distance is equal to the vibration amplitude at the tip of the tool electrode, as shown in Figure 5.16(c). The process is repeated at different probe voltages to make sure the accuracy of the amplitude measurement technique. A table representing the amplitude at the tip of the electrode using different input voltages with five repetitions (R1, R2, R3, R4, and R5) is provided in the Table. 5.2.

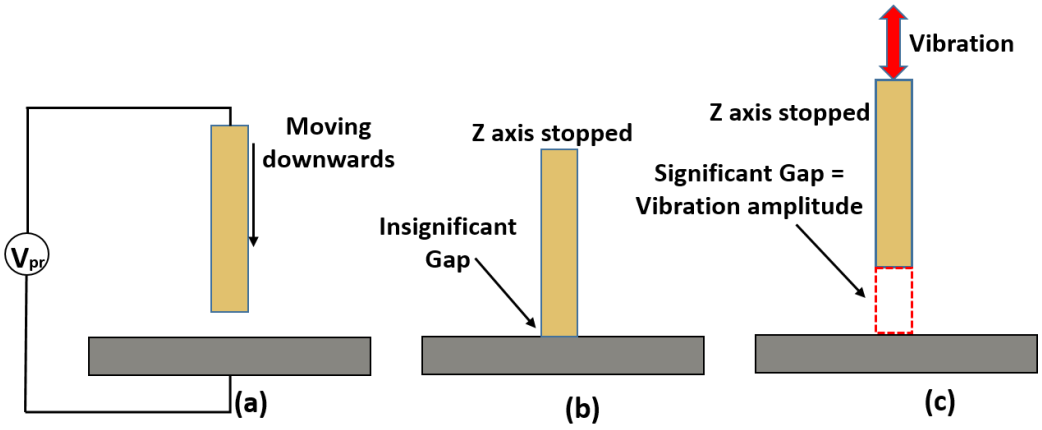

Figure 5.16 Amplitude measurement technique (a) Touch Probe (b) Without vibration (c) With vibration

Table 5.2 Vibration amplitude at the tip of the electrode using different input voltages

	Vibration amplitude at the tool tip (µm)				
Voltage (V)	**R 1**	**R 2**	**R 3**	**R 4**	**R 5**
90	5.2	4.8	5.3	5.2	4.9
100	5.3	5	5	5	5.1
110	5.4	5.1	5	5.1	5
120	5	5.1	5	5	5.1
130	4.9	5	5.2	5.2	5

Table 5.3 Experimental parameters and machining conditions of micro-EDM milling

Experimental conditions	
Parameters	micro-EDM milling
Workpiece (Anode)	Ti6Al4V plate of 2 mm thickness
Tool (Cathode)	Brass electrode of Ø1 mm
Process conditions	
Pulse on time	10 µs
Pulse off time	100 µs
Capacitance	1 nF and 10 nF
Open circuit voltage	100 V, 120 V, and 150 V
Feed Rate	1 µm/Sec, 1.5 µm/Sec, 2 µm/Sec
Vibration parameters	Frequency 20 KHz, Amplitude 5µm

Measured responses	
Offline responses	Surface roughness, MRR, TWR, Recast layer height,
Online responses	Percentage of the discharge pulses (contributing, semi- contributing, non-contributing)

5.3.3 Effect of vibration on the nature of discharge pulses

The main advantage of vibration assistance to the micro-EDM process is the increased frequency of useful discharges compared to the unassisted micro-EDM process. Figure 5.17 shows the nature of the discharge pulses during the micro-EDM milling with and without vibration assistance. An apparent difference was observed when the vibration was applied, as the delay time was reduced to almost negligible. This decrease in delay time, although marginal, increases the amplitude of the discharge current, which increases the discharge energy. The increase in the discharge frequency is attributed to frequent alterations in the discharge gap due to ultrasonic vibrations, which help effectively flush out the debris from the machining area to reduce frequent tool retractions. Hence, machining can be performed stable at high feed rates and input energy settings.

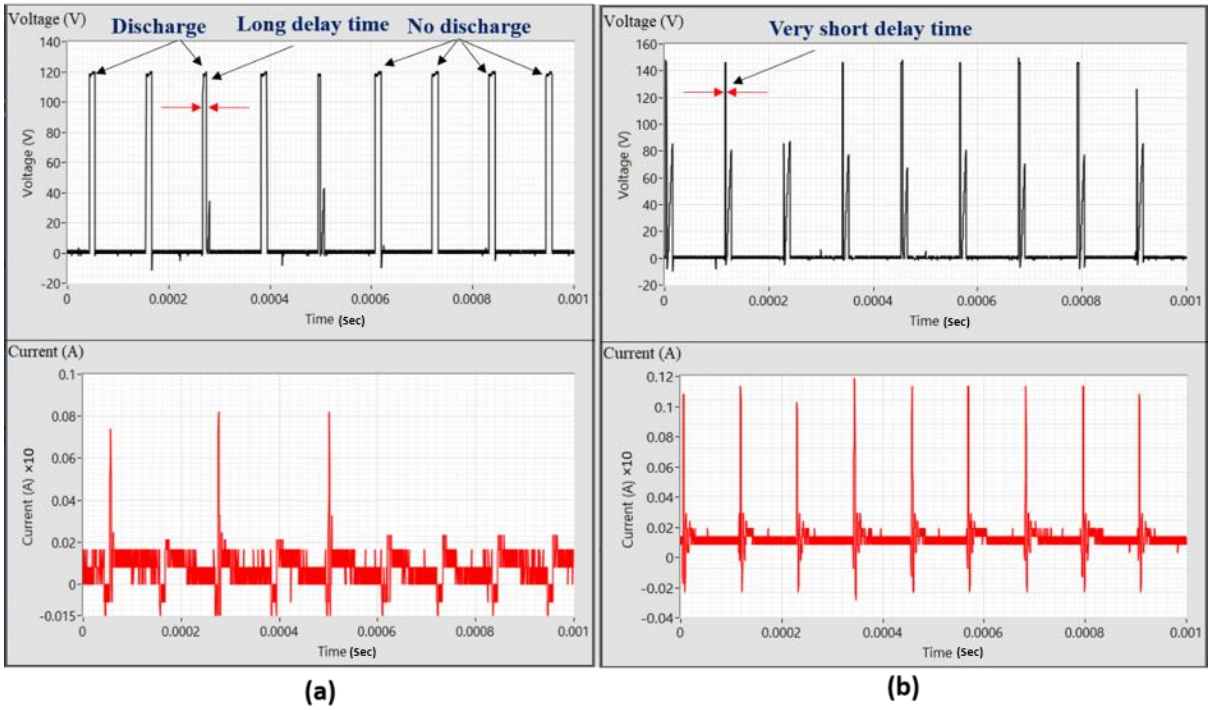

Figure 5.17 Nature of the discharge pulses (a) Without vibration (b) With vibration

Discharge pulses were continuously captured at all the parameters and simultaneously fed to the pulse discriminations system described in chapter 4. The percentages of three

different types of discharge pulses, i.e., contributing or normal (C), semi-contributing or effective (S), and non-contributing or arcing (N) at 100V and increasing feed rates, are shown in Figure 5.18. At both the capacitance settings, i.e., 1 nF and 10 nF, the vibration assistance to the tool electrode stabilized the micro-EDM process by increasing the percentage of contributing pulses while decreasing the proportion of the semi-contributing and non-contributing discharges. The percentage increase in the contributing pulses with vibration assistance reflects the effective flushing of the debris from the IEG, making it less contaminated at any given instance.

The probability of semi-contributing discharges is the most when the discharge occurs between the tool and the bridge of suspended debris instead of the workpiece surface, as illustrated in Figure 5.19. Vibration assistance to the tool electrode will give no room for the debris to hover around the IEG. It helps the dielectric quickly gain its original dielectric strength and decreases the probability of semi-contributing discharges. Increasing the feed rate also has an interesting effect on the nature of the discharging in the IEG. During the unassisted micro-EDM process, the percentage of contributing discharge decreases with an increase in the feed rate while the percentage of the semi-contributing and non-contributing pulses increases. The introduction of ultrasonic vibrations seems to steady the percentage of non-contributing pulses with rising feed rates and the percentage of semi-contributing pulses increases marginally. At higher capacitance, keeping the feed rate constant, broader and deeper craters were formed, allowing the sub-microscopic debris a little more space to evacuate. This may have contributed to a slightly increased percentage of contributing discharge. However, when the feed rate was increased at constant capacitance, the percentage of contributing discharges decreases, and the process loses its stability.

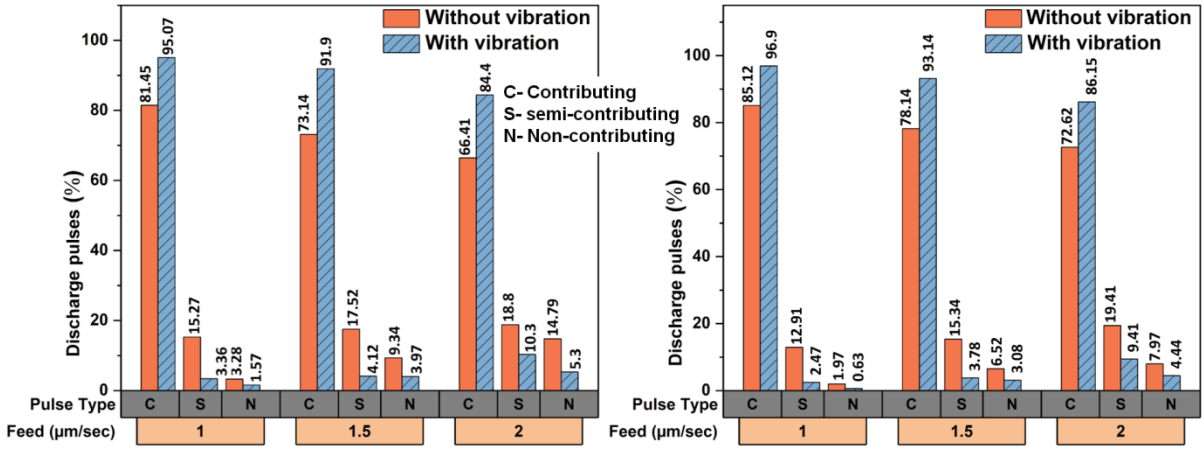

Figure 5.18 Percentage of different types of discharges with and without vibration at (a) 1 nF (b) 10 nF

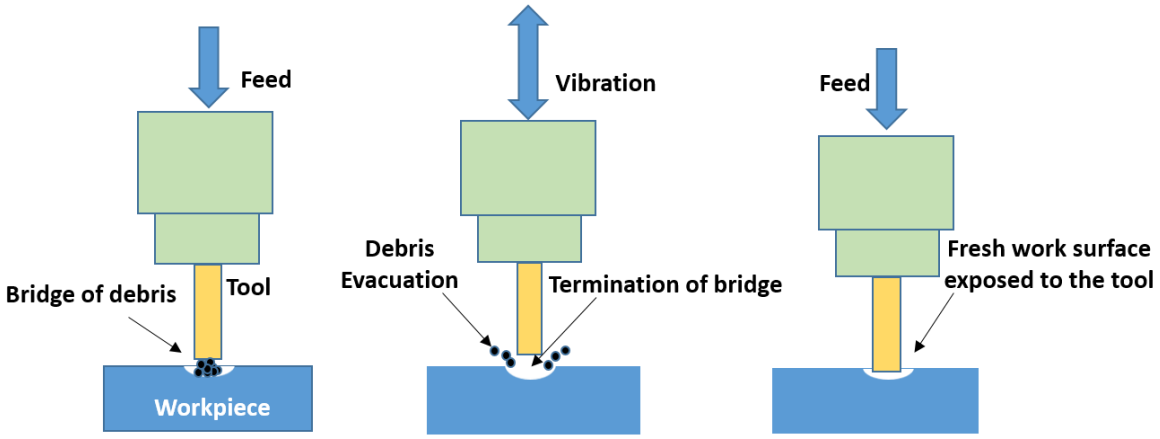

Figure 5.19 (a) Bridge of suspended debris (b) Vibration assisting in debris evacuation (c) Fresh tool-work interface for the subsequent discharge

5.3.4 Effect of vibrations on MRR and TWR

Figure 5.20 and 5.21 shows the variation of the MRR and TWR at different parametric settings with and without vibration assistance. An increase in the feed rate increases the TWR at all input voltages. Although an increase in the feed rate is expected to increase the MRR proportionately, the observed results for machining without vibrations indicate the flattening of the MRR curve. The reason behind the flattening of the MRR with increasing feed rate is the excessive arcing and short-circuiting phenomenon. As the tool moves downwards with a greater speed, there will be less time for debris to get evacuated than when the machining was performed at low feeds, producing arcing and short-circuiting. When the process was assisted with ultrasonic vibrations, the MRR significantly improved compared to the unassisted micro-EDM. Arcing and short-circuiting increased rapidly at the highest feed rate of 2 µm/Sec, as shown in Figure 5.18, also reflected on the MRR and tool wear graphs. Figure 5.20 and 5.21 shows a simultaneous rise in the TWR and flattening of the MRR at high feed rates, confirming the behavior of the discharge pulses categorized in Figure 5.18. The ultrasonic vibration assistance was observed to increase the MRR at both low-energy and high-energy settings.

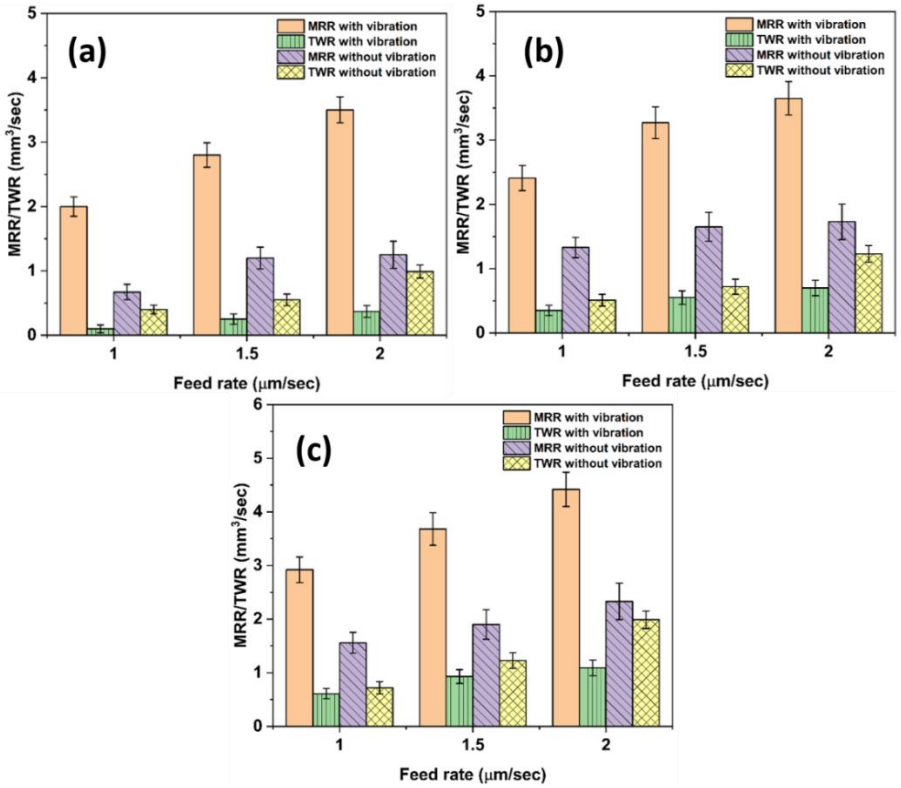

Figure 5.20 Variation in MRR and TWR with and without vibration at 1 nF and (a) 100 V, (b) 120 V, (c) 150 V

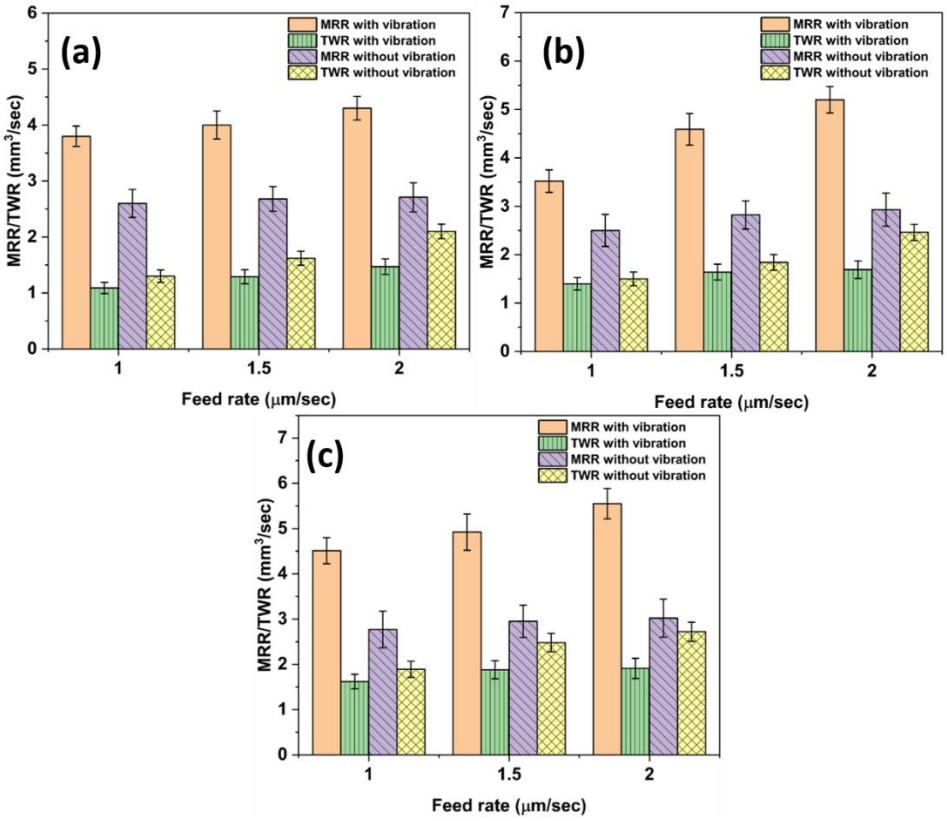

Figure 5.21 Variation in MRR and TWR with and without vibration at 10 nF and (a) 100 V, (b) 120 V, (c) 150 V

5.3.5 Effect of vibrations on dimensional accuracy and surface topographies

SEM images of the machined slots and the respective enlarged view of the slot surfaces are shown in Figure 5.22. The slot machined without vibration in Figure 5.22(a) exhibits dimensional inaccuracy and surface defects, which were negligible in the case of ultrasonic vibration assistance. An apparent difference in the re-solidification of the debris can be seen between the machined surfaces when the vibrations were introduced, as shown in Figure 5.22(c) and (d). The probability of the debris sticking to the machined surface was very low, and almost a clean micro surface can be seen when the machining was assisted with the vibrations in Figure 5.22(d). The periodic alteration of the discharge gap at high frequency facilitates the easy removal of the debris from the IEG without allowing them to stick. It produces a cleaner surface and is expected to be smoother. Figure 5.23 shows the SEM images of the tool electrode without and with vibration assistance. The micro slots were machined with precisely half of the diameter of the tool electrode so that the actual bulk tool wear and the frontal wear on the cylindrical surface of the tool electrode could be observed clearly. The frontal wear on the cylindrical surface of the tool electrode occurred when the debris coming up from the IEG was trapped between the workpiece's finished wall and the tool electrode's circumferential surface to produce arcing. This unwanted arcing not only deteriorates the finished wall of the micro slots, as shown in Figure 5.22 (a), but also erodes the tool's cylindrical surface, which later negatively affects the dimensional accuracy of the slots.

On the other hand, vibration assistance addresses this issue reasonably by reducing the actual wear and the less damaged frontal surface of the tool electrode. It can be seen that the depth of the tool wear reduces to 157 µm from a very high 208 µm when the slot was machined using ultrasonic vibration, increasing the dimensional accuracy. The extent of tool wear on the outer surface of the tool is also very high for unassisted micro-EDM compared to the same in the case of vibration assistance. The benefit of ultrasonic vibrations on the tool wear can also be seen in the TWR graph of Figure 5.20. A comparison of the TWR with and without vibration shows that the micro-EDM suffers a massive amount of tool wear without vibration. The vibration assistance showed a significant reduction in the TWR at all the parametric settings.

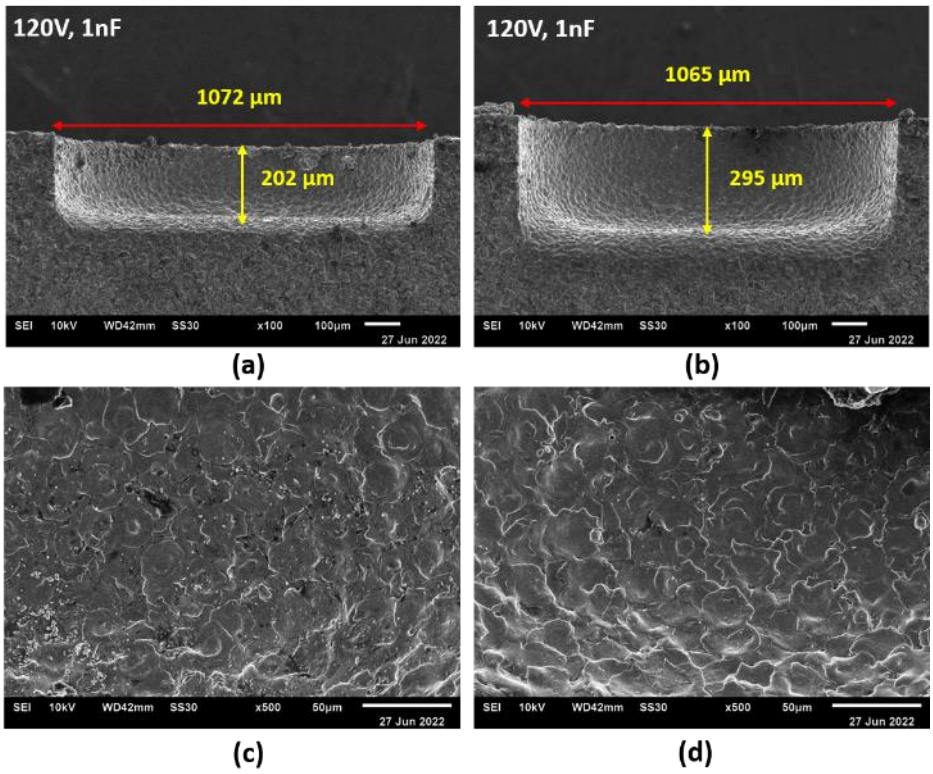

Figure 5.22 SEM images and enlarged views of the machined slot at 100 V, 1nF (a) &(c) without vibration (b) & (d) with vibration

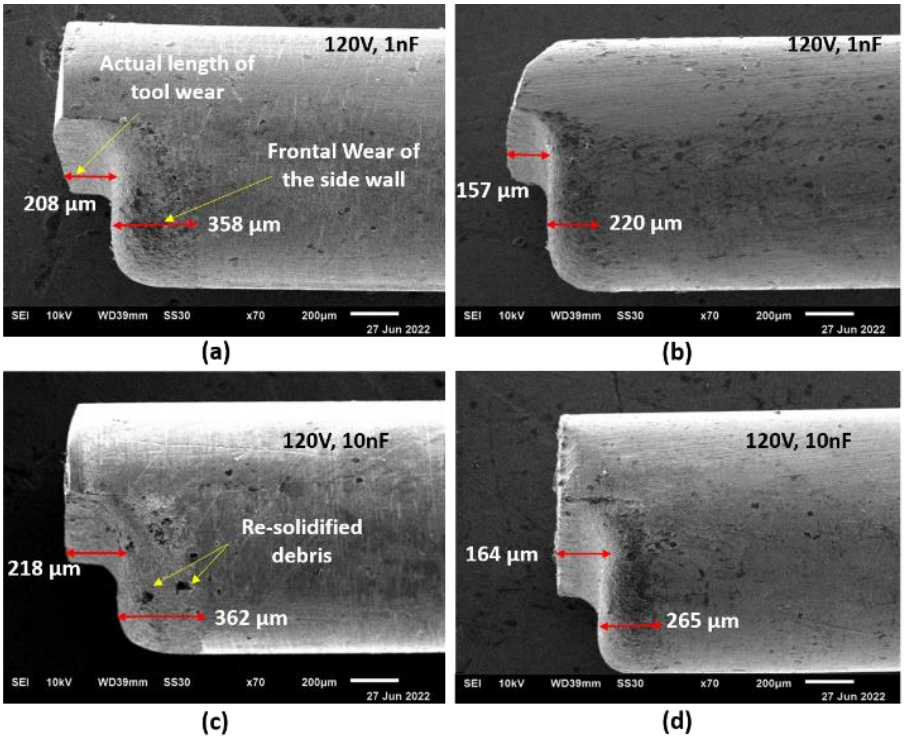

Figure 5.23 SEM images of the tool electrode (a) & (c) without vibration (b) & (d) with vibration

5.3.6 Effect of vibration on recast layer formation

Recast layer formation is an inherent phenomenon during the micro-EDM process due to the re-solidification of the part of molten metal formed at the end of each discharge. The SEM images showing the thickness of the recast layers formed at different input energy settings with and without the vibration assistance are shown in Figure 5.24. An apparent decrease in the recast layer's thickness was observed when the micro-EDM process was assisted with ultrasonic vibrations. The recast layer formed with vibration assistance was smaller in thickness and observed to be smoother compared to that without vibration assistance. The reason behind the smoothness of the recast layer with vibration assistance may be the induced cavitation effect, which helps form a smoother and denser layer without debris adhesion. The intense ultrasonic vibration produces cavitation bubbles in the small IEG, which collapses to form high-velocity liquid-vapor jets to remove the molten material more effectively. In addition, the ultrasonic pressure increases the component of the normal force on the molten metal pool to counteract the tangential shear stresses developed inside the melt pool due to temperature gradients and forces more amount of metal to flow out of the molten pool. As a result, less amount of metal resolidifies at the edges of the crater and gets flushed away in the form of debris to produce a thinner and smoother recast layer. The recast layer without vibration contains irregularities and voids that would harm the surface's hardness and increase the surface's roughness. The variation of the recast layer at all the parametric settings is shown in Figure 5.25. It can be observed that the recast layer showed a strong dependence on the feed rate compared to the voltage. When the feed rate was increased, keeping other parameters constant, the IEG remained small as it is a voltage function, and debris evacuation became difficult. This increases the arcing phenomenon and the abnormal discharges, contributing to a thick and broken recast layer. The recast layer without vibration was proportional to the energy settings, as the increase in the capacitance has almost doubled the thickness of the recast layer at most of the energy settings. The reason behind this is as the capacitance was increased from 1 nF to 10 nF, a ten-time increase in the input energy was realized in the IEG, which melts quite a lot of material compared to that at low capacitance settings. The introduction of vibrations was effective at low capacitance and equally good at high capacitance as the impact of vibration does not allow the re-solidified metal to get stuck at the surface of the workpiece, promoting the decrease in the thickness of the recast layer.

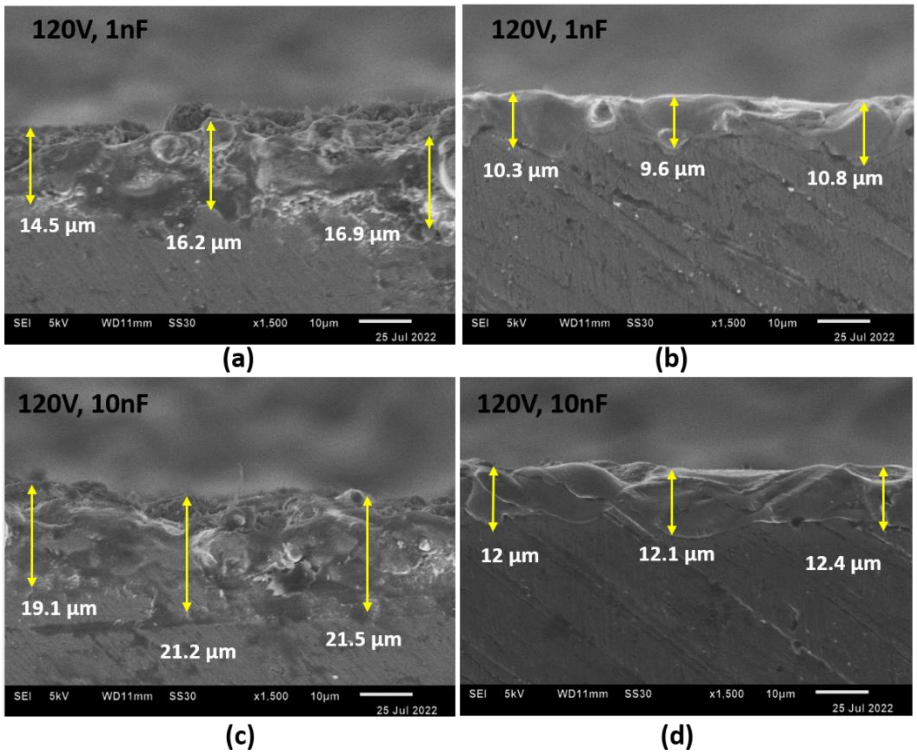

Figure 5.24 SEM images of the recast layer (a) & (c) without vibration (b) & (d) with vibration

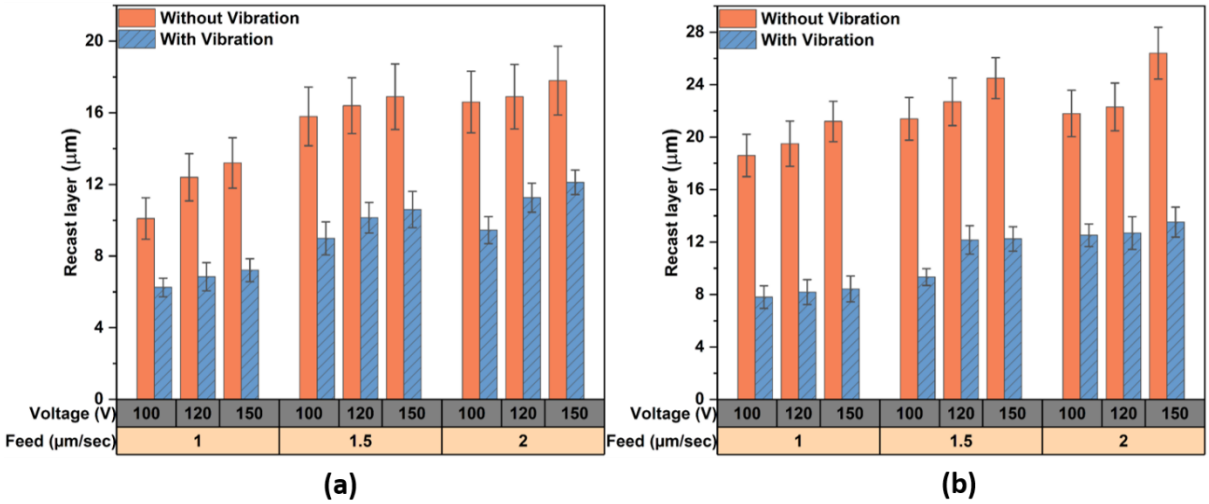

Figure 5. 25 Variation in recast layer thickness with and without vibration at (a) 1 nF (b) 10 nF

The optical images of the machined surfaces at different capacitances with and without vibration assistance are shown in Figure 5.26. The machined surface, without vibration, contained a large concentration of re-solidified debris that was deposited during the machining, leading to a rough and rugged surface. In contrast, the finished surface with ultrasonic vibrations appears clean without the deposition of much sub-microscopic dirt and re-solidified molten metal. Similar observations were reported by Unune et al. [170] while visualizing the

cross-section of the micro-holes fabricated with and without vibration assistance. The discharge craters were more significant in diameter at higher capacitance settings as the discharge energy increased rapidly. As a result, the surface roughness was higher compared to low capacitance settings. The reason behind this could be the sizeable molten metal pool formation at higher capacitance, which require effective flushing for the instant removal of the debris. The application of the vibration appeared to have almost removed the large re-solidified areas, as shown in Figure 5.26(b) and (d).

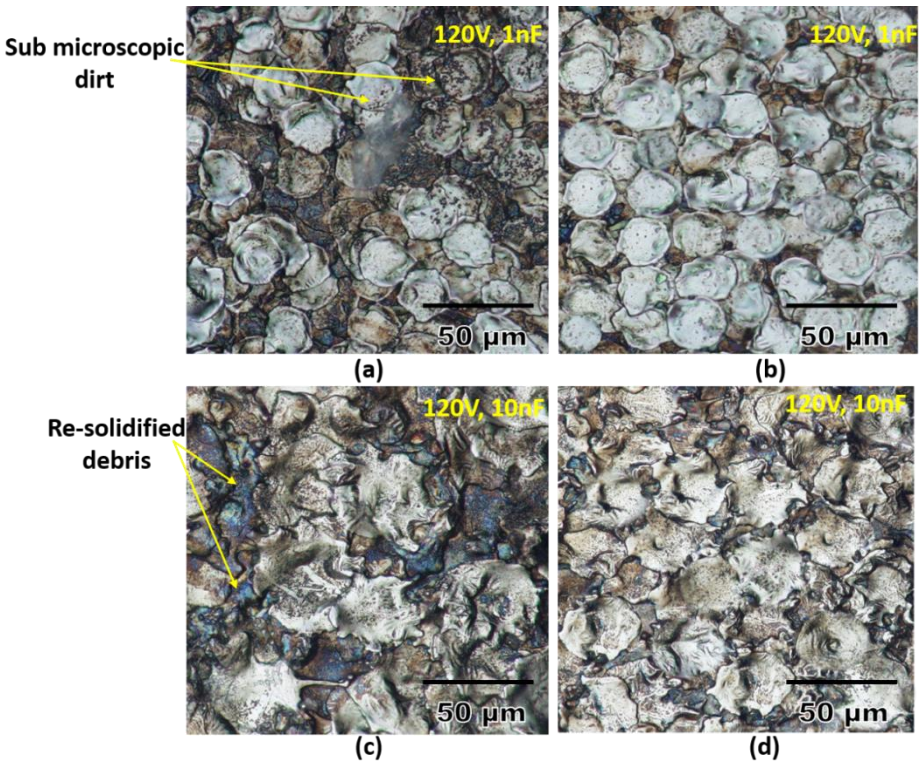

Figure 5.26 Optical images of the machined surfaces (a) & (c) without vibration (b) & (d) with vibration

5.3.7 Effect of vibration on the surface roughness

Surface roughness is the most critical outcome to assess the feasibility of the micro-EDM process, as the majority of the components at the micro scale require a superior surface finish. 3D surfaces with roughness profiles of the machined slots with and without vibration assistance are shown in Figure 5.27. At 120 V and 1 nF settings, an Ra value of 1.42 µm was observed without vibration compared to 0.33 µm with vibration assistance, indicating a four-time decrease in the surface roughness. It can be seen that the machined surface without vibration contains more red peaks, which can be attributed to the re-solidification of the debris as well as the formation of the recast layer. The machined surface with vibrations appeared flatter and contained fewer abnormalities, as shown in Figure 5.27(b). The roughness of the

micro-EDM milled slots with and without vibration assistance at all the parametric settings is shown in Figure 5.28. At low feed rates, the machined surface with vibration assistance showed an approximate four-time decrease in the Ra value at all voltage and capacitance settings. As expected, the surface roughness was proportional to the voltage and capacitance settings, with the effect of capacitance more dominant than the voltage. This is because surface roughness measures the height of peaks and valleys from a mean height, and deeper craters would result in rougher surfaces. Vibration assistance at high capacitance creates deeper craters. The high frequency of the discharging and cavitation effect with vibration produces a smoother surface compared to that without vibration assistance.

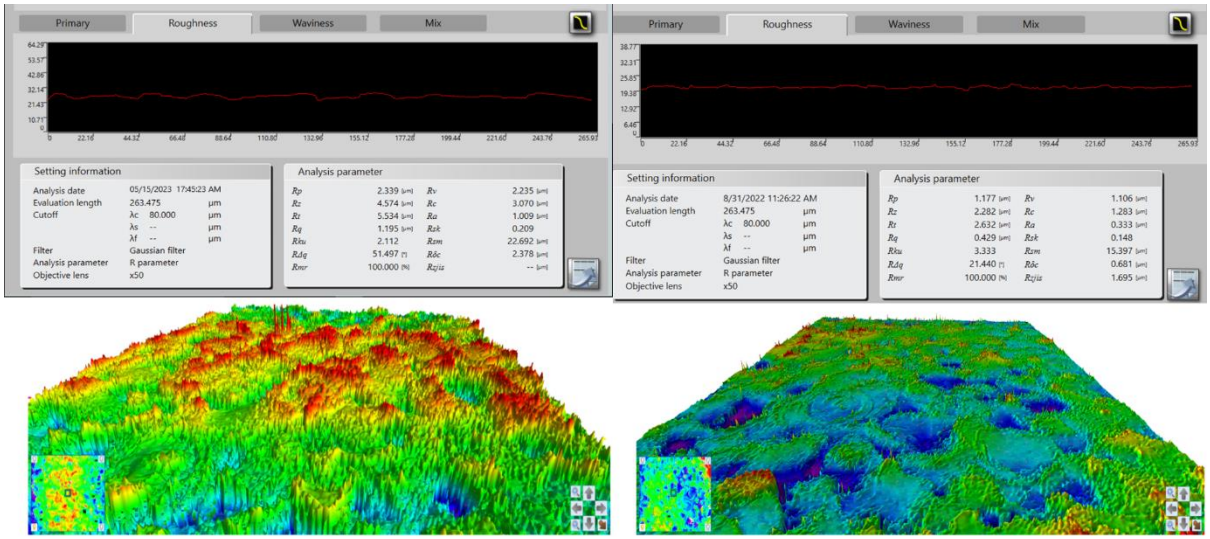

Figure 5.27 Variation in surface roughness and Ra value at 120V, 1nF (a) with vibration and (b) without vibration

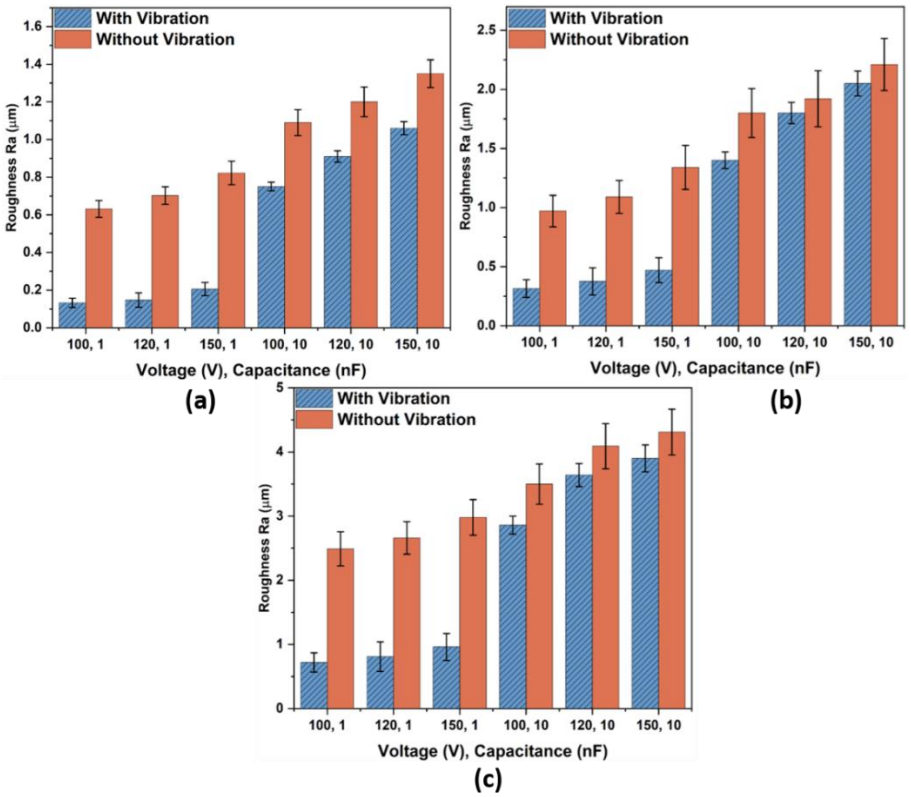

Figure 5.28 Variation in surface roughness with and without vibration at (a) 1 µm/Sec (b) 1.5 µm/Sec (b) 2 µm/Sec feed rate

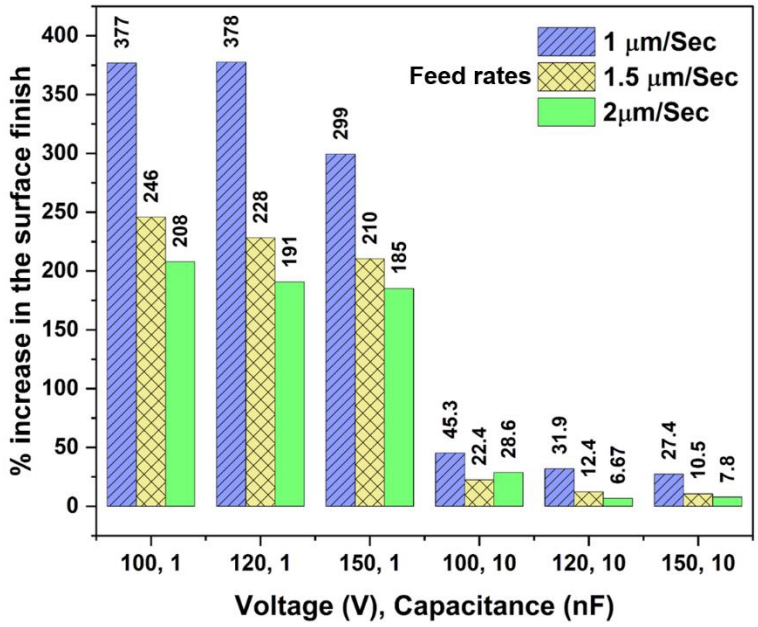

Figure 5.29 Percentage increase in surface finish after vibration assistance at different parameters

5.4 Vibration-assisted Micro-EDM Drilling

The issue of low MRR and poor surface finish is more prominent during micro-EDM drilling, especially when drilling blind micro holes with high aspect ratios. The process suffers

frequent tool retractions mainly due to the accumulation of unflushed debris in the deeper holes resulting in a frequent arcing phenomenon. Vibration assistance to micro-EDM drilling has proven contributions to the MRR and surface finish enhancement, but the intrinsic information on discharge pulses variation due to the vibration is unclear. This section provides a comparative study to understand the nature of discharge pulses during unassisted and ultrasonic vibration-assisted micro-EDM drilling. The discharge pulses are acquired at a sufficiently high sampling rate using NI LABVIEW-based data acquisition through a pulse monitoring system (PMS). The developed PMS is simultaneously used to estimate the real-time discharge energies of individual pulses and their histograms with the machining progress. The acquired information from the developed PMS is used to justify the variations in discharge energy, discharge frequency, surface roughness, and accuracy with increasing machining depth.

5.4.1 Experimental setup

Micro-EDM experiments were performed at the center of the two Ti6Al4V plates joined together with the dimensions of 50x20x2 mm in length, width, and thickness, respectively. The two titanium alloy plates were cut from a single plate using wire EDM to make a perfect joint between the identical edges, as shown in Figure 5.30. After the experiment, the two plates were detached for the SEM analysis to measure the quality and accuracy of the drilled micro holes. Micro-EDM drilling experiments were performed using a controlled RC-based machine, Hyper 15 (Make: Synergy Nanosystems), with a 300µm diameter tool electrode made of tungsten with straight polarity (Tool –ve, work +ve). The experimental setup with all the sensors, the data acquisition system, and the vibration-assisted tool holder used in the previous section is utilized in the current study. The close view of the machining setup is shown in Figure 5.31. The experimental conditions with the input parameters and the measured machining responses are shown in Table 5.4.

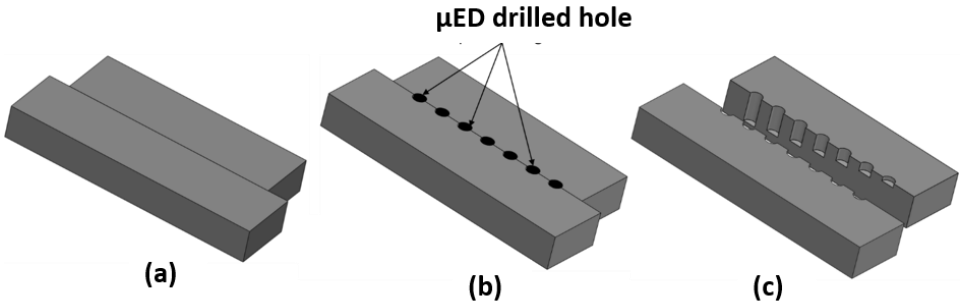

Figure 5.30 Schematic representation of workpiece (a) before machining, (b) after machining, and (c) after splitting the workpiece

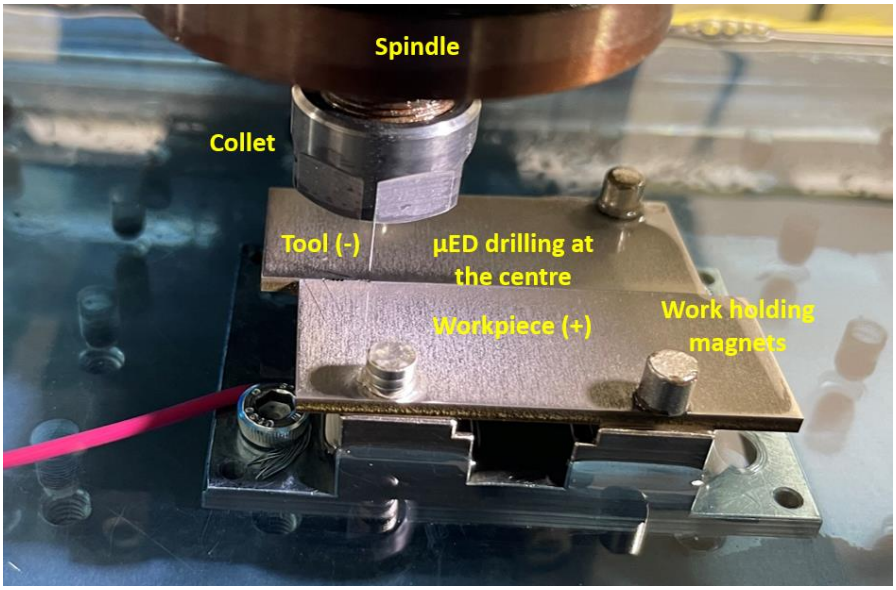

Figure 5.31 Pictorial view of the machining zone

Table 5.4 Experimental parameters and machining conditions of micro-EDM drilling

Experimental conditions	
Parameters	micro-EDM drilling
Workpiece material (Anode)	Titanium plates (2 nos.) of 2 mm thickness
Tool material (Cathode)	Tungsten electrode of Ø300µm
Number of experiments	20 experiments at 4 settings Set 1: capacitance1nF and voltage 100V Set 2: capacitance10nF and voltage 100V Set 3: capacitance1nF and voltage 120V Set 4: capacitance10nF and voltage 120V
Process conditions	
Transistor on time	10 µs
Pulse off time	100 µs
Capacitance	1 nF and 10 nF
Open circuit voltage	100V and 120V
Vibration parameters	Frequency 20 KHz, Amplitude 5 µm
Measured responses	
Offline responses	Overcut in depth, surface roughness.
Online responses	1. Frequency of discharge pulses 2. The energy of each discharge pulse, Total energy, and Average energy of pulses

5.4.2 Effect of vibrations assistance on the machining outcomes

This section describes the effect of ultrasonic vibrations on the discharge frequency, discharge energy, and surface quality of the micro-EDM drilling samples. Figure 5.32 shows the current and voltage waveforms during micro-hole drilling with and without vibration assistance. A total machining duration of 1000 microseconds was captured and compared for the actual discharge and idle pulses. It can be seen that during the vibration-assisted micro-EDM, the frequency of the normal discharges per unit time is higher than the same during unassisted micro-EDM. It has also been observed that the peak current during the normal discharge is slightly greater during the vibration assistance. The reason behind the increase in the frequency of discharge is the effective and immediate flushing of the debris from the machining area, which decreases the tool retraction time. Hence, the frequency of idle or non-productive pulses decreases. A comparison of the discharge frequency at various energy settings and different depths of the machined holes is shown in Figure 5.33. The discharge frequency showed an increasing trend with the increase in machining depth. The reason behind this increase is the debris accumulation in the IEG, resulting in frequent discharges. The discharge frequency was lower when machining was performed with higher capacitance, i.e., at 10nF. This is obvious as the capacitor takes more time to charge, and the high energy discharge results in a large amount of debris that also consumes some time to flush out. This results in decreased discharge frequency. A clear difference is observed in the discharge frequency when the vibrations were introduced in the IEG at all input energies and depths of the machined holes. When the machining was performed at deeper and deeper depths, the curve of the discharge frequency became flattered for unassisted micro-EDM, indicating that it was becoming difficult to evacuate the debris. When the machining was assisted with the ultrasonic vibrations, the curve of the discharge frequency maintained the increasing trend, indicating the effective removal of the debris from the machining area.

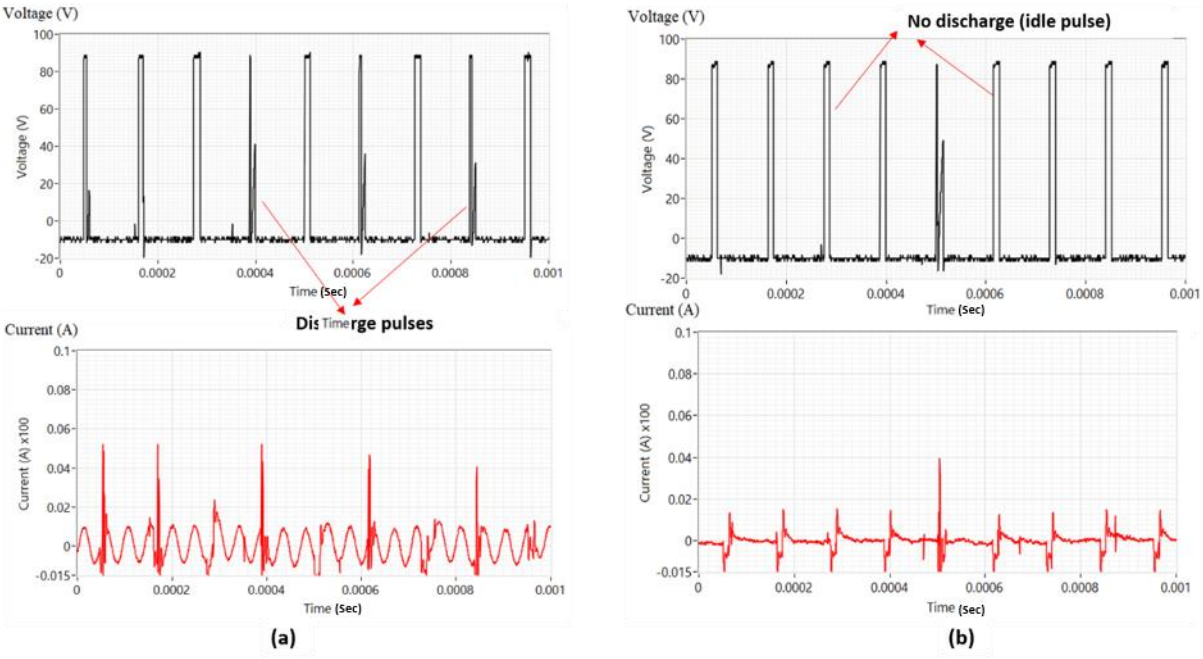

Figure 5.32 Nature of the discharge pulses (a) With vibration (b) without vibration

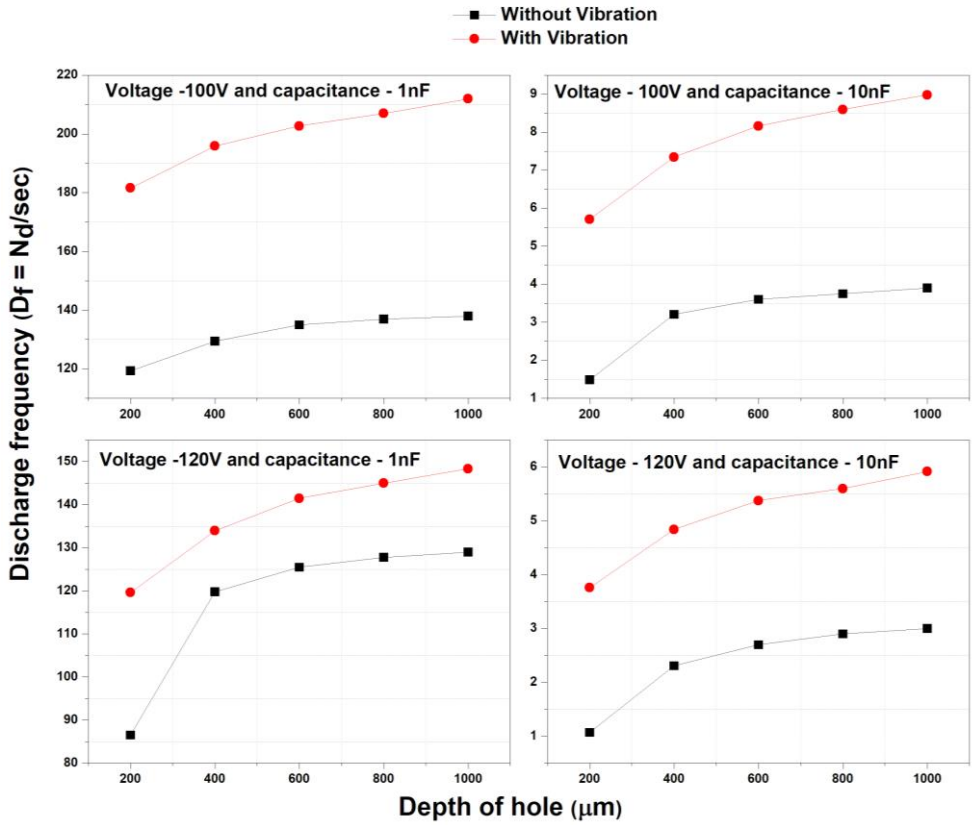

Figure 5.33 Variation of the discharge frequency with the depth of the machined hole

The discharge energy is the most important indicator to assess the efficiency of the micro-EDM process, as it is responsible for the material removal. The discharge energy responsible for material removal differs from the input energy as various losses, such as the

heating of the electrodes and heat loss in the surrounding dielectric, occur. The effect of the ultrasonic vibration assistance on the discharge energy of the pulses is shown in Figure 5.34. The discharge energy depends not only upon the input parameters, such as voltage and capacitance but also on the effective pulse on time and the condition of the IEG. It can be seen that the vibration assistance increases the discharge energy at all input energy settings. The reason behind this can be seen by looking closely at the behavior of a single discharge pulse, as shown in Figure 5.35. It shows that the delay time before the actual discharge is much shorter in the case of vibration assistance than the unassisted micro-EDM. This instant discharge is due to the effect of vibration, and it not only increases the current pulse's amplitude but also gives the capacitor some extra time to get ready to charge for the next cycle fully. Whereas in the case of unassisted micro-EDM, the delay time is much more due to the tool retraction. The reason is the contaminated IEG, which suppresses the current amplitude and increases the possibility of an idle pulse in the next cycle.

The low decrement in the discharge energy per pulse with the machining depth during vibration assistance shown in Figure 5.34 can be understood with respect to the debris accumulation in the IEG. When the machining was performed at more significant depths, the accumulation of debris in the IEG and between the tool's circumference and the finished wall of the drilled hole was increased. This increase in debris accumulation leads to the contamination of the discharge gap, resulting in lower discharge energies per pulse. When the machining was assisted with ultrasonic vibrations, the concentration of the debris at the IEG decreased, leading to a decrease in the contamination of the IEG, and the dielectric regained its strength instantly to increase the discharge energy per pulse. The difference in the discharge energy per pulse with and without vibration assistance was higher for 100V than that at 120V. It means the vibration assistance was more beneficial at 100V compared to 120V. The reason behind this is the height of the IEG, which is directly proportional to the applied voltage. Hence, due to low IEG at 100V, debris accumulation was more significant, and vibration assistance proved more beneficial.

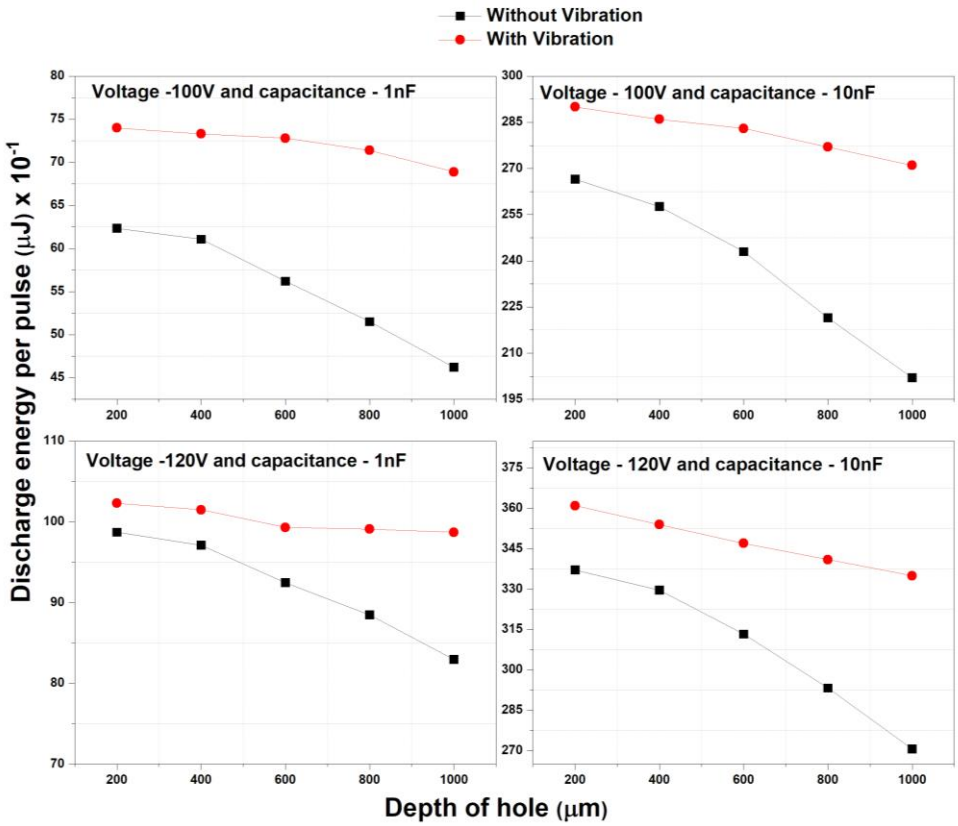

Figure 5.34 Variation of the discharge energy with the depth of the machined hole

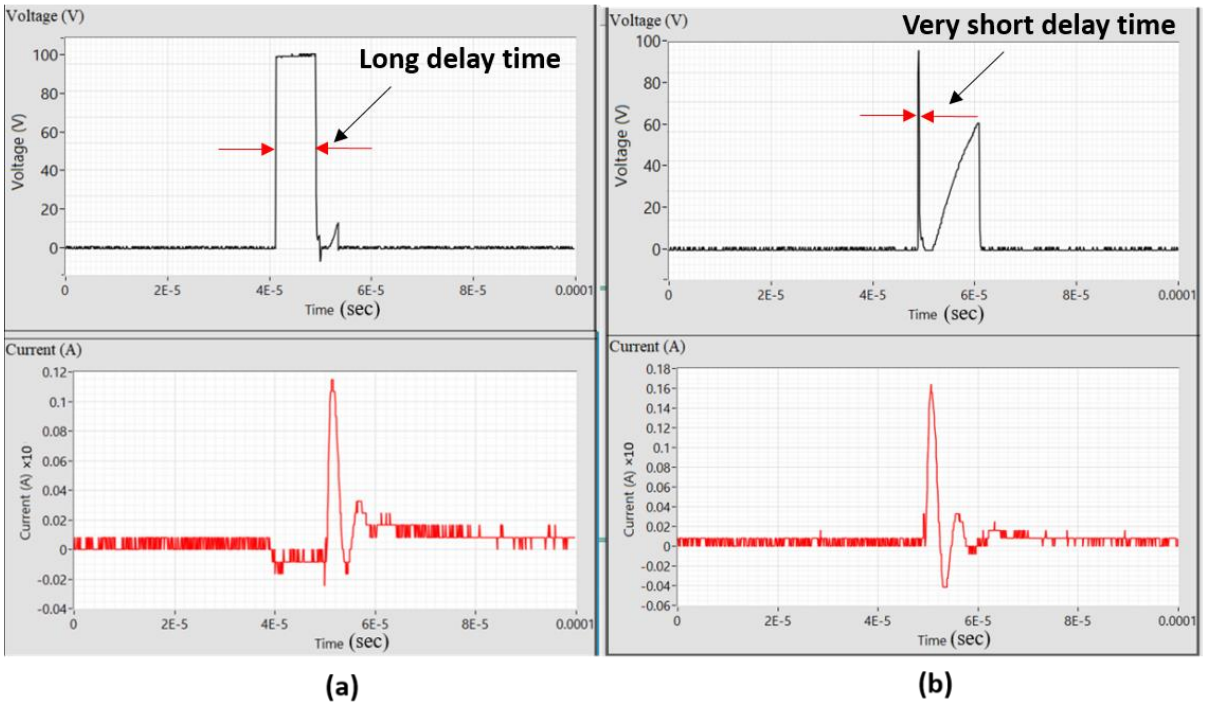

Figure 5.35 Nature of single discharge pulses (a) Without vibration, (b) with vibration

The histograms depicting the variation of the number of discharges with their energy content for 100 V and 1 nF input settings are shown in Figure 5.36. It shows that the vibration

assistance has increased the average energy per discharge at the beginning and end of the micro-EDM drilling process. A considerable decrease in the discharge energy was observed when the machining was done in the depth of the holes in case of unassisted micro-EDM due to the contamination of the discharge gap. In contrast, this decrease in the discharge energy was insignificant during the vibration-assisted micro-EDM showing an increase in the stability of the process.

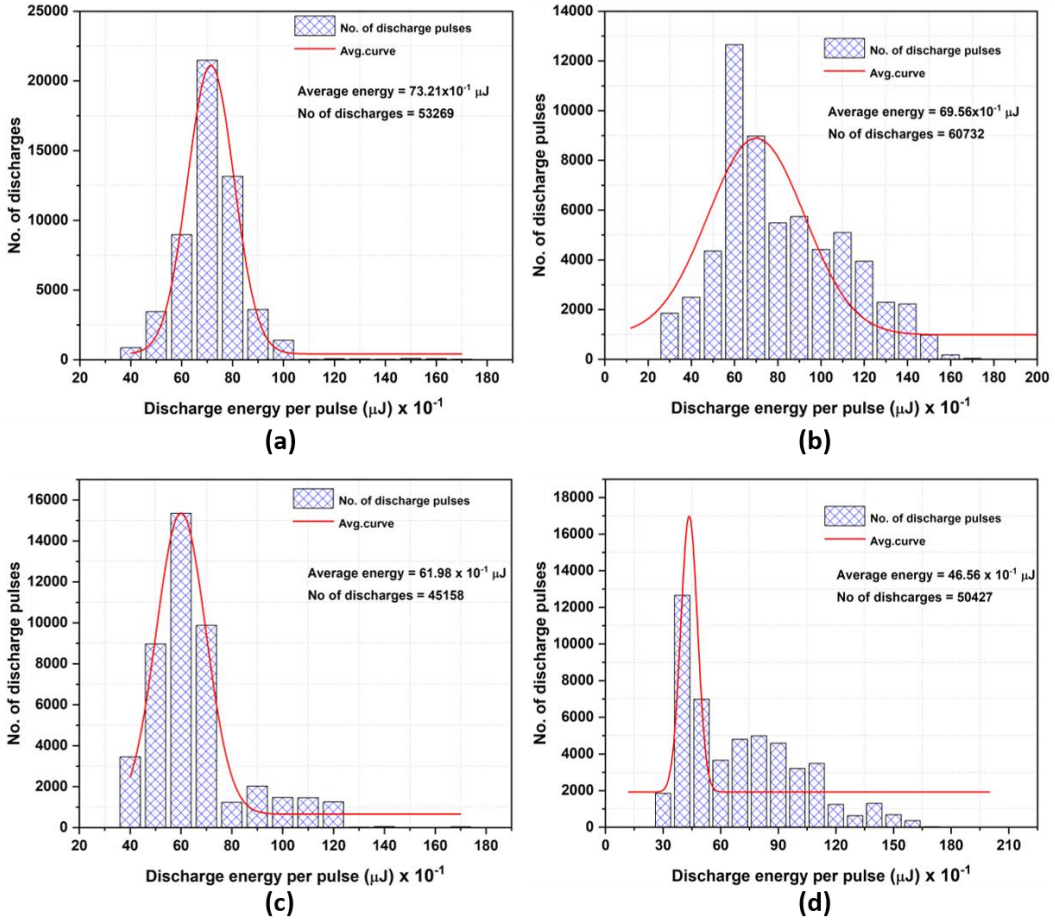

Figure 5.36 Histograms of the discharge energy (a) at the beginning With vibration, (b) at the end with vibration pulses, (c) at the beginning Without vibration, (b) at the end without vibration

SEM analysis was carried out to understand the effect of the ultrasonic vibrations on the accuracy and the machined surface quality, as shown in Figure 5.37 for the 120V, 10nF experiment. A clear difference was observed in the SEM images of the drilled micro holes between the unassisted and vibration-assisted micro-EDM. The micro-holes machined with vibration assistance showed good accuracy and surface quality. A closer look at the wall surface of the holes with vibration reveals that effective flushing and high discharge frequency prevent the debris from sticking. Without vibration, the molten metal re-solidifies on the freshly machined surface, decreasing the surface quality. The frequent arcing phenomenon during the

unassisted machining increases the tool wear, adversely affecting the micro holes' dimensional accuracy as the holes become tapered and less accurate in depth. A comparison between the unassisted and vibration-assisted micro-EDM for the percentage error with increasing depth of the machined hole at different energy settings is shown in Figure 5.38. It shows that the error in depth is less in the case of vibration assistance at all energy settings. The percentage error shoots up for unassisted micro-EDM at more significant depths due to the difficulty in debris removal. In comparison, it increases steadily for vibration-assisted machining. The error magnitude was more significant for the high energy settings than other input energy settings.

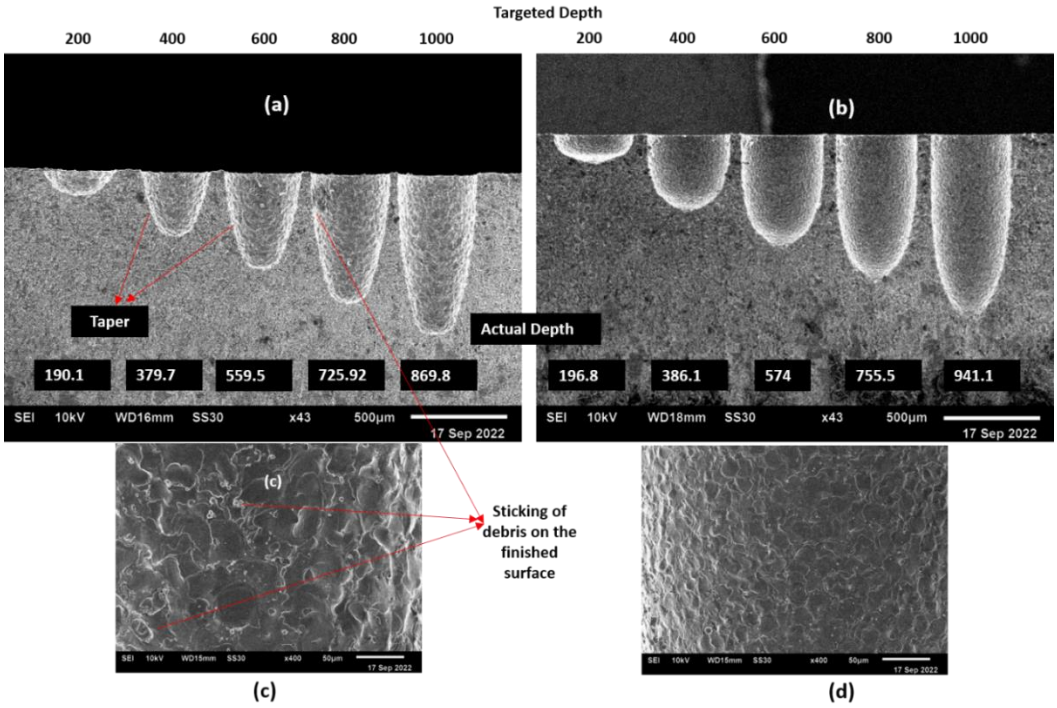

Figure 5.37 SEM images of the fabricated micro holes at 120V, 10nF (a) without vibration (b) with vibration assistance (c) machined surface without vibration (d) machined surface with vibration assistance

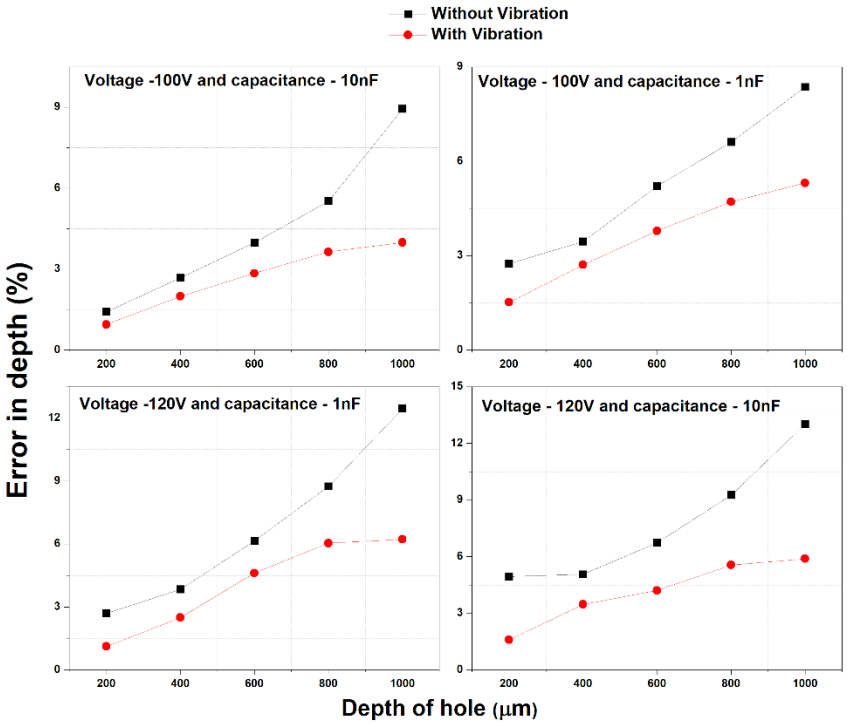

Figure 5.38 Variation of the percentage error in depth with the depth of the machined hole

The roughness of the walls of the machined surface was measured to explain the effect of vibrations on the surface quality, as shown in Figure 5.39. It can be observed that the machined surface without vibration is rougher compared to the surface machined with ultrasonic vibration assistance. The roughness increases due to the re-solidification of the molten metal from the freshly machined surface and the re-solidified debris on the machined surface. When the process was assisted with vibrations, the collapse of micro-jets on the molten metal pool due to the cavitation effect helps enhance debris flushing from the freshly machined surface. A comparison of the Ra values at all input energy settings is shown in Figure. 5.40. It can be seen that the vibration assistance substantially decreased the surface roughness. The effect of vibrations was more pronounced at high capacitance settings by an approximate 8-time decrement in the Ra value. The surface finish was severely hampered when machining was performed at 10 nF without vibration due to the resolidification of the debris from a larger melt pool formed by high capacitance. Vibrations assistance left no room for the deposition of the resolidified debris; hence, a substantial improvement in the Ra was observed.

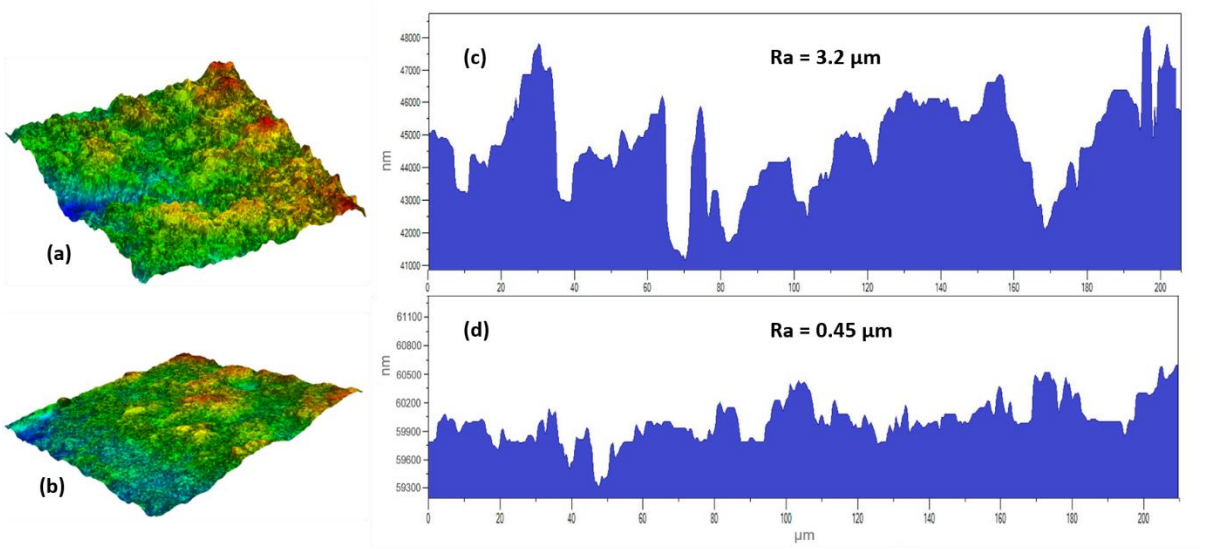

Figure 5.39 Surface profile of the drilled surface for 120V, 10nF (a), (c) without vibration (b), (d) with vibration assistance

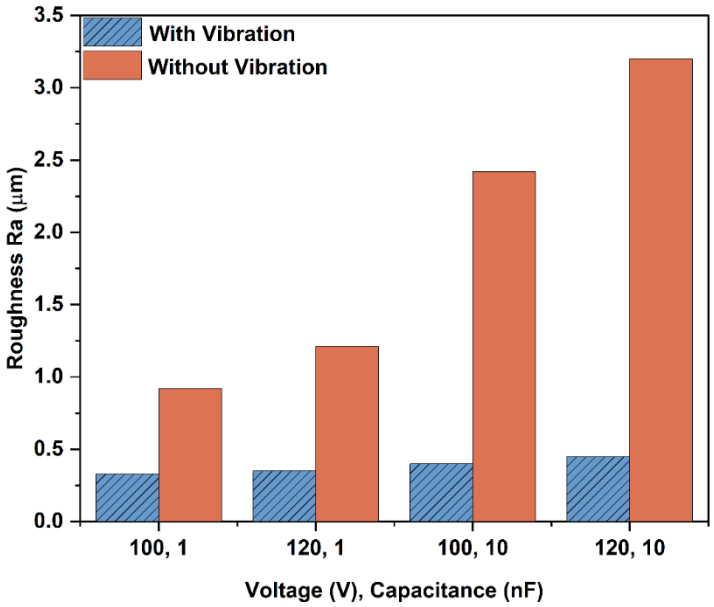

Figure 5.40 Variation in surface roughness with and without vibration at all input parameters

5.5 Summary

Experimental investigations on the vibration assistance to the micro-EDM are explained in this chapter. First, a low-frequency vibrating tool holder is developed as a preliminary setup to explain the effect of low-frequency vibrations on the micro-EDM. The tool holder works on the principle of driven harmonic vibrations controlled by an eccentric motor. Micro-EDM milling and reverse micro-EDM experiments were performed without vibration and at 100 Hz and 150 Hz with vibration assistance to study the effect of vibration on the machining outcomes. Micro-EDM milling showed a 48.2 % reduction in machining

time, while the reverse micro-EDM showed a 57 % reduction with vibration assistance. Although the MRR was enhanced, the vibration assistance resulted in poor straightness of the micro rods. Given the high frequency of the discharge pulses in micro-EDM, an ultrasonic vibration-assisted tool holder is developed to overcome the shortcomings of the low-frequency setup. The micro-EDM milling process was then assisted with ultrasonic vibrations of 20 kHz frequency and 5 µm amplitude to the tool electrode for machining micro slots in Ti6Al4V material. The discharge pulses were captured continuously during the machining progress, and the following conclusions can be made after measuring the online and offline responses.

- The non-productive time during the micro-EDM milling process decreased significantly as the discharge frequency improved, and the percentage of normal discharges increased by 19 % with vibration assistance. A very little delay time before the discharge was observed with the introduction of vibrations, increasing the energy content of the discharges.
- The arcing phenomenon was more sensitive toward the increasing feed rates, and the vibration assistance stabilized it by increasing the percentage of contributing and semi-contributing discharges. Hence machining can be performed stable at high feed rates with vibration assistance.
- The frequent alterations of the discharge gap due to vibration assistance proved beneficial, increasing the MRR by a maximum of 35 % among all parametric settings. The rate of tool wear increased abruptly at high feed rates. It resulted in poor dimensional accuracy, which the vibration assistance took care of, and resulted in stabilized tool wear.
- Surfaces machined with the vibration assistance were smoother, with an approximate four-time decrease in the Ra value. The accumulation and re-solidification of the debris were resolved to a reasonable extent.
- A comparatively thin and uniform recast layer was formed while machining with vibration assistance, while the recast layer was thicker, rugged, and broken without vibration assistance. The intense cavitation effect due to the introduction of vibrations was responsible for the disruption and reduced recast layer thickness.

This final section pesented the benefits of vibration assistance to the micro-EDM drilling process. Following are the important observations.

- A significant increase in the discharge frequency and the discharge energy was observed with the ultrasonic vibrations at all input energy settings due to the less contamination and effective flushing of the IEG.
- The micro-holes fabricated with the vibration assistance were less tapered and produced a good surface finish compared to the unassisted micro-EDM process. A maximum decrease of 7.14% in the percentage error in depth among all sets of experiments with the vibration assistance further indicates the enhanced discharging phenomenon and increased stability of the process.
- Vibration assistance to the micro-EDM process was beneficial, with an 18% increase in the discharge energy. Ultrasonic vibration assistance reduces surface roughness at high-energy settings from 3.2 µm to 0.45 µm.
- The effect of vibrations was more pronounced at high capacitance settings than at low capacitance, with an approximate 8-time decrement in the Ra value.

Chapter 6

Modeling of crater formation during Micro-EDM

6.1 Introduction

The extensive experimentation with the vibration assistance to the micro-EDM process showed a definite improvement in the machining performance and reduced the roughness and recast layer formation. As the material removal in the micro-EDM process is a cumulative effect of the individual discharges, a single discharge study would be crucial in understanding the reasons behind the improved machining performance. The intense ultrasonic vibration produces cavitation bubbles in the small IEG, which collapses to form high-velocity liquid-vapor jets to remove the molten material more effectively. In addition, the ultrasonic pressure increases the component of the normal force on the molten metal pool to counter act the tangential shear stresses developed inside the melt pool due to temperature gradients and forces more amount of metal to flow out of the molten pool. As a result, less amount of metal resolidifies at the edges of the crater and gets flushed away in the form of debris to produce a thinner and smoother recast layer. This chapter aims to demonstrate the modeling of the single discharge crater formation during the micro-EDM for Ti6Al4V material. The simulated crater geometry is validated using the investigations of the single discharge craters at different input parameters.

6.2 Modeling of Crater Formation

With the help of the plasma parameters obtained through modeling the plasma channel in Chapter 3, crater formation during vibration assistance can be simulated. A 2D axis-symmetric model for the crater formed during the micro-EDM is developed in the COMSOL Multiphysics finite element software, as shown in Figure 6.1. The following section contains the assumptions, governing equations, and experimental details.

6.2.1 Basic assumptions

Figure 6.1 shows the numerical model and different boundary conditions applied to the calculation domain. Some of the critical assumptions are as follows.

1. A single discharge is considered in the simulation to compare it with the experimental crater formation.
2. The molten metal pool is assumed as laminar, incompressible, and transient.
3. Heat flux distribution obtained from the plasma model is applied on the top free surface.

4. Deformed geometry and moving mesh methods are used for simulating the material removal.
5. The influence of the magnetic field and ionization of the metal vapor are not considered.
6. The conduction mechanism dissipates the heat inside the workpiece while radiation and convection are considered at the top surface.

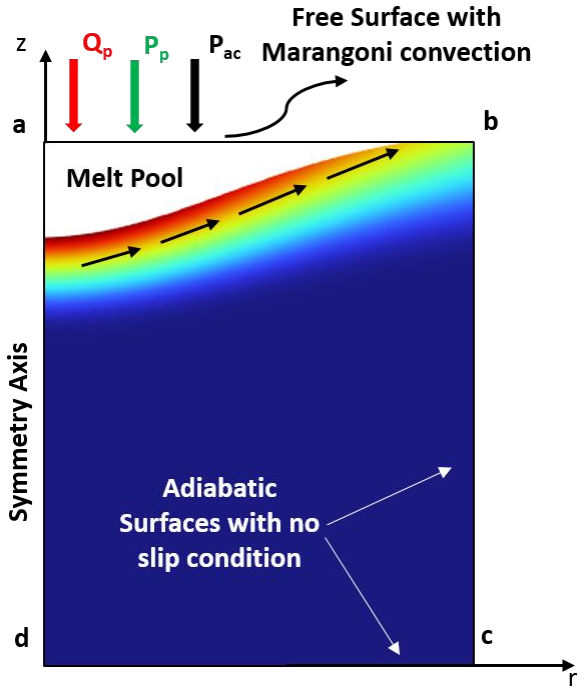

Figure 6.1 Numerical model of crater formation with boundary conditions

6.2.2 Governing equations and boundary conditions

In the present micro-EDM crater model, the molten metal pool forms due to the applied plasma heat flux Q_p and the plasma pressure at the top surface of the workpiece. The temperature distribution in the workpiece as a result of the energy of a single discharge is calculated by solving the classical convection/diffusion equation as follows.

$$\rho C_p \frac{\partial T}{\partial t} + \rho C_p (u \cdot \nabla) T = \nabla \cdot (q) \tag{6.1}$$

$$q = k \nabla T \tag{6.2}$$

Where k, Cp, and ρ are the thermal conductivity, specific heat, and density of the workpiece. T and t are the temperature and time, respectively.

To account for the endothermic reaction during the phase change from solid to liquid at the melting point, the specific heat is modified by incorporating the latent heat of fusion given by

$$C_{peff} = C_p(T) + \frac{\exp\left[-(\frac{T - T_m}{\delta T})^2\right]}{\sqrt{\pi}\delta T} H_f \tag{6.3}$$

Where T_m is the melting point, H_f is the latent heat of fusion. δT is a numerical constant.

Once the material starts melting, the melt flow dynamics are governed by the mass and momentum conservation equations, i.e., the naiver-stokes equation in the laminar flow interface.

$$\rho(\nabla \cdot u) = 0 \tag{6.4}$$

$$\rho\left(\frac{\partial u}{\partial t} + u \cdot \nabla u\right) = \nabla \cdot \left[-pI + K - \frac{2}{3}\mu(\nabla \cdot u)\right] + F \tag{6.5}$$

Where u is the velocity vector, p is the fluid pressure, F is the volume force vector consisting of buoyant and gravitational forces in the melt pool, μ is the dynamic viscosity, and K is the viscous stress tensor in Pa given by

$$K = \mu\left(\nabla u + (\nabla u)^T\right) \tag{6.6}$$

During the crater formation, the temperature in the molten pool increases beyond the melting point and, in most cases, reaches sufficiently above the boiling point, depending upon the pressure. As a result, the mass loss and evaporation of the molten material can be significant and need to be considered in the model. The evaporative metal vapor flux from the surface can be calculated as follows.

$$F_{ev} = \frac{1}{4}\frac{P}{K_b T}\sqrt{\frac{8K_b}{\pi m}} \tag{6.7}$$

Kb is the Boltzmann constant, m is the mass of the workpiece metal per atom, and P is the saturated vapor pressure. The evaporative heat flux q_{ev} is then calculated using the equation

$$q_{ev} = F_{ev} \times q_{lv} \tag{6.8}$$

Where q_{lv} is the latent heat of vaporization.

During the heat flux application, the region where the temperature is less than *Tm* is considered infinitely high viscous fluid and will restrict the flow and convective movements of the material in the domain. Due to the short spark duration, the heat transfer distance is negligible at the bottom and side of the calculation domain and is set as adiabatic boundaries. So for the base and side of the calculation area, the following equation is used.

$$-n \cdot q = 0 \tag{6.9}$$

The top surface of the calculation area is considered a free surface, and different heat fluxes are applied on the top surface. The energy equation of the top free surface of the workpiece can be expressed as

$$-n\cdot q = Q_P - q_{ev} - \varepsilon\sigma(T^4 - T_0^4) - h(T - T_0) \tag{6.10}$$

Q_P is the plasma heat flux, q_{ev} the evaporative heat flux, ε is the emissivity, T_0 is the initial temperature of the workpiece, h is the heat transfer coefficient, and σ is the Stefan-Boltzmann constant. This boundary condition is applied for $R < R_{p,}$ where R_p is the radius of the plasma channel. Outside $R_{p,}$ only the convection condition is present on the free surface. The value of the R_p is taken from the plasma channel's high-speed imaging, and the heat flux distribution is taken from the plasma model presented in Chapter 3. It was discussed in section 5.4.2 in chapter 5 that the average discharge energy per pulse increased with vibration assistance to the Ti6Al4V workpiece. The magnitude of plasma heat flux was adjusted accordingly for simulating the crater formation with vibration assistance.

6.2.3 Forces acting on the melt pool

High-density heat fluxes from plasma are imposed on the workpiece surface, causing the material to melt and evaporate. The vaporization of the metal will impart a force against the fluid's free surface, called the recoil pressure, *Precoil*. Temperature gradients subsequently result in thermally induced shear stresses (Marangoni effect). This tangential force, called Marangoni flow or thermocapillary, drives the molten metal tangentially to the work surface, as shown in Figure 6.2. Capillary forces also play a crucial role in deciding the final morphology of the melt pool surface, giving the molten metal pool normal velocity to the curvature. The tangential stress can be provided directly as a boundary condition in the simulation, as COMSOL provides the Marangoni effect as a ready-made boundary condition. The normal stress due to capillary action must be written using the weak form provided in [192]. Thus, one can express the forces per unit normal in a single equation [193,194]

$$F = P_{recoil} + \mathrm{P}_{plasma} + \mathrm{P}_{capillary} + \mathrm{P}_{marangoni} + \mathrm{P}_{ultrasonic} \tag{6.11}$$

$$F = (P_{recoil} + P_p)\vec{n} + \gamma(k)\vec{n} + \frac{\partial\gamma}{\partial T}\{\nabla T\}\cdot t + P_{ac}\sin wt \tag{6.12}$$

$$P_{recoil} = 0.54\times P_{atm}\exp\left\{\frac{M_a\times L_v}{R}\left(\frac{1}{T_v} - \frac{1}{T_s}\right)\right\} \tag{6.13}$$

M_a is the mass per metal atom, L_v is the latent heat of vaporization, Tv is the vaporization temperature, Ts is the saturation temperature, γ is the surface tension, k is the surface curvature, and R is the gas constant.

$$P_{ac} = \pm 2\pi f_{us} A \rho C_s \tag{6.14}$$

Where f_{us} is the ultrasonic frequency in Hz, A is the amplitude in m, ρ is the density of the dielectric fluid in kg/m^3, and Cs is the sound velocity in the dielectric in m/s.

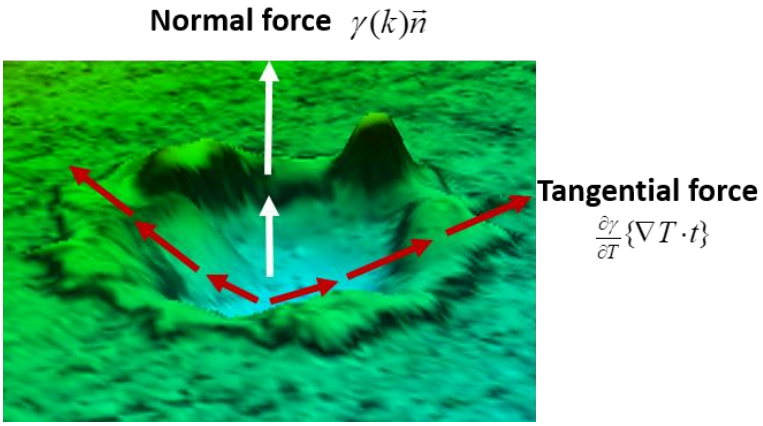

Figure 6.2 Forces acting on the melt pool due to Marangoni effect and surface tension

The crater formation is simulated using the simultaneous application of deformed geometry and moving mesh interfaces in COMSOL Multiphysics. The deforming domain interface uses the evaporation temperature as the limit to ablate the material, whereas the moving mesh interface simulates the flow of the liquid metal. The moving mesh method is based on the arbitrary Lagrangian-Eulerian technique, in which the fluid dynamics equations govern the displacement of the mesh [195,196]. The boundary nodes follow the Eulerian, while the domain nodes follow the Lagrangian description. The velocity of the mesh is obtained from the Naiver Stokes equation as the velocity of the molten metal pool, using the following equation for V_{mesh}.

$$V_{mesh} \cdot n = u \cdot n \tag{6.15}$$

Figure 6.3 and 6.4 shows the captured high-speed images of the plasma channel with and without vibration assistance at various input voltages and capacitances. It can be seen that the diameter of the plasma channel increases with the vibration assistance. The plasma channel showed a clear difference, with debris exploding and ejecting normally outwards due to

vibration assistance. This could be because of the increased normal component of the force and the cavitation effect explained in the previous chapter.

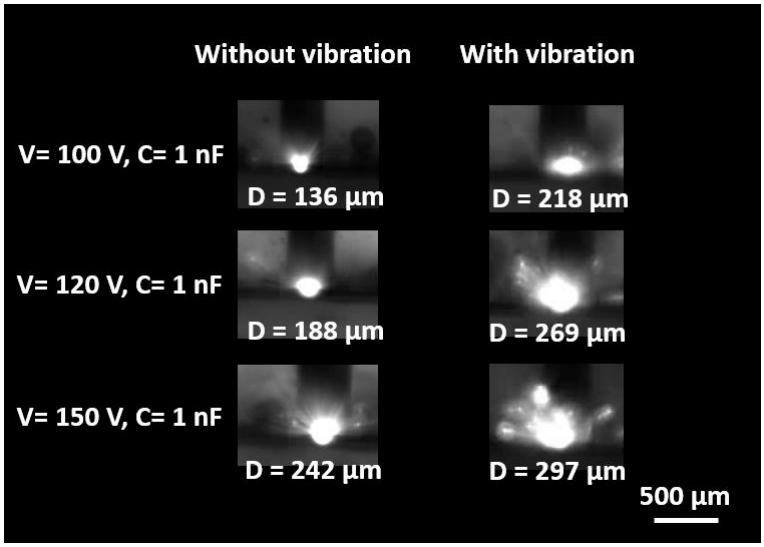

Figure 6.3 High-speed images of the plasma channel with and without vibration at 1nF and varying voltages

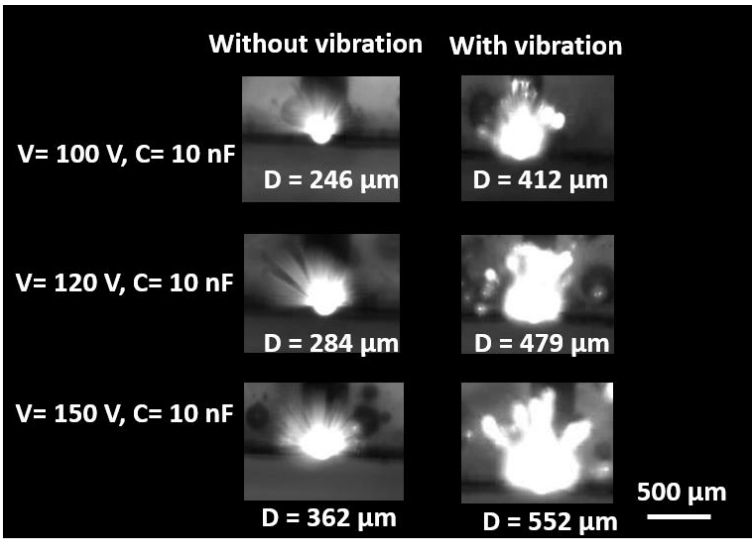

Figure 6.4 High-speed images of the plasma channel with and without vibration at 10 nF and varying voltages

6.2.4 Single discharge experimental approach

RC circuit-based micro-EDM delivers recurring discharges between the workpiece and the tool operated by the servo feed motor. The servo motor lets the tool scan for the close proximity of a workpiece after every discharge to make successive discharges which normally remain beyond the operator's control until it is forced to stop by terminating the CNC program. A contact probe, which is programmed to scan for the conducting workpiece and to creat a

discharge as soon as it locates the workpiece in the feed direction, is used for this purpose. Skip function command in the form of G-code through the CNC user panel is used to control the feed of the tool attached to the Z-axis servo system. The tool must be attached to the micro-EDM power supply and set to a parameter desired for the single discharge. The skip function command here is given in the form of G31, essentially meant to record a probed location after the feed is terminated after making contact with the workpiece. The continuous feed terminates with a spark producing a crater at the micro-EDM parameter set before providing the skip function command. Figure 6.5 shows the single discharge approach discussed above and the skip function command (G31) based single discharges captured for ultrasonic and without assisted micro-EDM.

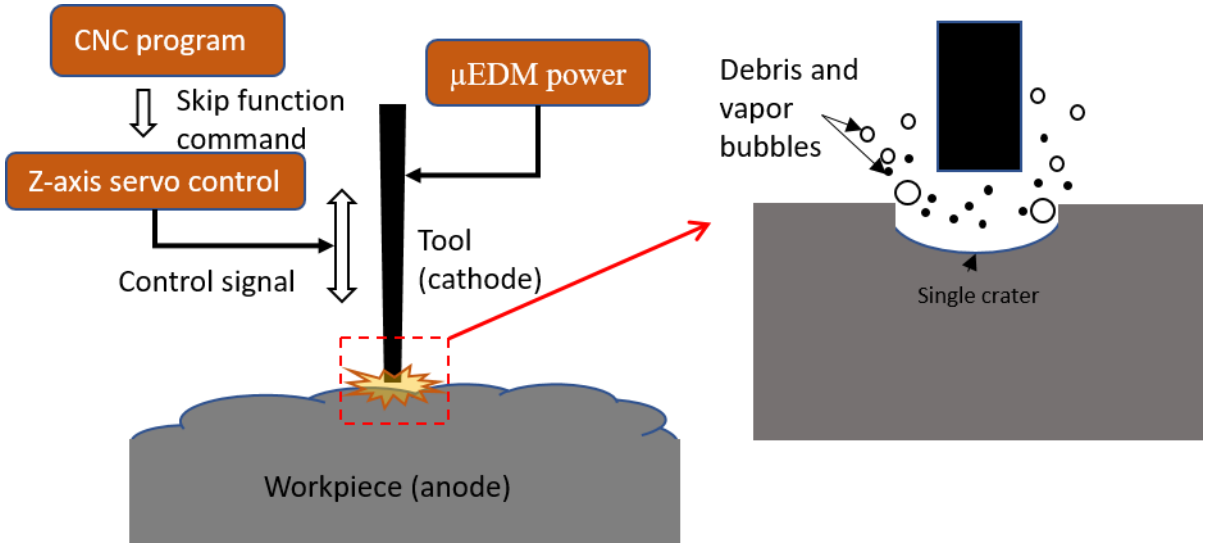

Figure 6.5 Scheme of the single discharge experiment

6.2.5 Temperature-dependent material properties

Temperature-dependent material properties are used in the present model to accurately simulate the behavior of the heat transfer and melt flow phenomenon [194,197].

Table 6.1 Temperature-dependent material properties for TI6Al4V used in the simulation

Property (unit)	Nomenclature	Value
Solidus temperature (K)	Ts	1877
Liquidus temperature (K)	T_l	1923
Melting temperature (K)	T_m	1900
Evaporation temperature (K)	T_e	3315
Solid density (kg/m3)	ρs	$4420 - 0.154(T - 298K)$
Liquid density (kg/m3)	ρ_l	$3920 - 0.68(T - 1923K)$
Latent heat of melting (J/kg)	Lm	2.86×10^5

Thermal expansion coefficient (K^{-1})	β	1.1×10^{-5}
Specific heat (J/(kg K)	Cp	$483.04 + 0.215T(\ T \leq 1268K)$ $412.7 + 0.1801T(\ 1268K < T \leq 1923K))$ $831.0(\ 1923K < T < 3315K)$
Thermal conductivity (W/m K)	K	$1.2595 + 0.0157T(\ T \leq 1268K)$ $3.5127 + 0.0127T(\ 1268K < T \leq 1923K))$ $-12.752 + 0.024T(\ 1923K < T < 3315K)$
Radiation emissivity	ε	$0.1536 + 1.8377 \times 10^{-4}(T - 300K)$
Convective coefficient (W/m^2 K)	h	10
Temperature derivative of the surface tension (N/(m K))	$\frac{\partial \gamma}{\partial T}$	-2.8×10^{-4}
Dynamic viscosity (Pa. s)	μ	$\mathbf{-2.8 \times 10^{-3}}$ $\mathbf{(1923K)}$, $\mathbf{3.03 \times 10^{-3}}$ $\mathbf{(1973K)}$, $\mathbf{2.66 \times 10^{-3}}$ $\mathbf{(2073K)}$, $\mathbf{2.36 \times 10^{-3}}$ $\mathbf{(2773K)}$

6.3 Comparison of the Simulated and Experimental Results

Figure 6.6 shows the simulated craters formed at 120 V and 10 nF with and without vibration. A significant increase in the crater's diameter and depth was observed when the vibration was applied at the top free surface. The increase in the crater diameter and depth can be attributed to the increased temperature of the melt pool, which facilitates more material to get vaporized and ejected. The maximum temperature rise during the crater formation increased from 4860 K to 5120 K due to the extra pressure boundary condition and the adjusted heat flux applied to the workpiece. A very minute and negligible increment in the crater dimensions was observed when the crater formation was simulated with the adjusted plasma heat flux. It means the simulated crater dimensions were more sensitive towards the ultrasonic pressure boundary applied at the top free surface of the workpiece. The increase in the melt pool dimensions with vibration assistance can also be understood with respect to the simulated velocity of the molten metal. Figure 6.7 shows the difference in the velocity field vectors' magnitude and direction with and without vibration assistance during the crater formation. The combined action of the different forces, such as due to vibration, the capillary action, and the tangential force due to the Marangoni effect, drives the melt flow in case of vibration assistance. The component of the normal force out of the melt pool is more significant in the case of vibration assistance. It overcomes the tangential Marangoni effect to drive more molten metal out of the melt pool. This forces the molten metal pool to have the normal velocity to the curvature, as shown in Figure 6.7 (b). In case of no vibration, the Marangoni effect dominates the capillary action due

to high-temperature gradients inside the melt poll. It makes the melt flow more tangential to the workpiece surface. The direction of the velocity field was pointing more outwards and out of the melt pool for the case with vibration compared to the same without vibration. This facilitates more material to be ejected out of the melt pool, increasing the crater's dimensions and less molten metal to get re-solidified at the crater's edges. The respective spark images captured at the same parameters confirm more violent plasma explosion and debris fragmentation with vibration assistance in a normally outwards direction.

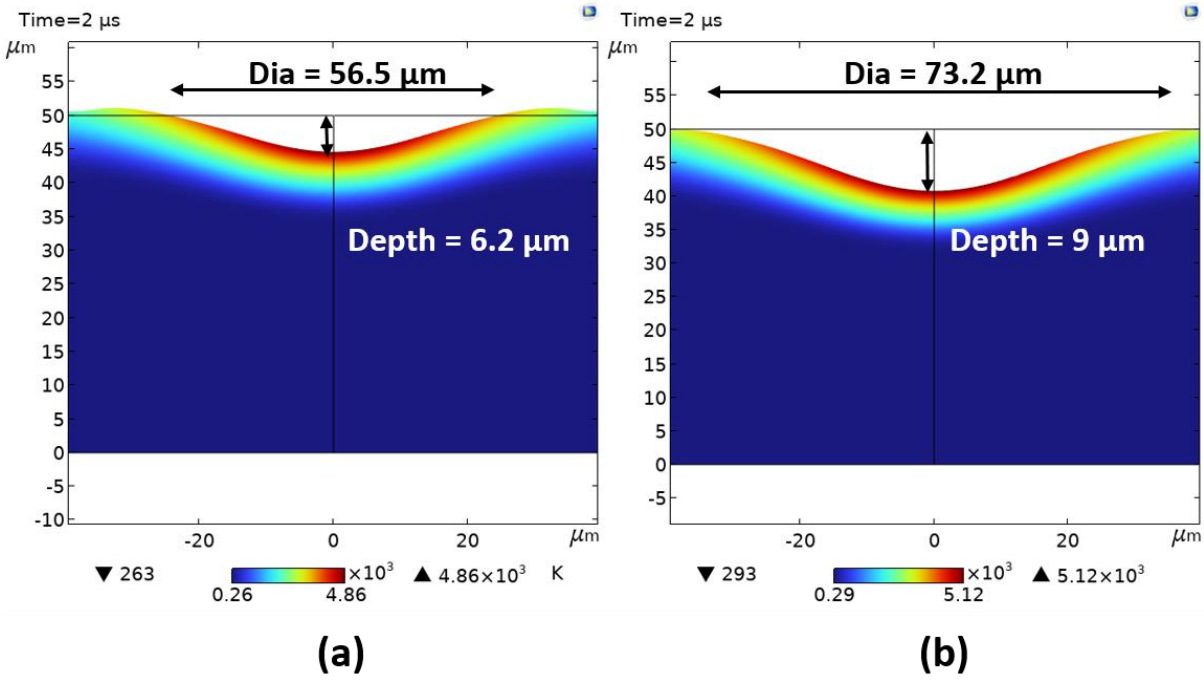

Figure 6.6 Simulated crater profiles (a) without vibration (a) with vibration

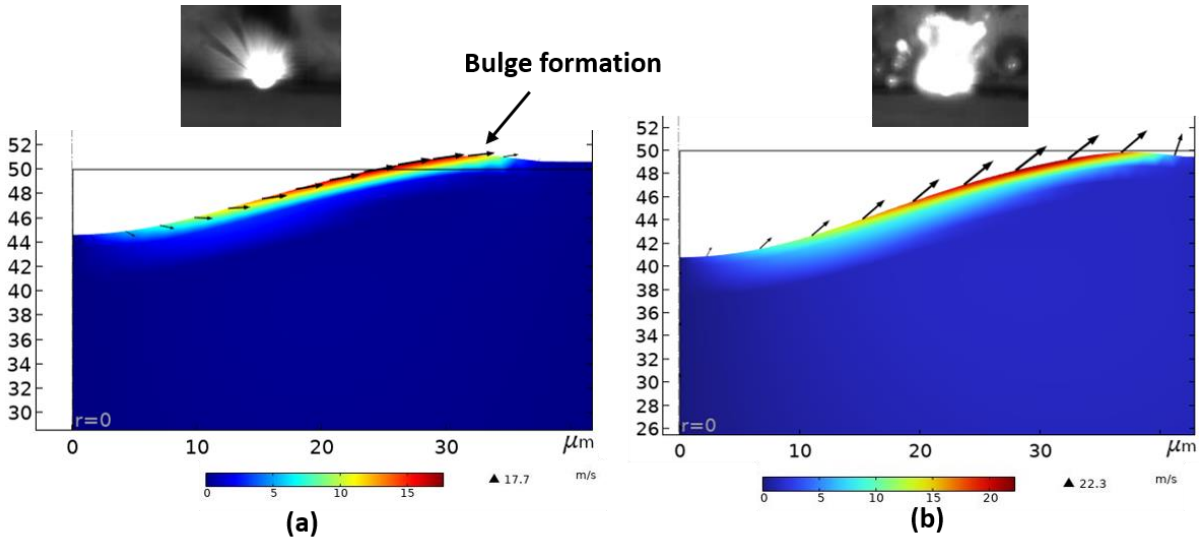

Figure 6.7 Simulated crater velocity profiles with plasma image (a) without vibration (b) with vibration

Figure 6.8 and 6.9 compares the maximum temperature and velocity achieved in the molten pool with and without vibration assistance. It can be seen that the maximum temperature and velocity of the melt pool increase with the increasing voltage and capacitance settings. An interesting observation can be made by comparing the trend of the temperature and velocity graphs at all input energy settings. The increment in the maximum temperature is around 15-20%, while the velocity of the molten metal pool increased in the 30-40% range. This observation signifies the dominance of the flushing action on the thermal action during the vibration assistance. As a result, less deposition of the molten metal on the machined surface decreases the recast layer formation with vibration assistance discussed in Chapter 5. The experimental images of the craters formed with their profile can be seen in Figures 6.10 and 6.11 without and with vibration assistance. It can be seen that the increase in the depth and diameter of the crater was more significant with vibration assistance at the capacitance setting of 10 nF. Also, the crater profiles without vibration assistance showed bulge formation indicating the debris re-solidification at the craters' edge and less effective flushing from the melt pool. The reason behind the effective removal of the molten metal with vibration can be understood with the help of the plasm images captured as shown in the Figures 6.3 and 6.4. The discharges captured with vibration assistance were bigger in diameter and more voilent eruption of debris inclined towards the normally outward direction was obseerved. The tendency of the debris to flow outwards of the melt pool instead of flowing in the tangential direction to the crater edge reduces the chances of bulge formation and re-solidification at the edge. A comparison of the simulated and the experimental 3D profile of the craters is shown in Figure 6.12. It can be seen that the simulation model predicts bigger and deeper craters compared to the experimental results. This is due to the assumption of full flushing efficiency, which is not the case in reality, as the re-solidified debris can be seen in the experimental crater images. In addition, bulge formation can also be observed in the crater without vibration assistance due to the more tangential nature of the velocity vector field compared to the vibration case. With vibration assistance, the melt pool velocity points more axially outwards due to the flow reversal resulting from vibration. It has a greater tendency to get flushed out instead of re-solidifying at the edges of the crater.

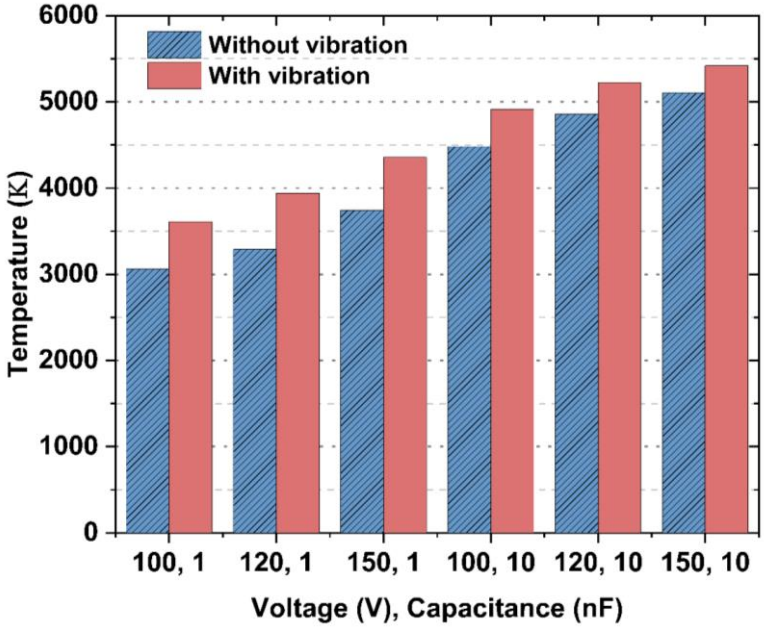

Figure 6.8 Comparison of the melt pool temperature with and without vibration

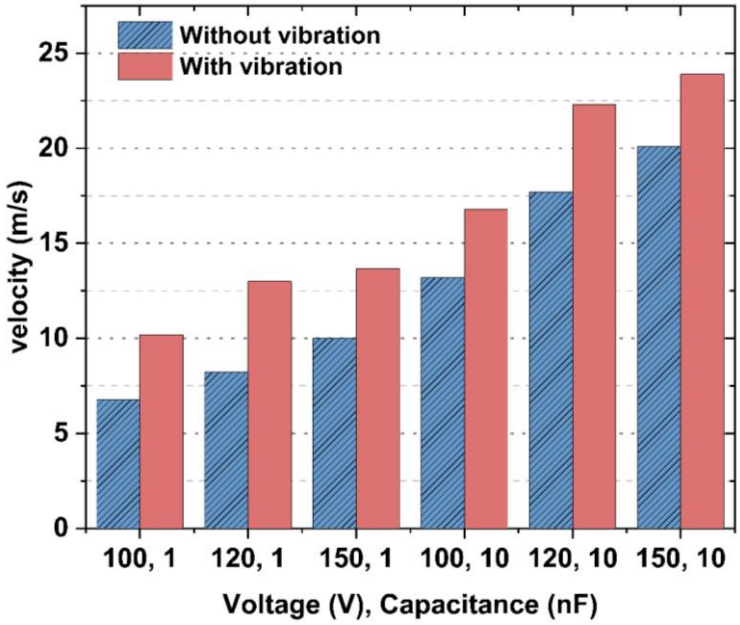

Figure 6.9 Comparison of the melt pool velocity with and without vibration

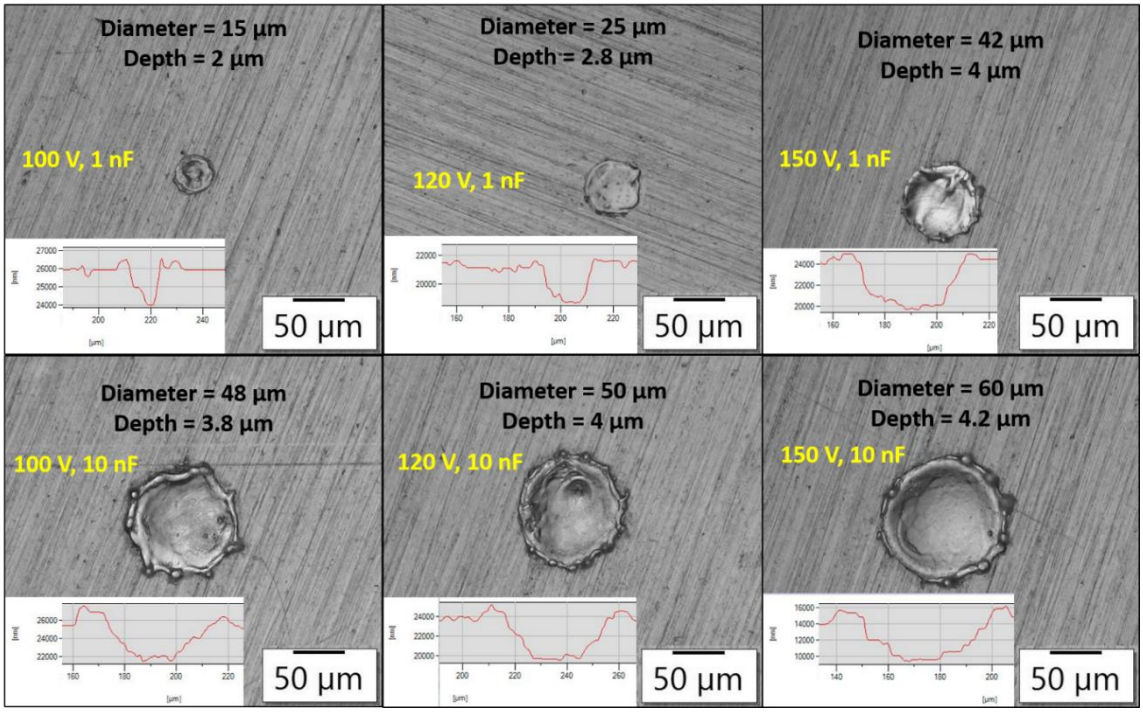

Figure 6.10 Single discharge craters with the profiles at different input energy without vibration

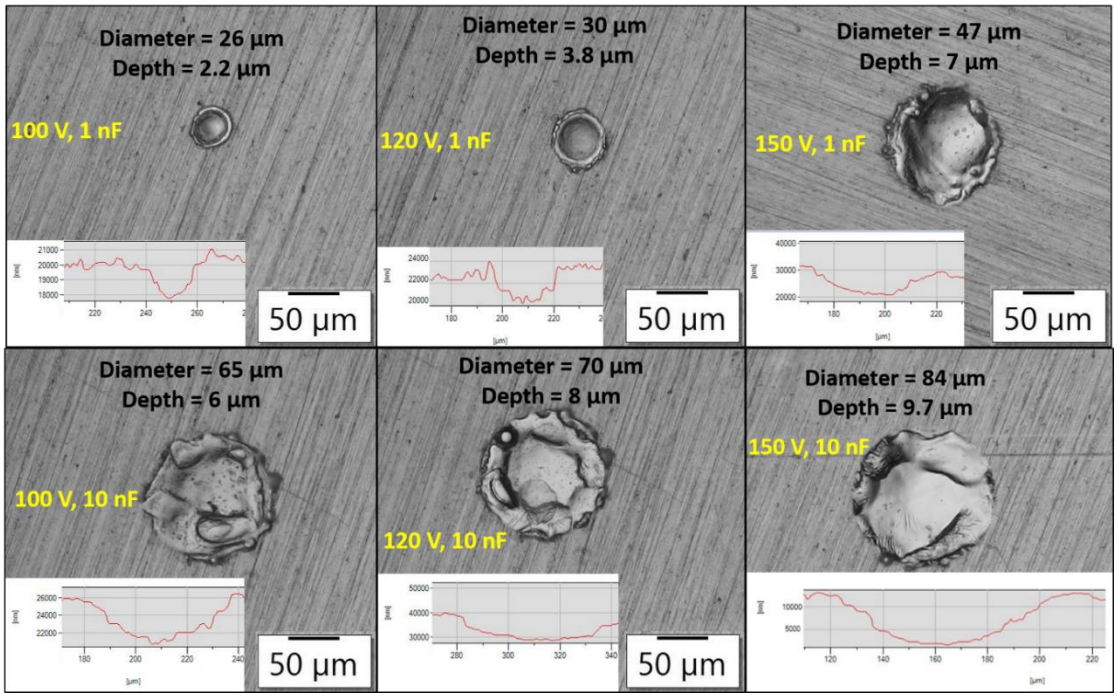

Figure 6.11 Single discharge craters with the profiles at different input energy with vibration assistance

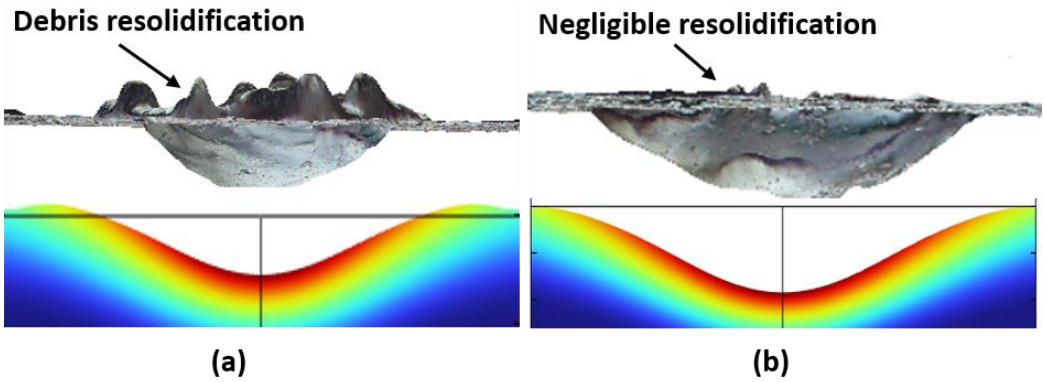

Figure 6.12 Comparison of the simulated and experimental crater profiles (a) without vibration (b) with vibration

Figure 6.13 and 6.14 shows the bar charts for comparing the simulated and the experimental depth and the diameters of the single craters at various parametric settings. There observed an insignificant increase in the depth of the craters at low energy settings with vibration assistance, as the Marangoni effect was sufficient to eject out the less volume of the molten material. As the energy of the discharge increases, more volume of the material melts, and the ultrasonic effects impart its advantage by increasing the normal component of the resultant force acting on the melt pool. This effectively removes the molten metal from the melt pool to form deeper and larger craters. In addition, less deviation can be observed between the predicted and experimental diameter and depth with the vibration assistance. This is due to the increased flushing efficiency with vibration assistance. The error bars were broader at high capacitance settings, depicting the flushing phenomenon's variability at higher energy settings.

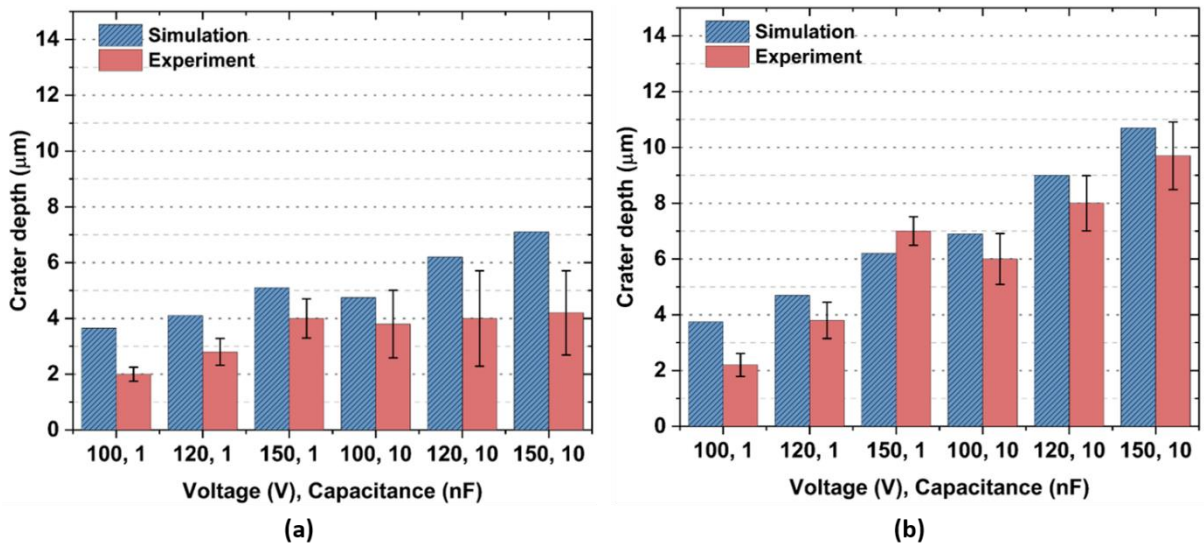

Figure 6.13 Comparison of the simulated vs. experimental crater depths (a) without vibration (b) with vibration

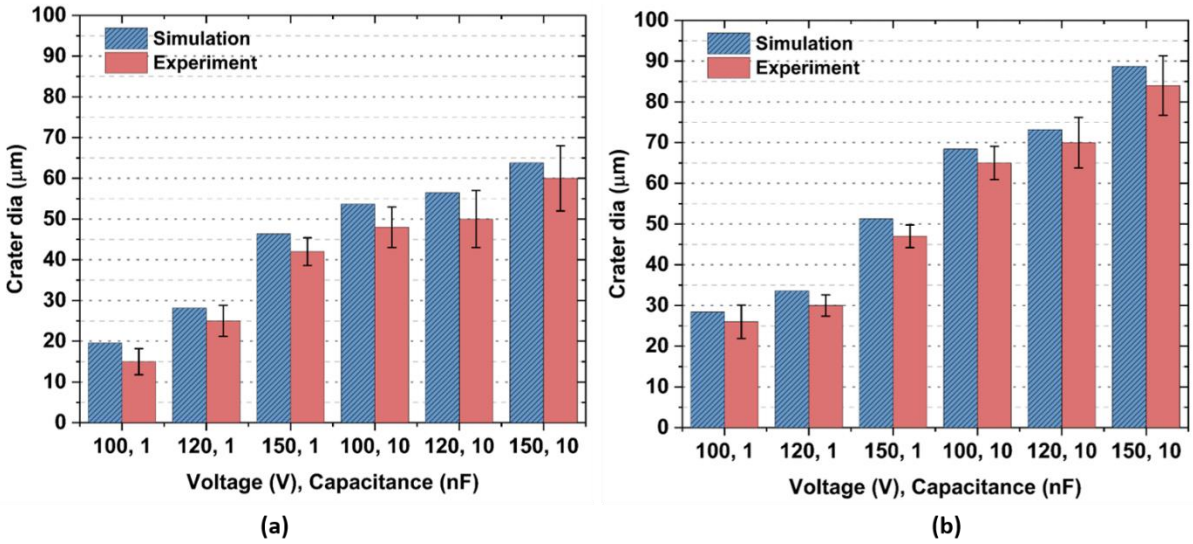

Figure 6.14 Comparison of the simulated vs. experimental crater diameters (a) without vibration (b) with vibration

6.4 Summary

In the present chapter, the modeling and simulation of the crater formation were performed with and without vibration after seeing the advantages of the vibration assistance to the micro-EDM. The output of the plasma model developed in Chapter 3 is used to simulate the crater formation. The model results were compared with the experimental craters formed using the single discharge to discuss the material removal mechanism with vibration assistance. Following are the important conclusions of the study.

- With vibration assistance, the maximum temperature rise in the melt pool during the crater formation increased from 4860 K to 5120 K.
- The simulation results showed a difference in the direction of the velocity vector field with vibration assistance, pointing more towards the vertical direction with increased magnitude similar to the behavior of the plasma channel.
- The increase in temperature and velocity of the melt pool (from 17 to 22 m/s) facilitates more material to be ejected, increasing the crater's dimensions.
- Negligible re-solidification of the molten metal was observed at the crater's edges with vibration assistance.

Chapter 7

Conclusions and Future Scope

7.1 Conclusions

A numerical model for the plasma channel formation during the micro-EDM was proposed in this work to understand the Plasma-electrode interactions in the IEG. The output of the plasma model and the high–speed imaging of the plasma channel were used to study the crater formed during the single discharge micro-EDM process. A pulse monitoring system is developed for the controlled RC-based micro-EDM power supply to monitor and categorize the discharge pulses during continuous machining. Hybridization of the micro-EDM with vibration assistance to the tool electrode was performed to tackle the challenges such as low MRR and arcing/short-circuiting with the help of the developed PMS. In the final chapter, modeling and simulation of the crater formation were performed with and without vibration after exploring the advantages of the vibration assistance to the micro-EDM. The overall conclusions of the study are as follows.

- A numerical model is proposed to predict the diameter of the plasma channel and the discharge crater formed during the µEDM operation. The model could predict the plasma channel diameter with a maximum error of 14.5%. The simulation and experimental results were close to each other at low energy settings compared to high-energy settings.
- The increase in the plasma channel radius was rapid at the start of the pulse on time. It gradually stabilized, confirming the similar behavior of the temperature and heat flux distributions.
- The non-iso-energetic nature of the discharge pulses has been thoroughly discussed based on the voltage and current signals and by quantifying the discharge energy per pulse. It has been found that the MRR and VRD are the functions of discharge energy and continuously decrease with the depth of the machined hole.
- Discharge frequency and energy of contributing and semi-contributing discharge pulses showed opposite trends with respect to the depth of machining.
- Ultrasonic vibration assistance reduced the non-productive time during the micro-EDM milling process. The discharge frequency improved, and the percentage of normal discharges increased by 19 %. A very little delay time before the discharge was observed with the introduction of vibrations, increasing the energy content of the discharges.

- The frequent alterations of the discharge gap due to vibration assistance proved beneficial by increasing the MRR by a maximum of 35 % and reducing the tool wear with a four-time decrease in Ra value and reduction of recast layer formation.
- The micro-holes fabricated with the vibration assistance were less tapered and produced a good surface finish compared to the unassisted micro-EDM process. A maximum decrease of 7.14% in the percentage error in depth among all sets of experiments with the vibration assistance further indicates the enhanced discharging phenomenon and increased stability of the process.
- Vibration assistance to the micro-EDM drilling process was beneficial, with an 18% increase in the discharge energy. Ultrasonic vibration assistance reduces surface roughness at high-energy settings from 3.2 μm to 0.45 μm.
- With vibration assistance, the maximum temperature rise in the melt pool during the crater formation increased from 4860 K to 5120 K.
- The increase in temperature and velocity of the melt pool (from 17 to 22 m/s) facilitates more material to be ejected, increasing the crater's dimensions.
- Negligible re-solidification of the molten metal was observed at the crater's edges with vibration assistance.

7.2 Future Scope

- The numerical model for the plasma channel formation can be improved further by incorporating the plasma sheath formation near the electrode walls, which introduces thermal non-equilibrium into the problem. In such a case, the plasma model would become more complex but close to the realistic micro-EDM discharge.
- High-speed imaging of the plasma channel can be combined with optical emission spectroscopy to explain the plasm channel's thermodynamic properties accurately.
- The PMS developed in the current study is based on the simultaneous monitoring and comparison of the current and voltage data. However, a PMS based on the energy of each discharge would be more helpful and accurate.
- The ultrasonic tool holder can be further improved by introducing the rotation of the tool with variable amplitudes during continuous machining to fabricate micro features with higher aspect ratios.

References

[1] Liu, X., DeVor, R. E., Kapoor, S. G., and Ehmann, K. F., 2004, "The Mechanics of Machining at the Microscale: Assessment of the Current State of the Science," J. Manuf. Sci. Eng., **126**(4), pp. 666–678.

[2] Rajurkar, K. P., Levy, G., Malshe, A., Sundaram, M. M., McGeough, J., Hu, X., Resnick, R., and DeSilva, A., 2006, "Micro and Nano Machining by Electro-Physical and Chemical Processes," CIRP Ann., **55**(2), pp. 643–666.

[3] Qin, Y., Brockett, A., Ma, Y., Razali, A., Zhao, J., Harrison, C., Pan, W., Dai, X., and Loziak, D., 2010, "Micro-Manufacturing: Research, Technology Outcomes and Development Issues," Int. J. Adv. Manuf. Technol., **47**(9–12), pp. 821–837.

[4] Yang, X., Guo, J., Chen, X., and Kunieda, M., 2011, "Molecular Dynamics Simulation of the Material Removal Mechanism in Micro-EDM," Precis. Eng., **35**(1), pp. 51–57.

[5] Roy, T., Datta, D., and Balasubramaniam, R., 2020, "Debris Based Discharge Segregation in Reverse Micro EDM," Meas. J. Int. Meas. Confed., **153**.

[6] Raza, S., Kishore, H., Nirala, C. K., and Rajurkar, K. P., 2023, "Multiphysics Modelling and High-Speed Imaging-Based Validation of Discharge Plasma in Micro-EDM," CIRP J. Manuf. Sci. Technol., **43**, pp. 15–29.

[7] Sundaram, M. M., Billa, S., and Rajurkar, K. P., 2007, "Generation of High Aspect Ratio Micro Holes by a Hybrid Micromachining Process," *Proceedings of the ASME International Manufacturing Science and Engineering Conference 2007, MSEC2007*, pp. 243–248.

[8] Kunieda, M., Lauwers, B., Rajurkar, K. P., and Schumacher, B. M., 2005, "Advancing EDM through Fundamental Insight into the Process," CIRP Ann., **54**(2), pp. 64–87.

[9] Zheng, S., Kang, Z., Li, L., Zhang, A., Zhao, K., and Zhou, Y., 2021, "Influence of Series RC Circuit Parameters on the Streamer Discharge Process of Gas Spark Switch," Vacuum, **193**, p. 110518.

[10] Raza, S., and Nirala, C. K., 2021, "Multiphysics Simulation of Plasma Channel Formation during Micro-Electrical Discharge Machining," AIP Adv., **11**(2), p. 025138.

[11] Katz, Z., and Tibbles, C. J., 2005, "Analysis of Micro-Scale EDM Process," Int. J. Adv. Manuf. Technol., **25**(9–10), pp. 923–928.

[12] Dhanik, S., and Joshi, S. S., 2005, "Modeling of a Single Resistance Capacitance Pulse Discharge in Micro-Electro Discharge Machining," J. Manuf. Sci. Eng., **127**(4), pp. 759–767.

[13] Yadav, U. S., and Yadava, V., 2015, "Experimental Investigation on Electrical Discharge Drilling of Ti-6Al-4V Alloy," http://dx.doi.org/10.1080/10910344.2015.1085316, **19**(4), pp. 515–535.

[14] Huang, S. H., Huang, F. Y., and Yan, B. H., 2005, "Fracture Strength Analysis of Micro WC-Shaft Manufactured by Micro-Electro-Discharge Machining," Int. J. Adv. Manuf. Technol., **26**(1–2), pp. 68–77.

[15] Yan, B. H., Chang, G. W., Chang, J. H., and Hsu, R. T., 2007, "Improving Electrical Discharge Machined Surfaces Using Magnetic Abrasive Finishing," http://dx.doi.org/10.1081/MST-120034246, **8**(1), pp. 103–118.

[16] Soni, J. S., 1994, "Microanalysis of Debris Formed during Rotary EDM of Titanium Alloy (Ti 6A1 4V) and Die Steel (T 215 Cr12)," Wear, **177**(1), pp. 71–79.

[17] Endo, T., Tsujimoto, T., and Mitsui, K., 2008, "Study of Vibration-Assisted Micro-EDM—The Effect of Vibration on Machining Time and Stability of Discharge," Precis. Eng., **32**(4), pp. 269–277.

[18] Schumacher, B. M., 1990, "About the Role of Debris in the Gap During Electrical Discharge Machining," CIRP Ann., **39**(1), pp. 197–199.

[19] Tsai, Y. Y., and Masuzawa, T., 2004, "An Index to Evaluate the Wear Resistance of the Electrode in Micro-EDM," J. Mater. Process. Technol., **149**(1–3), pp. 304–309.

[20] Mohd Abbas, N., Solomon, D. G., and Fuad Bahari, M., 2007, "A Review on Current Research Trends in Electrical Discharge Machining (EDM)," Int. J. Mach. Tools Manuf., **47**(7–8), pp. 1214–1228.

[21] Bojorquez, B., Marloth, R. T., and Es-Said, O. S., 2002, "Formation of a Crater in the Workpiece on an Electrical Discharge Machine," Eng. Fail. Anal., **9**(1), pp. 93–97.

[22] Rahman, M., Wong, Y. S., and Nguyen, M. D., 2014, "Compound and Hybrid Micromachining: Part II – Hybrid Micro-EDM and Micro-ECM," Compr. Mater. Process., **11**, pp. 113–150.

[23] Masuzawa, T., 2000, "State of the Art of Micromachining," CIRP Ann., **49**(2), pp. 473–488.

[24] Li, G., and Ding, S., 2020, "Machining of Medical Device Components," Met. Biomater. Process. Med. Device Manuf., pp. 137–157.

[25] Hourmand, M., Sarhan, A. A. D., Noordin, M. Y., and Sayuti, M., 2017, "1.10 Micro-EDM Drilling of Tungsten Carbide Using Microelectrode with High Aspect Ratio to Improve MRR, EWR, and Hole Quality," Compr. Mater. Finish., **1**–**3**, pp. 267–321.

[26] Liu, Q., Zhang, Q., Zhang, M., and Zhang, J., 2016, “Review of Size Effects in Micro Electrical Discharge Machining,” Precis. Eng., **44**, pp. 29–40.

[27] Takahata, K., and Takahata, K., 2009, “Micro-Electro-Discharge Machining Technologies for MEMS,” Micro Electron. Mech. Syst.

[28] Kurnia, W., Tan, P. C., Yeo, S. H., and Wong, M., 2008, “Analytical Approximation of the Erosion Rate and Electrode Wear in Micro Electrical Discharge Machining,” J. Micromechanics Microengineering, **18**(8), p. 085011.

[29] Tao, J., Ni, J., and Shih, A. J., 2012, “Modeling of the Anode Crater Formation in Electrical Discharge Machining,” J. Manuf. Sci. Eng., **134**(1).

[30] Wong, Y. S., Rahman, M., Lim, H. S., Han, H., and Ravi, N., 2003, “Investigation of Micro-EDM Material Removal Characteristics Using Single RC-Pulse Discharges,” J. Mater. Process. Technol., **140**(1–3), pp. 303–307.

[31] Jahan, M. P., Rahman, M., Wong, Y. S., and Fuhua, L., 2010, “On-Machine Fabrication of High-Aspect-Ratio Micro-Electrodes and Application in Vibration-Assisted Micro-Electrodischarge Drilling of Tungsten Carbide,” Proc. Inst. Mech. Eng. Part B J. Eng. Manuf., **224**(5), pp. 795–814.

[32] Yi, S. M., Park, M. S., Lee, Y. S., and Chu, C. N., 2008, “Fabrication of a Stainless Steel Shadow Mask Using Batch Mode Micro-EDM,” Microsyst. Technol., **14**(3), pp. 411–417.

[33] Zahiruddin, M., and Kunieda, M., 2012, “Comparison of Energy and Removal Efficiencies between Micro and Macro EDM,” CIRP Ann., **61**(1), pp. 187–190.

[34] Jahan, M. P., 2013, “Micro-Electrical Discharge Machining,” Nontradit. Mach. Process. Res. Adv., **9781447151791**, pp. 111–151.

[35] Ho, K. H., and Newman, S. T., 2003, “State of the Art Electrical Discharge Machining (EDM),” Int. J. Mach. Tools Manuf., **43**(13), pp. 1287–1300.

[36] Yu, Z. Y., Masuzawa, T., and Fujino, M., 1998, “Micro-EDM for Three-Dimensional Cavities - Development of Uniform Wear Method -,” CIRP Ann., **47**(1), pp. 169–172.

[37] Rajurkar, K. P., and Yu, Z. Y., 2000, “3D Micro-EDM Using CAD/CAM,” CIRP Ann., **49**(1), pp. 127–130.

[38] Raju, L., and Hiremath, S. S., 2016, “A State-of-the-Art Review on Micro Electro-Discharge Machining,” Procedia Technol., **25**, pp. 1281–1288.

[39] Han, F., Wachi, S., and Kunieda, M., 2004, “Improvement of Machining Characteristics of Micro-EDM Using Transistor Type Isopulse Generator and Servo Feed Control,” Precis. Eng., **28**(4), pp. 378–385.

[40] Matsuhara Y, O. H., 2004, “Study on High Finish Machining in Wire EDM,” J Elec Mach Technol, **28**(90), pp. 19–22.

[41] Sidpara, A. M., and Malayath, G., 2019, “Introduction to Micro EDM,” *Micro Electro Discharge Machining*, CRC Press, pp. 1–35.

[42] Han, F., Chen, L., Yu, D., and Zhou, X., 2007, “Basic Study on Pulse Generator for Micro-EDM,” Int. J. Adv. Manuf. Technol., **33**(5–6), pp. 474–479.

[43] Liew, J., Yee Yap, C., Wang, J., -, al, Dong, X.-X., Zhao, S.-M., Zhang, H.-B., Zhao, R., Dong, H., Zhou, J., Li, R., Chen, C., and You, P., 2023, “State of the Art in Power Supply of Electrical Discharge Machining, Electrochemical Machining and Their Variants,” J. Phys. Conf. Ser., **2433**(1), p. 012011.

[44] Erawan, M. A., Azli, Y., Nor Hisham, K., Syahrullail, S., Zurkarmawan, A. B., and Trias, A., 2014, “Power Generator of Electrical Discharge Machining (EDM) System,” Appl. Mech. Mater., **554**, pp. 638–642.

[45] Raza, S., Nadda, R., and Nirala, C. K., 2023, “Real-Time Data Acquisition and Discharge Pulse Analysis in Controlled RC Circuit Based Micro-EDM,” Microsyst. Technol., **29**(3), pp. 359–376.

[46] Joshi, S. N., and Pande, S. S., 2009, “Development of an Intelligent Process Model for EDM,” Int. J. Adv. Manuf. Technol., **45**(3–4), pp. 300–317.

[47] Descoeudres, A., Hollenstein, C., Wälder, G., Demellayer, R., and Perez, R., 2008, “Time- and Spatially-Resolved Characterization of Electrical Discharge Machining Plasma,” Plasma Sources Sci. Technol., **17**(2), p. 024008.

[48] U. Maradia, K. Wegener, 2015, “EDM Modelling and Simulation,” *Electrical Discharge Machining (EDM): Types, Technologies and Applications*, pp. 67–121.

[49] Kliuev, M., Florio, K., Akbari, M., and Wegener, K., 2019, “Influence of Energy Fraction in EDM Drilling of Inconel 718 by Statistical Analysis and Finite Element Crater-Modelling,” J. Manuf. Process., **40**, pp. 84–93.

[50] Dhanik, S., Joshi, S. S., Ramakrishnan, N., and Apte, P. R., 2005, “Evolution of EDM Process Modelling and Development towards Modelling of the Micro-EDM Process,” Int. J. Manuf. Technol. Manag., **7**(2–4), pp. 157–180.

[51] Maradia, U., Hollenstein, C., and Wegener, K., 2015, “Temporal Characteristics of the Pulsed Electric Discharges in Small Gaps Filled with Hydrocarbon Oil,” J. Phys. D. Appl. Phys., **48**(5), p. 055202.

[52] DiBitonto, D. D., Eubank, P. T., Patel, M. R., and Barrufet, M. A., 1989, “Theoretical Models of the Electrical Discharge Machining Process. I. A Simple Cathode Erosion Model,” J. Appl. Phys., **66**(9), pp. 4095–4103.

[53] Yeo, S. H., Kurnia, W., and Tan, P. C., 2007, “Electro-Thermal Modelling of Anode and Cathode in Micro-EDM,” J. Phys. D. Appl.

Phys., **40**(8), pp. 2513–2521.

[54] Zahiruddin, M., and Kunieda, M., 2010, "Energy Distribution Ratio into Micro EDM Electrodes," J. Adv. Mech. Des. Syst. Manuf., **4**(6), pp. 1095–1106.

[55] Erden, A., and Kaftanoğlu, B., 1981, "Thermo-Mathematical Modelling and Optimization of Energy Pulse Forms in Electric Discharge Machining (EDM)," Int. J. Mach. Tool Des. Res., **21**(1), pp. 11–22.

[56] Salonitis, K., Stournaras, A., Stavropoulos, P., and Chryssolouris, G., 2009, "Thermal Modeling of the Material Removal Rate and Surface Roughness for Die-Sinking EDM," Int. J. Adv. Manuf. Technol., **40**(3–4), pp. 316–323.

[57] Ishfaq, K., Muhammad, ·, Mahmood, A., Ahmad, ·, Khan, R., and Rehman, · Mudassar, "Mathematical Modelling with Experimental Correlations for Multiple Craters Dimensions, Material Removal Rate and Surface Roughness in Electrical Discharge Machining," Int. J. Adv. Manuf. Technol., **1**, p. 3.

[58] Chen, Y. F., Lin, Y. J., Lin, Y. C., Chen, S. L., and Hsu, L. R., 2009, "Optimization of Electrodischarge Machining Parameters on ZrO2 Ceramic Using the Taguchi Method," http://dx.doi.org/10.1243/09544054JEM1437, **224**(2), pp. 195–205.

[59] Ablyaz, T. R., Shlykov, E. S., and Muratov, K. R., 2021, "Improving the Efficiency of Electrical Discharge Machining of Special-Purpose Products with Composite Electrode Tools," Materials (Basel)., **14**(20).

[60] Lyubimov, V. V., Volgin, V. M., Gnidina, I. V., and Salomatnikov, M. S., 2018, "The Discharge Channel Formation and the Mechanism of Material Removal during Electrical Discharge Micromachining by Nanosecond Pulses," *Procedia CIRP*, Elsevier, pp. 325–329.

[61] Crichton, B. H., 1996, "Gas Discharge Physics," IEE Colloq., (173).

[62] Finkelnburg, W., and Maecker, H., 1950, "Electric Arcs and Thermal Plasmas," Handb. Phys., **22**((S. Flügge,ed.), (Berlin: Springer-Verlag)), p. 254.

[63] Nirala, C. K., and Saha, P., 2015, "Evaluation of MEDM-Drilling and MEDM-Dressing Performances Based on Online Monitoring of Discharge Gap Conditions," Int. J. Adv. Manuf. Technol. 2015 859, **85**(9), pp. 1995–2012.

[64] Habedank, U., 1993, "Application of a New Arc Model for the Evaluation of Short-Circuit Breaking Tests," IEEE Trans. Power Deliv., **8**(4), pp. 1921–1925.

[65] Thomas, R., Lahaye, D., Vuik, C., and Van Der Sluis, L., 2015, "Simulation of Arc Models with the Block Modelling Method," *International Conference on Power Systems Transients (IPST2015) in Cavtat, Croatia*.

[66] Marković, N., Bjelić, S., Živanić, J., and Jakšić, U., 2013, "Numerical Simulation and Analytical Model of Electrical Arc Impedance in the Transient Processes," Prz. Elektrotechniczny, **89**(2 A), pp. 113–117.

[67] Hsu, K. C., and Pfender, E., 1983, "Two-Temperature Modeling of the Free-Burning, High-Intensity Arc," J. Appl. Phys., **54**(8), pp. 4359–4366.

[68] Hsu, K. C., and Pfender, E., 1983, "Analysis of the Cathode Region of a Free-Burning High Intensity Argon Arc," J. Appl. Phys., **54**(7), pp. 3818–3824.

[69] Hsu, K. C., Etemadi, K., and Pfender, E., 1983, "Study of the Free-Burning High-Intensity Argon Arc," J. Appl. Phys., **54**(3), pp. 1293–1301.

[70] Gonzalez, J. J., Gleizes, A., Proulx, P., and Boulos, M., 1993, "Mathematical Modeling of a Free-Burning Arc in the Presence of Metal Vapor," J. Appl. Phys., **74**(5), pp. 3065–3070.

[71] Murphy, A. B., and Tam, E., 2014, "Thermodynamic Properties and Transport Coefficients of Arc Lamp Plasmas: Argon, Krypton and Xenon," J. Phys. D. Appl. Phys., **47**(29), p. 295202.

[72] Cressault, Y., Murphy, A. B., Teulet, P., Gleizes, A., and Schnick, M., 2013, "Thermal Plasma Properties for Ar-Cu, Ar-Fe and Ar-Al Mixtures Used in Welding Plasmas Processes: II. Transport Coefficients at Atmospheric Pressure," J. Phys. D. Appl. Phys., **46**(41), p. 415207.

[73] Aitken, F., Mcluskey, F. M. J., and Denat, A., 1996, "An Energy Model for Artificially Generated Bubbles in Liquids," J. Fluid Mech., **327**, pp. 373–392.

[74] Denat, A., Gosse, J. P., and Gosse, B., "ELECTRICAL CONDUCTION OF PURIFIED CYCLOHEXANE IN A DIVERGENT ELECTRIC FIELD."

[75] André, D., 2011, "Conduction and Breakdown Initiation in Dielectric Liquids," Proc. - IEEE Int. Conf. Dielectr. Liq.

[76] Beroual, A., and Tobazeon, R., 1987, "Propagation et Génération Des Streamers Dans Les Diélectriques Liquides," Rev. Phys. Appliquée, **22**(9), pp. 1117–1123.

[77] Beroual, A., 1993, "Electronic and Gaseous Processes in the Prebreakdown Phenomena of Dielectric Liquids," J. Appl. Phys., **73**(9), pp. 4528–4533.

[78] M. Wiessner, F.T.B. Macedo, C.P. Martendal, F. Kuster, K. W., 2018, "Fundamental Investigation of EDM Plasmas, Part I: A Comparison between Electric Discharges in Gaseous and Liquid Dielectric Media," Procedia CIRP, **68**, pp. 330–335.

[79] Dhanik, S., and Joshi, S. S., 2005, "Modeling of a Single Resistance Capacitance Pulse Discharge in Micro-Electro Discharge

Machining," J. Manuf. Sci. Eng. Trans. ASME, **127**(4), pp. 759–767.

[80] Zhang, Y., Liu, Y., Shen, Y., Ji, R., Li, Z., and Zheng, C., 2014, "Investigation on the Influence of the Dielectrics on the Material Removal Characteristics of EDM," J. Mater. Process. Technol., **214**(5), pp. 1052–1061.

[81] Maradia, U., Hollenstein, C., and Wegener, K., 2015, "Temporal Characteristics of the Pulsed Electric Discharges in Small Gaps Filled with Hydrocarbon Oil," J. Phys. D. Appl. Phys., **48**(5), p. 055202.

[82] Watson, P. K., 1985, "Electrostatic and Hydrodynamic Effects in the Electrical Breakdown of Liquid Dielectrics," IEEE Trans. Electr. Insul., **EI-20**(2), pp. 395–399.

[83] Kunhardt, E. E., and Tzeng, Y., 1988, "Development of an Electron Avalanche and Its Transition into Streamers," Phys. Rev. A, **38**(3), p. 1410.

[84] Schoenbach, K., Kolb, J., Xiao, S., Katsuki, S., Minamitani, Y., and Joshi, R., 2008, "Electrical Breakdown of Water in Microgaps," Plasma Sources Sci. Technol., **17**(2), p. 024010.

[85] Mujumdar, S., Curreli, D., Kapoor, S. G., and Ruzic, D., 2014, "A Model of Micro Electro-Discharge Machining Plasma Discharge in Deionized Water," J. Manuf. Sci. Eng. Trans. ASME, **136**(3), pp. 1–12.

[86] Nagahanumaiah, Ramkumar, J., Glumac, N., Kapoor, S. G., and Devor, R. E., 2009, "Characterization of Plasma in Micro-EDM Discharge Using Optical Spectroscopy," J. Manuf. Process., **11**(2), pp. 82–87.

[87] Liew, J., Yee Yap, C., Wang, J., -, al, Albí nski, K., Musio, K., Miernikiewicz, A., Labuz, S., and Ma lota, M., 1996, "The Temperature of a Plasma Used in Electrical Discharge Machining," Plasma Sources Sci. Technol., **5**(4), p. 736.

[88] Adineh, V., Coufal, O., and Zivny, O., 2012, "Thermodynamic and Radiative Properties of Plasma Excited in EDM Process through N 2 Taking into Account Fe," IEEE Trans. Plasma Sci., **40**(10 PART 2), pp. 2723–2735.

[89] R Snoyes, F. V. D., 1971, "Investigations of EDM Operations by Means of Thermo Mathematical Models," Ann. cirp, **20**, pp. 35–36.

[90] Lhiaubet, C., and Meyer, R. M., 1981, "Method of Indirect Determination of the Anodic and Cathodic Voltage Drops in Short High-current Electric Discharges in a Dielectric Liquid," J. Appl. Phys., **52**(6), pp. 3929–3934.

[91] Pandey, P. C., and Jilani, S. T., 1986, "Plasma Channel Growth and the Resolidified Layer in Edm," Precis. Eng., **8**(2), pp. 104–110.

[92] Eubank, P. T., Patel, M. R., Barrufet, M. A., and Bozkurt, B., 1993, "Theoretical Models of the Electrical Discharge Machining Process. III. the Variable Mass, Cylindrical Plasma Model," J. Appl. Phys., **73**(11), pp. 7900–7909.

[93] Mujumdar, S. S., Curreli, D., Kapoor, S. G., and Ruzic, D., 2014, "A Model of Micro Electro-Discharge Machining Plasma Discharge in Deionized Water," J. Manuf. Sci. Eng., **136**(3), p. 031011.

[94] Chu, X., Zhu, K., Wang, C., Hu, Z., and Zhang, Y., 2016, "A Study on Plasma Channel Expansion in Micro-EDM," Mater. Manuf. Process., **31**(4), pp. 381–390.

[95] Singh, A., and Ghosh, A., 1999, "A Thermo-Electric Model of Material Removal during Electric Discharge Machining," Int. J. Mach. Tools Manuf., **39**(4), pp. 669–682.

[96] Clauser, F. H., 1960, *Symposium of Plasma Dynamics*, Addison-Wesley Publishing Company.

[97] Mujumdar, S. S., Curreli, D., and Kapoor, S. G., 2018, "Effect of Dielectric Conductivity on Micro-Electrical Discharge Machining Plasma Characteristics Using Optical Emission Spectroscopy," J. Micro Nano-Manufacturing, **6**(3).

[98] Subbu, S. K., Dhamodaran, S., and Ramkumar, J., 2012, "Microelectric Discharge Plasma: Characterization and Applications," http://dx.doi.org/10.1080/10426914.2012.663127, **27**(11), pp. 1208–1212.

[99] Shao, B., and Rajurkar, K. P., 2013, *Micro-EDM Pulse Energy Distribution Ratio Determination*, 8th International Conference on MicroManufacturing (ICOMM 2013).

[100] Shabgard, M., Ahmadi, R., Seyedzavvar, M., and Oliaei, S. N. B., 2013, "Mathematical and Numerical Modeling of the Effect of Input-Parameters on the Flushing Efficiency of Plasma Channel in EDM Process," Int. J. Mach. Tools Manuf., **65**, pp. 79–87.

[101] Hoang, K. T., Gopalan, S. K., and Yang, S. H., 2015, "Study of Energy Distribution to Electrodes in a Micro-EDM Process by Utilizing the Electro-Thermal Model of Single Discharges," J. Mech. Sci. Technol., **29**(1), pp. 349–356.

[102] Xia, H., Kunieda, M., and Aki, N. N., 1996, "Removal Amount Difference between Anode and Cathode in EDM Process," Int. J. Electr. Mach., **1**(0), pp. 45–52.

[103] Tariq Jilani, S., and Pandey, P. C., 1982, "Analysis and Modelling of Edm Parameters," Precis. Eng., **4**(4), pp. 215–221.

[104] Beck, J. V., 1981, "Large Time Solutions for Temperatures in a Semi-Infinite Body with a Disk Heat Source," Int. J. Heat Mass Transf., **24**(1), pp. 155–164.

[105] Tan, P. C., and Yeo, S. H., 2008, "Modelling of Overlapping Craters in Micro-Electrical Discharge Machining," J. Phys. D. Appl. Phys., **41**(20), p. 205302.

[106] Patel, M. R., Barrufet, M. A., Eubank, P. T., and DiBitonto, D. D., 1989, "Theoretical Models of the Electrical Discharge Machining

Process. II. The Anode Erosion Model," J. Appl. Phys., **66**(9), pp. 4104–4111.

[107] Das, S., Klotz, M., and Klocke, F., 2003, "EDM Simulation: Finite Element-Based Calculation of Deformation, Microstructure and Residual Stresses," J. Mater. Process. Technol., **142**(2), pp. 434–451.

[108] Mujumdar, S. S., Curreli, D., Kapoor, S. G., and Ruzic, D., 2015, "Modeling of Melt-Pool Formation and Material Removal in Micro-Electrodischarge Machining," J. Manuf. Sci. Eng. Trans. ASME, **137**(3).

[109] Zhang, F., Gu, L., and Zhao, W., 2015, "Study of the Gaussian Distribution of Heat Flux for Micro-EDM," *International Manufacturing Science and Engineering Conference*, American Society of Mechanical Engineers Digital Collection.

[110] Tan, P. C., and Yeo, S. H., 2008, "Modelling of Overlapping Craters in Micro-Electrical Discharge Machining," J. Phys. D. Appl. Phys., **41**(20).

[111] Jithin, S., Raut, A., Bhandarkar, U. V., and Joshi, S. S., 2018, "FE Modeling for Single Spark in EDM Considering Plasma Flushing Efficiency," Procedia Manuf., **26**, pp. 617–628.

[112] Dilip, D. G., Ananthan, S. P., Panda, S., and Mathew, J., 2019, "Numerical Simulation of the Influence of Fluid Motion in Mushy Zone during Micro-EDM on the Crater Surface Profile of Inconel 718 Alloy," J. Brazilian Soc. Mech. Sci. Eng., **41**(2), pp. 1–14.

[113] Ikai, T., Fujita, I., and Hashiguchi, K., 1992, "Heat Input Radius for Crater Formation in the Electric Discharge Machining," IEEJ Trans. Ind. Appl., **112**(10), pp. 943–949.

[114] Allen, P., and Chen, X., 2007, "Process Simulation of Micro Electro-Discharge Machining on Molybdenum," J. Mater. Process. Technol., **186**(1–3), pp. 346–355.

[115] Murali, M. S., and Yeo, S. H., 2005, "Process Simulation and Residual Stress Estimation of Micro-Electrodischarge Machining Using Finite Element Method," Japanese J. Appl. Physics, Part 1 Regul. Pap. Short Notes Rev. Pap., **44**(7 A), pp. 5254–5263.

[116] Kumar, R., and Yadava, V., 2008, "Finite Element Thermal Analysis of Micro-EDM," Int. J. Nanoparticles, **1**(3), pp. 224–240.

[117] Weingärtner, E., Kuster, F., and Wegener, K., 2012, "Modeling and Simulation of Electrical Discharge Machining," Procedia CIRP, **2**(1), pp. 74–78.

[118] Mujumdar, S. S., Curreli, D., Kapoor, S. G., and Ruzic, D., 2014, "Modeling of Melt-Pool Formation and Material Removal in Micro Electro-Discharge Machining," *ASME 2014 International Manufacturing Science and Engineering Conference, MSEC 2014*, American Society of Mechanical Engineers Digital Collection.

[119] Shao, B., and Rajurkar, K. P., 2015, "Modelling and Simulation of the Crater Formation Process in Micro-EDM," *International Conference on MicroManufacturing*, Research Publishing Services, pp. 58–61.

[120] Kuriachen, B., Varghese, A., Somashekhar, K. P., Panda, S., and Mathew, J., 2015, "Three-Dimensional Numerical Simulation of Microelectric Discharge Machining of Ti-6Al-4V," Int. J. Adv. Manuf. Technol., **79**(1–4), pp. 147–160.

[121] Somashekhar, K. P., Panda, S., Mathew, J., and Ramachandran, N., 2015, "Numerical Simulation of Micro-EDM Model with Multi-Spark," Int. J. Adv. Manuf. Technol., **76**(1–4), pp. 83–90.

[122] Guo, J., Zhang, G., Huang, Y., Ming, W., Liu, M., and Huang, H., 2014, "Investigation of the Removing Process of Cathode Material in Micro-EDM Using an Atomistic-Continuum Model," Appl. Surf. Sci., **315**(1), pp. 323–336.

[123] Chavoshi, S. Z., and Luo, X., 2015, "Hybrid Micro-Machining Processes: A Review," Precis. Eng., **41**, pp. 1–23.

[124] Rajput, V., Goud, M., and Suri, N. M., 2021, "Review on Recent Advances, Research Trends, and Gas Film in Electrochemical Discharge-Based Micromachining," J. Micro Nano-Manufacturing, **9**(1).

[125] Nau, B., Roderburg, A., and Klocke, F., 2011, "Ramp-up of Hybrid Manufacturing Technologies," CIRP J. Manuf. Sci. Technol., **4**(3), pp. 313–316.

[126] Rajurkar, K. P., Zhu, D., McGeough, J. A., Kozak, J., and De Silva, A., 1999, "New Developments in Electro-Chemical Machining," CIRP Ann., **48**(2), pp. 567–579.

[127] Tak, M., and Mote, R. G., 2021, "Anodic Dissolution Behavior of Passive Layer during Hybrid Electrochemical Micromachining of Ti6Al4V in NaNO3 Solution," J. Micro Nano-Manufacturing, **9**(4).

[128] Schuh, G., Kreysa, J., and Orilski, S., 2009, "'hybrid Production' Road Map," ZWF Zeitschrift fuer Wirtschaftlichen Fabrikbetr., **104**(5), pp. 385–391.

[129] Cao, P., Tong, H., and Li, Y., 2022, "Pulsed Power Supply Superposed With Radio Frequency Oscillating Wave for the Improvement of Micro-Electrical Discharge Machining Process," J. Micro Nano-Manufacturing, **10**(1).

[130] Sonia, P., Jain, J. K., and Saxena, K. K., 2021, "Influence of Ultrasonic Vibration Assistance in Manufacturing Processes: A Review," Mater. Manuf. Process., **36**(13), pp. 1451–1475.

[131] Tsai, M. Y., Fang, C. S., and Yen, M. H., 2018, "Vibration-Assisted Electrical Discharge Machining of Grooves in a Titanium Alloy (Ti-6A-4V)," Int. J. Adv. Manuf. Technol., **97**(1–4), pp. 297–304.

[132] Unune, D. R., and Mali, H. S., 2018, "Experimental Investigation on Low-Frequency Vibration-Assisted μ-ED Milling of Inconel 718," Mater. Manuf. Process., **33**(9), pp. 964–976.

[133] Prihandana, G. S., Mahardika, M., Hamdi, M., Wong, Y. S., and Mitsui, K., 2009, "Effect of Micro-Powder Suspension and Ultrasonic Vibration of Dielectric Fluid in Micro-EDM Processes-Taguchi Approach," Int. J. Mach. Tools Manuf., **49**(12–13), pp. 1035–1041.

[134] Liew, P. J., Yan, J., and Kuriyagawa, T., 2014, "Fabrication of Deep Micro-Holes in Reaction-Bonded SiC by Ultrasonic Cavitation Assisted Micro-EDM," Int. J. Mach. Tools Manuf., **76**, pp. 13–20.

[135] Mastud, S. A., Kothari, N. S., Singh, R. K., and Joshi, S. S., 2015, "Modeling Debris Motion in Vibration Assisted Reverse Micro Electrical Discharge Machining Process (R-MEDM)," J. Microelectromechanical Syst., **24**(3), pp. 661–676.

[136] Abdullah, A., Shabgard, M. R., Ivanov, A., and Shervanyi-Tabar, M. T., 2009, "Effect of Ultrasonic-Assisted EDM on the Surface Integrity of Cemented Tungsten Carbide (WC-Co)," Int. J. Adv. Manuf. Technol., **41**(3–4), pp. 268–280.

[137] Prihandana, G. S., Mahardika, M., Hamdi, M., Wong, Y. S., and Mitsui, K., 2009, "Effect of Micro-Powder Suspension and Ultrasonic Vibration of Dielectric Fluid in Micro-EDM Processes-Taguchi Approach," Int. J. Mach. Tools Manuf., **49**(12–13), pp. 1035–1041.

[138] Tsai, M. Y., Fang, C. S., and Yen, M. H., 2018, "Vibration-Assisted Electrical Discharge Machining of Grooves in a Titanium Alloy (Ti-6A-4V)," Int. J. Adv. Manuf. Technol. 2018 971, **97**(1), pp. 297–304.

[139] Tong, H., Li, Y., and Wang, Y., 2008, "Experimental Research on Vibration Assisted EDM of Micro-Structures with Non-Circular Cross-Section," J. Mater. Process. Technol., **208**(1–3), pp. 289–298.

[140] Garn, R., Schubert, A., and Zeidler, H., 2011, "Analysis of the Effect of Vibrations on the Micro-EDM Process at the Workpiece Surface," Precis. Eng., **35**(2), pp. 364–368.

[141] Lin, Y. C., Chuang, F. P., Wang, A. C., and Chow, H. M., 2014, "Machining Characteristics of Hybrid EDM with Ultrasonic Vibration and Assisted Magnetic Force," Int. J. Precis. Eng. Manuf., **15**(6), pp. 1143–1149.

[142] Mastud, S. A., Kothari, N. S., Singh, R. K., Samuel, J., and Joshi, S. S., 2014, "Analysis of Debris Motion in Vibration Assisted Reverse Micro Electrical Discharge Machining," p. V001T03A017.

[143] Mastud, S. A., Kothari, N. S., Singh, R. K., and Joshi, S. S., 2015, "Modeling Debris Motion in Vibration Assisted Reverse Micro Electrical Discharge Machining Process (R-MEDM)," J. Microelectromechanical Syst., **24**(3), pp. 661–676.

[144] Zhao, W., Wang, Z., Di, S., Chi, G., and Wei, H., 2002, "Ultrasonic and Electric Discharge Machining to Deep and Small Hole on Titanium Alloy," J. Mater. Process. Technol., **120**, pp. 101–106.

[145] Shitara, T., Fujita, K., and Yan, J., 2020, "Direct Observation of Discharging Phenomena in Vibration-Assisted Micro-Electrical Discharge Machining," Int. J. Adv. Manuf. Technol., **108**(4), pp. 1125–1138.

[146] Chang, W., Xi, Y., Li, H., Chen, S., Dong, B., Yang, Q., and Zhang, J., 2020, "Experimental Research on the MRR of Ultrasonic Vibration Aided Electric Discharge Milling of Ceramic Materials Using Deionized Water as Processing Medium," Mach. Sci. Technol., **24**(1), pp. 136–150.

[147] Schubert, A., Wolf, N., Zeidler, H., and Schneider, J., 2011, "Indirect Approach to Ultrasonic Superposition in Micro-EDM," pp. 427–434.

[148] Mollik, M. S., Saleh, T., Bin Md Nor, K. A., and Ali, M. S. M., 2022, "A Machine Learning-Based Classification Model to Identify the Effectiveness of Vibration for MEDM," Alexandria Eng. J., **61**(9), pp. 6979–6989.

[149] Singh, J., Satsangi, P. S., Walia, R. S., and Singh, V. P., 2011, "Micro-Hardness and Machined Surface Damage Study for Continuous and Discontinuous Ultrasonic Vibration Assisted Electrical Discharge Machining," Mater. Manuf. Process.

[150] Jafferson, J. M., Hariharan, P., and Ram Kumar, J., 2014, "Effects of Ultrasonic Vibration and Magnetic Field in Micro-EDM Milling of Nonmagnetic Material," Mater. Manuf. Process., **29**(3), pp. 357–363.

[151] Sabyrov, N., Jahan, M. P., Bilal, A., and Perveen, A., 2019, "Ultrasonic Vibration Assisted Electro-Discharge Machining (EDM)-An Overview," Materials (Basel)., **12**(3).

[152] Zhang, J. H., Lee, T. C., Lau, W. S., and Ai, X., 1997, "Spark Erosion with Ultrasonic Frequency," J. Mater. Process. Technol., **68**(1), pp. 83–88.

[153] Uhlmann, E., and Domingos, D. C., 2016, "Investigations on Vibration-Assisted EDM-Machining of Seal Slots in High-Temperature Resistant Materials for Turbine Components -Part II," Procedia CIRP, **42**, pp. 334–339.

[154] Thoe, T. B., Aspinwall, D. K., and Killey, N., 1999, "Combined Ultrasonic and Electrical Discharge Machining of Ceramic Coated Nickel Alloy," J. Mater. Process. Technol., **92**–**93**, pp. 323–328.

[155] Sundaram, M. M., Billa, S., and Rajurkar, K. P., 2009, "Generation of High Aspect Ratio Micro Holes by a Hybrid Micromachining Process," pp. 243–248.

[156] Xing, Q., Yao, Z., and Zhang, Q., 2021, "Effects of Processing Parameters on Processing Performances of Ultrasonic Vibration-Assisted Micro-EDM," Int. J. Adv. Manuf. Technol., **112**(1–2), pp. 71–86.

[157] Hirao, A., Gotoh, H., and Tani, T., 2018, "Some Effects on EDM Characteristics by Assisted Ultrasonic Vibration of the Tool Electrode," Procedia CIRP, **68**(April), pp. 76–80.

[158] Kishore, H., Nirala, C. K., and Agrawal, A., 2020, "Feasibility Demonstration of MEDM for Fabrication of Arrayed Micro Pin-Fins

of Complex Cross-Sections," Manuf. Lett., **23**, pp. 14–18.

[159] Schubert, A., Zeidler, H., Oschätzchen, M. H., Schneider, J., and Hahn, M., 2013, "Enhancing Micro-EDM Using Ultrasonic Vibration and Approaches for Machining of Nonconducting Ceramics," Strojniški Vestn. – J. Mech. Eng., **59**(3), pp. 156–164.

[160] Ghiculescu, D., Marinescu, N., Nanu, S., and Ghiculescu, D., 2011, "Equipment for Ultrasonic Aiding of Wire Electrodischarge Machining," Acad. J. Manuf. Eng., **9**(2), pp. 18–23.

[161] Ichikawa, T., and Natsu, W., 2013, "Realization of Micro-EDM under Ultra-Small Discharge Energy by Applying Ultrasonic Vibration to Machining Fluid," Procedia CIRP, **6**, pp. 326–331.

[162] Unune, D. R., and Mali, H. S., 2017, "Experimental Investigation on Low-Frequency Vibration Assisted Micro-WEDM of Inconel 718," Eng. Sci. Technol. an Int. J., **20**(1), pp. 222–231.

[163] Lee, P. A., Kim, Y., and Kim, B. H., 2015, "Effect of Low Frequency Vibration on Micro EDM Drilling," Int. J. Precis. Eng. Manuf., **16**(13), pp. 2617–2622.

[164] Unune, D. R., and Mali, H. S., 2014, "Current Status and Applications of Hybrid Micro-Machining Processes: A Review," http://dx.doi.org/10.1177/0954405414546141, **229**(10), pp. 1681–1693.

[165] Jahan, M. P., Wong, Y. S., and Rahman, M., 2012, "Evaluation of the Effectiveness of Low Frequency Workpiece Vibration in Deep-Hole Micro-EDM Drilling of Tungsten Carbide," J. Manuf. Process., **14**(3), pp. 343–359.

[166] Jahan, M. P., Rahman, M., Wong, Y. S., and Fuhua, L., 2009, "On-Machine Fabrication of High-Aspect-Ratio Micro-Electrodes and Application in Vibration-Assisted Micro-Electrodischarge Drilling of Tungsten Carbide," http://dx.doi.org/10.1243/09544054JEM1718, **224**(5), pp. 795–814.

[167] Singh, S. K., and Mali, H. S., 2022, "Workpiece Dependency Exploration & Probabilistic Nonparametric Modelling of Vibration-Assisted Hybrid Micro-EDM Process," Arab. J. Sci. Eng., pp. 1–15.

[168] Singh, S. K., Mali, H. S., Unune, D. R., Abdul-Rani, A. M., and Wojciechowski, S., 2022, "Material Independent Effectiveness of Workpiece Vibration in μ-EDM Drilling," J. Mater. Res. Technol., **18**, pp. 531–546.

[169] Unune, D. R., and Mali, H. S., 2020, "Dimensional Accuracy and Surface Quality of Micro-Channels with Low-Frequency Vibration Assistance in Micro-Electro-Discharge Milling," Adv. Mater. Process. Technol.

[170] Unune, D. R., Nirala, C. K., and Mali, H. S., 2019, "Accuracy and Quality of Micro-Holes in Vibration Assisted Micro-Electro-Discharge Drilling of Inconel 718," Meas. J. Int. Meas. Confed., **135**, pp. 424–437.

[171] Raza, S., Nadda, R., and Nirala, C. K., 2022, "Discharge Pulse Analysis Based Machining Responses in Vibration Assisted MEDM Processes," Mapan - J. Metrol. Soc. India, pp. 1–16.

[172] Ogino, Y., Hirata, Y., Kawata, J., and Nomura, K., 2013, "Numerical Analysis of Arc Plasma and Weld Pool Formation by a Tandem TIG Arc," Weld. World, **57**(3), pp. 411–423.

[173] Zhou, X., Zhang, H., Wang, G., and Bai, X., 2016, "Three-Dimensional Numerical Simulation of Arc and Metal Transport in Arc Welding Based Additive Manufacturing," Int. J. Heat Mass Transf., **103**, pp. 521–537.

[174] Zheng, S., Liu, Y., Liu, J., Gong, Y., and Wang, X., 2004, "Two-Dimensional Numerical Simulation on Evolution of Arc Plasma," *Vacuum*, Pergamon, pp. 373–379.

[175] Almeida, N. A., and Benilov, M. S., 2008, "Understanding and Modelling Plasma–Electrode Interaction in High-Pressure Arc Discharges: A Review," J. Phys. D. Appl. Phys., **41**(14), p. 144001.

[176] Takeuchi, H., and Kunieda, M., 2007, "Effects of Volume Fraction of Bubbles in Discharge Gap on Machining Phenomena of EDM," *Proceedings of the 15th International Symposium on Electromachining, ISEM 2007*, pp. 63–68.

[177] YOSHIDA, M., and KUNIEDA, M., 1996, "Study on the Distribution of Scattered Debris Generated by a Single Pulse Discharge in EDM Process.," J. Japan Soc. Electr. Mach. Eng., **30**(64), pp. 27–36.

[178] Kojima, A., Natsu, W., and Kunieda, M., 2008, "Spectroscopic Measurement of Arc Plasma Diameter in EDM," CIRP Ann. - Manuf. Technol., **57**(1), pp. 203–207.

[179] Wang, C., **王春林**, Wu, Y., **吴翊**, Chen, Z., 陈喆歆, Yang, F., 杨飞, Feng, Y., 冯英, Rong, M., **荣命哲**, Zhang, H., and 张含天, 2016, "Thermodynamic and Transport Properties of Real Air Plasma in Wide Range of Temperature and Pressure*," Plasma Sci. Technol., **18**(7), p. 732.

[180] Shao, B., and Rajurkar, K. P., 2015, "Modelling of the Crater Formation in Micro-EDM," *Procedia CIRP*, Elsevier B.V., pp. 376–381.

[181] Singh, M., Saxena, P., Ramkumar, J., and Rao, R. V., 2020, "Multi-Spark Numerical Simulation of the Micro-EDM Process: An Extension of a Single-Spark Numerical Study," Int. J. Adv. Manuf. Technol., **108**(9–10), pp. 2701–2715.

[182] Liu, Q., Zhang, Q., Zhang, M., and Yang, F., 2020, "Study on the Discharge Characteristics of Single-Pulse Discharge in Micro-EDM," Micromachines, **11**(1), p. 55.

[183] Sisodiya, M. S., Shukla, S., and Bajpai, V., 2022, "Feasibility Analysis of Novel Maglev EDM by Comparing with Conventional Micro EDM," Sci. Rep., **12**(1), pp. 1–13.

[184] Dauw, D. F., Snoeys, R., and Dekeyser, W., 1983, "Advanced Pulse Discriminating System for EDM Process Analysis and Control," CIRP Ann. - Manuf. Technol., **32**(2), pp. 541–549.

[185] Dauw, D. F., R. Snoeys, and W. D., 1983, "EDM Electrode Wear Analysis by Real Time Pulse Detection," *11th NAMRC, North American Manufacturing Research Conference Proceedings*.

[186] Snoeys R, C. H., "Correlation between Electro-discharge Machining Data and Machine Settings," CIRP Ann., **24**(1), pp. 83–88.

[187] Nirala, C. K., Unune, D. R., and Sankhla, H. K., 2017, "Virtual Signal-Based Pulse Discrimination in Micro-Electro-Discharge Machining," J. Manuf. Sci. Eng., **139**(9), p. 094501.

[188] Yeo, S. H., Aligiri, E., Tan, P. C., and Zarepour, H., 2009, "An Adaptive Speed Control System for Micro Electro Discharge Machining," *AIP Conference Proceedings*, AIP Publishing, pp. 61–72.

[189] Pey Tee, K. Ter, Hosseinnezhad, R., Brandt, M., and Mo, J., 2013, "Pulse Discrimination for Electrical Discharge Machining with Rotating Electrode," Mach. Sci. Technol., **17**(2), pp. 292–311.

[190] Nirala, C. K., and Saha, P., 2016, "Evaluation of MEDM-Drilling and MEDM-Dressing Performances Based on Online Monitoring of Discharge Gap Conditions," Int. J. Adv. Manuf. Technol., **85**(9–12), pp. 1995–2012.

[191] Kishore, H., Nadda, R., Nirala, C. K., and Agrawal, A., 2019, "Modelling and Simulation Based Surface Characterization of Reverse- MEDM Fabricated Micro Pin-Fins," Procedia CIRP, **81**, pp. 1230–1235.

[192] Zhang, C., Zhou, J., and Shen, H., 2017, "Role of Capillary and Thermocapillary Forces in Laser Polishing of Metals," J. Manuf. Sci. Eng. Trans. ASME, **139**(4).

[193] He, X., Elmer, J. W., and Debroy, T., 2005, "Heat Transfer and Fluid Flow in Laser Microwelding," J. Appl. Phys., **97**(8).

[194] Li, K., Zhao, Z., Zhou, H., Zhou, H., and Jin, J., 2020, "Numerical Analyses of Molten Pool Evolution in Laser Polishing Ti6Al4V," J. Manuf. Process., **58**, pp. 574–584.

[195] Sharma, S., Mandal, V., Ramakrishna, S. A., and Ramkumar, J., 2018, "Numerical Simulation of Melt Hydrodynamics Induced Hole Blockage in Quasi-CW Fiber Laser Micro-Drilling of TiAl6V4," J. Mater. Process. Technol., **262**, pp. 131–148.

[196] MORVILLE, S., CARIN, M., MULLER, M., GHARBI, M., PEYRE, P., CARRON, D., LE, P., MASSON, and R. FABBRO, 2010, "2D Axial-Symmetric Model for Fluid Flow and Heat Transfer in the Melting and Resolidification of a Vertical Cylinder," *Proceedings of the COMSOL Conference 2010 Paris*.

[197] KC Mills, 2002, *Recommended Values of Thermophysical Properties for Selected Commercial Alloys*, Woodhead Publishing Ltd, Cambridge.